Constraining new physics with fiducial measurements at the LHC

David Paul Yallup
of University College London

A dissertation submitted to University College London
for the degree of Doctor of Philosophy

Declaration

I, David Paul Yallup confirm that the work presented in this thesis is my own. Where information has been derived from other sources, I confirm that this has been indicated in the thesis.

David Yallup

Abstract

As Run 2 of the LHC completes, a vast set of particle collision data has been recorded by the experimental collaborations on the ring. This has enabled the collaborations to perform many measurements of fiducial particle collision properties, which have been found to be in good agreement with predictions from the Standard Model of particle physics. This collected data has also been used to perform many searches for a variety hypothesised extensions to the Standard Model, which have thus far not observed any significant sign of new physics. In this thesis contributions to the precision measurement program within the ATLAS collaboration at the LHC are presented. These contributions are primarily made to the measurement of detector corrected observables sensitive to large imbalances of momentum observed in the transverse plane. Additionally the opportunity of using such precision fiducial measurements to understand the nature of physics beyond the Standard Model is explored. This is found to give rise to interesting, competitive and complementary information to that derived from the dedicated searches. This work has led to the release of a publicly available program that can be used to automatically confront a hypothesised physics model with precision LHC measurement data. This program is called CONTUR and applications of this to a variety of hypothesised physics models are presented.

Impact Statement

The impact of this work inside of academia is mostly covered in the thesis itself. A measurement was made using data recorded at the ATLAS experiment at the LHC of a final state that previously had not been made. An investigation was also carried out in this work into using the measured data in a novel way, applying measurements of predicted processes to constrain potential hypothesised signals of new physics. The impact of this work outside of the field will mostly be via techniques developed to increase to legacy of the collider data. By maximizing the utility of the data taken going forward, the vast person power and money invested into the LHC will be useful for years to come.

Acknowledgements

First and foremost I would like to thank my supervisor Jon. This PhD has been an opportunity to follow a unique path, and without the opportunities and support to pursue this route, the work shown here wouldn't have been possible.

The work presented in this thesis has always been dependant on collaboration, for the phenomenological work presented I'd like to particularly thank all the collaborators on CONTUR and Rivet throughout the years. Within ATLAS I'd like to thank all members of the METJet analysis team, and Alex for teaching me the ins and outs of ATLAS software.

I gratefully acknowledge the award of an STFC studentship that funded this work. I would also like the thank MCnet, via European Union's Horizon 2020 research and innovation programme under the Marie Sklodowska-Curie grant agreement No 722104 (MCnetITN3), for additional funding affording some unique travel and learning opportunities. In particular Stefan Gieseke and all of the ITP members in Karlsruhe for hosting me during my stay there.

Contents

Chapter 1.

Introduction

In this thesis various aspects of the precision measurement program at current high energy particle colliders will be explored. The focus of the work is on the LHC and its associated experimental collaborations, particularly ATLAS, a collaboration of which the author is a member. The LHC has embarked, and continues to make excellent progress, on a vast program of precision measurements of various properties and processes predicted by the Standard Model. The LHC experiments also conduct a varied program of searches for signs of physics beyond the Standard Model, which thus far have not observed any significant deviation from the Standard Model. These two types of results are different in their apparent goals, but similar in many ways. This work primarily explores how the precision measurement program can be used to inform the available space for physics beyond the Standard Model, as an alternative approach to direct searches for such effects.

This thesis begins in Chapter 2, where a review of the Standard Model of particle physics is presented. A particular focus is given to the implementation of this theory in event generators as a predictive tool for the LHC experiments. Some samples of contributions the author has made as the ATLAS Herwig event generator expert are shown to demonstrate how these tools work. Some motivation for investigation beyond the Standard Model is also given.

In Chapter 3 a review of the ATLAS experiment and the LHC accelerator are given, to motivate how one constructs a measurement of particle collisions and the limitations one faces when working with ATLAS. Contributions the author made to the ATLANTIS event display are also shown, a component of the ATLAS online monitoring software used in data taking.

Chapter 4 brings these two concepts together, reviewing how one makes a particle level measurement with the ATLAS detector. A measurement of particle level missing energy is presented, which the author contributed to in preliminary studies. Ongoing work on the next generation of a similar measurement with an expanded dataset is presented, highlighting contributions made in optimally designing this measurement for reinterpretation.

With the concept of making a particle level measurement at the LHC defined, the focus of this thesis shifts into how one can utilise these measurements. Chapter 5 introduces the mechanics of reinterpreting LHC results, developing the tools needed to construct limits on physics beyond the Standard Model. The main purpose is to develop the methods needed to make use of the types of particle level measurements detailed in the previous chapters, in a beyond the Standard Model reinterpretation context. Comparison to the more typical LHC reinterpretation tools that utilise the various null detector level search results to set limits is made, where appropriate. The toolkit developed as a result is dubbed Contur, of which the author is one of the primary developers.

Applications of Contur are then demonstrated in Chapter 6. The methodology is applied to some example hypothesised extensions to the Standard Model, where Contur is used to highlight regions in the models that demonstrate tension with the precision measurement program. Where appropriate comparison is drawn to the typical approach of transposing null search results for different models onto the target model. Future directions of the Contur approach are also highlighted.

It is hoped that this thesis will provide insight on the LHC physics program by approaching the problem of making sense of the vast breadth and depth of results from an atypical angle. The overarching problem of identifying physics beyond the Standard Model is one that is going on on many fronts, beyond the LHC and beyond the scope of particle physics even. This body of work represents some steps taken that aim to contribute to the larger picture in two ways. Firstly by performing a measurement with the ATLAS detector of a final state that is not typically measured, and is designed to be sensitive to some hypothesised extensions to physics beyond the Standard Model. Secondly by making sense, in a systematic repeatable fashion, of what has been measured at the LHC using Contur. It is hoped that going forward as ever more precise measurements are made, Contur will continue to be a useful guide.

Chapter 2.

Predictions at the energy frontier

The theoretical model underpinning modern particle physics experimentation is often touted as one of the most accurately tested theories in all of physics. It was realised in its current form as early as the 1970's and has undergone an examination at increasing energy and intensity ever since. Whilst there are some phenomena the model fails to provide an explanation for, it can explain with a good level of agreement observables across a wide range of energies and intensities. This model is known as the Standard Model of particle physics (SM).

In this chapter a brief summary of the construction of the SM is given in Section 2.1. This is a well established construction so in this review key elements of the standard formulation will be highlighted. More detail is given in Section 2.2 to making predictions of high energy particle collisions using the SM, particularly focusing on aspects of the strong nuclear force, as this has a dominant influence on hadron collision physics. In Section 2.3 a review of how these models are technically implemented for LHC physics is given. Lastly some review of the deficiencies and consequent extensions of the SM are presented in Section 2.4.

2.1. The Standard Model

The SM is a relativistic Quantum Field Theory (QFT) based on a $\mathrm{SU}(3)_C \times \mathrm{SU}(2)_L \times \mathrm{U}(1)_Y$ gauge symmetry. The formal construction of this is well established and reviewed in plenty of standard texts [1, 2]. The summary given here is intended to highlight some important features and follows notation and definition conventions from these sources. Figure 2.1 shows the particle content of the SM. This can be subdivided into fermions, or matter particles, with half integer spin and bosons, or force carriers, with integer spin. The predicted particle content of the SM has been defined for some time, and a focus of particle physics experimentation over the course of the previous 50 years has been to confirm this structure. The final fermionic particle content was realised in the quark sector with the observation of the top quark at the

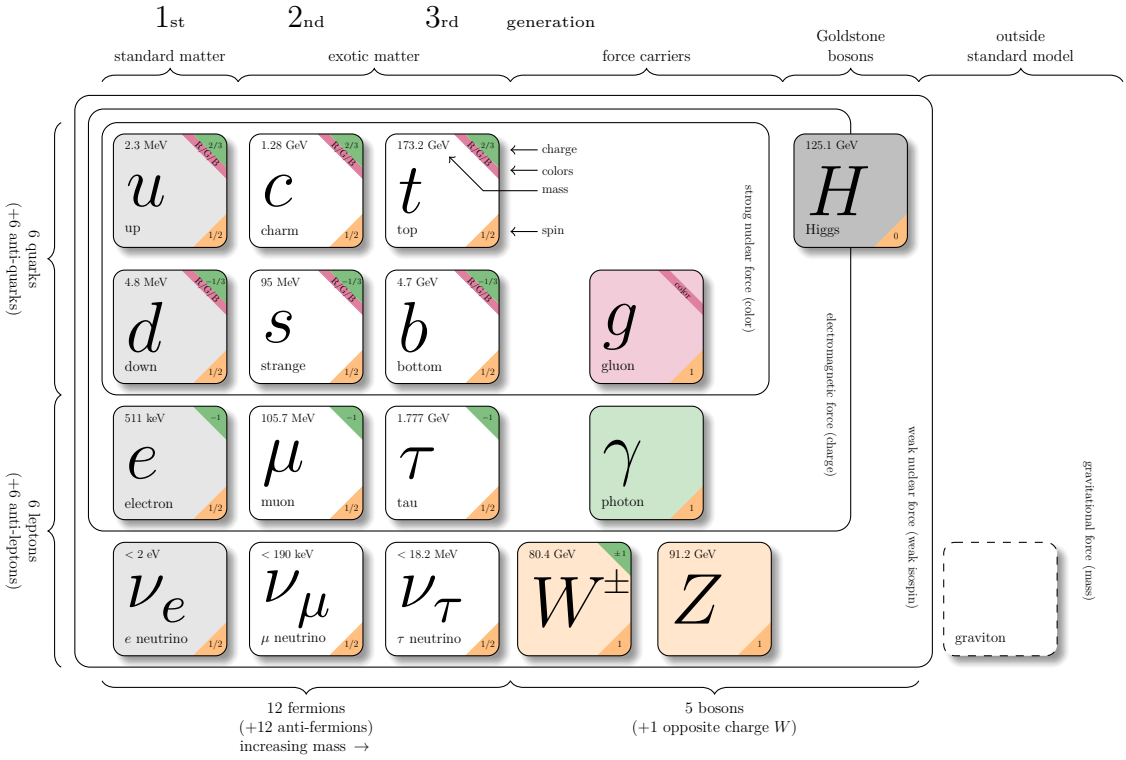

Figure 2.1.: A representation of the particle content of the SM [8].

Tevatron at Fermilab in the 90's [3, 4], and in the lepton sector by the observation of the tau neutrino shortly after [5]. The final piece missing in the run up to the commencement of LHC operation, was the observation of the Higgs boson, and indeed the observation of this particle was one of the fundamental design goals of the ATLAS and CMS experiments. Observations conforming with the expectations of a SM Higgs boson occurred during the first run of the LHC by the ATLAS and CMS collaborations [6, 7]. Continual experimentation has revealed this observation to be consistent with the SM, this is considered now to complete the experimental observation of the SM particle content.

Notation in this thesis is given in natural units ($\hbar = c = 1$), where dimensional quantities are given they are typically expressed in units of electron volts (eV).

2.1.1. A model for electroweak physics

The larger $\mathrm{SU}(3)_C \times \mathrm{SU}(2)_L \times \mathrm{U}(1)_Y$ symmetry group contains within it an electroweak (EW) symmetry, denoted $\mathrm{SU}(2)_L \times \mathrm{U}(1)_Y$. Often this is referred to as the Glashow-Salam-Weinberg

model [9–11]. Fermion fields, ψ, are described by a Dirac Lagrangian ($\mathcal{L}_{\text{Dirac}}$) as,

$$\mathcal{L}_{\text{Dirac}} = \bar{\psi}(i\gamma^{\mu}\partial_{\mu} - m)\psi\,. \tag{2.1}$$

Gauge transformations of the fields under $\text{SU}(2)_L$ and $U(1)_Y$ rotations can be written as,

$$\psi \to \psi' = \left[e^{-i\tau_k\omega_k(x)} + e^{-iY\mathbb{1}\alpha(x)}\right]\psi\,, \tag{2.2}$$

with τ_k being the generators of $\text{SU}(2)_L$ and $\omega_k(x)$ being the 'angle' of rotation. In the same manner Y and $\alpha(x)$ are the generator and angle of the $U(1)_Y$ transformation. The angles of rotation are taken in the infinitesimal limit. In order for the kinetic term of the lagrangian to be invariant under these transformations, the partial derivative is replaced by the gauge covariant derivative, D_{μ}, defined as,

$$D_{\mu} = \partial_{\mu}\mathbb{1} - ig\tau_k W_k^{\mu}(x) - ig'Y\mathbb{1}B^{\mu}(x)\,, \tag{2.3}$$

where $W_k^{\mu}(x)$ are introduced as the gauge fields, with gauge coupling strength g, for the $\text{SU}(2)_L$ transformation. Similarly $B^{\mu}(x)$ and g' are the gauge field and coupling corresponding to the $U(1)_Y$ transformation. The gauge fields transform under the gauge transformations such that $D_{\mu}\psi$ transforms as ψ did. Revisiting the Dirac Lagrangian, this can now be upgraded to a form that is invariant under the imposed symmetry groups,

$$\mathcal{L}_{\text{EW}} = \bar{\psi}(\not{D}_{\mu})\psi - \frac{1}{4}W_{k,\mu\nu}W_k^{\mu\nu} - \frac{1}{4}B_{\mu\nu}B^{\mu\nu}\,. \tag{2.4}$$

The dual field strength tensors have been introduced, the dual field of the $\text{SU}(2)_L$ gauge field is defined as,

$$W_{k,\mu\nu} = \partial_{\mu}W_{k,\nu} - \partial_{\nu}W_{k,\mu} - g\epsilon_{kqp}W_{q,\nu}W_{p,\nu}\,, \tag{2.5}$$

with ϵ_{ijk} being the structure constants of the Lie algebra of the group. The abelian $U(1)_Y$ group has a similarly defined dual field, but due to its abelian nature the structure constant in this case is vanishing. The terms involving these expressions correspond to gauge boson kinetic terms which are also invariant under $\text{SU}(2)_L \times \text{U}(1)_Y$. The generic fermion fields can be expanded to the standard model fermions, since the SM is a chiral theory the fields are decomposed into left and right handed components. Left handed fermion spinors ψ_L are arranged into doublets with weak isospin $T = \frac{1}{2}$ and right handed spinors ψ_R are singlets with $T = 0$. Table 2.1 shows the quantum numbers of the generations of both left and right handed fermions under the EW symmetry groups.

Mass terms for all fields have been omitted at this stage, naive gauge boson mass terms such as $\frac{1}{2}m_V V_{\mu}V^{\mu}$ wouldn't be gauge invariant under $\text{SU}(2)_L \times \text{U}(1)_Y$ rotations so an alternative

	Generation			EW Quantum Numbers			
	1^{st}	2^{nd}	3^{rd}	T	T^3	Y	Q
quarks	u_L	c_L	t_L	$\frac{1}{2}$	$+\frac{1}{2}$	$+\frac{1}{3}$	$+\frac{2}{3}$
	d_L	s_L	b_L	$\frac{1}{2}$	$-\frac{1}{2}$	$+\frac{1}{3}$	$-\frac{1}{3}$
	u_R	c_R	t_R	0	0	$+\frac{4}{3}$	$+\frac{2}{3}$
	d_R	s_R	b_R	0	0	$-\frac{2}{3}$	$-\frac{1}{3}$
leptons	$\nu_{e,L}$	$\nu_{\mu,L}$	$\nu_{\tau,L}$	$\frac{1}{2}$	$+\frac{1}{2}$	-1	0
	$\nu_{e,R}$	$\nu_{\mu,R}$	$\nu_{\tau,R}$	0	0	0	0
	e_L	μ_L	τ_L	$\frac{1}{2}$	$-\frac{1}{2}$	-1	-1
	e_R	μ_R	τ_R	0	0	-2	-1

Table 2.1.: SM fermion properties under the EW group symmetries. The quantum numbers given are; weak isospin T with eigenvalues T^3, hypercharge Y and electric charge $Q = T^3 + Y/2$.

mass generation mechanism is needed. The chiral nature of the theory means Dirac mass terms for the fermion fields are also not gauge invariant under $\mathrm{SU}(2)_L \times \mathrm{U}(1)_Y$ transformations so will also need an alternative mechanism. The right handed neutrinos shown in Table 2.1 are often omitted from the formal construction of the SM as they have not been observed experimentally, but they appear in many hypothesised models for generating the experimentally observed neutrino masses [12, 13].

2.1.2. Electroweak symmetry breaking

The Brout-Englert-Higgs mechanism [14, 15] can be used to introduce gauge invariant mass terms for the particles into equation (2.4). A new hypothesised field is added which has gauge invariant transformations under $\mathrm{SU}(2)_L \times \mathrm{U}(1)_Y$ and a non vanishing vacuum expectation value. This is a complex scalar, isospin doublet with hypercharge $Y = \frac{1}{2}$,

$$\Phi = \frac{1}{\sqrt{2}} \begin{pmatrix} \phi_1 + i\phi_2 \\ \phi_3 + i\phi_4 \end{pmatrix}, \tag{2.6}$$

which then has its own Lagrangian using the covariant derivative as defined in equation (2.3),

$$\mathcal{L}_\Phi = (D_\mu \Phi)^\dagger (D^\mu \Phi) - V(\Phi) = (D_\mu \Phi)^\dagger (D^\mu \Phi) - \lambda (\Phi^\dagger \Phi)^2 + \mu^2 (\Phi^\dagger \Phi)\,. \tag{2.7}$$

Working in the unitary gauge, and finding the values of Φ that minimize the potential $V(\Phi)$. One finds degenerate solutions (under gauge transformations) for the ϕ_i component fields that minimize this. Convention is to choose $\phi_0 = \phi_1 = \phi_4 = 0$ and $\phi_3 = v + h(x)$, with the vacuum expectation value (vev) introduced as $v = \mu/\sqrt{\lambda}$. The vev is defined by the coefficients of $V(\Phi)$ where $\mu^2 > 0$ gives spontaneous symmetry breaking. The residual scalar field, $h(x)$, is identified as the Higgs field, representing excitations along the axis of the vacuum. Choosing a vev spontaneously breaks the $\mathrm{SU}(2)_L \times \mathrm{U}(1)_Y$ symmetry to a residual $U(1)_{\mathrm{EM}}$ symmetry below the EW symmetry breaking scale (EWSB). The vanishing degrees of freedom under $\mathrm{SU}(2)_L$ rotations in Φ correspond to goldstone bosons and are 'eaten' to give mass to the associated gauge fields of the gauge transformation. Φ can be written after symmetry breaking as,

$$\Phi = \frac{1}{\sqrt{2}} \begin{pmatrix} 0 \\ v + h(x) \end{pmatrix}. \tag{2.8}$$

This form of Φ can then be reinserted into equation (2.7). Expanding the kinetic, $(D_\mu \Phi)^\dagger (D^\mu \Phi)$, term gives rise to a series of terms determining interactions of the gauge bosons with the vacuum and the Higgs field. First a re-parameterization of the gauge fields is made that gives the physical gauge bosons,

$$W_\mu^\pm = \frac{1}{\sqrt{2}}(W_\mu^1 \mp i W_\mu^2)\,, \tag{2.9}$$

$$Z_\mu = \frac{1}{\sqrt{g^2 + g'^2}}(g W_\mu^3 - g' B_\mu)\,, \tag{2.10}$$

$$A_\mu = \frac{1}{\sqrt{g^2 + g'^2}}(g' W_\mu^3 - g B_\mu)\,. \tag{2.11}$$

Collecting the terms from the expansion of the kinetic term in the form as above, one finds that mass terms (functions of v) appear for $W_\mu^\pm$ and Z_μ, with $m_W = gv/2$ and $m_Z = (\sqrt{g^2 + g'^2})v/2$. Additional interaction terms including interactions with the Higgs field are also generated.

Fermion masses can now be incorporated as well by using the Higgs doublet, Φ. Taking an example of just the first generation of quarks and defining the $\mathrm{SU}(2)_L$ double for left handed quarks as $Q_L = (u_L, d_L)$, a *Yukawa* term Lagrangian can be written,

$$\mathcal{L}_{\mathrm{Yukawa}} = -\lambda_d Q_L \Phi d_R - \lambda_u Q_L \tilde{\Phi} u_R + \mathrm{h.c.}\,. \tag{2.12}$$

Here λ_q are the Yukawa couplings of the respective quark types, h.c. refers to the addition of the Hermitian conjugate of the expression and the conjugate Higgs doublet is introduced as $\tilde{\Phi} = i\tau_2 \Phi^\star$. Expansion with the form of the Higgs doublet after symmetry breaking gives mass

terms of the form $m_q q_L q_R$ where $m_{u,d} = \lambda_{u,d} v/\sqrt{2}$. When including all generations there is the possibility to have non zero Yukawa couplings that mix flavour generations. These would not be physical mass terms but the resultant general complex matrix can be diagonalised by rotation from flavour basis to mass basis by a unitary matrix. This rotation gives rise to CP violation in charged current interactions, parametrized by the CKM matrix [16,17] in the quark sector and the PMNS matrix [18,19] in the lepton sector. Yukawa mass terms for the neutrinos are often omitted from the SM construction due to the lack of observation of the right handed neutrinos. Including them would also require a very large hierarchy in the Yukawa coupling strengths to explain the observed very small neutrino masses, this is considered as motivation for an alternative mechanism to generate neutrino masses.

2.1.3. A model of the strong nuclear force

In addition to the symmetry groups described so far, a $\mathrm{SU}(3)_C$ symmetry is imposed on the quark sector. This corresponds to the strong nuclear force and its interactions are described by Quantum Chromodynamics (QCD) [20,21]. Much of the structure and notation of the resultant gauge interactions are the same as for the SU(2) discussed already, but there are important differences in the consequences of the expanded SU(3) group. Analogously to the dual field strength tensor for the SU(2) group in equation (2.5), the QCD dual field strength tensor can be written as,

$$G_{k,\mu\nu} = \partial_\mu G_{k,\nu} - \partial_\nu G_{k,\mu} - g_s f_{kqp} G_{q,\nu} G_{p,\nu}\,, \tag{2.13}$$

where g_s is the strong coupling, often for convenience in calculations written as $\alpha_s = g_s^2/4\pi$, and f_{kqp} is the structure function of the SU(3) group. This is derived in the same manner as the SU(2) case, introducing a gauge transformation and imposing local gauge invariance on the Lagrangian. A representation of the generators of this gauge group are the Gell-Mann matrices whose Lie algebra define the structure function. The Casimir constant of the group C_A defined by summing over the adjoint representation can be written in the general SU(N) case and specifically for SU(3) as, $C_A = N = 3$. Additional constants appearing in physical calculations based off the group algebra are $T_R = \frac{1}{2}$ and $C_F = (N^2-1)/2N = 4/3$. Quark fields are colour triplets in the fundamental representation of SU(3) and the gluons form an octet in the adjoint representation. Experimentally observable bound states of quarks are colour singlets (or *colourless*).

To make a prediction in an interacting QFT such as the SM, the scattering amplitude between initial and final state particles is calculated. Provided the coupling strength is sufficiently small amplitudes can be calculated using perturbation theory, expanding as a power series in the coupling parameter. This can be represented diagrammatically by Feynman diagrams, which

represent the Feynman rules of the theory. These Feynman rules can be derived from the Lagrangian components shown already and are given explicitly in the reference texts to these sections. One feature that will be expanded on is the presence of divergences in the calculations that appear as higher order QCD corrections are included into the scattering amplitude. In a QFT there will be ultraviolet (UV) divergences manifest in diagrams containing loops, the UV divergence corresponds to very large loop momenta. The SM has been proven to be a renormalizable QFT [22]. Renormalization is a procedure which involves including a scale in the theory, μ_R, above which the UV divergences are removed. However this leaves a residual dependence on the choice of this scale, which will not be manifest in any physical observable. The coupling therefore will *run*, i.e. its strength will depend on the scale it is evaluated at. The beta function defines the scale (Q^2) dependence of the coupling via the renormalization group equation (RGE),

$$Q^2 \frac{\partial \alpha_s}{\partial Q^2} = \beta(\alpha_s)\,. \tag{2.14}$$

The QCD β function has a perturbative expansion in powers of the strong coupling as,

$$\beta(\alpha_s) = -\beta_0 \alpha_s^2 (1 + \beta_1 \alpha_s + \beta_2 \alpha_s^2 + O(\alpha_s^3))\,, \tag{2.15}$$

where the β_i coefficients are parameters dependant on the number of active (entering the calculation at the scale Q^2) quark flavours, n_f and the Casimir constants of the group. The first coefficient is given as $\beta_1 = (11C_A - 2n_f)/12\pi$. This β function of QCD be negative for $n_f \leq 16$, whereas the analogous QED beta function is positive. The couplings of the two forces run in opposite directions.

Taking equation (2.14) and equation (2.15) as a partial differential equation in $\alpha_s(Q^2)$, and considering only terms up to β_1 results in,

$$\alpha_s(Q^2) = \frac{\alpha_s(\mu_R^2)}{1 + \alpha_s(\mu_R^2)\beta_0 \log \frac{Q^2}{\mu_R^2}}\,. \tag{2.16}$$

As Q^2 is increased the running coupling $\alpha_s(Q^2)$ tends to 0. This phenomena is termed *asymptotic freedom*, and is observed experimentally by extracting a value for the running coupling at different scales, as shown in Figure 2.2. Calculations involving a perturbative expansion in the strong coupling parameter will be increasingly valid for large Q^2, or in the *hard* regime. However perturbative QCD in the small Q^2, or *soft* regime, will be increasingly invalid and this breakdown of a perturbative description leads to the observed phenomena of *confinement*, that is that the quarks and gluons are confined to be bound inside hadrons [24]. Confinement was a proven phenomena for Yang Mills gauge theories by application of *lattice* techniques, such non-pertubative approaches are needed when the field becomes strongly

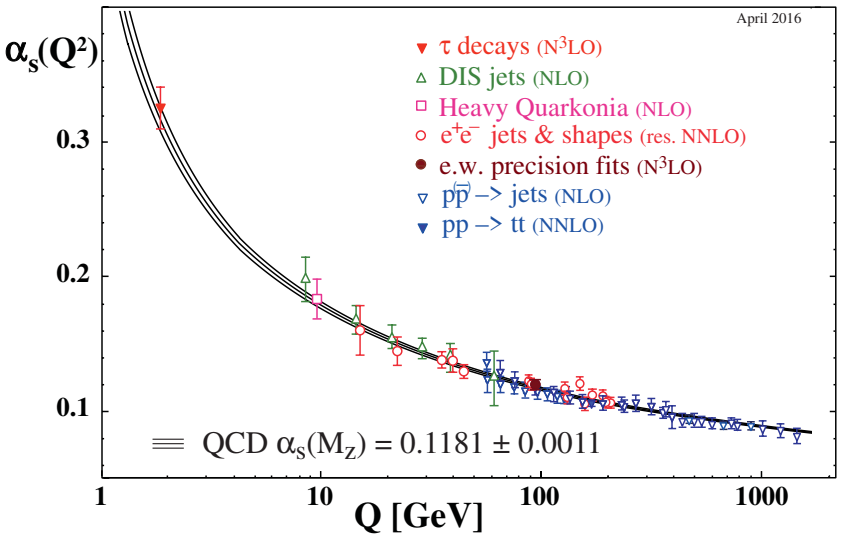

Figure 2.2.: Summary of experimental extractions of α_S [23].

interacting. Lattice QCD techniques continue to be used to probe this soft regime, however these are slow and not suited for the large samples of events needed at the LHC. A cutoff in the scale is introduced at low Q^2 that defines this region, $\Lambda_{\text{QCD}} \sim \mathcal{O}(100)$ MeV, and phenomenological models will be used instead.

2.2. Theory as a predictive tool for the LHC

The LHC is a machine that collides hadrons, which are bound states of the fundamental quarks in the SM. The colliding constituent quarks can interact via any of the gauge bosons, but the interactions will be dominated by QCD effects. Generating predictions for the outcomes of hadron collisions has been an area of much phenomenological work on aspects of QCD. In this section some of the challenges faced in modelling these collisions are highlighted, following closely notation and discussion from some standard texts [25, 26]. The current state of the most precise predictions for the LHC are also reviewed.

The cross-section, σ, is the quantity that gives the probability of a certain interaction happening. This is typically expressed in units of barn, b, which in natural units this has dimension [eV^{-2}]. By taking the sum of all connected, amputated Feynman diagrams to a process, and squaring this to the squared matrix element (ME) $|\mathcal{M}|^2$, the cross-section can be

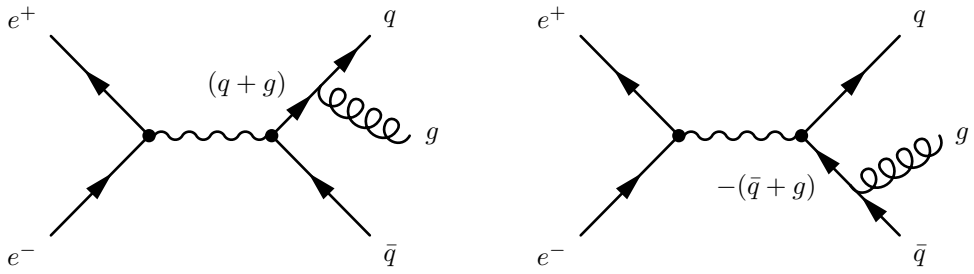

Figure 2.3.: Feynman diagrams of the leading corrections to the $e^+e^- \to q\bar{q}$ process by emission of a gluon.

calculated as,

$$\mathrm{d}\sigma = \frac{1}{\text{flux}} \times |\mathcal{M}|^2 \times \mathrm{d}\Phi_n \,. \tag{2.17}$$

Implicitly squaring the matrix element involves summing over the colours and spins of outgoing particles and averages over the colours and spins of incoming particles. This formula gives the differential form of the cross-section, including a flux factor which in the case of a $2 \to 2$ head on collision is approximately twice the centre of mass energy of the colliding particles. This differential form is a function of the differential phase space for a $2 \to n$ body process, $\mathrm{d}\Phi_n$. Integration over this phase space is complicated, the number of particles outgoing and their degrees of freedom makes this an integration over a large number of dimensions, with any number of divergent structures to deal with. This can't be done generically analytically so numerical Monte Carlo (MC) integration techniques are used [27]. This is naturally congruent with the idea of particle collisions being stochastic. The sampled points to numerically integrate this function can be interpreted as individual particle collision events, with a weight dictated by the likelihood from the integral, this will be revisited when the practical implementation of these calculations is reviewed in Section 2.3.

2.2.1. Divergences in QCD calculations

To understand the consequences of QCD, it is clearest to start with a simple example process. The simplest example to study QCD is in electron positron annihilations, $e^+e^- \to$ hadrons. It is by study of this process that the discovery of the gluon originally came about [28]. The simplest description of this process can be described by the $2 \to 2$ process $e^+e^- \to q\bar{q}$, but as this doesn't contain any QCD effect, the next to leading process with the emission of one gluon $e^+e^- \to q\bar{q}g$, is considered. The two diagrams corresponding to this are shown in Figure 2.3. The Feynman rules of QCD, derived from the Lagrangian of QCD given in Section 2.1.3 can be

used to write down the hadronic part of the amplitude of these two processes as,

$$\mathcal{M}_{q\bar{q}g} = iee_q g_s T^a_{ij} \bar{u}(q) \left[\gamma_\sigma \frac{(\not{q} + \not{g} + m_q)}{(q+g)^2 - m_q^2} \gamma_\mu + \gamma_\mu \frac{-(\not{\bar{q}} + \not{g}) + m_q}{(\bar{q}+g)^2 - m_q^2} \gamma_\sigma \right] v(\bar{q}) \epsilon^\sigma(g) \,, \tag{2.18}$$

which is then contracted with the leptonic part of the amplitude, then the tracing over the colour and spin indicies and the averaging over outgoing states performed. This gives the differential cross-section,

$$\frac{\mathrm{d}^2\sigma}{\mathrm{d}x_q \mathrm{d}x_{\bar{q}}} = \sigma_0 \frac{\alpha_s}{2\pi} C_F \frac{x_q^2 + x_{\bar{q}}^2}{(1-x_q)(1-x_{\bar{q}})} \,, \tag{2.19}$$

where σ_0 is the cross-section of the leading $e^+e^- \to q\bar{q}$ process and x_i being the energy fraction of the i-th final state particle. This energy fraction is defined as,

$$x_i = 2\frac{p_i \cdot Q}{Q^2}, \qquad x_q + x_{\bar{q}} + x_g = 2 \,, \tag{2.20}$$

with Q_μ the four momenta of the Z/γ mediator. The form of the cross-section given in equation (2.19) reveals some important behaviour. There are two points in phase space where singularities in the cross-section can be classified,

- When the gluon is soft, i.e. $x_g \to 0$, $x_q, x_{\bar{q}} \to 1$.
- When the gluon is emitted collinearly to the quark/anti-quark, i.e. $2(q \cdot g) = (1 - x_{\bar{q}})Q^2 \to 0$.

Both of these effects correspond to long distance, *infrared* (IR) divergences. To give a sensible physical prediction there has to be some effect that cancels these singularities otherwise the cross-section will not be a finite number when integrated over all of the phase space. The process shown in Figure 2.3 is considered as the first QCD emission correction to the *Born* level diagram for $e^+e^- \to$ hadrons, $e^+e^- \to q\bar{q}$. The matrix element squared of all QCD corrections to this process could be written as a power series in α_s,

$$|\mathcal{M}|^2 = \left|\mathcal{M}^{(0)}_{q\bar{q}}\right|^2 \; + \; \alpha_s \left(\left|\mathcal{M}^{(0)}_{q\bar{q}g}\right|^2 + 2\mathcal{R}e\left\{ \mathcal{M}^{(0)}_{q\bar{q}} \mathcal{M}^{(1)}_{q\bar{q}} \right\} \right) + \ldots \,, \tag{2.21}$$

where the power in brackets represents the number of internal loops in the amplitude. There is an interference term in this power series between the 1-loop *virtual* correction to the Born process and the Born process itself which enters the series with the same power of α_s that the previously calculated real emission matrix element squared did. An example of part of the diagrams entering the 1-loop amplitude is shown in Figure 2.4. The matrix element of this

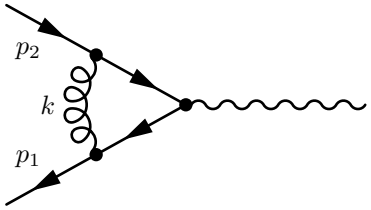

Figure 2.4.: One of the diagrams entering as a loop correction to the $e^+e^- \to$ hadrons process, the vertex correction.

sub-diagram is proportional to the following,

$$i\mathcal{M} \sim \int \frac{d^4k}{(2\pi)^4}\gamma_\nu \frac{\not{k} - \not{p}_1}{(k-p_1)^2}\gamma^\mu \frac{\not{k} - \not{p}_2}{(k-p_2)^2}\gamma_\lambda \frac{g^{\lambda\nu}}{k^2}\,, \tag{2.22}$$

where only the key part of this amplitude has been kept, the integral over the undetermined momentum in the loop k. The matrix element squared will also have IR divergences similar to those noted in the real emission case, this is revisited shortly. First however, an additional complication has arisen in these loops. In the case of four spacetime dimensions, the integral given in equation (2.22) is proportional to,

$$i\mathcal{M} \sim \int \frac{d^4k}{2\pi^4}\frac{k^2}{(k^2)^3} \sim \int^\Lambda \frac{dk}{k} \sim \ln\Lambda\,, \tag{2.23}$$

where the integral has been cut off by introducing an upper limit on the loop momenta scale, Λ. This short distance ultraviolet (UV) divergence has to be treated as well. The treatment of both the UV and IR singularities is dealt with typically first by applying dimensional regularization, which involves performing the calculations not in four spacetime dimensions but $4-2\epsilon$ dimensions. This classifies the divergent poles in powers of ϵ, with the divergences manifest in the limit $\epsilon \to 0$. The UV divergences in the loop integrals are renormalized, cancelling these divergences and absorbing the finite parts of the calculation into the coupling and field definitions. At each order in the power series expansion the remaining poles arising from the IR singularities in both the real and virtual diagram contributions appear with opposite signs so cancel, rendering the cross-section finite for the expansion to a given order for a suitably inclusive observable.

2.2.2. Partons and factorization

An additional result arising from similar arguments that will be needed to extend this simple picture to a full LHC case is the result of factorization of the QCD cross-section. The cross-section of an LHC collision of the type $hh \to X$, with X being any final state and h denoting

hadron, can be written,

$$\sigma_{h_1 h_2 \to X} = \sum_{a,b} \int_0^1 dx_1 f_a^{h_1}(x_1, \mu_F^2) \int_0^1 dx_2 f_b^{h_2}(x_2, \mu_F^2) \hat{\sigma}_{ab\to X} \,, \tag{2.24}$$

where the partonic cross-section $\hat{\sigma}_{ab\to X}$ would correspond to similar matrix elements to those discussed in Section 2.2.1. The quantities $f_a^{h_i}(x_i, \mu_F^2)$ are the structure functions (more commonly parton distribution functions, PDF) of the colliding hadrons, where a parton of type a, with momentum fraction x_i has been resolved at a scale μ_F. The nature of these functions are driven by fits to experimental data as they are not analytically calculable. These data points are extracted at various experimentally accessible energy scales, but the results can be evolved to different scales following the DGLAP equation [29],

$$\frac{\mathrm{d} f_q(x, \mu_F)}{\mathrm{d}\, \log(\mu_F^2)} = \int_x^1 \frac{\mathrm{d}z}{z} \frac{\alpha_s}{2\pi} P_{ij}(z) f_j\left(\frac{x}{z}, \mu_F\right) , \tag{2.25}$$

where z corresponds to the fraction of momenta retained when a particle j transitions to a particle i emitting the corresponding allowed particle with a momentum $1 - z$. The introduced $P_{ij}(z)$ are the regularized Altarelli-Paresi splitting kernels that define these splittings. The unregularized form of the leading order splitting kernels are,

$$\hat{P}_{gg}(z) = C_A \left[\frac{z}{1-z} + \frac{1-z}{z} + z(1-z) \right] , \tag{2.26}$$

$$\hat{P}_{qg}(z) = \mathrm{Tr}[z^2 + (1-z)^2] \,, \tag{2.27}$$

$$\hat{P}_{gq}(z) = C_F \frac{1 + (1+z)^2}{z} \,, \tag{2.28}$$

$$\hat{P}_{qq}(z) = C_F \frac{1 + z^2}{1-z} \,, \tag{2.29}$$

which can be derived in a similar way to the case of real emission corrections shown previously considering small angle limits of the splittings. Providing the factorization holds, the effect of unresolvable IR divergent QCD splittings has been included in the definition of the structure of the colliding hadrons.

These splitting kernels can be used to characterize the effect of additional emissions. This is the basis of the *parton shower* (PS). Considering again the diagrams for $e^+e^- \to q\bar{q}g$ in Figure 2.3, the singularities noted could be approximated in the collinear limit by application of the appropriate splitting function to the Born process. A Sudakov factor is defined based on

the splitting kernels as,

$$\Delta_i(t) \equiv \exp\left[-\sum_j \int_{t_0}^{t} \frac{\mathrm{d}t'}{t'} \int \mathrm{d}z \frac{\alpha_s}{2\pi} \hat{P}_{ji}(z)\right], \tag{2.30}$$

which corresponds physically to the probability of a parton evolving from a scale t_0 to t without a branching. There is a residual IR singularity from using the unregularised splitting functions corresponding to $z = 1$, emission of a soft gluon. This is treated by introducing a cutoff such that the Sudakov factor generates resolvable branching. Defining a no emission probability as such is a vital tool for LHC predictions as it allows a prediction to made in terms of a realistic multiplicity of particles in an LHC collision, which can be $\mathcal{O}\left(10^3\right)$ particles. Predicting such an event would be computationally infeasible in a diagrammatic perturbative expansion since the number of diagrams involves grows factorially with the number of outgoing particles, before even considering complexity of evaluating at a decreasing scale. As one is working in the soft and collinear approximations for these emissions, the additional coloured particles generated will tend to be soft and collimated with the original showered parton.

The techniques to predict LHC observables diverge somewhat at this point. One can stick to just using analytic perturbation theory, expanding to a given *fixed order* in the matrix element [30]. This predicts the high energy hard process partons distributions, but ignores the tendency of these partons to increasingly emit more coloured particles as they evolve to lower scales. Depending on the observable of interest these additional emissions can have a large effect. Such a prediction could alternatively be dressed by analytically extracting the logarithmically enhanced terms characterising these emissions and *resumming* [31] the effect of these on an observable. This gives a formally accurate prediction of an observable based on a perturbative expansion to a low multiplicity of partons, but now including the effects of divergent soft coloured emissions to some logarithmic order.

Both of these approaches give formal QCD based analytic predictions, but have limitations in what they can be used to do. The alternative is to take the Sudakov form factors and use them in a MC to sample the possible shower histories, the *particle level event generator* approach. On top of the numerical integration needed in the hard process, there is now an additional numerical sampling introduced, if the observable of interest is sensitive to both of these effects this can be a very time consuming process to obtain a convergent MC estimate. Such a PS program should replicate, based on the accuracy of splitting kernels used in the PS, the accuracy of formal resummation to some logarithmic order [32].

2.2.3. Hadrons, jets and observables at the LHC

The PS gives a prediction of a high multiplicity of coloured partons that has been evolved down to the cut-off of perturbative understanding, Λ_{QCD}. However the existence of free colour-charged particles is not observed in nature, so the coloured partons have to be combined into bound state colourless hadrons. As perturbation theory can no longer be used, a phenomenological model of QCD is needed. Two prominent schemes to perform this *hadronization* are the Lund string model implemented in the Pythia event generator [33], and the cluster hadronization model implemented in the Herwig event generator [34]. The resultant hadrons can have short lifetimes so subsequently will be decayed to quasi-stable final states, as far as the LHC detectors are concerned. Additional effects can be included too, such as multiple parton interactions [35] the sum of these effects are typically bracketed together as *soft* physics. The soft physics model tends to have more impact on lower scale observables, such as jet shapes.

An event as a kinematic distribution of stable final state particles is called a *particle level* prediction, and the rest of this work will rely heavily on such predictions. One of the appeals of the particle level approach is that it can now be used to generate a prediction for almost any observable quantity at the LHC, provided sufficient events are generated such that after imposing the conditions of the observable a convergent MC estimate is obtained. Such flexibility comes with a safety warning however, a selection criteria imposed on the events could spoil the IR singularity cancellation built into the formalism this far. Such an observable is deemed IR unsafe, and is sensitive to additional soft coloured radiation. At the LHC sequential jet clustering algorithms are used to define hadronic jets as the physics objects of interest. Such objects are by design IR safe. Sequentially clustered jets are created from a collection of final state particles first by defining two distance metrics. Relating the distance between two particles as [36],

$$d_{ij} = \min\{p_{i,T}^{2p}, p_{j,T}^{2p}\} \frac{\Delta R_{ij}^2}{R^2}\,, \tag{2.31}$$

and the distance between a particle and the beam as,

$$d_{iB} = p_{i,T}^{2p}\,. \tag{2.32}$$

The algorithm then operates by iteratively performing the following,

1. Computing both metrics for all particles, and finding the minima of this set of metrics.
2. If d_{ij} is the smallest value, merge particles i and j and start over.
3. If d_{iB} is the smallest value, declare particle i as a jet and start over.

The parameter p in equation (2.31) defines three main variants of the same procedure. The original approach used $p = 1$, dubbed the k_t algorithm, clustering softer particles first. The variant with $p = 0$ is known as Cambridge-Aachen (CA) and produces the most geometric jets with the metric only being based on distance. The most widely used at the LHC is called the anti-k_t algorithm [37] and uses $p = -1$, clustering harder particles first. The radius parameter, R, is a feature of the algorithm that can be chosen and provides a limit on the size in the $\eta - \phi$ plane each jet can be made to. All of these plus additional jet algorithms are implemented in the Fastjet library [38].

2.3. Tools and Monte Carlo

Examining the effects of QCD manifest in an LHC collision showed that at different scales there are different emergent physical phenomena and different calculation techniques are needed. Whilst the other approaches have use, the need[1] to describe the full particle level final states at the experiments lends itself to the PS and general purpose MC event generator construction [39]. The noted factorization lends itself to modular implementations of these calculations, which in turn will aid in understanding the inherent uncertainties on the predictions made. Figure 2.5 shows a representation of an LHC event from a general purpose MC. The hard process and final state radiation parton shower are coloured red, the initial state radiation parton shower and multiple parton interactions are coloured in blue, and the hadronization and decay model are coloured green.

The factorization of the hadronic effects in the initial state is handled by groups making dedicated fits with particular implementations of data included and anzsatz on the implementation of parton evolution [41]. The different PDF sets can be accessed from the LHAPDF library [42] which is supported in most modern LHC event generators.

Calculation of matrix elements was historically, prior to the LHC, handled internally, with simple $2 \to 2$ processes implemented in the PS codes. The LHC required an NLO revolution, as the precision of the experiment, and the observables under consideration started to be sensitive to NLO QCD effects[2]. As illustrated already this splits effectively into two parts, automated generation of the various real emission amplitudes, as well as calculation of the loop integral amplitudes that enter at NLO. Codes such as MadGraph [44] that can compute arbitrary tree level amplitudes have become the core of many implementations of LHC calculations. Libraries that can efficiently perform the loop integrals on the fly such as OpenLoops [45] can

[1] For now an example motivation is that without a full particle content final state it is impossible to understand accurately the effect of material interactions in the detector

[2] See for example the precision wishlist from the Les Houches workshop series [43]

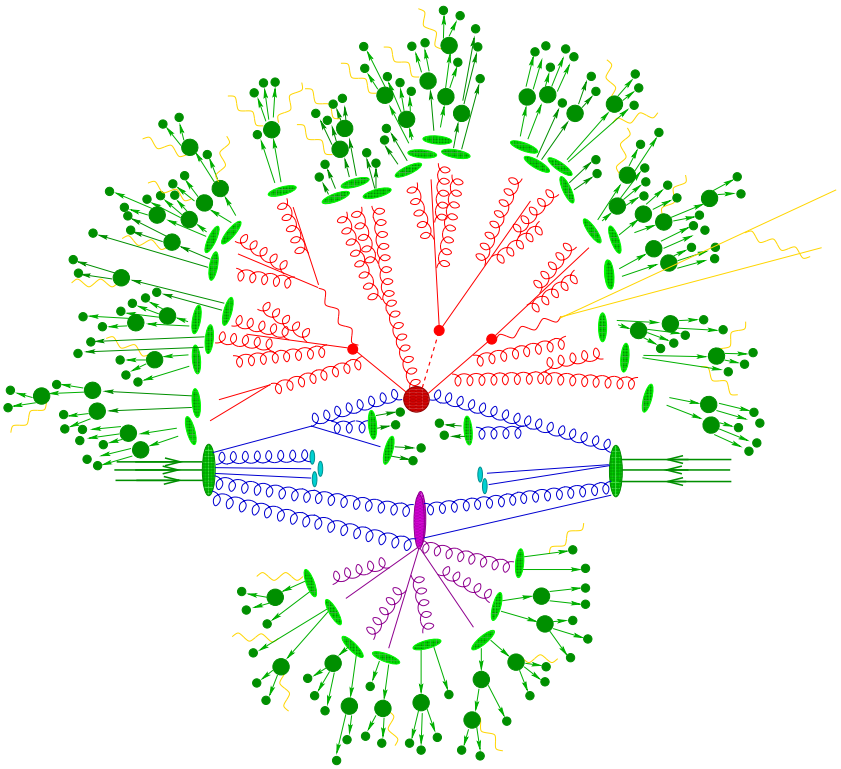

Figure 2.5.: Schematic of an example event generator event [40].

then be called to provide this piece of the calculation. The examples of full LHC calculations shown in Section 2.3.2 are built using HERWIG 7 which takes the tree level amplitudes from MADGRAPH, and the loop amplitudes from OpenLoops and internally constructs the full NLO matrix element. The key development of the NLO revolution is the automation for arbitrary processes, and there are many choices on the market that implement this in different ways. The construction of matrix elements and the interface to the PS has some subtleties which are covered in the next section, and can give rise to algorithmic uncertainties between different matching schemes. Additionally moving beyond NLO in QCD is one of the hot topics in LHC phenomenology.

The PS and soft physics are typically performed together. The PS is a tool that allows a calculation to transition in scale from perturbative to non perturbative QCD, so it is sensible to implement the non perturbative hadronization and decay pieces in the same codes. The two main PS algorithms on the market for many years were HERWIG and PYTHIA. Different shower implementations arise from the fact that the evolution variable integrated over in the Sudakov is not unambiguously defined. HERWIG historically implemented an angular ordered (AO) shower, where the evolution variable was the angle of emission, so the widest angle emission would happen first and sequentially the emissions would be more collinear. PYTHIA implemented a k_t ordered shower, where the evolution variable was the transverse momentum

of the emission, so the hardest emissions would be generated first and emissions would get sequentially softer. As mentioned already both implemented alternative soft models as well. Modern PS programs typically also include a shower structured on QCD dipoles [46], this is simpler to use in subtractive type matching.

Two other programs amongst a plethora of options worth specifically mentioning due to their widespread use at the LHC experiments are POWHEG-BOX and SHERPA. POWHEG-BOX [47], implements NLO ME calculations ready to interface to PS programs with multiplicative POWHEG matching (described in Section 2.3.1). SHERPA [40] is a full end-to-end event generation program primarily designed to construct multi-leg QCD MEs, and is synonymous with its multi-leg ME merging algorithms implemented (described in Section 2.3.1). SHERPA implements its own shower and soft physics model.

2.3.1. Matching and Merging

There is one last major point to clarify to achieve LHC MC beyond LO, is the overlap between the PS and the ME. It was already motivated that the PS applied to the Born ME could generate the first real emission correction shown in Figure 2.3. This overlap between the two schemes needs to be treated in order to make the PS approach valid for NLO ME and beyond. The NLO cross-section, implicitly including parton distributions and flux factors, can be written as [48],

$$\sigma^{\mathrm{NLO}} = \int \mathrm{d}\Phi_B \left[B(\Phi_B) + V(\Phi_B) + I(\Phi_B) \right] + \int \mathrm{d}\Phi_R \left[R(\Phi_R) - D(\Phi_R) \right] . \tag{2.33}$$

Now the squared matrix elements have been split into pieces corresponding to a $BVIRD$ scheme. B is the Born, V is the virtual loop correction, I is the integrated subtraction, R real emission and D divergent real subtraction matrix element. These matrix elements are sorted by integration over the phase space that are relevant, with Φ_B being the Born n body phase space and Φ_R being the $n+1$ body real emission phase space. This seemingly arbitrary decomposition is set such that the IR singularities present in R are similarly present in D, such that the integral over Φ_R is finite. Given a suitable operator $K(\Phi_1)$ that defines a single parton splitting, a function of the one emission phase space,

$$\mathrm{d}\Phi_R D(\Phi_R) = \mathrm{d}\Phi_B \mathrm{d}\Phi_1 [B(\Phi_B) \otimes K(\Phi_1)], \qquad I(\Phi_B) = \int \mathrm{d}\Phi_1 [B(\Phi_B) \otimes K(\Phi_1)] . \tag{2.34}$$

This is arranged such that these two pieces now cancel in the Born phase space. These splitting operators are not unambiguously defined, as long as they have the same singular structure as the corresponding real emission ME. An obvious choice is using the same factorization theorem

and resultant splitting functions as defined in Section 2.2.2. At this point, these definitions could be used to build a ME corrected (MEC) shower. By weighting the first emission of the PS with the ratio R/BK, one effectively obtains a local K-factor. Such a MEC shower could be run on the Born matrix element in a theoretically consistent manner. Integrating over such an expression however would not return the full NLO cross-section, necessary to claim an NLO accurate prediction. Instead the NLO-weighted Born cross-section, $\bar{B}$ can be defined as,

$$\bar{B}(\Phi_B) = B(\Phi_B) + V(\Phi_B) + I(\Phi_B) + \int \mathrm{d}\Phi_1 \left[R(\Phi_R) - D(\Phi_R) \right], \tag{2.35}$$

Which when integrating over the Born phase space with a suitably defined Sudakov [48] gives a cross-section that is accurate up to the next order in α_S with respect to the Born diagram. This can be written as,

$$\sigma^{\mathrm{NLO}}_{\textsc{Powheg}} = \int \mathrm{d}\Phi_B \bar{B}(\Phi_B) \left[\bar{\Delta}(t_0) + \int_{t_0} \mathrm{d}\Phi_1 \frac{R(\Phi_B, \Phi_1)}{B(\Phi_B)} \bar{\Delta}(t) \right], \tag{2.36}$$

This is the Powheg, or multiplicative, NLO cross-section [49]. This operates by weighting the hardest emission along with a suitably modified Born process such that overall NLO accuracy is obtained. An alternative matching scheme can be constructed in a similar vein, the MC@NLO or subtractive formalism [50]. This operates instead by retaining the subtractive counter terms in the cross-section, leading to generated events with negative weights. A comparison of the three methods (NLO, PS and MEC) for generating the first emission is shown in Figure 2.6a. A comparison of the two formalisms for consistent NLO matching (POWHEG and MC@NLO), with the inclusion of PS effects, is shown in Figure 2.6b.

If the increasing precision of the experiment necessitated the use of NLO MEs, including in the perturbative ME even higher order QCD corrections is going to be of interest. The 'obvious' approach would be to construct NNLO MEs and interface these to parton showers. This has been achieved for some simple cases such as $gg \to H$ production in the infinite top mass limit [52]. The limitation comes from the two loop matrix elements which unlike the one loop case needed for NLO have not been generically solved yet[3]. Another approach that the experiments make extensive use of is to merge multiple real emission matrices (and the corresponding one loop corrections if available). These merging approaches are built on similar ideas to the subtractive formalism used to match the NLO+PS case, and matching is achieved in a similar way. The CKKW algorithm [53] is an example of a way to combine multiple real emission matrix elements (forming a *multi-leg* calculation). The benefit of merging real emissions can be motivated from the similarity of the MEC and full NLO seen over a lot of the kinematic range in Figure 2.6a. All merging algorithms introduce an arbitrary merging

[3] There are also limitations from a lack of a defined generic approach to the PS matching.

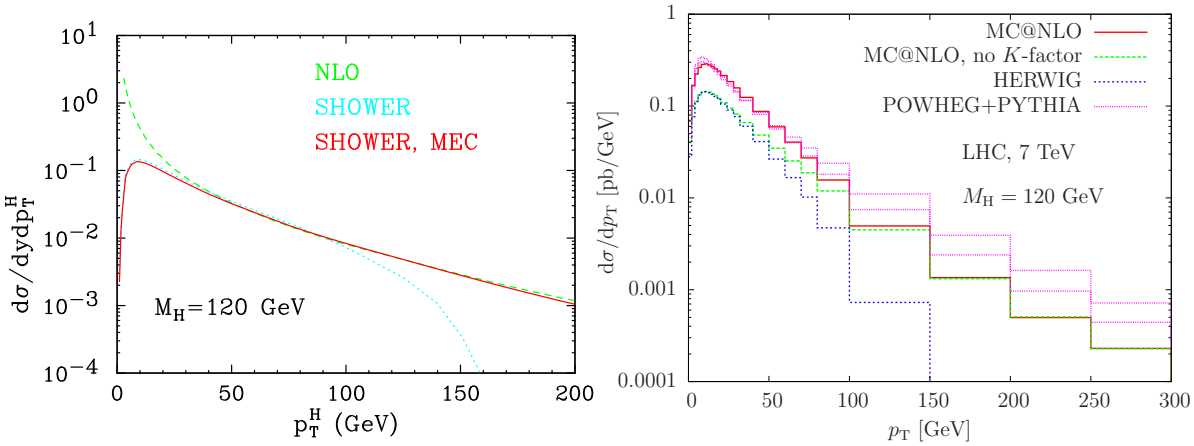

Figure 2.6.: Differential cross-sections of Higgs p_{T}. Figure 2.6a compares NLO, PS and ME corrected PS generations of the first emission. Figure 2.6b compares the POWHEG and MC@NLO formalisms matched to the PS [51].

scale into the calculation, defining the Sudakov region and the ME region. In the example of the CKKW algorithm, if an n parton ME, when matched to the PS, generates an $n+1$ 'jet' final state emission harder than the merging scale, the event is generated with the $n+1$ parton ME. More recent developments along similar lines include also the virtual one loop diagrams where available using a subtraction like formalism [54–57]. The presence of an unphysical scale introduced in merging has also been circumvented in the MINLO procedure [58], this is more theoretically attractive but often the experimental collaborations often put more emphasis on generating as many real emissions in the ME as possible. Dealing with the ME overlap with the PS is one of the bottlenecks in utilising the increasingly available NNLO fixed order results available in an event generator.

2.3.2. Particle level LHC predictions and their uncertainties

One undetermined aspect of the calculations thus far is an estimate of their uncertainty. The sources of uncertainty in a general purpose MC can be decomposed as [59]:

- Numerical - A convergent MC estimate is needed of an observable, this effect can usually be mitigated by additional computing resources.
- Parametric - Use of quantities estimated outside of the generators and used as input, for example PDF fit uncertainties. This has to be correctly propagated through the generator.
- Algorithmic - The implementations of the algorithms, for example POWHEG and MC@NLO. Both give formally the same accuracy but are quantitatively different. This is the

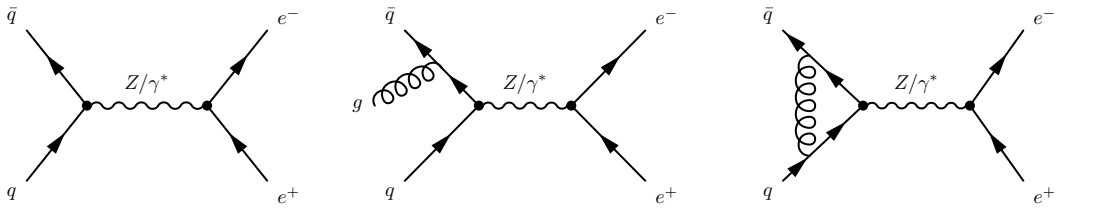

(a) $\mathcal{O}\left(\alpha^2\alpha_S^0\right)$ *Born* **(b)** $\mathcal{O}\left(\alpha^2\alpha_S^1\right)$ *real emission* **(c)** $\mathcal{O}\left(\alpha^2\alpha_S^2\right)$ *virtual correction*

Figure 2.7.: Three Feynman diagram components going into a Drell-Yan $Z(0^*, 1)$ merging algorithm. Figure 2.7a shows an example diagram contributing to the $Z + 0$ jet Born contribution, Figure 2.7b shows an example diagram from the $Z + 1$ jet real emission contribution and Figure 2.7c shows an example diagram from the virtual correction (the $Z + 0^*$ jet contribution in this notation).

motivation for having different tools and libraries, sometimes multiple calculations of the same quantity in different formalisms are needed.

- Perturbative - The arguments based on perturbation theory involved performing as much of the hard part of the calculation in the perturbative ME. This expansion has to be truncated and one is sensitive to the size of the remainder of the series not included. A proxy used to estimate this is the perturbative stability of the order of expansion. A generator requires a choice of scale to evaluate the hard process at, for convenience this is generally the same for μ_F and μ_R. This scale choice is varied up and down to understand how stable this order of expansion is.

- Phenomenological - The goodness of fit of the parameters of the phenomenological models (e.g. hadronization model) used.

In Figure 2.8 a comparison is made between data and predictions made using the unitarized merging procedure implemented in the Herwig 7 Matchbox [60, 61]. The notation used for this discussion follows closely the description of the Herwig 7 merging algorithm [60]. In this notation the lowest order process (and the process to which corrections are being calculated), is referred to as the Born process. When corrections from higher order emissions have been included, they are denoted by the additional outgoing parton multiplicity on top of the target Born process. When the corresponding one loop correction at this multiplicity is also included, this is denoted with an asterix. Explicitly, an approximate NLO calculation in a multileg merging algorithm of the Drell-Yan process, $pp \to ee$, would be written as $pp \to Z/\gamma^*(\to ee) + (0^*, 1)$ jets or for short, $Z(0^*, 1)$. In Figure 2.7, example diagrams corresponding to the three main parts of such a $Z(0^*, 1)$ generator are shown. Additionally in this figure another useful notation to label groups of diagrams based on the order of the EW and Strong couplings is shown.

Returning to figure Figure 2.8, the Born process under consideration is $pp \to e^+e^-$. In all cases here the predictions are run without any non-perturbative QCD modelling so correspond just to hard MEs merged and matched with a PS. In Figure 2.8a -2.8d a comparison is made between a $Z(\to ee) + (0^*, 1^*, 2)$ jet and $Z(\to ee) + (0^*, 1^*, 2^*, 3)$ jet generator matched to the Herwig 7 dipole shower using the scale chosen as the Z mass. These are also compared to a variety of differential cross-section measurements as a function of certain observables in ATLAS 7 TeV Z+jets data. For example in Figure 2.8a, the observable is the p_{T} of the first jet in the event. This should be described at NLO accuracy for $Z(0^*, 1^*, 2)$. However as can be seen, as the p_{T} of the first jet becomes larger, increasingly the prediction underestimates the observed data. The additional QCD emissions giving rise to these high leading jet p_{T} configurations are being generated by the parton shower. This situation is fixed somewhat by including more matrix elements in the $Z(0^*, 1^*, 2^*, 3)$ prediction. These predictions were produced with a preliminary version of the Herwig 7 merging and also have large numerical uncertainties reflecting the exploratory nature of this work. Figure 2.8b, Figure 2.8c and Figure 2.8d show the same setup described but the cross-section is binned in the second leading jet p_{T}, inclusive jet multiplicity and the scalar sum of jet p_{T} respectively. The same pattern noted in Figure 2.8a is seen in all cases.

In Figure 2.9, the construction of the full uncertainty envelope on the prediction in Figure 2.8 is shown, this time against ATLAS 7 TeV Drell-Yan data. This observable is calculable in the Born diagram so this is the sort of observable that is intended to be best improved by the merging techniques [4]. The μ_F, μ_R band in red is constructed by explicitly varying the scales in the hard process in a seven point envelope by taking the set of pairs corresponding to picking a value for each from the set of values, $\{0.5, 1, 2.0\}$, but excluding the two pairs of $(0.5, 2.0)$ and $(2.0, 0.5)$. This recipe is somewhat arbitrary but is the usual standard for these perturbative uncertainties in the experiment. It is noted that in the Herwig Matchbox these cannot currently be computed by reweighing the default scale choice events so have to be run as explicit generator runs, this is computationally costly and also opens up additional sources of numerical error. The μ_Q band is formed from varying the scale at which the PS starts up and down by a factor of two, and similarly for the merging scale. These three sources are treated as orthogonal so the full band is made by adding these in quadrature, uncertainties from the PDF set chosen and soft model should also be propagated to a true full envelope. One of the primary motivations for this however is to help understand the algorithmic uncertainty on the merging algorithm, the unitarized merging shown here is different to the Sherpa implementation of MEPS@NLO used in a lot of ATLAS vector boson plus jets simulations.

[4] The rule of thumb is that the observable of interest should be present in the Born diagram, the experiments often use the fact that merging describes higher jet multiplicity observables at approximately the accuracy quoted in the merging, but this is somewhat an abuse of the intended design.

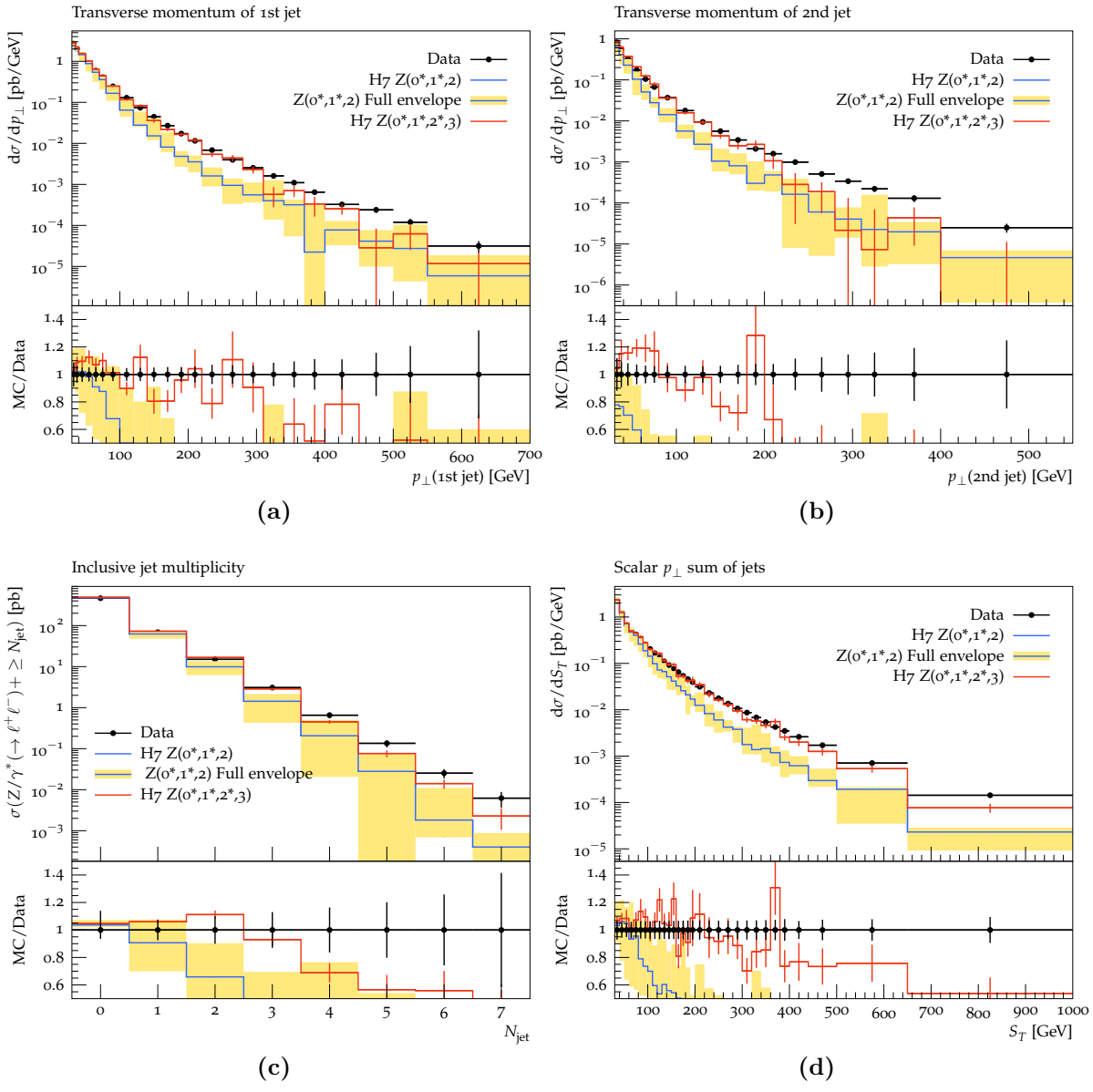

Figure 2.8.: Comparing HERWIG 7 predictions for the Born process $pp \to Z \to e^+e^-$. In Figure 2.8a-2.8d two different multiplicity merges are compared to ATLAS 7 TeV Z+jets data [62].

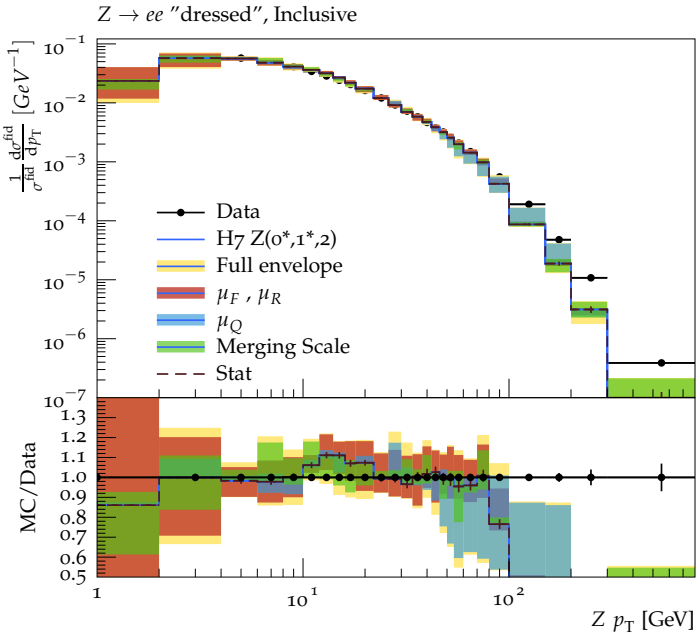

Figure 2.9.: The composition of an error band on one of the merged predictions described in Figure 2.8 is shown against ATLAS 7 TeV Drell-Yan data [63].

2.4. Physics beyond the Standard Model

To conclude a review of the SM it is worth considering some of its shortcomings. The predicted particle content of the SM has been observed and various properties have been measured at many experiments and found to be remarkably consistent with the SM across a large range of energy scales, but there are hints towards physics beyond the Standard Model (BSM). The SM mechanism to generate neutrino masses would rely on an as of yet unobserved right handed neutrino, and would require large parameter tuning to explain the relative smallness of observed neutrino masses. Many theories can more naturally explain these two phenomena by extending the SM. At the other end of the distance scales to the SM of particle physics is the standard model of cosmology [64]. Observations on the cosmological scale favour a universe composed of a weakly interacting dark matter candidate, which the SM of particle physics does not provide in sufficient abundance (the SM neutrinos can explain a portion of this). These two mentioned shortcomings correspond to observations that cannot be catered for in the SM, models that can address these are explored in Chapter 6.

There are additional observational shortcomings, but one of the strongest motivations is an internal inconsistency in the SM itself [65]. The Higgs is observed to have a mass of approximately 125 GeV and is a product of a scale in the theory, the EWSB scale. There is then an apparent desert above this, with no other scale present until the Planck scale, M_{Planck}. The Planck scale being the scale where quantum gravity effects become dominant, occurring at

approximately $M_{\text{Planck}} \sim \mathcal{O}\left(10^{19}\right)$ GeV. Due to the spin zero nature of the scalar Higgs boson, its mass is not protected by any gauge symmetries. The Higgs mass is hence unprotected from large vacuum fluctuations so will receive corrections proportional to the range of allowed particle virtualities. Without new physics between the two scales these corrections fix the Higgs mass to close to the maximum scale in the theory, M_{Planck}. This large hierarchy of scales leads to a *fine tuning* of the parameters of the theory, which is seen as being in tension with arguments of *naturalness*. One approach to mitigate this is via supersymmetry (SUSY) [66]. In its basic form this introduces a superpartner for each fermion and spin one boson in the SM (as well as an extended scalar spin zero boson sector). These superpartners have opposite spin statistics so cancel the loops that correct the Higgs mass. SUSY is observed to be broken, as it hasn't been observed thus far, introducing a new SUSY breaking scale in the theory and generally necessitating some fine tuning. The more the LHC probes energy ranges above the EWSB scale and into the TeV scales, the larger this second *little hierarchy* problem becomes. An alternative approach is to invoke some large extra dimensions (LED) [67], rather than introducing a new scale this allows gravity to propagate in these new dimensions which can fix the high scale the Higgs is sensitive to to instead be at the EW scale.

Historically BSM model building drew inspiration from the symmetry principles that lead to the construction of the $\mathrm{SU}(3)_C \times \mathrm{SU}(2)_L \times \mathrm{U}(1)_Y$ group. The idea behind grand unified theories (GUT) is to attempt to unify the SM gauge groups into some larger symmetry group. For example the SM group can be embedded into larger SU(5) or SO(10) symmetry groups. When these symmetry groups are broken at some high scale, the SM gauge symmetry structure can be retrieved. These larger gauge groups can accommodate the particle content of classes of supersymmetric models, which can run to $\mathcal{O}(100)$ in even the most minimal realisations of SUSY[5]. The large number of free parameters also give a great deal of freedom allowing these complete models to accommodate some of the shortcomings in observations, such as providing a dark matter candidate. For a long time this *top-down* approach was prevalent, starting from a UV complete theory (defining a consistent theory valid even to very high scales), and constructing the observations within that framework. Due to the aforementioned lack of observations of new BSM heavy states at the LHC that indicate such classes of models, the focus is shifting more to *bottom-up* model building. Starting with a simplified model that doesn't have a full UV completion and targeting particular phenomena, again such as providing a dark matter candidate. The bottom-up, *simplified model* approach will be examined throughout this thesis.

[5] E.g. the minimal standard supersymmetric model (MSSM) [66]

Chapter 3.

Experiments at the energy frontier

Studying the properties of particles at the energy frontier has historically required construction of large particle accelerators colliding particles at high energies. The accelerator currently operating at the energy frontier is the Large Hadron Collider (LHC) [68] located at the European Organisation for Nuclear Research (CERN) in Geneva, Switzerland. In Section 3.1 of this chapter an introduction to the LHC machine is given.

The four main experiments currently operating at the LHC are ATLAS [69], CMS [70], ALICE [71] and LHCb [72]. The description of experimentation at this frontier machine is based on the ATLAS experiment as that is the collaboration where the experimental work presented in this thesis was conducted. However the phenomenological work presented later, in Chapter 5 and Chapter 6 builds on results from all four collaborations. A description of the ATLAS detector is given in Section 3.2, with Section 3.3 detailing how physics objects are reconstructed from the detector readouts. Lastly, Section 3.4 shows contributions made to the ATLANTIS event display [73], and the resulting data visualisations are used to demonstrate some features of the experimental setup.

3.1. The LHC Machine

The LHC is a two-ring-superconducting-hadron accelerator and collider. It was built to fit onto existing infrastructure at CERN, installed into the 27 km circular tunnel that used to house the accelerator rings for the LEP collider [74] and using the existing chain of hadron accelerators to inject hadrons into the LHC ring. The main data taking mode is to collide a pair of protons (pp), at energies of $\sqrt{s}$ =13 TeV in Run 2 (energies of $\sqrt{s}$ =7 TeV and 8 TeV were achieved in Run 1). This is achieved by accelerating two beams of protons in opposite directions along the ring using RF cavities, requiring superconducting dipole magnets of strength $\sim$5 T to keep the

beams inside the ring. The machine can also accelerate heavy ions to create different collision conditions but for this work the *pp* mode is all that is described.

A schematic of the CERN accelerator complex including the LHC ring is shown in Figure 3.1. The pre-accelerator chain to achieve the aforementioned energies in the LHC ring is as follows:

1. Hydrogen gas is ionised to protons in an electric field.
2. Linac2 accelerates the protons to 50 MeV.
3. The Proton Synchotron Booster accelerates these again to 1.4 GeV.
4. The Proton Synchotron (PS) accelerates these to 25 GeV.
5. The Super Proton Synchotron (SPS) accelerates again to 450 GeV.

The protons from the SPS are then split and injected into the two LHC rings in bunches containing up to 1.1×10^{11} protons, with the proton bunches spaced by 25 ns. The LHC accelerates these bunches to an energy of 6.5 TeV in Run 2. The beams are then made to collide at various defined points around the ring where the resulting collisions are captured by the experiments. Throughout Run 2 the LHC delivered approximately 150 fb^{-1} integrated luminosity of *pp* collisions to the ATLAS and CMS experiments.

At the time of composing this document the LHC is in its Long Shutdown 2 (LS2) period. A time-line of the life cycle of the LHC and its future upgrade into the High Luminosity (HL-LHC) project is shown in Figure 3.2. Upgrades to the detectors and the LHC machine itself are planned with the goal to realise a data set of total integrated luminosity of approximately 3ab^{-1}, achieved by increasing the instantaneous luminosity of the bunch crossings up to seven times the current rate. The LHC and its associated experiments are to continue being at the cutting edge of the energy frontier for the next few decades.

3.2. The ATLAS detector

The ATLAS (A Toroidal LHC ApparatuS) detector is one of the four main detectors on the LHC ring and is one of two (along with CMS) of the so called general purpose detectors. A general purpose detector is designed to have, as far as possible, coverage of instrumentation over the entirety of the 4π solid angle around the collision point. Additionally it should be able to detect or infer as wide as possible an array of final state particles in as broad a possible energy range.

A graphic of the ATLAS detector is shown in Figure 3.3, with the main components labelled. ATLAS is a cylindrical shape centred around the target collision point, approximately 44m

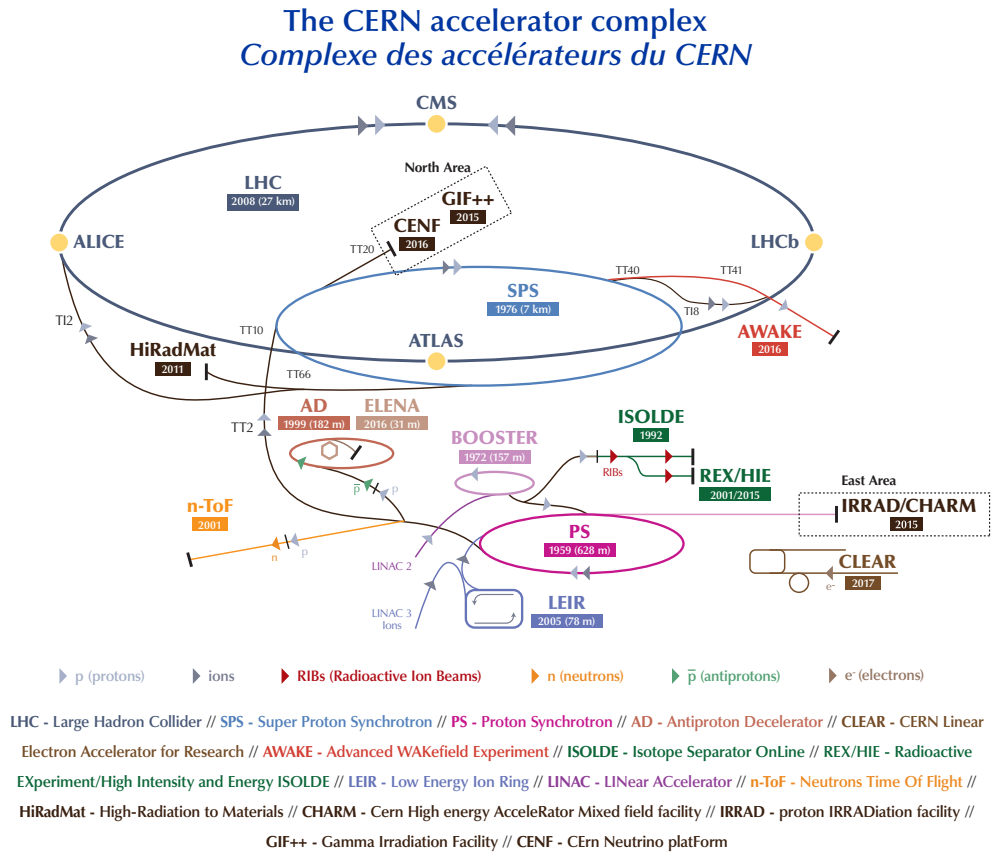

Figure 3.1.: A schematic of the CERN accelerator complex [75].

in length, 25m in diameter and weighing 7000 tonnes. The detector is composed of a barrel, containing subsystems that are radially symmetric around the beampipe and two end caps at either end to improve coverage of forward physics. The following three subsections review the three main detector systems in ATLAS in order based on distance from the beampipe.

A right handed Cartesian coordinate system is used to describe objects in the detector. The z-axis runs along the beampipe with the positive x-axis pointing towards the centre of the LHC and the positive y-axis pointing towards the sky. Often a polar coordinate system is used interchangeably, where the radial coordinate (r) is the distance from the beampipe in the transverse $x-y$ plane, the polar angle (θ) being the angle from the beampipe and the azimuthal angle (ϕ) being the angle around the beam axis. It is common to discuss particle kinematics in the transverse plane, where the transverse momentum, p_{T}, can be written,

$$p_{\mathrm{T}} = \sqrt{(p_x^2 + p_y^2)}\,. \tag{3.1}$$

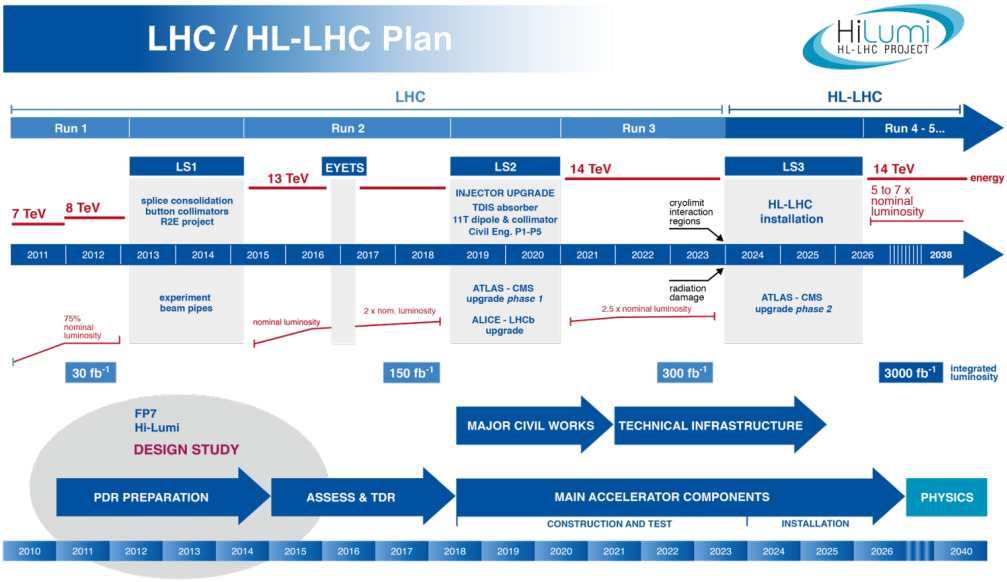

Figure 3.2.: The timeline of the LHC project including its continuation into the HL-LHC [76].

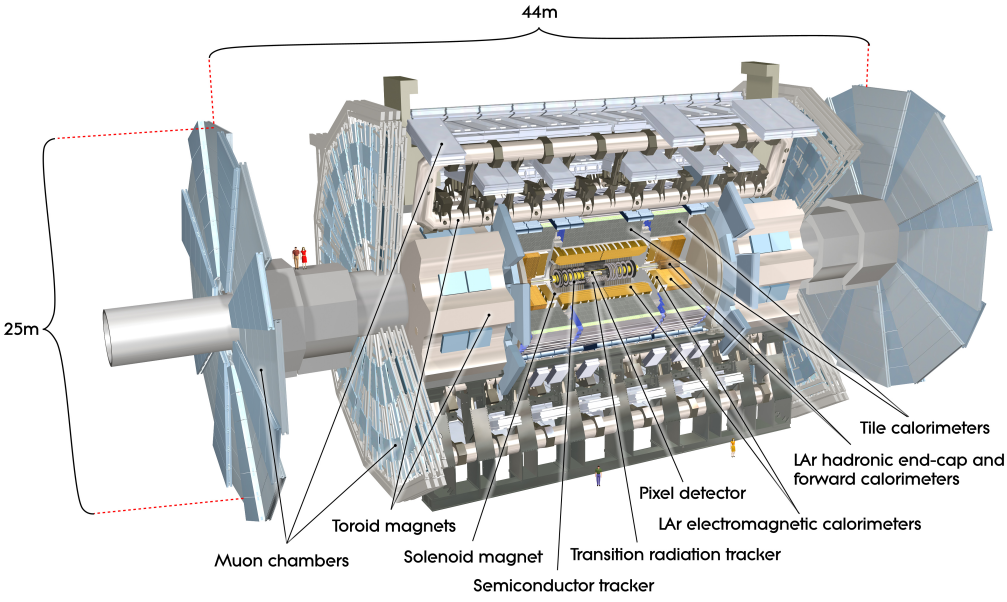

Figure 3.3.: Graphic showing the ATLAS detector [77].

Another commonly defined quantity is to transform the polar angle, θ, to the pseudorapidity, η, as

$$\eta = -\log\left(\tan\left(\frac{\theta}{2}\right)\right), \tag{3.2}$$

which is equivalent to the rapidity, $y = \frac{1}{2}\log\left(\frac{E+p_z}{E-p_z}\right)$, in the limit where the object is massless. Rapidity is invariant under Lorentz boosts in the z-axis. Distances between objects are commonly written in terms of separation in the $\eta - \phi$ plane as,

$$\Delta R^2 = \Delta\eta^2 + \Delta\phi^2 \,. \tag{3.3}$$

3.2.1. Inner Detector

The Inner Detector (ID) is the collection of tracking detectors closest to the beampipe designed to detect the positions of highly ionising charged particles as they move through the detector. Moving radially outwards from the beampipe the subsystems composing the ID are as follows:

- Insertable B-Layer (IBL) - A new addition inserted during LS1. A layer of silicon pixels (described in the next bullet point) in the barrel approximately 30mm from the beampipe and covering a range of $|\eta| \leq 2.5$. Additional pixels closer to the beampipe aid in identification of particles not originating from the primary collision vertex.

- Pixel detector - Three cylindrical layers of silicon pixels around the beampipe and three layers of disks of pixels at both ends. Around the barrel the pixels occupy the range 50.5 mm $< r <$ 122.5 mm, and again covering $|\eta| \leq 2.5$. The pixels are $(50 \times 400)\mu\text{m}^2$ in $r - \phi \times z$ and give a resolution of 10µm in r and 115µm in z.

- Semiconductor Tracker (SCT) - Four layers of overlapping silicon microstrips covering 255 mm $< r <$ 549 mm around the beampipe and nine layers of strips arranged in a disk, covering 275 mm $< r <$ 560 mm and 839 mm $< |z| <$ 2735 mm, at both ends. The strips give a resolution of 17µm in r and 580µm in z.

- Transition Radiation Tracker (TRT) - Composed of straw gas drift tubes aligned along the beam axis cylindrically around the beampipe covering a range of 560 mm $< r <$ 1080 mm and $|z| <$ 720 mm and with end caps where the tubs are arranged in a fan layout covering 617 mm $< r <$ 1106 mm and 827 mm $< z <$ 2774 mm. The TRT covers $|\eta| \leq 2$ and gives a resolution of 130µm for hits in the $r - \phi$ plane. The TRT also performs a degree of particle identification (PID). A particle transitioning between the different media inside and outside the tubes induces transition radiation of photons. The rate of this

is proportional to the Lorentz boost, and hence mass of the particle, so can be used to distinguish pions and electrons for example.

These technologies are designed to give a series of hits as a charged particle passes through the various subsystems. The entire ID is immersed in a 2T magnetic field generated by a solenoid. Tracking algorithms can then fit the observed hits with the most likely tracks, and the curvature of the resultant track due to the magnetic field is a function of the particles momentum and charge.

3.2.2. Calorimetry

Next system in ATLAS moving outwards from the beampipe are the calorimeters. These are designed to measure the energy of particles that interact in the calorimeters medium by sampling the energy of the interaction products. There are two main types of sampling calorimeter used in ATLAS; The electromagnetic (ECAL) and hadronic (HCAL) calorimeters. As the names suggest the former is primarily to measure the energies of electrons and photons, whereas the latter is predominantly to measure hadrons such as pions. Electromagnetic calorimeters are best characterised by their radiation length, X_0, the distance over which an electromagnetically interacting particle loses all but $1/e$ of its energy. Hadronic calorimeters are best described by their characteristic depth, λ_I, the distance over which a hadron loses all but $1/e$ of its energy. Inducing a hadronic shower will typically induce a portion of the initial energy to be emitted in decays to electromagnetic particles. The ATLAS calorimetry is non-compensating, having a different response to hadrons and electrons, which is an effect that has to be accounted for in calibration.

The ECAL is the innermost of the two and is composed of a liquid argon (LAr) active material with a lead absorber. To facilitate full coverage in ϕ the ECAL has a concertina geometry. In the barrel the ECAL covers $|\eta| < 1.475$ and the end-caps are composed of two concentric wheels at both ends of the cylinder, covering $1.375 < |\eta| < 2.5$ and $2.5 < |\eta| < 3.2$. The LAr has $X_0 > 22$ in the barrel and $X_0 > 24$ in the end caps, such that the majority of an electromagnetically showering particles energy is captured.

The HCAL is the next layer out and uses two distinct technologies for the barrel and end-cap. In the barrel, it is composed of scintillating tiles as the active materials with steel absorbers, segmented into an inner barrel layer and and outer layer. The inner barrel covers $|\eta| < 1.0$ and has 3 layers of different thickness, $\lambda_I = 1.5, 4.1$ and 1.8. The outer barrel covers $0.8 < |\eta| < 1.7$ and also has 3 layers of varying thickness, $\lambda_I = 1.5, 2.6$ and 3.3. The hadronic end-cap calorimeter (HEC) and additional forward calorimeters instead use LAr as the active material with copper absorbers. The end-caps are both composed of two wheels covering

$1.5 < |\eta| < 3.2$ with a thickness of $\lambda_I = 12$. The additional forward hadronic calorimeters also use LAr active material with three absorbers, one copper and two tungsten. They cover $3.1 < |\eta| < 4.9$ with a thickness of $\lambda_I = 10$.

3.2.3. Muon spectrometer

The outermost of the main systems of ATLAS is the muon system (MS). As the name suggests this is used primarily to identify muons, which are weakly ionising particles with suppressed rate of bremsstrahlung radiation relative to electrons due to their higher mass. As such they tend to pass through the previously described systems with minimal interactions. Like the ID the MS records positions of charged particles passing through it, so is immersed in a toroidal magnetic field, however due to the aforementioned weakly ionising nature of muons it is required to be very large in order to capture sufficient ionised particles to form a track. Hence the MS uses different technologies to the ID. There are four main technologies composing the MS:

- Monitored Drift Tubes (MDT) - Tracking chambers covering $|\eta| < 2.7$.
- Cathode Strip Chambers (CSC) - Additional tracking chambers for more forward muons, covering $2.0 < |\eta| < 2.7$
- Resistive Plate Chambers (RPC) - Trigger system for the central region, covering $|\eta| < 1.0$
- Thin Gap Chambers (TGC) - Trigger system for the end-cap regions, covering $1.05 < |\eta| < 2.4$

3.2.4. Triggering and data acquisition

With the main hardware defined, the strategy to record the desired data has to be defined as well. Since the bunches of protons are 25ns apart, collisions (alternatively bunch crossings) occur at a rate of 40MHz. ATLAS employs a tiered trigger system to filter down the collisions, aiming to maximise efficiency of recording collisions of interest whilst discarding background collisions where less interesting things are happening. For Run 2 the ATLAS trigger system had two levels; the Level 1 (L1) hardware trigger and the High Level Trigger (HLT) software trigger. Together this reduces the readout rate to $\sim$1kHz [78].

The L1 trigger operates by selecting regions of interest (RoIs) in the calorimeters or MS. Due to latency of reconstruction, information from the ID is not included at the hardware decision level but this is something the collaboration is striving to achieve [79]. The L1 trigger selects RoIs that appear to contain high p_{T} tracks in the MS or large deposits of energy in the calorimeters. Overall this reduces the initial collision rate from 40MHz to 100kHz.

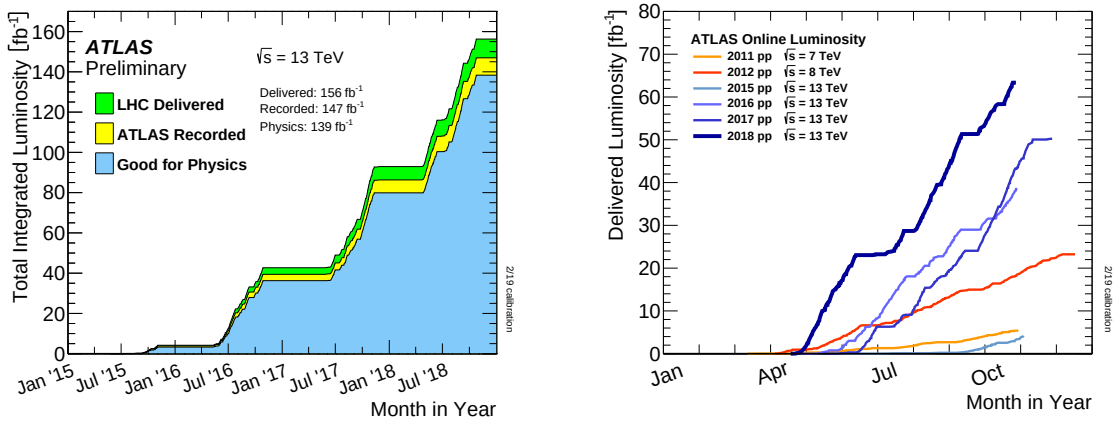

(a) Run 2 **(b)** All runs

Figure 3.4.: Plots showing the dataset sizes, in integrated luminosity, recorded at ATLAS [81]. Figure 3.4a shows the delivered and recorded dataset during the 13 TeV Run 2. Figure 3.4b shows the recorded dataset size for all runs thus far.

The HLT subsequently processes the selected L1 events by using software running on a PC farm. The events from the L1 trigger are reconstructed using faster, but similar algorithms to the full offline reconstruction. The HLT has a defined menu of interesting physics objects targeted from this partial reconstruction, with an overal output bandwidth of 1kHz. The menu is budgeted to cover everything the analyses need. In cases where the output rate of events would be too large from a particular trigger, this trigger is only partially read out and has a *prescale* that can be applied to scale the recorded data to the true rate. The event output stream from the detector is then at a manageable size so can be saved to disk for full offline reconstruction and analysis. Figure 3.4 shows the approximate data set sizes recorded with the ATLAS detector for different runs. This is recorded in units of time integrated luminosity, L, which relates to the number of events in the time period, N as,

$$N = \sigma L \,, \tag{3.4}$$

where σ is the total inelastic cross-section for pp beam collisions. The integrated luminosity is the integral over time of the instantaneous luminosity, this changes with run conditions and is measured using dedicated sub-detectors [80].

3.3. Physics with the ATLAS detector

The technologies described produce an output data stream with features that can be used to infer the result of the pp collision that was recorded in that snapshot. Offline processing in

ATLAS is designed to reconstruct the quasi-stable particles that emerged from the interaction, using a vast array of algorithms to process each event to be ready for the analysis stage. From the detector outputs described, two building blocks can be defined that group things together usefully. The tracking detectors show positions of charged particles passing through them. The readout of these sub-systems form a set of *space points* (or hits), which can then be fitted with tracks. To form ID tracks a minimum of seven hits are needed [82]. Calorimeter cells are formed into clusters with algorithms that combine cells based on significance of energy signal over noise and cell proximity [83].

3.3.1. Physics objects in ATLAS

From the building blocks, the physics objects that gave rise to the observed detector patterns can be inferred. Electrons are identified by the presence of an ID track pointing to an EM cluster. Similarly photons are identified by requiring an EM cluster with no corresponding track. Muons are reconstructed by fitting tracks to the MS and then to a combination of the MS and ID hits. Reconstructed objects typically have likelihood based discriminators which are used as quality cuts. Such cuts have working points which can be tightened to give higher purity of positive identification at the expense of efficiency of reconstruction. For example electron reconstruction in ATLAS uses a variety of information from both the track and calorimeter quantities [84]. One of the likelihood components for electron identification is the impact parameter, d_0, which helps distinguish non-prompt decays of particles into electrons. Additionally requirements on object isolation are also usually imposed, primarily to increase the purity of promptly produced objects in busy collision environments. Charged leptons are typically *dressed*, whereby nearby energy deposits from QED radiation in some cone around the lepton are summed into the lepton definition. In this work dressed leptons will almost always be used as this is the standard particle level definition for a lepton at the LHC [85].

Hadronic jets are primarily reconstructed by clustering calorimeter cells, the ATLAS collaboration uses a *Particle Flow* based definition [86], combining additional information from tracking into the jet definition. For the purposes of this thesis many older analysis discussed utilise a purely calorimeter based jet definition so that is what is described here. Jet clustering from topological calorimeter cell clusters uses a similar anti-k_t based clustering algorithm as defined for the phenomenological hadron clustering case in Section 2.2.3. Due to the non-compensating nature of the calorimeter, jets measured in ATLAS have energies that can be significantly lower than their true values. This is corrected for in the process of calibrating a jet which is a multi-step process. A jet energy scale (JES) correction [87], derived from MC simulation in conjunction with the p_{T} balance in standard candle measurements of Z/γ+jets is applied. Calibration also includes steps to mitigate the effects of pile-up (multiple

collisions in the same bunch crossing). Another uncertainty that has a large impact on jet measurements is the jet energy resolution (JER), this is accounted for using the dijet balance method [88]. Additional information can be incorporated by associating the calorimeter based jet with ID tracks. Production of beauty or charm hadrons from the primary interaction will give rise to tracks pointing to an apparent secondary interaction point, since they have relatively long lifetimes so will travel some distance in the beampipe before decaying. It can be useful to additionally tag a jet as a b-jet [89], which as a likelihood based discriminator also has quality working points defined.

3.3.2. Event level variables in ATLAS

With the base physics objects defined, some event-level properties can be interrogated. One key quantity that is presented in the experimental work of this thesis is the reconstruction of the missing transverse momentum, $E_{\mathrm{T}}^{\mathrm{miss}}$, of an event [90]. Due to the nature of a pp collision there is only conservation of momentum in the hard process of a collision guaranteed in the transverse plane, since an undetectable fraction of the beam energy will travel undetected longitudinally down the beampipe. The transverse momentum balance can be used to infer the presence of objects that were undetected by all previously described techniques. In the SM this is provided primarily by neutrinos, however it is also a common signature of many hypothesised BSM models so is subject to lots of searches involving observations of events with large amounts of $E_{\mathrm{T}}^{\mathrm{miss}}$. It is defined first by calculating the component of the energy observed in the $x-y$ plane,

$$E_{x(y)}^{\mathrm{miss}} = E_{x(y)}^{\mathrm{miss},\,\mu} + E_{x(y)}^{\mathrm{miss},\,\gamma} + E_{x(y)}^{\mathrm{miss,\,jet}} + E_{x(y)}^{\mathrm{miss},\,\tau} + E_{x(y)}^{\mathrm{miss},\,e} + E_{x(y)}^{\mathrm{miss,\,soft}}\,, \tag{3.5}$$

where $E_{x(y)}^{\mathrm{miss,\,object}}$ is the $x(y)$ component of the negative vector sum of the momenta of the objects as defined previously. $E^{\mathrm{miss,\,soft}}$ corresponds to all remaining physics objects not passing the selection criteria of physics objects, such as calorimeter clusters not included in a jet. The $E_{\mathrm{T}}^{\mathrm{miss}}$ is then accordingly defined as,

$$E_{\mathrm{T}}^{\mathrm{miss}} = \sqrt{(E_x^{\mathrm{miss}})^2 + (E_y^{\mathrm{miss}})^2}\,. \tag{3.6}$$

Events are also often subject to overlap removal criteria, to remove instances where a single true particle is reconstructed as two separate physics objects. For example, if an electron and a jet are reconstructed in the same event with separation $\Delta R < 0.2$, it would be common to discard the jet as this would most likely have resulted from the electrons calorimeter deposits. This increases the purity of the selected events.

The base physics objects can also be used to infer the presence of heavier particles in the interaction. For example a candidate Z boson can be reconstructed by looking for events with two electrons with a combined invariant mass of close to m_Z. The goal of a physics analysis at ATLAS is generally to extract some inference on events with such patterns.

3.4. The ATLANTIS Event Display

The ATLANTIS event display is one of the two main displays of the ATLAS collaboration. The other main display is VP1 [91] which is more modern and makes 3D representations of the events. ATLANTIS provides a 2D representation of events and detector geometry, with many options to display different representations of the detector systems and the physical objects that are overlaid. It has uses in production of event displays for complementary information to ATLAS publications, as an online monitoring tool in the ATLAS control room and as an outreach tool for education.

3.4.1. Event storage in ATLAS

After an event has passed the trigger chain, all the information describing the event has to be recorded to disk. A representation of a complex object like an ATLAS event needs an Event Display Model (EDM) [92], the key stages of the ATLAS EDM are shown schematically in Figure 3.5. The main goal of the experiment is to perform physics analyses, as such the EDM is designed primarily to serve this goal. The main requirement of the physics analyses is speed of reading in the large number events needed, and disk storage space needed. The initial events read in as raw bytestream information from the detector are large, running to $\sim$1.5MB in Run 1, and ever increasing in size throughout Run2 and beyond. This format is then transformed to an Event Summary Data (ESD), containing the reconstructed detector information. An ESD should retain all information needed to reconstruct and calibrate all objects needed in a physics analysis [1]. The next set of reconstruction transforms are then intended to build and calibrate the physics objects. This is stored in an Analysis Object Data (xAOD in run 2, AOD in run 1) and is intended to contain everything one needs summarizing an event for an analysis, but without keeping any unnecessary information to reduce the filesize as much as possible.

As the schematic shows, the goal of an Event Display is somewhat orthogonal to the goal of a physics analysis. The ATLANTIS event display in ATLAS implements a custom format based on the XML markup language, known as JiveXML. The goal of an event display is to display

[1] It is noted that in Run 2, typically no physical ESD files are saved, it generally functions as a virtual step in the reconstruction from RAW to xAOD.

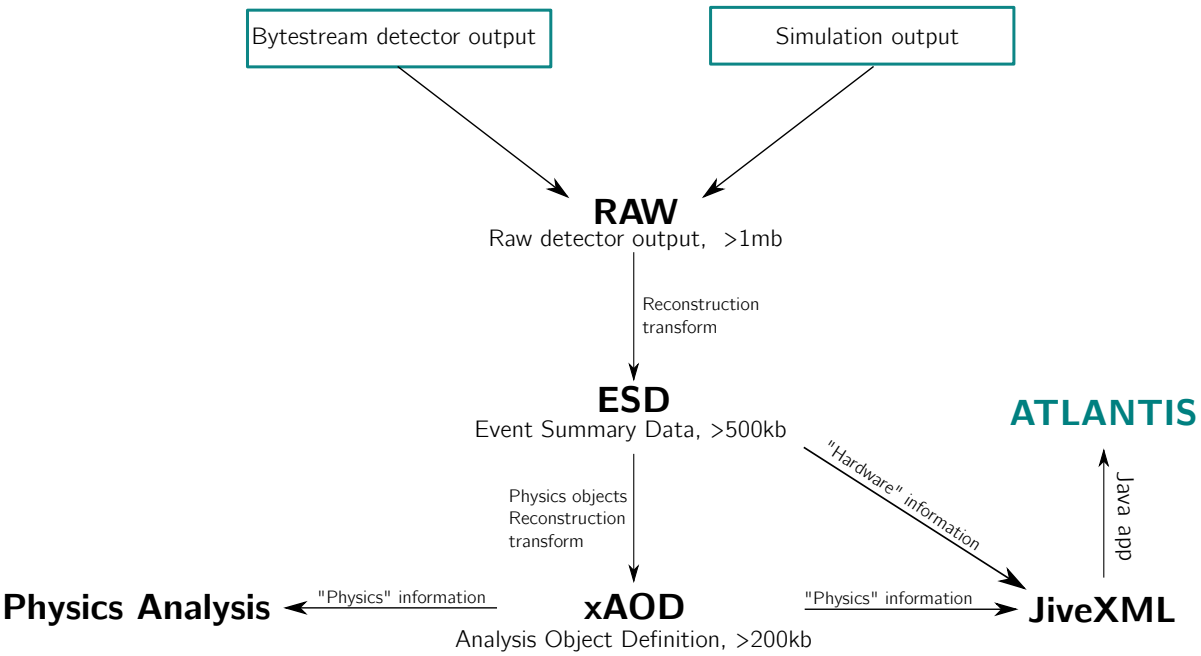

Figure 3.5.: ATLAS EDM schematic.

both the calibrated physics objects needed in an analysis, and their relation to the underlying detector information. Such a link between these two information sources is what gives the physical intuition in graphical format as to what is happening in the detector. A separate set of transform algorithms have been designed to run on top of the usual set of packages, to extract information from different parts of the workflow, taking the "Hardware" information from the ESD level, and the "Physics" information from the xAOD level. A separate data format, especially a non binary format, is useful as events stored in this manner can be accessed without the proprietary software of the collaborations toolchain. This lets even external users make use of physics events for outreach with little assistance, for example the Quantizer project to sonificate ATLAS events is based on the JiveXML format [93]. The downside is that when major changes are made to the data formats from which the JiveXML is derived, these require manual intervention, this is discussed in the subsequent section.

3.4.2. Response to an updated data model

Between Run 1 and Run 2, the AOD part of the ATLAS EDM was replaced by the xAOD format [94]. The reasons for these changes are rooted in decisions made with improved physics analysis usability in mind. This however necessitated a rewrite of the part of the JiveXML transforms that extracted physics information, due to the non-trivial differences between the AOD and xAOD format that these transforms were based off. The main difference was that the links between the ESD detector information and the xAOD physics objects was broken. As

noted already this is one of the keys to giving a picture that highlights physical intuition of how the experiment actually works.

A specific example of type of link needed, is that one would like to highlight the connection between a series of hits in the calorimeter cells (ESD level information) and their links to reconstructed calorimeter clusters and the resulting jets (xAOD level information). This is information that was restored to the displays in this work. An example of the current state of the ATLANTIS event display is given in Figure 3.6. The panels shown in that figure, in clockwise order starting in the top left, are:

- Unfolded η vs ϕ projection of the calorimeter cell energy deposits
- A transverse slice through the barrel of the detector, zoomed into to highlight especially the tracking detectors.
- The event information.
- Unfolded η vs ϕ projection, with squares showing calorimeter cells and lines showing fitted tracks.
- A longitudinal slice through the barrel and end-caps of the detector, zoomed to show the calorimetry, tracking and as much of the muon system as possible.

In this event, four high ($\geq$ 100 GeV) p_{T} anti-k_t R=0.4 jets have been reconstructed and drawn as blue, orange, green and red cones. These are overlaid on the underlying detector information, where tracks are drawn with grey lines, and hits in the calorimeter cells are shown as grey boxes. The size of the grey boxes representing calorimeter hits are proportional to the energy read out of the cell, and the amount the fitted track bends in the magnetic field is proportional to the p_{T} of the particle. If one of the detector hits is found to be related to one of the jets it is coloured accordingly. Two additional cyan and yellow track clusters are visible that don't relate to a visible physics object. These tracks represent tracks associated to jets that did not meet the jet cuts imposed. This is a typical format for ATLANTIS event displays in ATLAS.

A complementary image of the same event is shown in Figure 3.7. This image is designed to show off what the combination of detector and physics object information can do to display intuitively the sorts of physical phenomena an analysis can be sensitive to. In Figure 3.7a the same jet cuts as before are ran for an anti-k_t R=0.4 jet finding algorithm, where the colours match those in Figure 3.7. In Figure 3.7b, the same event has instead had a wider radius, anti-k_t R=1.0 jet finding algorithm run. Some interesting features of this comparison are:

- The larger radius algorithm finds fewer jets in the event, and has in effect merged the green and orange jets from Figure 3.7a to one (red) jet in Figure 3.7b. This red jet has a

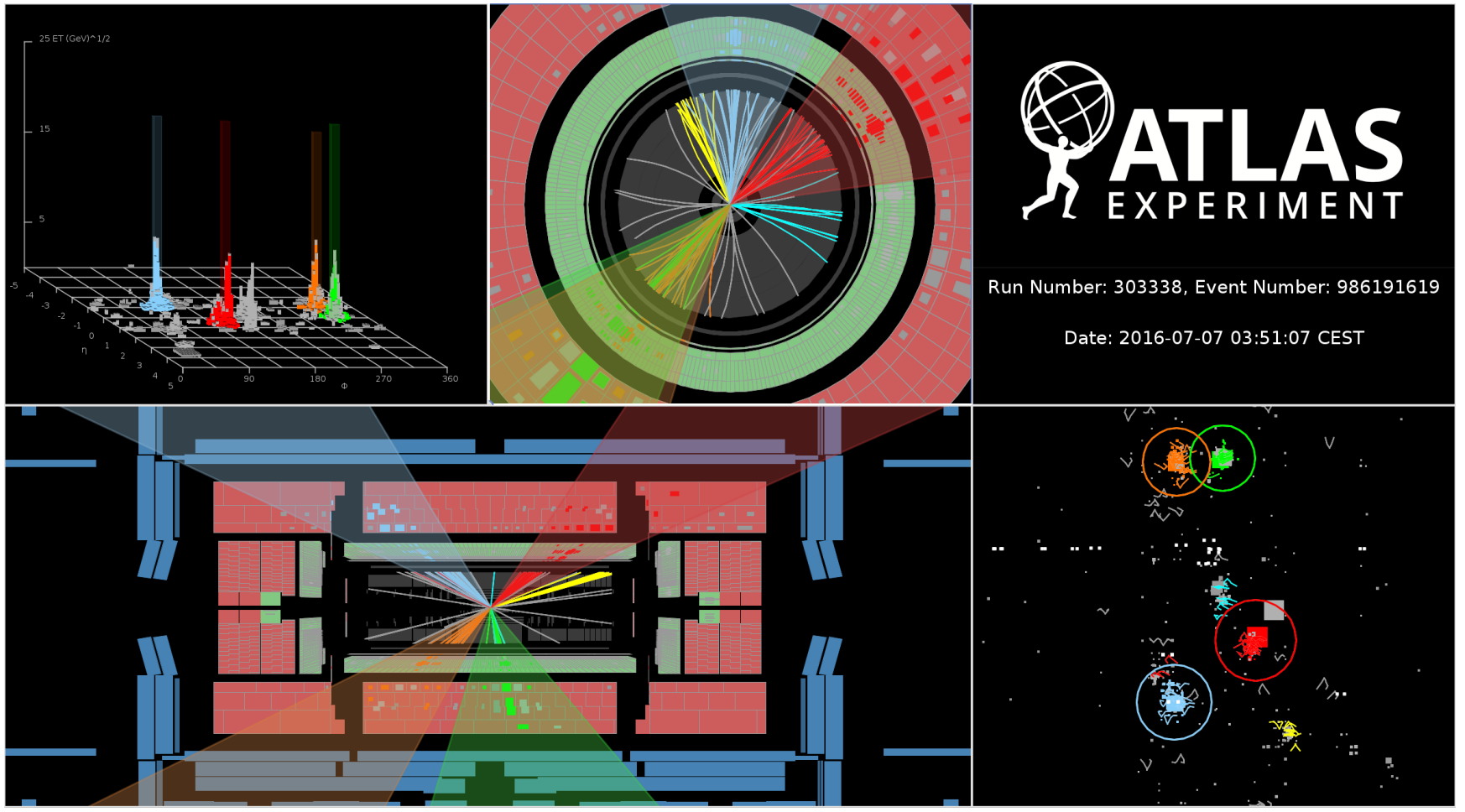

Figure 3.6.: An event display for data taken during the 2016 13 TeV LHC run recorded with the ATLAS detector. Various projections of the detector are shown to highlight different aspects of the event.

distinctive shape now compared to the other two remaining (green and blue) jets, with two high energy deposit cores visible. It is this jet *substructure* that has become a very active area of inquiry for collider experiments at the LHC [95].

- The jets in the smaller radius case appear more regularly distributed around a hard core, whereas the larger jets appear to include cells that were not considered as being part of any smaller radius jets passing the jet cuts. This is a reminder that a jet is a representation of the calorimeter cell (and associated tracks) information, and is subjective to an algorithmic choice. There are no canonical jets in an event.

3.4.3. Online operation

One of the other functions of the ATLANTIS event display, aside from illustrations for publication is a part of the online monitoring suite in the ATLAS control room. As a final visual check on the Data Quality Monitoring (DQM) desk, this gives high level feedback as to the overall functioning of the detector. This stream of event visualisations is sampled from the currently recorded events on the fly and refreshed with a new event on a time-scale typically of $\mathcal{O}(1)$ minute, with some lag time to allow for the reconstruction algorithms to run and provide the XML file. One of the times when such visual representation is most important is during changes of beam condition, where run conditions are changing there is a higher probability of subsystems not functioning which needs monitoring. One of the most notable events at the beginning of each data taking run is known as beam splashes, when the protons circling the LHC ring are made to collide with the collimators upstream of the detector, showering the entire detector with particles lighting up readouts across the board allowing the detector to sync with the LHC clock. This is a literal and figurative champagne moment to commence each run, a display made to accompany a press release of the first beam collisions of the 2017 data run are shown in Figure 3.8.

The event display is still an active part of the operation of the detector so needs to keep up with changes to the data model and detector outputs as the collider continually evolves. For example b-tagging algorithms and trigger menus also needed work to be populated for operation work. The online event display will continue to be a challenge particularly as the LHC enters its HL period, more busy events put strain on all aspects of event reconstruction and serving live events is one area that is expected to require work as when the LHC gears up for Run 3.

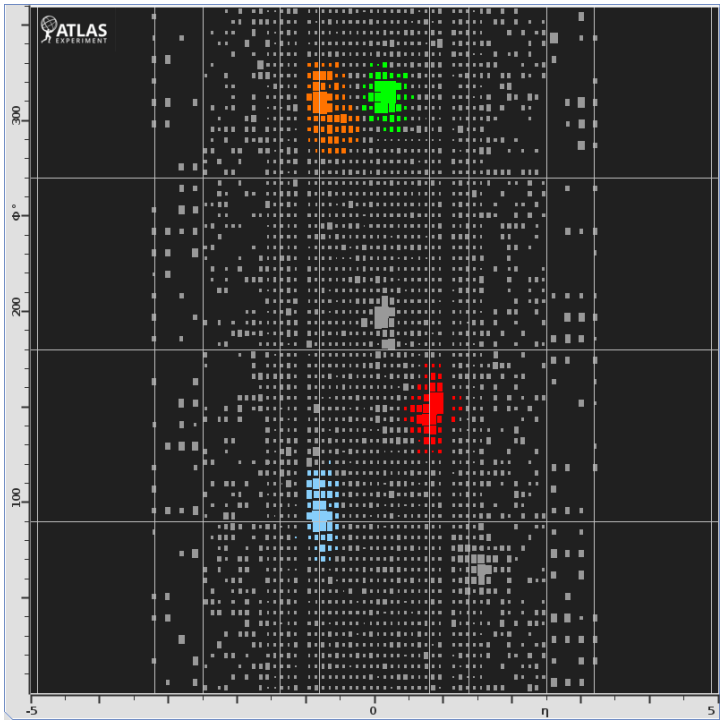

(a) Clustered jets with anti-k_t R=0.4

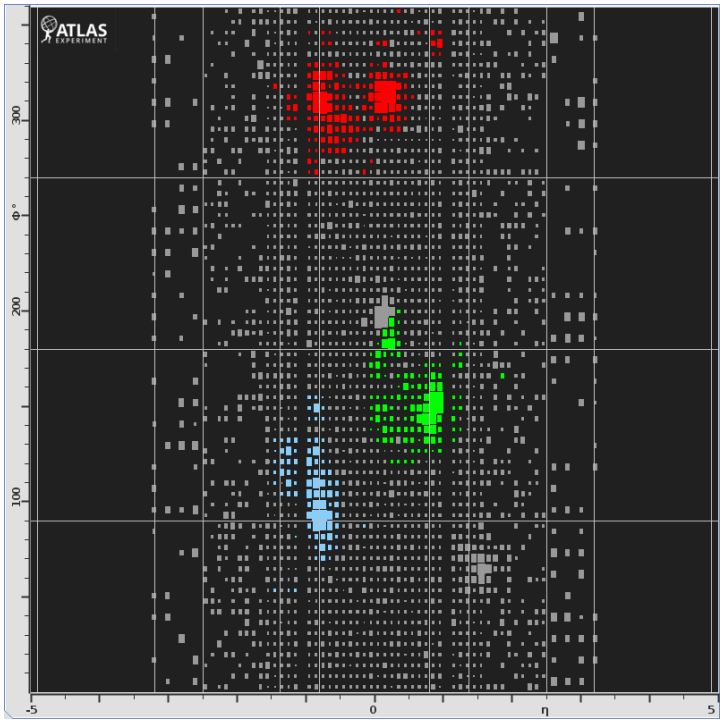

(b) Clustered jets with anti-k_t R=1.0

Figure 3.7.: Comparison of two different radii used in the anti-k_t algorithm applied to the same event. In both cases the event is displayed as an unfolded view of the barrel hadronic calorimeter in the η-ϕ plane. The event matches that shown in the full display in Figure 3.6.

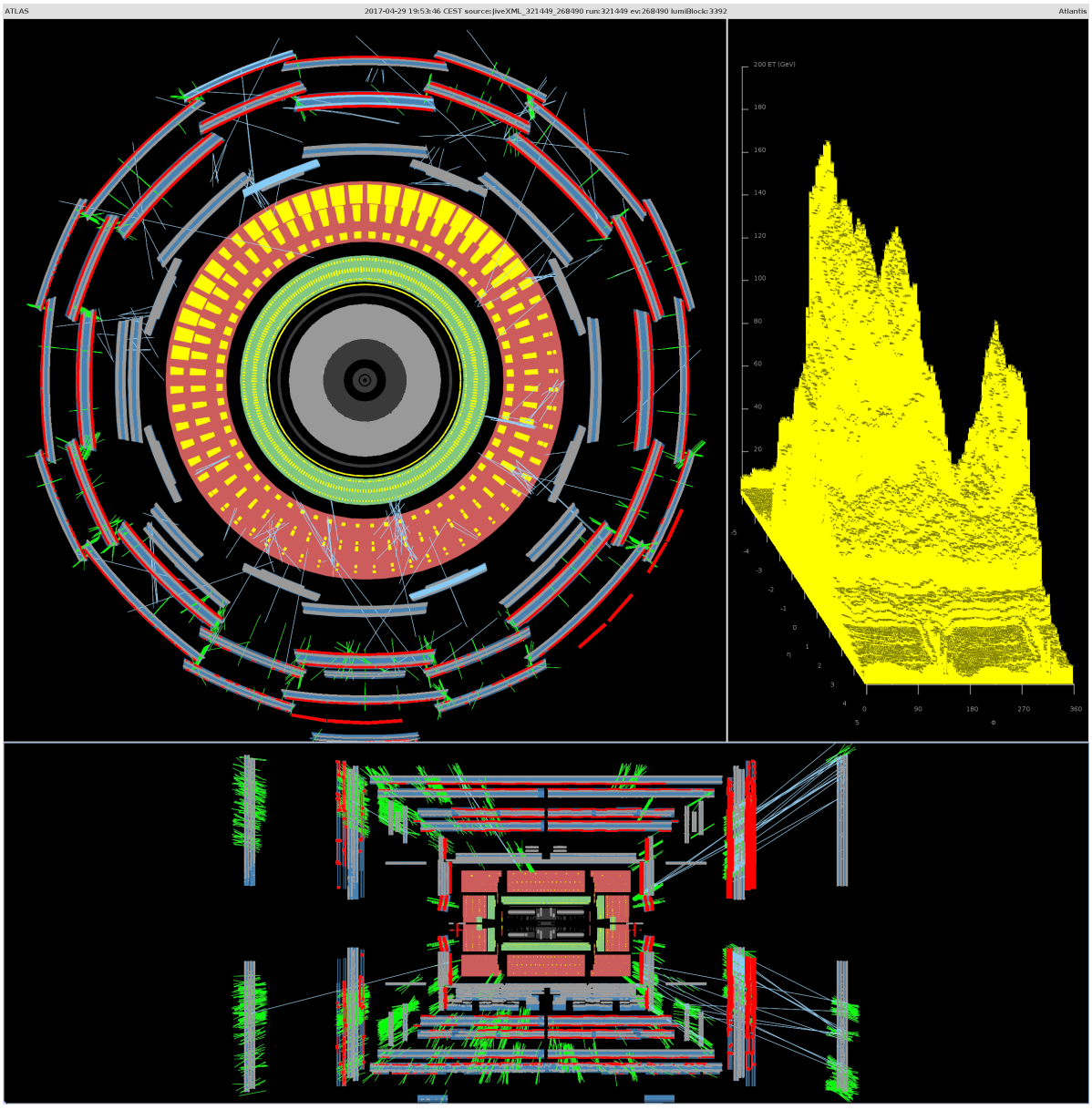

Figure 3.8.: Event display of a beam splash event from the start of the 2017 data taking run. The beam splash enters from the left hand in the bottom panel showing the longitudinal slice of the detector [96].

Chapter 4.

Making a measurement

The ATLAS experiment is equipped to measure a variety of final states from collisions. A fiducial measurement is a measurement of the properties of particle collisions as observed by the ATLAS detector. Making such a measurement involves defining a fiducial phase space region, a set of definitions (cuts) on physics objects that matches the detector acceptance closely and is built from observable final states [85]. Using this construction ensures that the extrapolation from what is observed with the detector to what is predicted with the event generator is as independent of the short distance physics model as possible. Ideally it should only be dependent on the well understood long distance physics effects modelled in the detector material simulation.

In this chapter, a fiducial measurement of events with large $E_{\mathrm{T}}^{\mathrm{miss}}$ in the early 2015 13 TeV ATLAS dataset is presented in Section 4.2. Of particular interest is the procedure of detector correction applied to the data as this will be a cornerstone of building a re-interpretable result. In Section 4.1, some tools for fiducial particle level analysis are introduced, as well as reviewing the experimental coverage of the measurement phase space. Lastly in Section 4.3, some work towards defining the next iteration of the fiducuial $E_{\mathrm{T}}^{\mathrm{miss}}$ analysis with the full ATLAS Run 2 dataset is presented.

4.1. Fiducial cross-section measurements

The ATLAS collaboration has performed many particle level measurements throughout the LHC operation thus far, and will continue to produce more using the full Run 2 dataset. A summary of the current coverage of final state particle level cross-sections measured by ATLAS is shown in Figure 4.1. The philosophy of these measurements is to impose particle level selections that will enhance the acceptance of a particular underlying SM process. For example the Z measurements are particle level measurements of charged lepton pairs with some cut

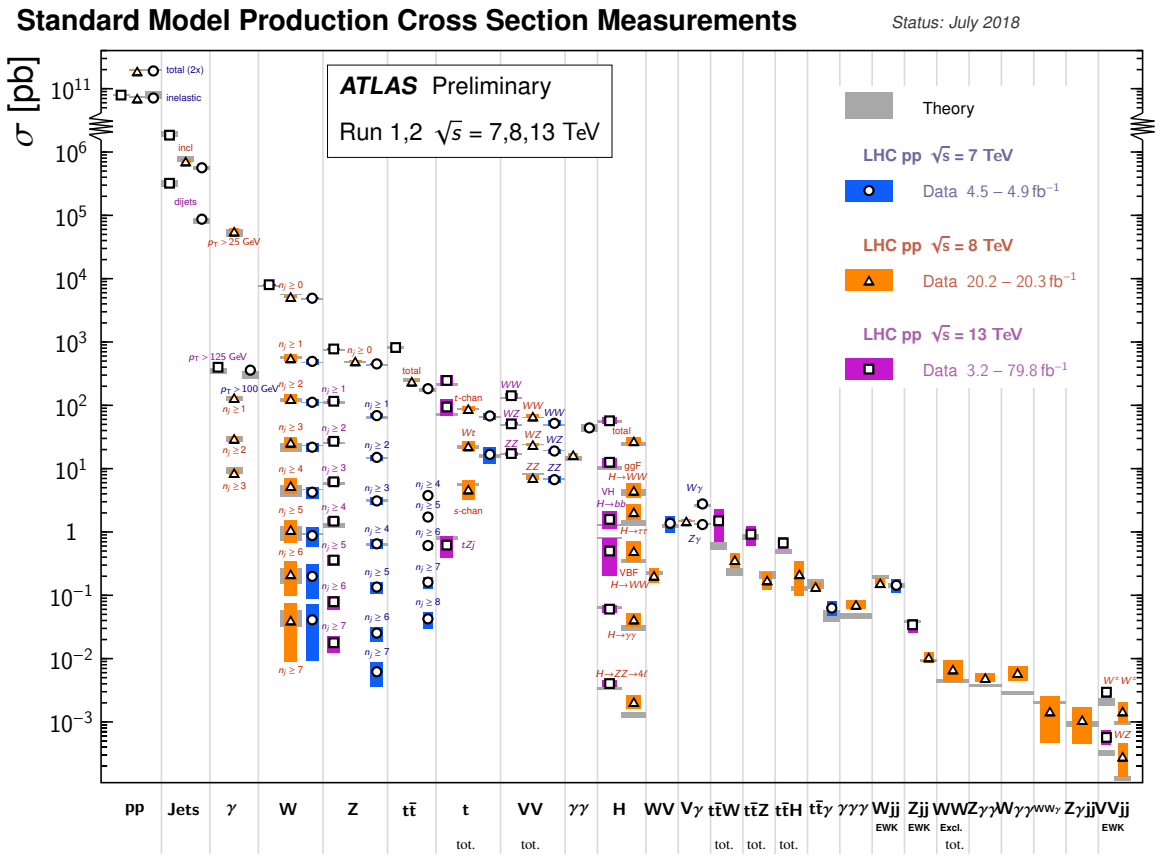

Figure 4.1.: Summary of the status of the ATLAS collaborations SM cross-section measurements [97].

imposed on the invariant mass of the dilepton system and the rapidity of the leptons to ensure they are in the fiducial well measured region of the detector. It is important to note this is a measurement of the rate of observed lepton pairs in a mass window, not a measurement of the SM Z production rate, for various reasons there is some model dependence on the SM but steps are taken to reduce this as far as possible. That said, the results in the figure across many orders of magnitude show consistent agreement with the SM, so are often called *SM measurements*.

This summary shows the total fiducial cross-sections, with some binning for example in jet multiplicities. With increasing dataset sizes these cross-sections can increasingly be measured differentially, binning in kinematic variables that will increasingly test the SM predictions. Collisions with very hard jets observed for example will have a large phase space open for QCD corrections which can expose limitations in the truncation of the perturbation series used in the hard process calculation. Where appropriate such measurement results can be used to improve the predictions for the very tail ends of distributions where a lot of the searches for

new physics operate. Increasingly LHC measurement data for example is being incorporated into the PDF fits, as the only experiment that is continually probing the structure of the proton at such scales is the LHC itself. This opens an obvious pitfall of incorporating potential new physics effects into the parameterization of the proton content, as such this is something that is done with great care. For example maintaining PDF fits with and without LHC data included, checking for any unexpectedly large change in resulting observables. Similarly the parameters of the non perturbative soft physics models used in the event generators can also be tuned to such measurement data [98]. Again this is something that great care is taken over to not sweep potential non SM effects into SM modelling.

In both the tuning and PDF example the current choices of these parameters are mostly gathered from experiments other than the LHC, primarily from ee collisions gathered at LEP for soft model tuning and ep collisions gathered at HERA for PDF fits. These collisions are very well suited laboratories to study their respective effects as they are cleaner environments than in pp collisions, however as the LHC appears to be the only experiment at the energy frontier for the next decades it will increasingly become limited by the energy range and dataset size of these experiments which are no longer running. Typically the measurements from the LHC that are included factorise from the search program style final states, using minimum bias events to understand the soft model for example. However it is clear at some point that if many searches are becoming systematically limited by their PDF uncertainty in a consistent way that this represents a measurement of the proton structure.

One of the most widespread uses of these measurements perhaps is in comparison of algorithmic differences in physics implementations in generators. Rather than an uncertainty based on a measurement this is a comparison that is much harder to quantify. For example there is a clear ambiguity between an AO and a k_t ordered PS. Such measurements can be used in the phenomenological development of such algorithms and inform their construction. In a similar vein one could also think to use these measurements to quantify the difference between the compatibility of the physics model used in the perturbative calculation with this data; this idea will form the basis of the work presented in Chapter 5 and Chapter 6.

4.1.1. Correcting for detector effects

A distinction has been made between results that are presented as searches for phenomena and results that are measurements of the particle level collision properties. The same data and reconstruction techniques are used within the experiment but the key difference is in how these are presented. In Figure 4.2 a schematic of the flow to the various defined levels used in the discussion is presented for MC generated events. Generated events are translated to detector level by using the ATLAS simulation stack [99] which at its core involves the simulation of

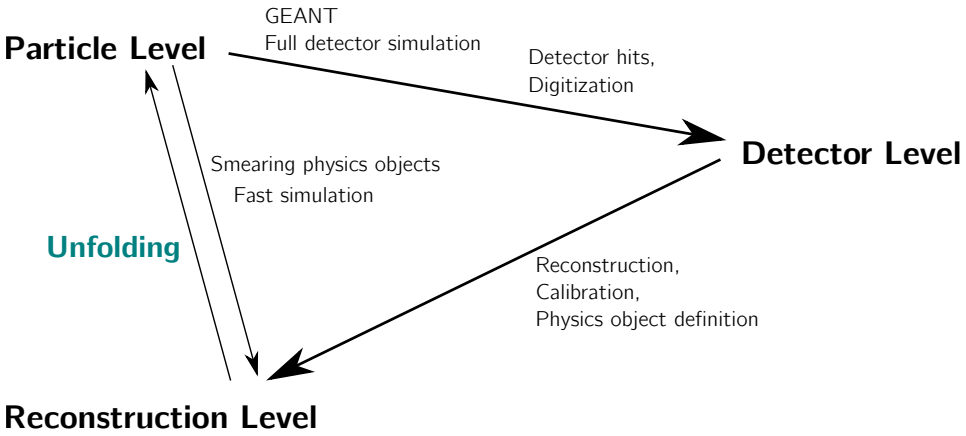

Figure 4.2.: Schematic of the reconstruction and unfolding process.

particle interactions with the material of the detector using the Geant4 package [100]. The simulation can be read out at detector level in an identical manner to the recorded collision data, so can then be subject to the same reconstruction algorithms as the data itself. This translation defines reconstruction level. Translations between particle level and reconstruction level are then the goal to define, without having to invoke the full simulation by translating to detector level first. An important point to emphasise is that the reconstruction algorithms used in the experiment already move the events closer to their particle level definition, translations in either direction between particle and reconstruction level distributions are not as intensive as the operation of detector simulation needed to translate between particle and detector level. In part this is also the motivation behind the fiducial phase space definition of physics objects, this enables similar quantities to be defined on the particle level as the reconstruction level so the translation between these two is actually quite close. Correcting for detector effects or *unfolding* is then the operation that translates between reconstruction level and the particle level.

Following some standard formulation [101], the problem of correcting for detector effects can be phrased as follows. First the operation that translates a vector of particle level *truth* histogram bins, t_i, to their corresponding reconstruction level histogram bin vector, r_i, is defined. This operation can be parameterized by introducing a response matrix, R_{ij} as,

$$r_i = R_{ij} t_j \,, \tag{4.1}$$

where the response matrix can be written as the probability,

$$R_{ij} = \mathrm{P}(\text{reconstructed in bin i} \mid \text{in true bin j}) \,. \tag{4.2}$$

This response encodes the effect of migrations between bins, and the efficiency of reconstruction. Additionally unwanted experimental backgrounds, such as one type of physics object faking another, can be subtracted prior to unfolding or included in the response composition. It also isn't necessary to unfold to the particle level, one could unfold all the way back to the partonic matrix element definition for example. However this folds an unwanted degree of short distance physics modelling dependence into the response for the purposes of this and the following discussions. To derive the response matrix one constructs t_i and r_i using MC events, since MC events are defined at both levels. To first order, the goal is to invert this response and apply it as a correction to the reconstruction level data histogram, giving the *unfolded* particle level data histogram. There are a number of methods employed in ATLAS to derive the corrections needed to unfold. Most commonly iterative Bayesian unfolding [102] is used. In the analysis presented in the subsequent section, due to the minimal bin migrations and the fact that the majority of experimental effects cancel in a ratio measurement, a simpler method based on bin by bin correction factors is used [103].

It is here that one would fix the widths of the bins used in a differential cross-section analysis, basing this decision on the experimental resolution of the variable one wants to bin in, the statistics in each bin and the stability of migrations between bins. Typically a minimum number of events based on the expected number of events of ten per bin is imposed. Having sufficient statistics keeps the unfolding process stable and will be useful in defining statistical tests based off the resultant distributions.

4.1.2. Accessing unfolded cross-sections

In this section it was noted that one of the main purposes of a SM unfolded cross-section is its use in phenomenological studies, typically by people external to the collaboration. As such, for such a wide array of results to be useful they have to presented and accessible in a consistent manner in a way that decouples from the experimental software. To that end the HEPData project [104] is a central repository for all HEP data from any experiment. It allows custom data types to be uploaded but the unfolded cross-section results can be sufficiently captured there with data tables for histograms and additional corresponding systematic and statistical correlation matrices.

The missing piece is the ability to interface the event generator MC events to these data histograms. All modern LHC event generators use the common HEPMC framework to describe and save events [105] so the particle level generator output is available in a consistent way. A framework to analyse HEPMC events is provided by the Rivet [106] library, which is the generally accepted standard for particle level analysis. Rivet provides tools to implement the fiducial phase space selection on a stream of HEPMC events, it is in essence a toolkit for

HEPMC analysis. To ease the comparison between prediction and observation, Rivet also synchronises directly with the data on HEPData and each Rivet release comes with an ever growing library of experimentally validated plugins that replicate the phase space definitions of various analyses. The production of particle level MC prediction histograms and representation of observed particle level detector corrected data is thus automated in the same framework.

4.2. Detector corrected observables sensitive to events with large imbalances of energy in the transverse plane

At the LHC, the presence of large $E_{\mathrm{T}}^{\mathrm{miss}}$[1] in an event is a selection often used to discriminate for potential new physics. The initial goal of the analysis was to measure final states composed only of large $E_{\mathrm{T}}^{\mathrm{miss}}$ produced with hadronic jets. The only particles in the SM that can contribute to particle level $E_{\mathrm{T}}^{\mathrm{miss}}$ are the neutrinos, these will only be produced in hadronic collisions via production of the massive EW bosons. Nearly all existing fiducial measurements with $E_{\mathrm{T}}^{\mathrm{miss}}$ observed in the event are of leptonically decaying W bosons, so come with a visible charged lepton. The all hadronic final state required means this is the first fiducial cross-section measurement of the $Z(\rightarrow \nu\nu)$+jets process made at ATLAS. The measurement was conducted using the early Run 2, 3.2 fb^{-1} 13 TeV dataset [107]. The leading Feynman diagrams of the SM contribution to the two selections made in this analysis are shown in Figure 4.3.

A typical fiducial cross-section measurement is designed to measure a target SM process, so the selection criteria are informed by the SM. This is a measurement designed to be sensitive to anomalous contributions of BSM physics, so the selection criteria are designed to be sensitive to some common classes of BSM signatures. As a measurement there is a balancing act made here however, the goal is not to optimise the selection to be optimally sensitive to any particular model at the expense of others. As such the selections are split into two classes that are common signatures often searched for for hints of BSM physics. Firstly there is a ≥ 1 jet (or *monojet* like) category, this will be sensitive to contributions from simple DM models, such as those in Figure 4.3c. This is a simpler signal region and mirrors one of the flagship analyses of the collaboration, the monojet search [108]; it is an inclusive search so is used to study a wide variety of BSM contributions.

A more complex signal region is the one designed to be sensitive to vector boson fusion (VBF). There is no colour exchanged between the interacting quarks, which gives rise to a

[1] Missing transverse energy, $E_{\mathrm{T}}^{\mathrm{miss}}$, is equivalently sometimes labelled $p_{\mathrm{T}}^{\mathrm{miss}}$ across ATLAS, both notations are used in this chapter.

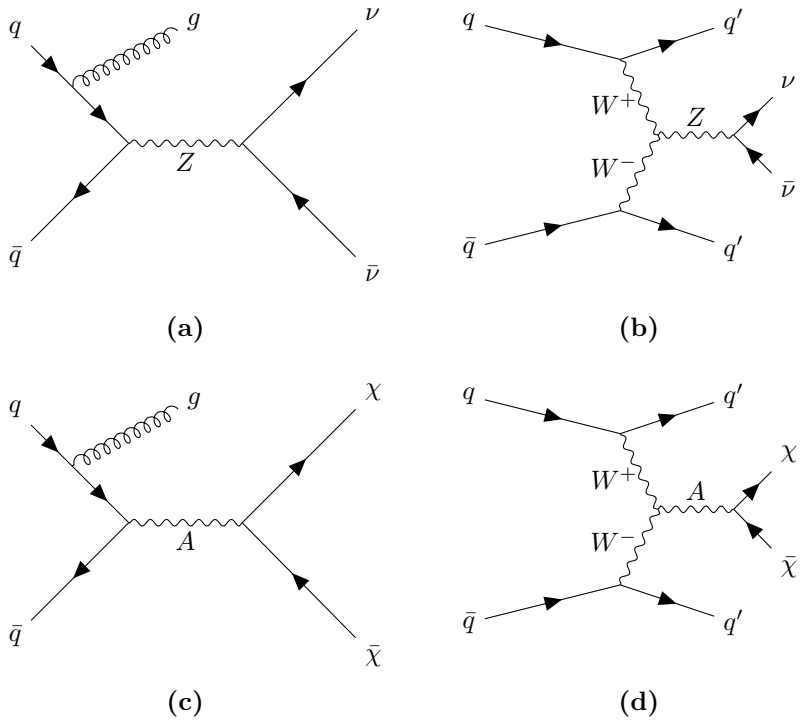

Figure 4.3.: Feynman diagrams of the processes this analysis is designed to be sensitive to in its two selection regions. In Figure 4.3a an example of the leading SM contributing to the monojet signal region is shown and in Figure 4.3c the corresponding hypothesised BSM production of a DM candidate χ via a boson mediator A. In Figure 4.3b the target leading SM process of the VBF signal region is shown and in Figure 4.3d VBF production of the DM candidate is shown.

distinctive event topology of the associated jets [109]. This lack of colour exchanged means the emission of additional radiation is suppressed (this can be motivated by the suppressed colour factors of the corresponding virtual correction), so can be identified experimentally at the LHC by the presence of two hard forward jets with suppressed hadronic activity in the rapidity range between these two. This was historically an idea proposed to extract Higgs measurements as this has a relatively large VBF production cross-section with respect to the dominant QCD induced background [110]. It can be used then to extract any colourless exchange interaction from the dominant QCD backgrounds at the LHC, such as the VBF Z production process shown in Figure 4.3b or an example BSM DM production with a different mediator boson produced, A. This selection criteria only serves to reduce the QCD contribution in the signal region, in reality due to the relative smallness of the EW gauge couplings with respect to the strong coupling there will still be a sizeable QCD contribution. Enhancing the EW diagram contribution also means the interference between QCD and EW diagrams, which would normally be negligibly small also needs to be kept in mind [111].

The reconstruction of the $E_{\mathrm{T}}^{\mathrm{miss}}$ in an event is sensitive to the uncertainty in measurement of every object in the event. These uncertainties reduce the power of the measurement to extract a BSM signal contribution. In order to control these, or reduce their impact, rather than the differential cross-section of events with large $E_{\mathrm{T}}^{\mathrm{miss}}$, a ratio observable is constructed, R^{miss}. This is based on the observation that the $Z \to \nu\nu$ SM events contributing to the signal region will be theoretically similar[2] to $Z/\gamma^* \to l^+l^-$ events (with l denoting the visible charge leptons μ, e). Measurement of these $Z/\gamma^* \to l^+l^-$ processes with a similar selection criteria can then be used to make control measurements of the signal process by marking the visible charge leptons as invisible in the $E_{\mathrm{T}}^{\mathrm{miss}}$ calculation, building the pseudo-$E_{\mathrm{T}}^{\mathrm{miss}}$ in such events. By measuring the number of events in the two regions, one can divide the signal region (SR or *numerator*) contribution by the control region (CR or *denominator*) contribution. The experimental uncertainties will largely be common between the two regions so should largely cancel out, this construction enables a distribution to be measured that will be sensitive to new physics. The selection criteria for the numerator and denominator are listed in Table 4.1. Taking for example the choice to impose a selection of $E_{\mathrm{T}}^{\mathrm{miss}}$ >200 GeV, this is motivated in part by the lowest unprescaled trigger, and in part to mitigate the background arising from multijet events. It is often a balance of quality of physics objects, trigger rates, background mitigation and other experimental considerations that define the cut choices. These are designed to be as inclusive to new physics as possible, but the cross-section will be binned differentially in key observables characterising the events which should enhance discriminating BSM power.

[2] Up to the off shell photon and NLO EW corrections

Numerator and denominator	≥ 1 jet	VBF
$p_{\mathrm{T}}^{\mathrm{miss}}$	> 200 GeV	
(Additional) lepton veto	No e, μ with $p_{\mathrm{T}} > 7$ GeV, $\lvert\eta\rvert < 2.5$	
Jet $\lvert y\rvert$	< 4.4	
Jet p_{T}	> 25 GeV	
$\Delta\phi_{\mathrm{jet_i,p_T^{miss}}}$	> 0.4, for the four leading jets with $p_{\mathrm{T}} > 30$ GeV	
Leading jet p_{T}	> 120 GeV	> 80 GeV
Subleading jet p_{T}	–	> 50 GeV
Leading jet $\lvert\eta\rvert$	< 2.4	–
m_{jj}	–	> 200 GeV
Central-jet veto	–	No jets with $p_{\mathrm{T}} > 25$ GeV
Denominator only	≥ 1 jet and VBF	
Leading lepton p_{T}	> 80 GeV	
Subleading lepton p_{T}	> 7 GeV	
Lepton $\lvert\eta\rvert$	< 2.5	
$m_{\ell\ell}$	66–116 GeV	
ΔR (jet, lepton)	> 0.5, otherwise jet is removed	

Table 4.1.: The fiducial selection requirements on the signal regions and control regions used in the analysis.

In the ≥ 1 jet SR one distribution is measured, the R^{miss} ratio binned as a function of the $E_{\mathrm{T}}^{\mathrm{miss}}$. In the VBF region three distributions are measured, R^{miss} as a function of $E_{\mathrm{T}}^{\mathrm{miss}}$, $\Delta\phi_{\mathrm{jj}}$ (the difference in the ϕ plane between the two leading jets) and m_{jj} (the mass of the two leading jets).

4.2.1. Reconstruction level and backgrounds

In both the numerator and denominator there will be contributions to the reconstruction level histograms from processes that are not the targeted $Z \to \nu\nu$ or $Z/\gamma^* \to l^+l^-$ processes, these are deemed to be background contributions and are subtracted from the final particle level corrected results. The reconstruction histograms for the number of events observed as a function of m_{jj} in the VBF SR is shown for the numerator in Figure 4.4a and the denominator in Figure 4.4b. The dominant background contribution to the numerator comes from $W \to l\nu$ processes with the lepton being out of the acceptance or not reconstructed; these are estimated

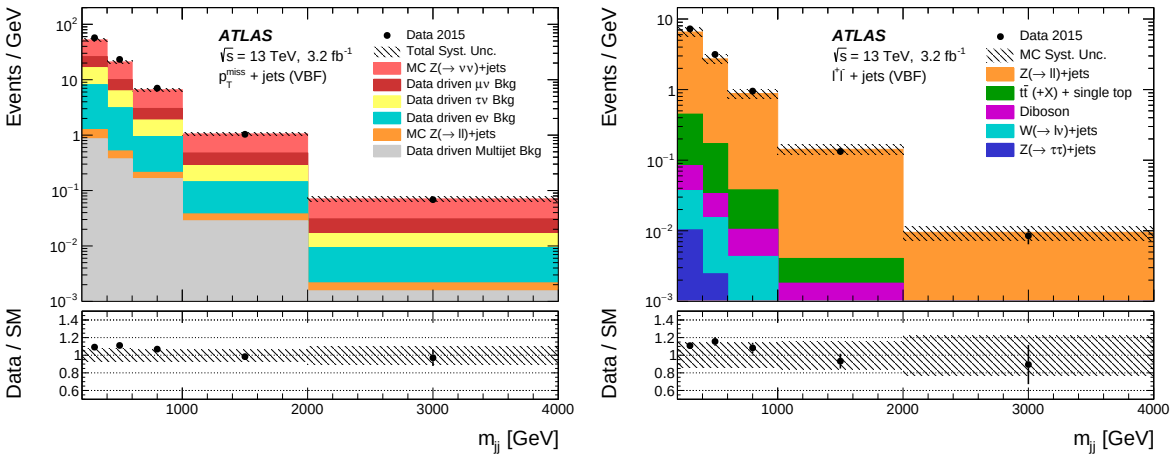

(a) (b)

Figure 4.4.: Reconstruction level histograms of number of events observed in the numerator (Figure 4.4a) and denominator (Figure 4.4b) as a function of m_{jj} in the VBF region [107].

from data driven control regions. The dominant background to the denominator comes from $t\bar{t}$ production and is estimated from MC. The backgrounds are all subtracted from the final ratio.

It is noted that this is the level a typical search for new physics would operate, the standard procedure would be to simulate some BSM model to work out the contribution that they would have to these histograms using the same chain of detector simulation and full ATLAS reconstruction as for the SM backgrounds. Then some statistical test could be performed to test whether such a contribution is likely to be present in the reconstruction level histogram or not. Such a result would skip out performing the detector correction steps which can be time consuming, and difficult to perform depending on how closely the particle level definition matches the reconstruction level selections.

4.2.2. Detector corrections and particle level distributions

The reconstruction level data histograms are corrected for detector effects using a bin by bin unfolding method. Since the majority of experimental uncertainties will cancel between the numerator and denominator by construction, the main remaining residual detector effect will come from the efficiency of reconstructing charged leptons in the denominator. Considering the width of the bins as well as the low rate of migration between bins due to these detector effects, this simple approach is well justified. Once the two lepton flavours in the denominator have been combined statistically, as well as the correction factors and background subtraction

all applied, the result are the detector corrected measurements of the R^{miss} ratio. These four distributions are shown in Figure 4.5, with additional information such as the statistical and systematic correlations between the bins of these distributions available in the paper [107]. As the data is at particle level, direct comparison between the SM particle level event generators and the data is made in these figures. Additionally some benchmark DM models are simulated at particle level and their contribution is added to the SM, to give a graphical sense of the potential to exclude these scenarios this data provides.

In all measured distributions the observed data is seen to be largely compatible with the calculated SM expectation, within the uncertainties on both of these quantities. The SM expectation for the R^{miss} quantity, solely from the branching ratio of the Z decays, is ~ 5.9 [23]. In both the observed data and the SM expectation for R^{miss} shown in Figure 4.5a and Figure 4.5b, R^{miss} is not constant as a function of $p_{\text{T}}^{\text{miss}}$. Both observation and expectation converge towards the branching ratio based expectation at high $p_{\text{T}}^{\text{miss}}$. However, at low $p_{\text{T}}^{\text{miss}}$, both the observed and expected R^{miss} are higher than the SM branching ratio based value. This is primarily driven by a difference in the fiducial definition between numerator and denominator. In the $Z/\gamma^* \to l^+l^-$ denominator, at lower Z p_{T}, there are a number of events lost due to fiducial cuts present on the charge lepton identification. An equivalent cut is not possible in the denominator. Additionally, a seemingly consistent upward fluctuation in the observed data is visible in Figure 4.5a, Figure 4.5b and Figure 4.5d. This was deemed to come from a statistical fluctuation in the observed $Z/\gamma^* \to l^+l^-$ rate.

4.2.3. Theory correlations and a photon denominator

Using a control region to constrain uncertainties is used throughout ATLAS. Searches for final states composed of $E_{\text{T}}^{\text{miss}}$ + jet commonly use a range of control regions as different processes will give better constraining power of the uncertainties depending on the magnitude of the $E_{\text{T}}^{\text{miss}}$ in the reconstructed event. The published analysis utilised a $Z/\gamma^* \to l^+l^-$ denominator, which is typically used for lower $E_{\text{T}}^{\text{miss}}$ regions in the corresponding searches. Control measurements of $W \to l\nu$ are often used for intermediate $E_{\text{T}}^{\text{miss}}$ ranges and the very high $E_{\text{T}}^{\text{miss}}$ regions make use of a single isolated photon as the control measurement. This can primarily be motivated by statistics (although experimental resolutions come into play), as seen in Table 4.2. This is comparing the EW production mechanism that will be significant in the VBF region; $pp \to lljj$ has a lower cross-section than $pp \to \nu\nu jj$ so the measurement will be statistically limited by the control region, clearly not an ideal scenario. The claim that the dominant hadronic experimental uncertainties largely cancel will still hold for a single photon denominator, but the cancellation of theory uncertainties is not guaranteed. This claim will be particularly stressed

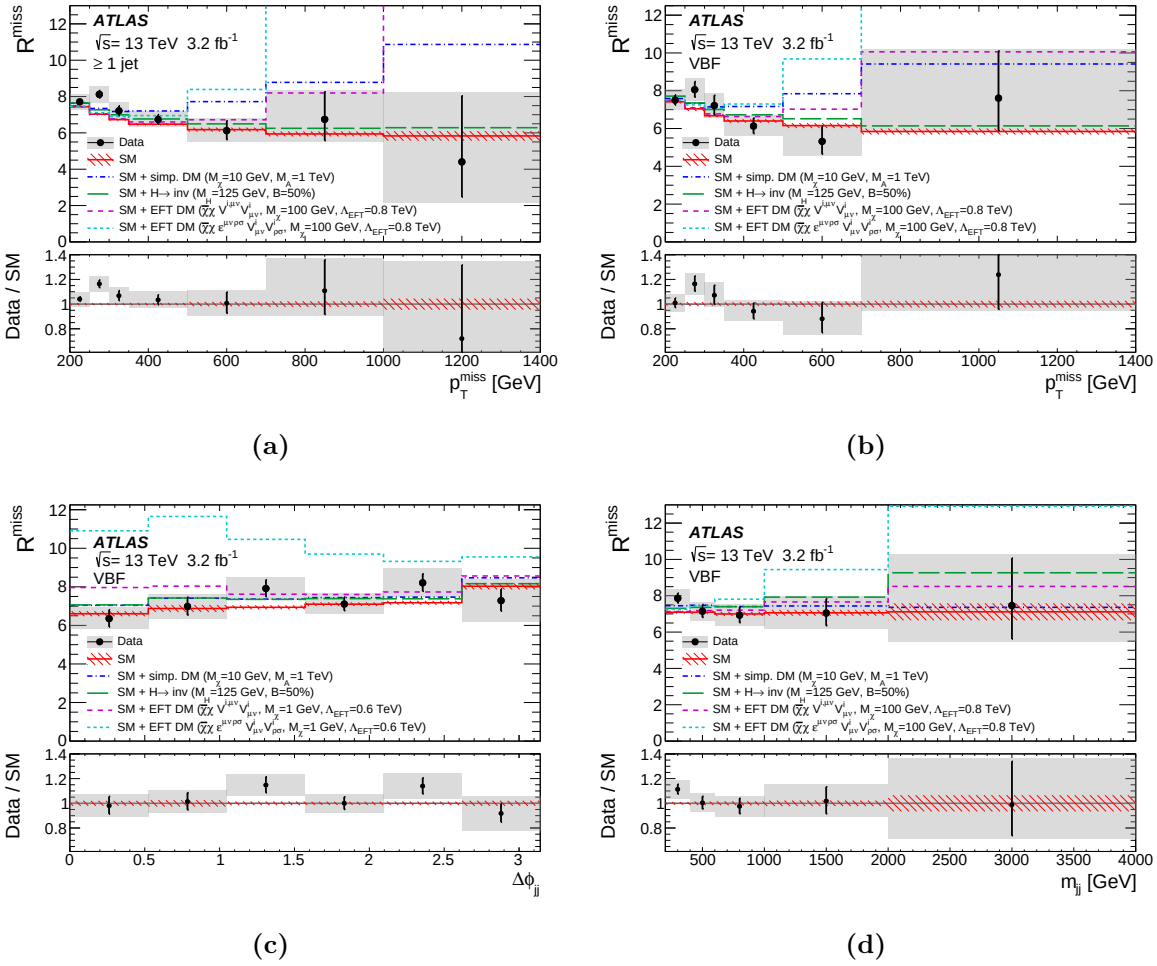

Figure 4.5.: The four detector corrected R^{miss} ratios measured in the analysis. Figure 4.5a shows the measured R^{miss} in the ≥ 1 jet SR as a function of $E_{\text{T}}^{\text{miss}}$. Figures 4.5b,4.5c and 4.5d show the measured R^{miss} in the VBF SR as a function of $E_{\text{T}}^{\text{miss}}$, $\Delta\phi_{\text{jj}}$ and m_{jj} respectively. Simulations of the SM prediction and including potential BSM contributions are shown in comparison [107].

Process (13 TeV)	σ_{LO} [fb]	σ_{NLO} [fb]	K	N_{events}, 35.8 fb^{-1}	N_{events}, 3.2 fb^{-1}
$pp \to \nu\nu jj$	714.3	750.8	1.05	$\sim$ 26900	$\sim$ 2400
$pp \to lljj$	265.7	274.5	1.03	$\sim$ 9800	$\sim$ 900
$pp \to \gamma jj$	5327.1	5528	1.04	$\sim$ 198000	$\sim$ 17700
$pp \to l\nu jj$	3706.7	3749.5	1.02	$\sim$ 134000	$\sim$ 12000

Table 4.2.: Fully inclusive cross-sections at LO and NLO in QCD for EW VBF processes under consideration [109]. Approximate number of events, N_{events}, for two potential datasets for analysis are also shown.

in the VBF SR as the choice of VBF cuts is sensitive to the mass of the centrally produced particle, which is quite different between SR and CR in this case.

By building a Rivet routine that uses the same basic selection criteria as given in Table 4.1, but extending it to include a single photon control region (using the same "mark invisible" procedure to build pseudo-$E_{\text{T}}^{\text{miss}}$ in the CR as already described) this process contribution can be studied in more detail. The selection is also extended to particularly study impact of the chosen cuts on the VBF signal region, so includes two extra regions based on tighter VBF cuts used in searches for invisibly decaying Higgs bosons [112]; these are displayed in Table 4.3. A new cut on the rapidity separation of the two leading jets is introduced, $\Delta\eta_{\text{jj}}$. The use of a prompt photon CR also necessitates an additional fiducial cut on the isolation requirement. For the purposes of this study a cut on the sum of energy of particles in a fixed radius cone around the photon, E_T^{iso}, is adopted similar to 8 TeV prompt photon measurements [113],

$$E_T^{\text{iso}} < 4.8 + (4.2 \times 10^{-3} \times E_T^{\gamma}) \text{ GeV} . \tag{4.3}$$

This cut is dependant on the reconstructed dressed photon energy E_T^{γ}. This cut cannot be implemented equivalently in the numerator SR so will be subject to some extrapolation. A comparison of the ATLAS cone isolation and the theoretical generator level Frixione isolation cut [114] is shown in Figure 4.6. It can be seen that the two approaches agree within the statistical errors, the two are generally thought to be pragmatically equivalent [43].

These particle level studies use a similar generator setup to the studies presented at the end of Chapter 2. This utilises the Matchbox framework in Herwig, ideal since it is a fully flexible NLO generator with a variety of algorithmic options available to compare within the same framework. For example this enables one to study the impact of using an AO or dipole PS, without having to fold in an additional difference between the Pythia and Herwig soft model as one would usually. The Matchbox framework in Herwig 7.0.3 is used to construct

	Current Analysis baseline	Loose VBF	Tight VBF
m_{jj} [GeV]	≥ 200	≥ 200	≥ 500
$\Delta\eta_{\mathrm{jj}}$	–	≥ 2.5	≥ 3
Leading jet p_T [GeV]	≥ 80	≥ 80	≥ 120

Table 4.3.: Additional cuts studied to those imposed in Table 4.1 (Current Analysis), to test the sensitivity to higher mass mediator particles produced via VBF.

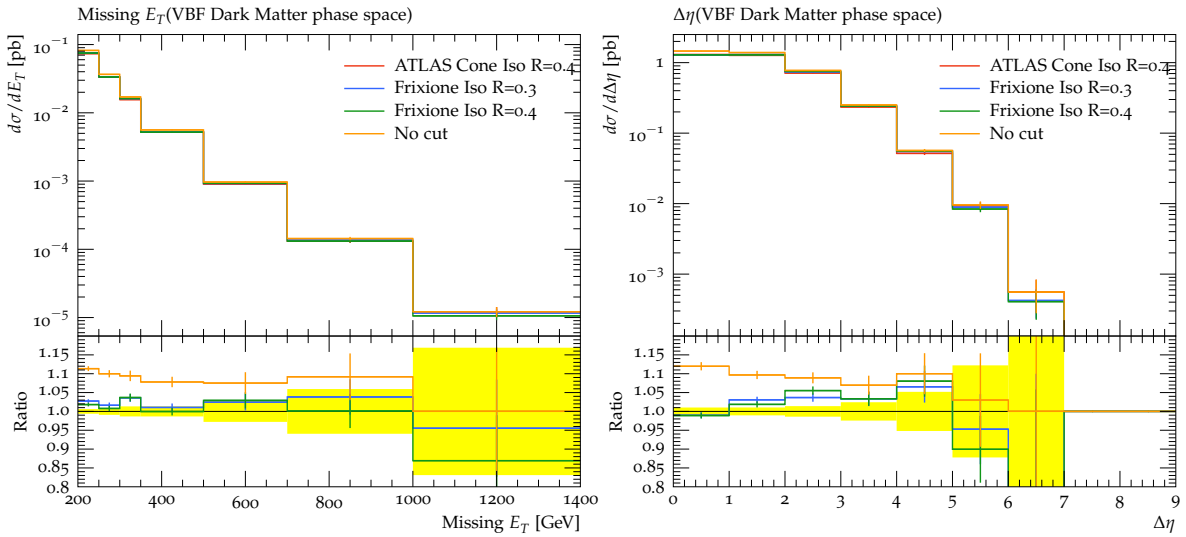

(a) **(b)**

Figure 4.6.: Comparison of photon isolation cuts to compare the experimentally implementable ATLAS cone with the theoretically motivated Frixione isolation cone [114]. The isolation requirements are imposed on VBF EW single photon production events and the cross-section is calculated differentially in $E_{\mathrm{T}}^{\mathrm{miss}}$ and $\Delta\eta_{\mathrm{jj}}$.

subtractive NLO ME matched to the dipole shower. The real emission amplitudes are taken from MadGraph and the one loop virtual amplitudes are taken from VBFNLO [115] for the VBF diagrams and OpenLoops for the QCD diagrams. By first examining the ratio of EW diagrams in isolation in the VBF region, with appropriate generator variations the degree to which the theoretical uncertainties on the R^{miss} ratio using a single photon (R_{γ}^{miss}) rather than a charged lepton denominator (R_{Z}^{miss}) can be estimated. It was already noted and shown that for R_{Z}^{miss} the numerator and denominator processes are similar enough that the theory uncertainties largely cancel, this is not necessarily true for R_{γ}^{miss}.

For the remainder of this discussion, only the calculated cross-section, and R^{miss} binned in m_{jj}, will be shown in the baseline VBF selection for simplicity although in principle any variable can be used. For the $Z \to \nu\nu$ process, all Born diagrams corresponding to $\mathcal{O}\left(\alpha^4\alpha_{\text{S}}^0\right)$ are generated for the $pp \to \nu\nu jj$ amplitude. For the single photon process, all Born diagrams corresponding to $\mathcal{O}\left(\alpha^3\alpha_{\text{S}}^0\right)$ are generated for the $pp \to \gamma jj$ amplitude. The perturbative uncertainty band on each generator prediction is constructed following a similar recipe to the Matchbox predictions shown in Chapter 2. The EW cross-section $pp \to \nu\nu jj$ prediction is shown at LO in Figure 4.7a and at NLO in Figure 4.7b, the EW single photon prediction is shown at LO in Figure 4.7c and at NLO in Figure 4.7d.

The interest behind this study is in the central jet veto applied to define the VBF signal region. This veto makes the acceptance of the detector level histograms being predicted very sensitive to QCD radiation effects. Since this vetoes any event with a central jet of p_{T} >25 GeV , predicting this quantity becomes a *multi-scale* problem, where the hard process centrally produced boson can be at arbitrarily hard scales. Such a problem is a challenge to understand theoretically. The standard recipe to understand the theoretical uncertainty on the ratio of these two predictions would be to fully correlate each individual variation between the two processes and construct the envelope on the ratio, this is shown for the two NLO predictions made in Figure 4.8b.

However this exposes somewhat of a flaw in the scales that are used as handles on the perturbative uncertainties. The cancellation of variations in the ratio, if the variations are treated as correlated between the numerator and denominator, only says that the truncation of the perturbation series at a given order are equally stable. If the central values of the cross-section are diverging with increasing order of perturbation theory then some behavior is not covered in by the variation of scales. To understand this a comparison of R_{γ}^{miss} calculated at LO and NLO is shown in Figure 4.8a. Any concrete conclusions are less clear as there is still a large uncertainty in MC statistics, particularly present in the NLO ratio. There does appear to be some small deviation between the two orders of calculation, particularly in the 1 TeV $< \text{m}_{\text{jj}} <$ 2 TeV bin. This is in line with similar observations which have been employed in a ratio of Z plus dijet and photon plus dijet [116], but is now explicitly checking both the

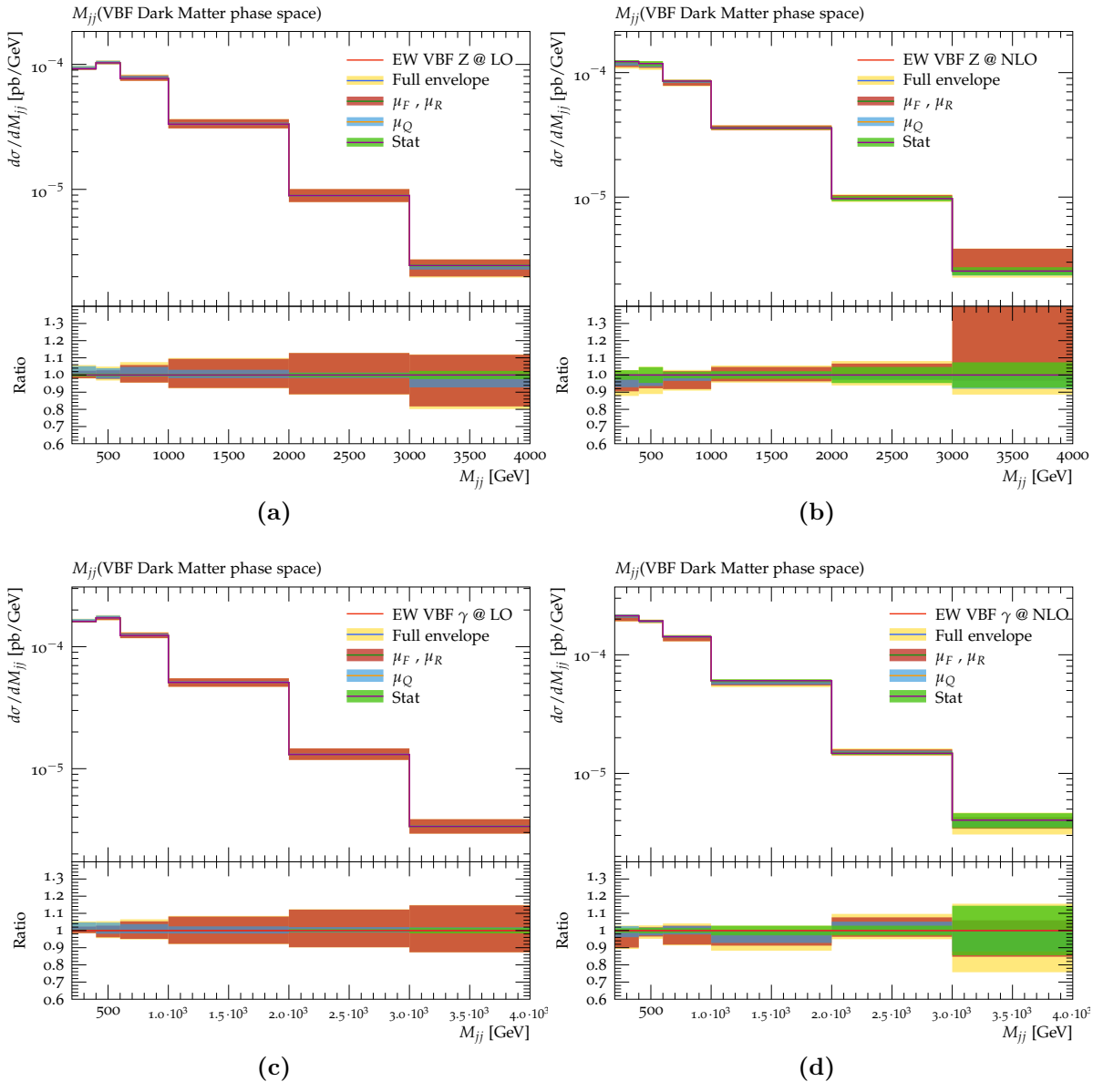

Figure 4.7.: A comparison of the differential cross-section distribution for EW production of a Z boson at LO (Figure 4.7a) and NLO (Figure 4.7b) in QCD. Similarly for single photon production at LO (Figure 4.7c) and NLO (Figure 4.7d).

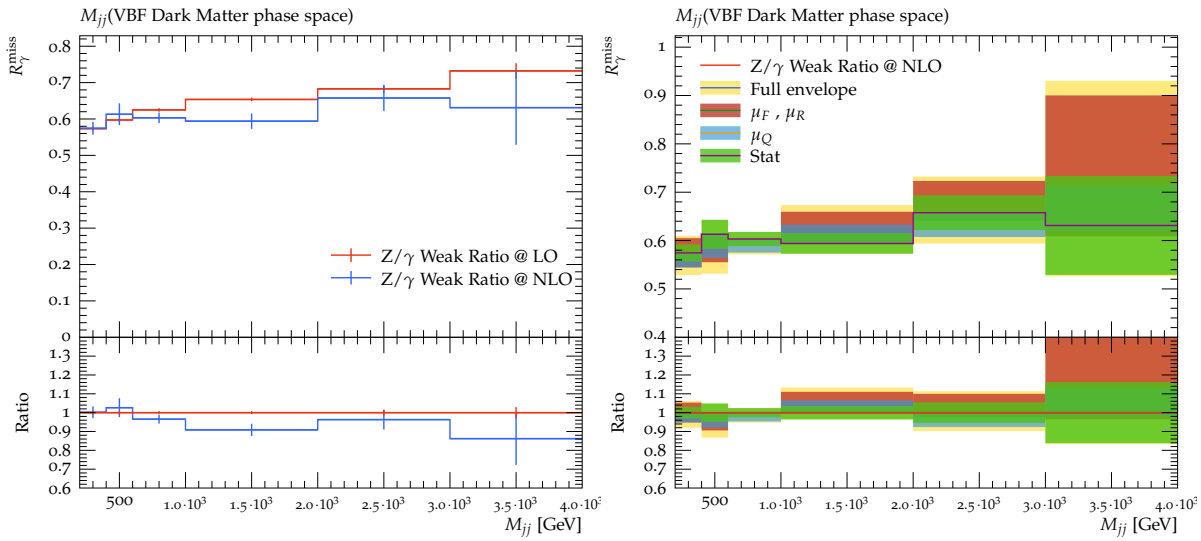

(a) **(b)**

Figure 4.8.: A comparison of R_γ^{miss} calculated at LO and NLO in QCD for EW VBF diagrams as a function of m_{jj}.

case of a jet veto and the EW diagrams. QCD diagrams were also included in this study but are not reproduced here. This bears some similarity to more recent collaborative theoretical effects to derive theory corrections to monojet production [117], with the observation that the case presented here is a more complicated observable and Born process to simulate.

Lastly this NLO ratio can be checked in the three VBF categories, as shown in Figure 4.9. Whilst the tight cuts remove the lower end of the spectrum, direct comparison of the baseline and loose VBF cuts, which differ only by a $\Delta\eta_{\text{jj}}$ cut, can be made. An appreciable shift in the NLO ratio is seen at low m_{jj}, the scale of the process here is closer to resolving the mass difference of the on shell photon and the on shell Z. Such a large shift demonstrates the dependence of these stability measures on the VBF phase space applied. This study can be extended to other potentially asymmetric effects between numerator and denominator, such as interference effects and the effect of the QED content of the proton [118].

4.3. The next generation of fiducial $E_{\text{T}}^{\text{miss}}$ measurements

The measurement discussed in Section 4.2 was performed using the 3.2 fb^{-1} 13 TeV dataset recorded early in Run 2 by ATLAS. As Run 2 has ended there is now an $\sim$150 fb^{-1} dataset at this centre of mass energy available for analysis, and an expanded version of the detector

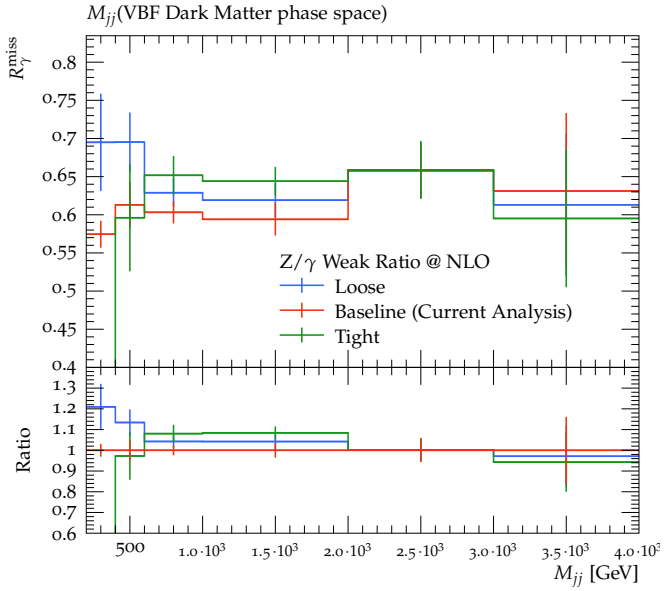

Figure 4.9.: Comparison of the EW VBF R_γ^{miss} as a function of m_{jj} calculated in three VBF phase spaces.

corrected $E_{\text{T}}^{\text{miss}}$ measurement is planned using this full dataset. Improvements to the analysis method include a new CR based on leptonic W events and a more advanced unfolding based on an iterative Bayseian procedure. It is also under consideration to provide differential cross-section measurements of the numerator and denominator rather than the R^{miss} ratio. Such a change would require a sophisticated publicly available limit setting framework to effectively utilise the results. One important feature is the dataset is now sufficiently large that the possibility opens up to perform this measurement double differentially. There are then a lot of possibilities for distributions to measure, that should be chosen based on motivations of what the most useful kinematic variables for distinguishing BSM physics are. In this section some contributions made to the design of this analysis are shown by studying the phase space of SM and BSM contributions. The studies shown here are made using a modified Rivet routine similar to that already described.

4.3.1. SM modelling issues encountered

It has been mentioned that modelling the QCD induced background processes, particularly in the VBF type topologies is tricky. In ATLAS the vector boson backgrounds are modelled using a $Z(\to ll) + (0^*, 1^*, 2^*, 3, 4)$ jet[3] accurate MEPS@NLO Sherpa [55] sample of generated events. This sample is sliced in a variety of kinematic variables to attempt to populate the full range of

[3] This notation was introduced in Chapter 2 in the context of Herwig 7 merging and is the same in this case.

phase space that this sample is used for, and $\mathcal{O}(100)$ million events are generated. Even so this setup has been noted to struggle to adequately describe more exclusive phase space selections. VBF topologies are a prime example of this as the motivation behind VBF cuts is to improve the discrimination of colourless exchange processes, actively vetoing against the QCD induced production. VBF searches often suffer from statistical limitation from the MC background generation. Additionally it has been observed in ATLAS data that the Sherpa sample poorly models the m_{jj} spectrum, which is a key signifier of this process [119]. Such a modelling issue is compounded by the lack of similar merged QCD ME samples in ATLAS, which was one of the motivations for introducing the Herwig 7 merging shown in Chapter 2 to ATLAS.

The m_{jj} modelling issue is shown in Figure 4.10, using a custom Rivet routine with similar VBF phase space cuts to those motivated in Section 4.2. A $Z + 3$ jet at LO in QCD Herwig 7 calculation is shown in red, with a perturbative uncertainty band from variation of the hard process and shower starting scales in orange. All diagrams of $\mathcal{O}\left(\alpha^2\alpha_{\mathrm{S}}^3\right)$ are generated for the $pp \to \nu\nu jjj$ amplitude in this generator configuration. It is expected that this should overestimate the observed cross-section in this region, the cross-section is strongly dependent on the event veto placed on events with central jets of p_{T} >25 GeV. When the two leading jets in the event are increasingly hard, this fixed scale veto becomes relatively very soft. This is what was meant when predictions for VBF topologies were called a multi-scale problem. A three jet Born ME will well describe three jets of roughly similar hardness but when one of the three is soft the Sudakov factor would best describe this emission. This is the motivation for instead using an NLO matched calculation with a two jet Born ME, as shown in the green prediction in the panels of Figure 4.10. This uses an NLO QCD ME matched subtractively to a dipole shower using the Herwig 7 Matchbox, only $\mathcal{O}(1)$ million events were generated in this case. All diagrams of $\mathcal{O}\left(\alpha^2\alpha_{\mathrm{S}}^2\right)$ are generated for the $pp \to \nu\nu jj$ Born amplitude in this generator configuration, with diagrams corresponding to NLO QCD corrections included. The ATLAS baseline Sherpa merged sample is shown in blue, the claim is that this merged setup should predict this observable to the same accuracy as the Herwig NLO matched calculation. All diagrams of $\mathcal{O}\left(\alpha^2\alpha_{\mathrm{S}}^0\right)$ are generated for the $pp \to \nu\nu$ Born amplitude in this generator configuration, additional jet activity is described by ME merging, including up to the $Z + 4$ jet ME. Figure 4.10a shows the differential cross-section binned in the subleading jet p_{T}, this exhibits the expected pattern of the Herwig 7 NLO matched and Sherpa MEPS@NLO merged predictions closely agreeing. The Herwig 7 LO three jet simulation included for reference increasingly overestimates the rate in this phase space as the jets in the event get harder. Figure 4.10b shows the differential cross-section binned in m_{jj} of the two leading jets in the event. A divergence btween the Herwig NLO matched and the Sherpa merged prediction can be seen, for increasing m_{jj} the Sherpa prediction tends towards the LO three jet prediction. As noted the LO three jet prediction is already expected to be too hard. Preliminary studies with the unitarized NLOPS merging procedure in Herwig, shown in Chapter 2 indicate it

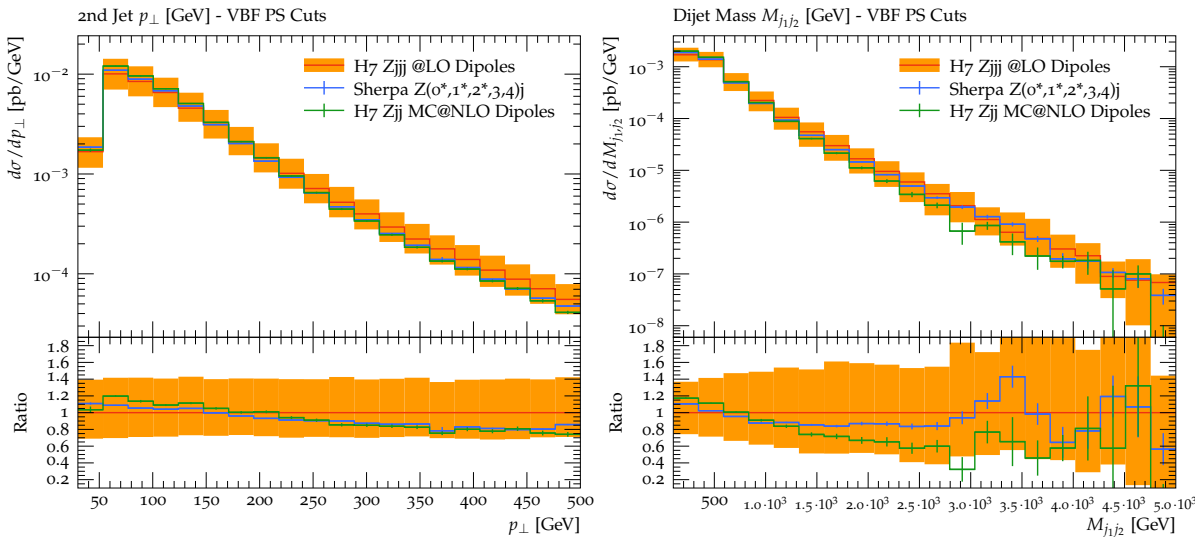

(a) **(b)**

Figure 4.10.: Comparison of three alternative event generators for a VBF selection in two kinematic variables. A HERWIG $Z + 3$ jet at LO generator is shown in red with a perturbative uncertainty band in orange, a HERWIG $Z + 2$ jet MC@NLO generator in green and the ATLAS baseline SHERPA sample shown in blue. Figure 4.10a shows the cross-section as a function of the p_{T} of the second hardest jet in the event, and Figure 4.10b shows the cross-section as a function of dijet mass of the two leading jets.

follows more closely the pattern of the formally NLO matching. To extend this, this comparison should be formally made to data.

Studying the modelling of the phase space of the analysis in such a manner is important. Firstly it is demonstrated that more bespoke generator configurations can and should be used to target more exclusive selections. When jet vetoes are involved in an observable the benefits of a multi-leg ME merging are essentially nullified. Even worse there can be unexpected issues arising which are compounded by the complexity of the multi-leg techniques. It is difficult for the collaborations to maintain multiple samples of the same complexity, and dependence on any one algorithmic implementation is not ideal. Secondly with far less events the NLO+PS matched prediction in HERWIG can populate the same phase space with comparable statistics, this allows a realistic study of phase space cuts in an analysis to be factored entirely outside of the ATLAS collaboration.

4.3.2. Exploring the phase space with a prototype analysis

Now that Section 4.3.1 has demonstrated that the fiducial phase space of the analysis phase space can be effectively populated, the goal is to explore the possibilities in the full dataset measurement. In short this means defining as many observables as possible and calculating some example BSM signals to study what cuts to make and observables to measure, this will be achieved using another similar modified Rivet routine. In addition to the two existing SRs, one based off of a ≥ 2 jet inclusive selection is included, motivated by considerations of scalar dark matter models [120] and VH searches. All signal regions are limited to final states composed of only $E_{\mathrm{T}}^{\mathrm{miss}}$ and hadronic jets, so the question is how to optimally arrange the cuts. Defining the regions such that they are as inclusive to as many BSM signatures as possible but without having suboptimal sensitivity to key benchmark models.

Figure 4.11 shows three different process predictions in a representative histogram from the ≥ 1 jet SR, formed as a double differential cross-section measurement in $E_{\mathrm{T}}^{\mathrm{miss}}$ and leading jet p_{T} ($j_{1,p_{\mathrm{T}}}$). The bin widths are chosen as twice the detector resolution from the 1D distribution in each variable, a criteria of at least 20 events expected in each bin is imposed. Figure 4.11c shows a SM background calculation for this region composed of Herwig NLO+PS matched $Z(\rightarrow \nu\nu) + 1$ jet and $W(\rightarrow l\nu) + 1$ jet contributions similar to those described in Section 4.3.1[4]. Although it has little effect in the ≥ 1 jet SR, Herwig NLO+PS EW VBF $Z(\rightarrow \nu\nu) + 2$ jet are also included as described in Section 4.2.3, this will be important for modelling the VBF region. As a comparison two BSM contributions to this same distribution are calculated and shown in Figure 4.11a and Figure 4.11b, the BSM model corresponds to one that is used as a benchmark for the monojet search, a simplified dark model as described in Chapter 6, Section 6.2. Figure 4.11a corresponds to a model with dark matter mass $M_{\mathrm{DM}} = 900$ GeV mediated by Z' boson with $M_{Z'} = 2000$ GeV. Figure 4.11b corresponds to the same model but with $M_{\mathrm{DM}} = 100$ GeV and $M_{Z'} = 350$ GeV. The dark matter masses are chosen in both cases such that the invisible decays are kinematically accessible. It can be seen that when the mediator is light, the shape in this 2D plane is similar to the SM background, as expected. However when the mediator is heavy, there is now a clear shape difference between the SM and BSM contribution. Importantly the 2015 dataset analysis described in Section 4.2 only measured the differential cross-section (in the guise of R^{miss}) as a function of $E_{\mathrm{T}}^{\mathrm{miss}}$ in the ≥ 1 jet region. It appears that by incorporating the leading jet p_{T} even more power to distinguish the shapes of these two contributions will be available.

The shape compatibility can be expressed as a measure of the significance, Z [121]. More detail on constructing statistical inference is given in Chapter 5, here all that is needed is that

[4] In the VBF SR the predictions used will be for 2 jets in the Born ME, exactly as described in that section.

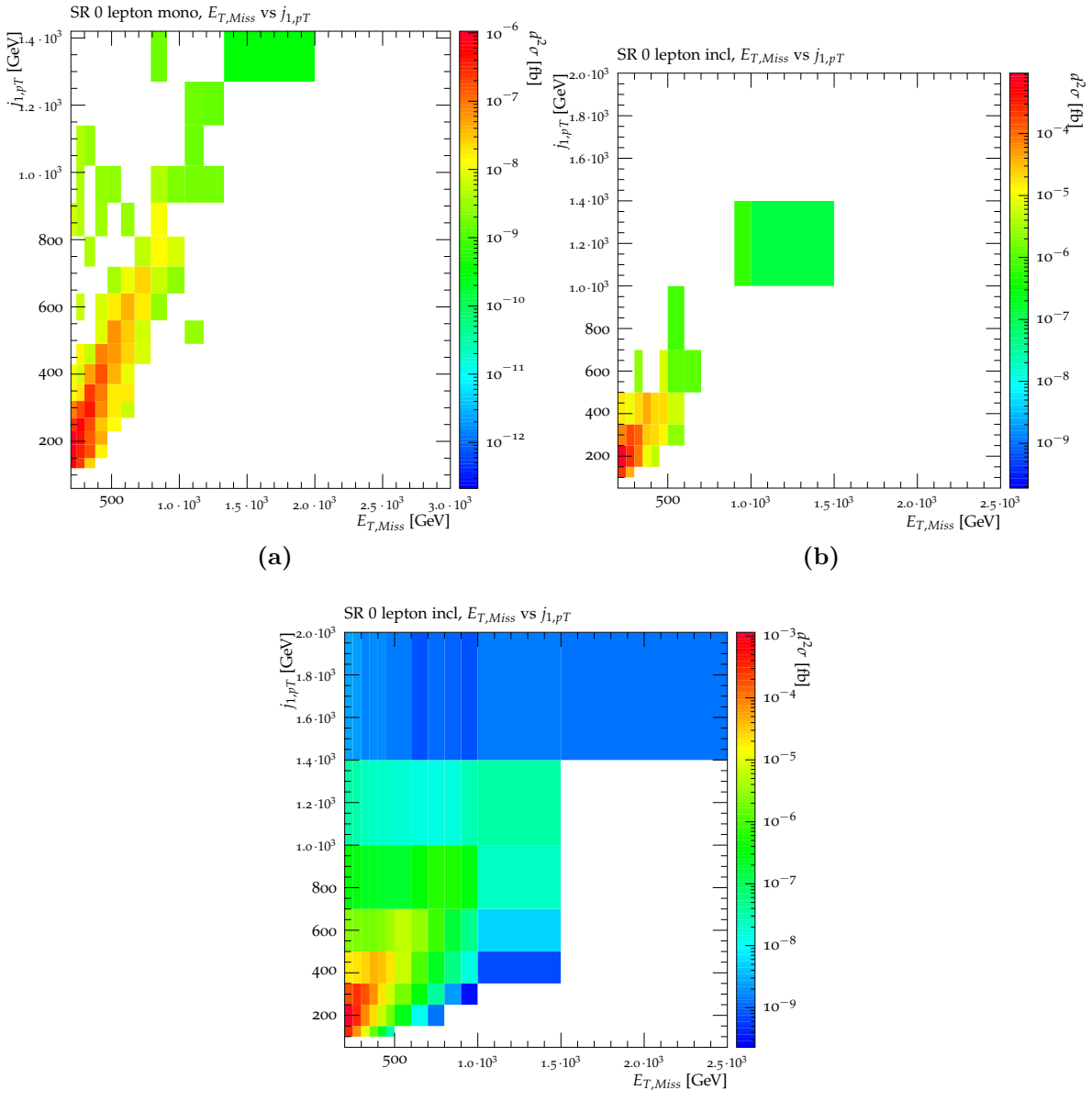

Figure 4.11.: The differential cross-section predicted by HERWIG for three different processes in the $E_{\mathrm{T}}^{\mathrm{miss}}$ vs $j_{1,p_{\mathrm{T}}}$ plane of the ≥ 1 jet SR. Figure 4.11a and Figure 4.11b show simulation of a BSM contribution from a dark matter model with a heavy and light mediator respectively. Figure 4.11c shows the contribution arising from NLO QCD $Z + 1$ jet and $W + 1$ jet SM backgrounds.

the larger significance (or equivalently larger confidence level (CL) of exclusion quoted), the stronger the measurement made will be at constraining BSM. One metric of significance in terms of the predicted background count b_i in each bin i in a histogram where n_i events are observed is given as,

$$Z = \sqrt{2 \sum_i \left(n_i \ln \left[\frac{n_i}{b_i} \right] - (n_i - b_i) \right)}, \tag{4.4}$$

where the *expected* significance calculated in this case inputs the observed counts as $n_i = s_i + b_i$, where s_i is the hypothesised signal contribution in a bin. This significance is based on the asymptotic form [122] of a Poisson likelihood, as such this is a *statistical only* expected significance. Alternatively a systematic uncertainty can be included on the background model in the significance as,

$$Z = \sqrt{2 \sum_i \left(n_i \ln \left[\frac{n_i}{\hat{\hat{b}}_i} \right] + \hat{\hat{b}}_i - n_i + \frac{(b_i - \hat{\hat{b}}_i)^2}{2\sigma^2} \right)}, \tag{4.5}$$

where $\hat{\hat{b}}_i$ is a maximum likelihood estimate of b_i, calculated as described in Chapter 5, Section 5.2.3. This would correspond to including a Gaussian constraint term on b_i with a variance of σ, into a Poisson Likeihood. Both likelihoods here are summed over all bins to quantify the shape difference between the signal and background histograms, the inclusion of the Gaussian constraint in this manner assumes each background constraint is uncorrelated which will be an unrealistic assumption in many cases.

Calculating the statistical expected significance of the signal for the DM model, shown in Figure 4.11, across two of its model parameters is shown in Figure 4.12a. This is derived from the differential measurement in $E_{\mathrm{T}}^{\mathrm{miss}}$ and $j_{1,p_{\mathrm{T}}}$ shown in Figure 4.11. The construction of this sort of exclusion plot is given in Chapter 5, and the phenomenology of this model for comparison is given in Chapter 6. The significance has been converted into an expected limit in the $\mathrm{CL_s}$ formalism. This is performed using a statistical only likelihood as in equation (4.4). It is noted at this stage that the statistical significance is a function of the size of the dataset; as this is increased the measurement will increasingly become systematically rather than statistically limited (Poisson counting statistics have an error that grows as $1/\sqrt{N}$, where N is the number of counting events). Limits in this manner will be increasingly misleading for larger datasets. In Figure 4.12b the results of calculating the significance for an array of possible 2D distributions in the ≥ 1 jet SR, and interpolating a 95% confidence contour for each histogram is shown. The purple contour, which corresponds to the interpolated version of the heatmap in Figure 4.12a, encloses the triangle of the largest area, so is the optimum distribution based on expected statistical significance for this model in this SR. Other combinations of cuts and selections can be tested rapidly using a similar framework. Some seemingly random noise is present in

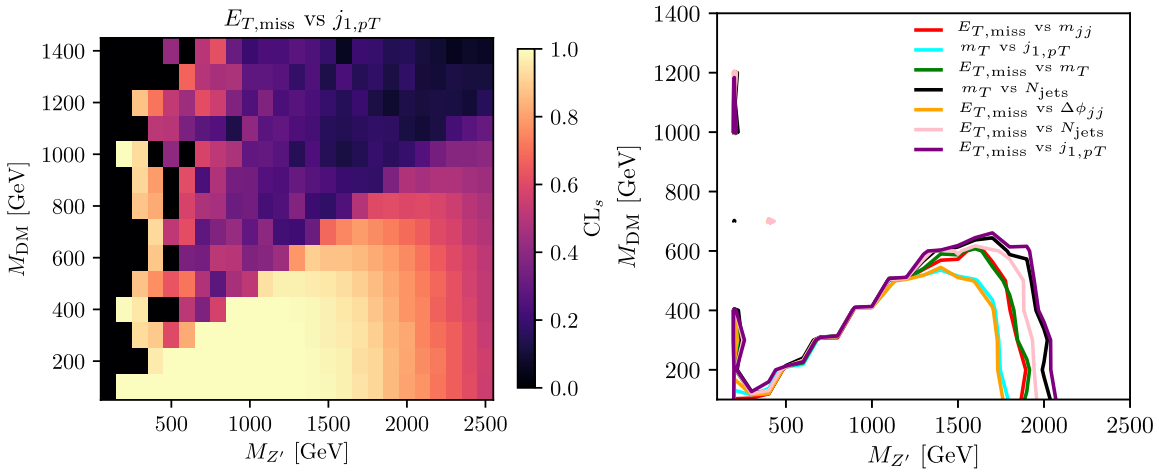

Figure 4.12.: Expected statistical significance for an example dark matter model in the $M_{\text{DM}} - M_{Z'}$ parameter plane. Figure 4.12a shows the calculation of a statistical expected exclusion in this model space for a $E_{\text{T}}^{\text{miss}}$ vs $j_{1,p_{\text{T}}}$ differential measurement in the ≥ 1 jet SR. Figure 4.12b shows a series of potential heatmaps corresponding to other 2D differential measurements interpolated to a 95% confidence level and overlaid.

the scan shown in Figure 4.12a, which leads to interpolated features in the limit contours in Figure 4.12b as low $M_{Z'}$ values. This is driven by events with mediator decays to SM particles, top pair production primarily, passing the SR fiducial selection. At low $M_{Z'}$ these small number of events have large cross sections so can give spuriously large apparent exclusion. More signal event generation would smooth out this issue.

It was noted in Section 4.3.1 that the VBF SR is particularly difficult to model, and it is also a region that has some interesting cuts that are potentially sensitive to new physics. These cuts were already motivated in Section 4.2.3, and the distributions used in the earlier analysis were given in Section 4.2. Figure 4.13a shows the background model as described in Figure 4.11c, now in a 1D differential measurement of m_{jj} in the VBF SR. It also shows the inclusion of a hypothesised Higgs invisible decay scenario. This contribution is calculated at LO in QCD in the Herwig Matchbox by constructing all diagrams of $\mathcal{O}\left(\alpha^4\alpha_{\text{S}}^0\right)$ for the $pp \to H(\to ZZ)jj$ amplitude, the on shell Z bosons are decayed to neutrinos and the cross-section is scaled such that the SM Higgs would have a 100% branching ratio (BR) to invisible particles (BR($H \to$ invis)). This is included in Figure 4.13a scaled such that the SM Higgs would decay with BR($H \to$ invis) = 0.2. The VBF SR is studied using this invisble Higgs decay model in a similar manner to the ≥ 1 jet SR case already presented, to explore possible cut values and distributions. The most statistically sensitive distribution is a double differential measurement in $\Delta\phi_{\text{jj}}$ and m_{jj}, the background calculation for this histogram is shown in Figure 4.13b.

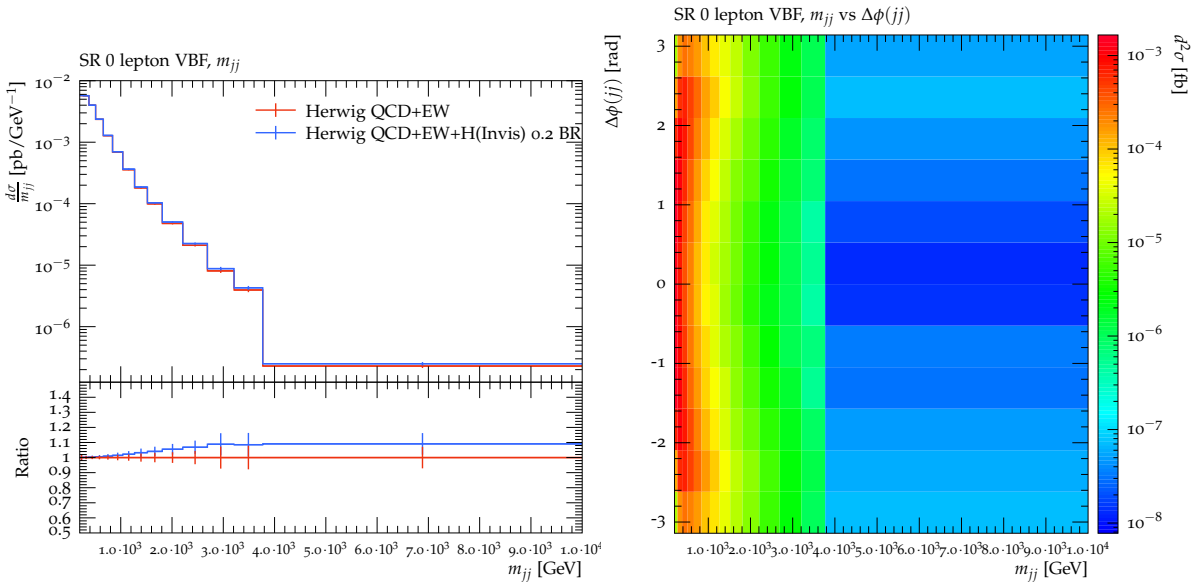

(a) **(b)**

Figure 4.13.: Differential cross-section in the VBF signal region. Figure 4.13a shows the background model in red and the background plus a Higgs to invisible decay at 20% branching ratio signal included in blue, the prediction is of a differential cross-section measurement binned in the mass of the two leading jets, m_{jj}. Figure 4.13b shows the corresponding 2D differential distribution binned in terms of m_{jj} and the gap between the two jets in the ϕ plane.

Constraining the BR of SM Higgs decaying invisibly is one of the key targets of the VBF SR; it is important that this analysis does an optimal job of this. Whilst there may be more exotic models contributing to this SR they are not the main aim of this region. The current ATLAS combination of 7 and 8 TeV searches places a limit on BR($H \to$ invis) ≤ 0.26 at 95% confidence [123]. Accurately calculating the expected reach of this analysis is challenging as systematic effects become important, using the statistical only significance to evaluate cuts is easier. Whilst the implied expected confidence of exclusion may be overstated if no systematic effects are accounted for, the shape difference of the signal and background models will still be reliably quantified by the statistical significance. One can still evaluate potential cut choice and other fiducial definitions based on a statistical metric, even without a realistic model for the systematic uncertainties. The challenge of converting to an expected confidence of hypothesis exclusion is illustrated in the three panels of Figure 4.14. A significance based on a likelihood including a 10% systematic error incorporated as a Gaussian error, as in equation (4.5), is used. The expected limit on the BR is found by iteratively scaling the signal BR between one and zero, and calculating the CL_s at each point. Figure 4.14a and Figure 4.14b show for 4 proposed dataset sizes the calculated expected upper limit, when the curve crosses the dashed line this represents the 95% confidence upper limit. Figure 4.14a shows a significance summing over all bins whereas Figure 4.14b just takes the bin showing the largest deviation. In a 2D distribution like this the significance will be spread over many of the high m_{jj} bins, so the full shape needs to be combined, but this then needs a more sophisticated model for the background uncertainty and its correlation. Figure 4.14c shows how the single bin case gets broken down into its relative statistical Poisson contribution and systematic Gaussian contribution, the dashed line indicates the expected dataset size for this analysis. Projection into the HL-LHC 3ab^{-1} dataset shows that even with the finer binning afforded using 2D histograms, the measurement becomes systematically limited.

Calculating the expected statistical only significance can be used to explore the regions of available phase space that should give the best discrimination of signal and background shapes. Extending these studies to give realistic expected limits is part of an ongoing program to include the full limit setting using this analysis into the framework described in Chapter 5 and Chapter 6. If the measurement is built with reinterpretation in mind, and the full results in terms of the BSM limits included in the paper are performed with a publicly available tool, the use of this data for comparison to arbitrary BSM signals is encouraged. This is an area of ongoing work, dealing with correlations and multiple control regions is of particular interest.

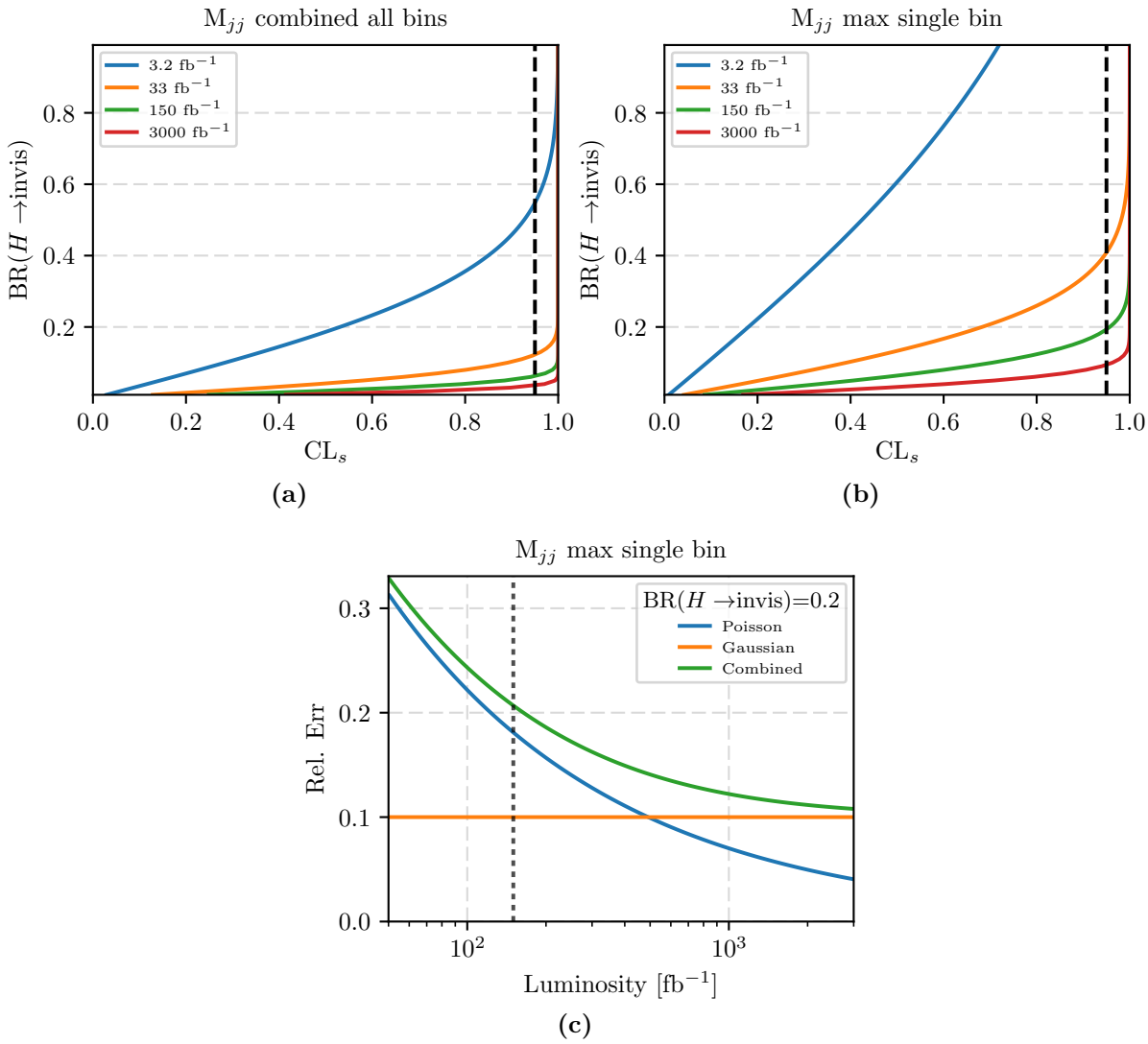

Figure 4.14.: Figure 4.14a and Figure 4.14b show the calculated CL_s for all BR($H \rightarrow$ invis) values, for 4 dataset sizes. The dashed line indicate the point at which the hypothesised BR drops below 95% confidence exclusion. Figure 4.14c shows the breakdown of the relative components from the Poisson and Gaussian components used the significance model as a function of the dataset size, with the dashed line indicating the target analysis dataset size.

Chapter 5.

Reinterpretation of LHC results

Working at the interface of theory and experiment in a high energy physics context requires a balance of considerations of what it is desirable to know with respect to a proposed theory, and what is feasible, or even possible, to say with the experimental data. The experiments employ increasingly complex data analyses techniques, making use of machine learning algorithms which are non trivial to translate outside of the collaborations. The theoretical landscape has also shifted, many of the historically favoured more naturally motivated signatures of BSM physics not appearing in the early 13 TeV datasets. Working on tools to facilitate the translation and reinterpretation of LHC experimental results for alternative hypotheses has increasingly become a field in its own right, with dedicated topical workshops and conferences. This can be extended beyond solely considering the LHC, to consideration of how to assess the compatibility of a model with observed data from many particle physics experiments, studying complementarity with direct dark matter detection for example [124]. This motivates design of frameworks for reinterpretation that are modular, or at least can combine the likelihood calculation from multiple sources.

In this chapter firstly the problem facing someone wanting to reinterpret the results of analyses at the LHC is explored in Section 5.1, with a consideration of how this fits into the broader phenomenological landscape of particle physics model building. This is expanded upon in Section 5.2 to outline what the common features and requirements are to reinterpret LHC results. Lastly in Section 5.3 the particular choices implemented in the design of Contur or 'Constrains On New Theories Using Rivet' is presented, with some demonstration of the technical developments made. This package is designed to set limits on arbitrary new theories using fiducial cross-section measurements made at the LHC, predominantly focussing on, but not limited to, results of the ATLAS and CMS collaborations.

5.1. The problem with reinterpretation at the LHC

What seems like a fairly simple question *"How compatible is a proposed physics model with the observed LHC data?"*, can have a perhaps unexpectedly complicated answer. Firstly one must understand what the desired observable is, as in the context of ATLAS and CMS there are a variety of different types of results. Broadly speaking one can split this into three classes:

- The extraction of fundamental parameters. For example the W boson mass measurement, m_W, made by the ATLAS collaboration [125]. This example uses a template fit, building predictions for the observable with multiple m_W values and using that to extract a measurement of the fundamental property itself. Such a result gives an experimental constraint on a SM parameter calculable analytically in perturbative field theory.

- The measurement of fiducial particle level observables. The construction of such observables was outlined in Chapter 4, along with the required unfolding procedure of such a measurement. Such a result is a measurement of properties of the observed particle collisions, which requires a calculation of a full LHC event to compare to. Such a calculation invokes perturbative field theory but relies on numerical MC techniques and approximations to the full field theory to effectively evaluate the observable. As such a particle level observable is a calculable quantity of the theory, but requires some approximations which were discussed at greater length in Chapter 2.

- The measurement of detector level[1] observables. This is the most common type of result for ATLAS and CMS, it is faster to produce but comes at the cost of having a larger degree of model dependence built in. These results are typically accompanied by a variety of supplementary material to aid efforts to reinterpret them. As these form the bulk of the LHC search program, the majority of reinterpretation tools focus on making use of these detector level results. A key common feature of these results, is that in addition to still needing the numerical methods to predict the particle distributions as in the fiducial particle level case, additional numerical modelling is needed to approximate the effect of the detector.

This categorization is written from the point of view of a phenomenologist, whereby accessing each result forms a hierarchy of complexity of numerical methods needed to approximate the true underlying theory. This is shown schematically in Figure 5.1, where the simplest data to access are fundamental parameters and the vertical arrows flow indicating increasing numerical complexity. From the point of view of the experiment the complexity is essentially in reverse, hence why there are many more detector level results produced than parameter extractions.

[1] These were previously refered to as reco level in the discussion on unfolding however it is typical in the phenomenological community to use detector and reco level interchangeably

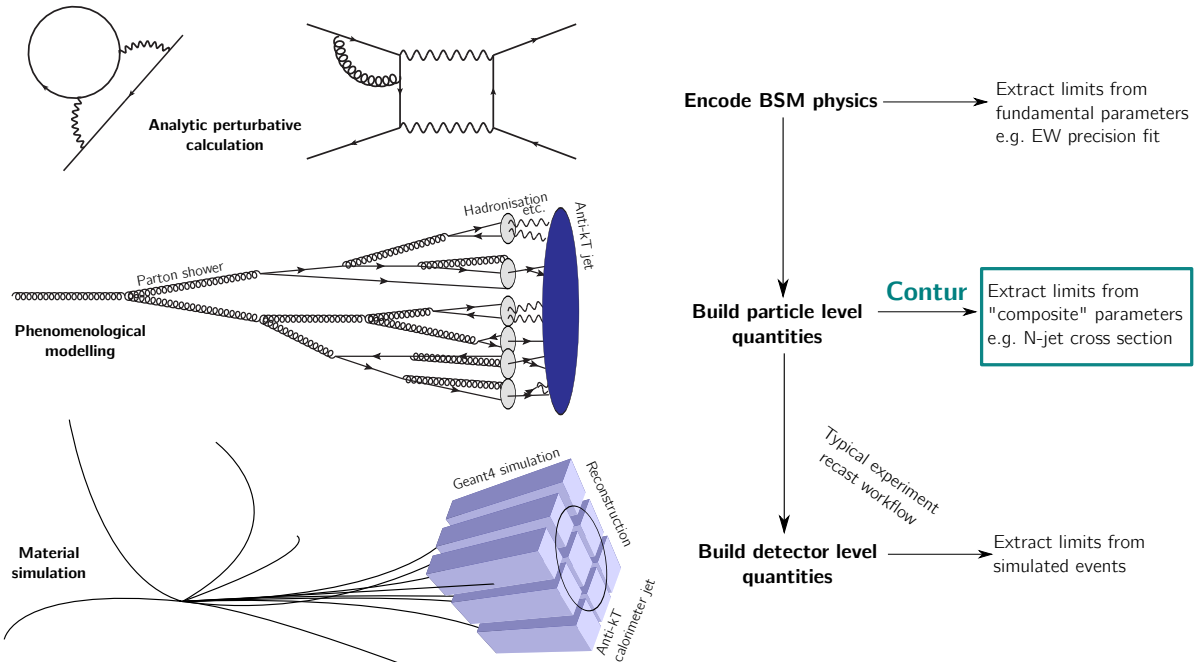

Figure 5.1.: A flow schematic of the concepts of extracting limits on BSM theories with collider data.

Whilst there are tools available to perform fast simulations of particle level events, and even detector simulations, it unavoidably requires a lot of numerical sampling to calculate LHC observables. This in a nutshell is the problem with reinterpretation at the LHC, that it is computationally expensive, typically requiring MC sampling of many distributions to populate an observable. This is compounded by the fact that it isn't often clear how to unambiguously reconstruct a given observable. All of this is before even considering the breadth of results one would like to simultaneously consider which is another consideration that will go into the design of Contur.

This statement can be made broader in fact, it is not just that an LHC observable is complicated to construct. If we are to survey a BSM model space in a *global scan*, including sources of experimental limits from other particle physics experiments outside the LHC. Understanding the LHC impact on the model space is by far the most time consuming aspect. This is why in general the impact of the LHC is often considered in isolation, where dedicated tools such as Checkmate [126], MadAnalysis [127] or SModelS [128] are used. Probably the most prominent example of a global particle physics fitting code that includes multiple experimental sources and theoretical constraints is Gambit [129]. Taking an example from one of the collaboration's recent global scans of EW SUSY [130], generation of $\mathcal{O}\left(10^6\right)$ LHC events for $\mathcal{O}\left(10^5\right)$ model parameter points was required. Evaluating the likelihood from LHC observables is the largest bottleneck in these more global scans and requires a great deal of development on top of already optimised code bases to make a convergent fit even possible.

CONTUR will share, at first glance, a more similar identity to the aforementioned dedicated LHC tools, but was designed to be a minimal layer on top of existing codebases which should aid in the ongoing quest for interoperability of reinterpretation tools. It is also worth noting that the ATLAS collaboration has also started developing the possibility to run the full analysis codes to recreate the full reconstruction and selection of the experiment, sidestepping many of the issues with accessing detector level results touched on in Section 5.2.2. This was dubbed the RECAST framework [131]. This naming has caught on in the community, and often the phrase recasting is used interchangeably with reinterpretation to refer more generically to the whole concept rather than the specific implementation of RECAST.

5.2. The anatomy of an LHC reinterpretation tool

To understand the design of CONTUR it is worthwhile examining at this point the requirements and structure needed to reinterpret an LHC result in general. To this point some of the common terminology is also defined. A sketch of the generic recipe needed is shown in Figure 5.2 which will serve as a guide for the following subsections.

5.2.1. Parameter Sampling

Within a hypothesised physics model there are a set of free parameters that dictate the dynamics of the particle interactions and can take a range of proposed values. The answer to the question posed at the beginning of Section 5.1 can now be understood more specifically as, *"Which parameter values in a proposed physics model are least compatible with the observed LHC data?"*. Building a map of the compatibility of data and theory across this parameter space can then either be used to point to regions where the agreement with data is actually improved by the new model (alternatively the *discovery* problem), or to point to regions that show the least compatibility (the *exclusion* problem). There will be parameter values from the set of possible values that are already disfavoured from sources outside of the LHC, for now this is set aside as it is always a valid question to ask what the LHC specifically tells us about a chosen set of parameters without having to fold in dependence on other observations of theoretical preconceptions.

Generally in particle physics terms the SM is considered the baseline hypothesis, with BSM contributions added onto the existing model. It is a feature of most BSM theories that they are required by construction to replicate the precision measurements made already, which are seen to already show excellent compatibility between data and the SM (it is precisely this feature that will be exploited in CONTUR). It is worth noting here that the problem described where an

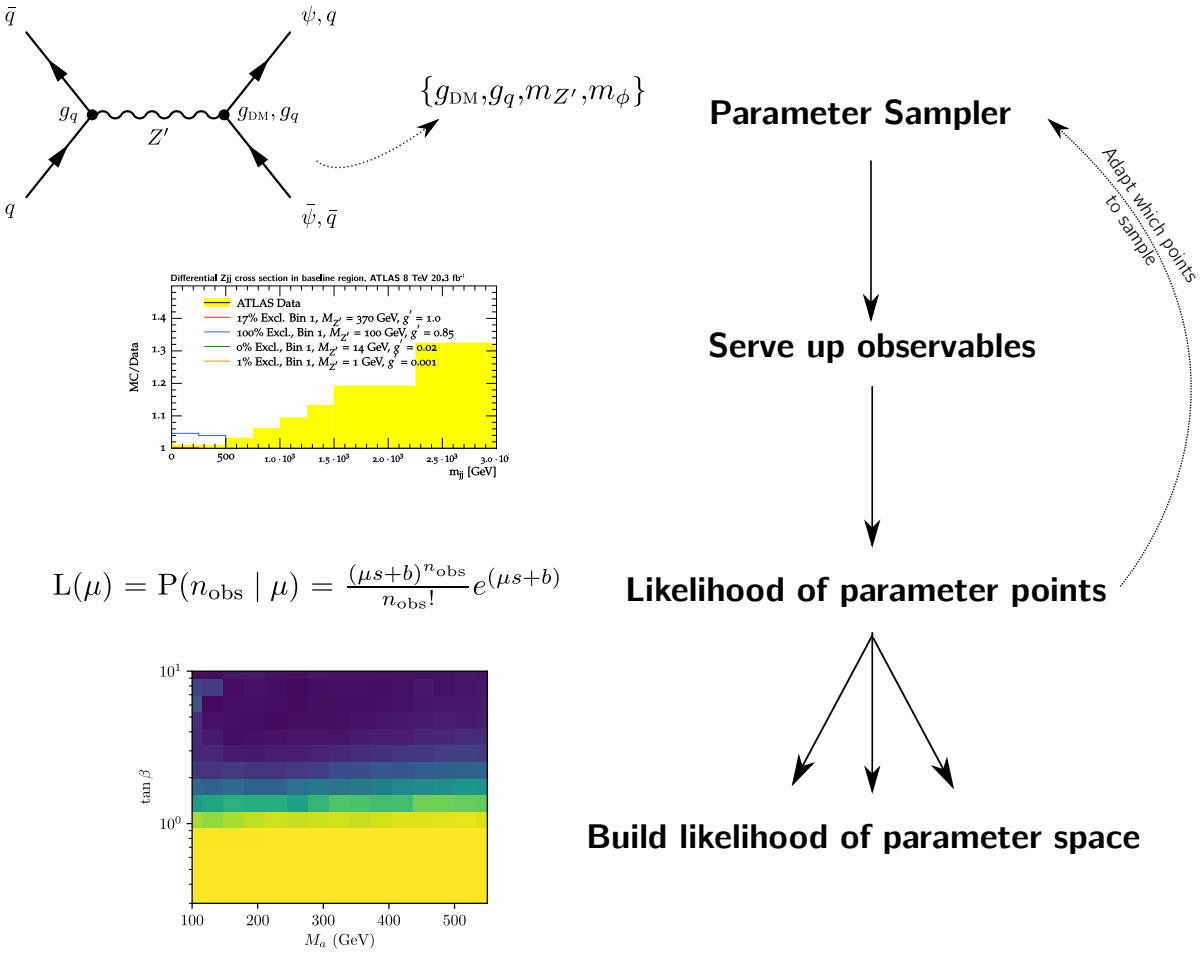

Figure 5.2.: A flow schematic of the common building block steps in an LHC reinterpretation tool.

arbitrary BSM theory has its parameters scoped, is not so different if the hypothesised physics model is the SM. As discussed in Chapter 2 the implementation of the SM in event generators also has some free parameters[2], in its parton shower model for example. This is an example of the type of problem already broadly referred to as the discovery problem, and in the case of the free parameters in the phenomenological modelling of the SM is known as tuning [98]. In general due to the lack of observation of any significant deviation from SM expectation thus far in the LHC operation, the rest of the discussion will mostly centre on the exclusion problem.

Denoting all the n number of free parameters in a given BSM model as $\{x_0 \dots x_n\}$, where each parameter in addition has a range of allowed values it can take. This combination of the allowed free parameters and their allowed ranges is referred to as the *parameter space* of the model. Picking an *ensemble* of values from the parameter space then fully describes a model

[2]Careful attention has to be paid here, for example the arbitrary scales entering the hard process calculation have a chosen form and a genuine ambiguity but should not be tuned to a specific form.

at a *parameter point* in its parameter space. One can then continue in the chain defined in Figure 5.2 to assess the validity of the chosen ensemble of parameters representing a point in parameter space. Typically one wouldn't consider the full set of n parameters present in a full model simultaneously, mainly due to the fact that a full UV complete new physics model can have upwards of $\mathcal{O}(100)$ undetermined parameters. Setting aside questions of internal consistency of the selected ensemble of parameters and ensembles that are already excluded from other sources, just the sheer number of points to consider to build a chart of the full model parameter space is computationally not feasible. Typically a reduced set of parameters are chosen using either physical motivations that some parameters have less impact on the observable dynamics, or even more simply motivated by a signature-driven approach, where a particular observable is sought to be produced. In Figure 5.2 it is noted that there is a connection between evaluating the likelihood and sampling the parameter space, this topic will be revisited in Section 5.2.5.

5.2.2. Serving up observables

As noted in Section 5.1 the core of any LHC reinterpretation tool, and the main bottleneck, is the ability to quickly calculate LHC observables. Setting aside the analytically calculable LHC observables, a reinterpretation tool has to be able to simulate the BSM model one wants to study, to a full particle simulation, from the chosen parameter point(s). In Chapter 2 the idea of an event generator to implement the physical theory to a particle level was introduced, along with some of the available tools of this type and their respective merits. There was a particular emphasis placed on simulation of the SM physics, and precise simulation of the SM is indeed a large part of the task of a reinterpretation tool as this forms the *background* model the BSM *signal* model is tested against. Typically this is a *static* data issue, which is to say that it is a task that typically has to be run once, and can often be taken from material published by the experiment. Precise calculation of the SM and its role in Contur is discussed further in Chapter 6. The main concern then is to calculate the signal component of the observable, the contribution arising from the hypothesised BSM model as the dynamics generated can change for any arbitrary choice of model parameters. For now the contributions will be considered as additive on top of the background expectation, effects such as the interference between signal and background at the amplitude level are left aside for now but are an interesting area for future.

Thankfully for BSM event generation purposes, and due in part to the noted factorization of the perturbative hard process, much of the simulation is similar between the BSM and the SM cases so can use the same tools. Signal generation in general purpose event generators for the LHC is generally seen as a solved problem these days, for most common classes of model to

the necessary degree of accuracy. There are two main identifiable approaches to particle level BSM event generation,

- Automated. This approach is based on MATHEMATICA, using packages such as FEYNRULES [132] and its corresponding event generator, UFO, interface [133] is used to encode the theory in an event generator parsable format. General purpose tools, MADGRAPH + PYTHIA, HERWIG and SHERPA can all then internally define the hard processes of interest and generate full LHC particle events.

- Bespoke. This approach factorises to production of a Les Houches Event file (LHE) [134]. Such a file contains a partonic simulation which can be interfaced to HERWIG or PYTHIA to produce a full LHC event. For example there is an NLO QCD implementation of one of the models studied in Chapter 6 available in POWHEG-BOX [135].

Both of these approaches are essentially equivalent in terms of embedding into the wider toolchain, provided that there is user control over the fundamental parameters of the BSM model one wants to study. These generators then need to be run until a large enough number of events is obtained such that an equivalent (or greater) integrated luminosity in MC is reached than in the observed data. The event generation is a simulation of a given process with cross-section, σ_{tot}. In terms of a recasting tool, this takes us to the point in Figure 5.1 where particle level quantities (now understood to mean σ_{tot}) have been built.

Borrowing the definitions and nomenclature from Chapter 4, the problem now diverges in two. If the data is detector corrected, i.e. unfolded to particle level, then the particle level generated events can be passed through the fiducial phase space selection to calculate the fiducial cross-section from the generator events, σ_{fid}. This operation can be written as,

$$\sigma_{\text{fid}} = \mathcal{A} \times \sigma_{\text{tot}} \,, \tag{5.1}$$

Where the fiducial region acceptance, $\mathcal{A}$, is the criteria that selects events. The generator will need to be run until a convergent estimate of σ_{fid} is obtained. Depending on how inclusive the cuts imposed by the fiducial region are, this can potentially be very time consuming so might require extensive event generation to populate the observable of interest. Experimental approved definitions of $\mathcal{A}$ are included in the Rivet library and Rivet will continue to be the main framework to provide this information for the foreseeable future.

If the observed data is left at detector level, then a recipe to convert from the particle level quantities to detector level observables (observed counts, N_{obs}) is needed. This can be written,

$$N_{\text{obs}} = \epsilon \times \mathcal{A} \times \mathcal{L} \cdot \sigma_{\text{tot}} \,, \tag{5.2}$$

Where the cross-section is converted to an event count by scaling by the integrated luminosity of the dataset. The problem of providing $\mathcal{A}$ and efficiency, ϵ, for a conversion to a detector level observable in equation (5.2) has a more ambiguous answer than naively expected. This is the crux issue for many recasting tools. Individual analyses within the experimental collaborations put out a varying degree of information to aid the translation between particle and detector level. If it is hard to come up with a generic recipe that can be reused consistently across all detector level results, bespoke effort has to be put in to understand how to use each result accurately given the material provided for reinterpretation. As an example, one of the most recent ATLAS search analyses at the time of composing this document is the search for W' resonances [136]. This analysis provides $\epsilon \times \mathcal{A}$ corrections derived for the BSM model considered in the paper. One can use these to recreate the results of the paper, but this method is harder to apply generically to a given BSM physics model outside of this scope.

The LHC recasting tools mentioned earlier in this chapter are all designed to reinterpret detector level results. MadAnalysis, for example, works by using a fast detector simulation, provided by DELPHES [137]. This provides the efficiency, and by implementing the selection criteria based on the paper analysis description [138] the acceptance is also accounted for. However this is a laborious task, often the experiments don't provide the acceptance of the detector level cuts, so it can be hard to validate the selection criteria. Additionally many analyses at the LHC use non-trivial selection criteria involving trained machine learning algorithms to distinguish the signal, whilst there are moves to make this information public it is not clear how to replicate such a selection in many cases. Lastly some care has to be taken with the use of fast simulation, it is often sufficient for simpler collider signatures, but given that even the full detector simulation when provided as unfolded corrected data can fail to model sufficiently well exotic signatures [139], it is reasonable to expect cases when the public fast simulation tools breakdown.

The end result of both approaches outlined here is very similar, the observables are represented in similar ways. A series of histograms containing signal predictions in each bin is calculated. The corresponding observed data and expected background prediction with their respective uncertainties is also available for each signal histogram. This defines the information needed to make a statement about the compatibility of the BSM model. The role of this stage of a reinterpretation tool is to be able to calculate the signal histograms at various different configurations of the model being studied as quickly as possible. An example of a calculated set of particle level observables from a Rivet analysis can be formed from each bin of the histograms in Figure 5.3a and Figure 5.3b. Where Figure 5.3a is the result of running a variety of SM predictions through the Rivet analysis for this measurement. Any of these histograms could be taken as a model for background counts, and envelope of other algorithmic variations could represent an uncertainty on this count. The response of passing a variety of signal models

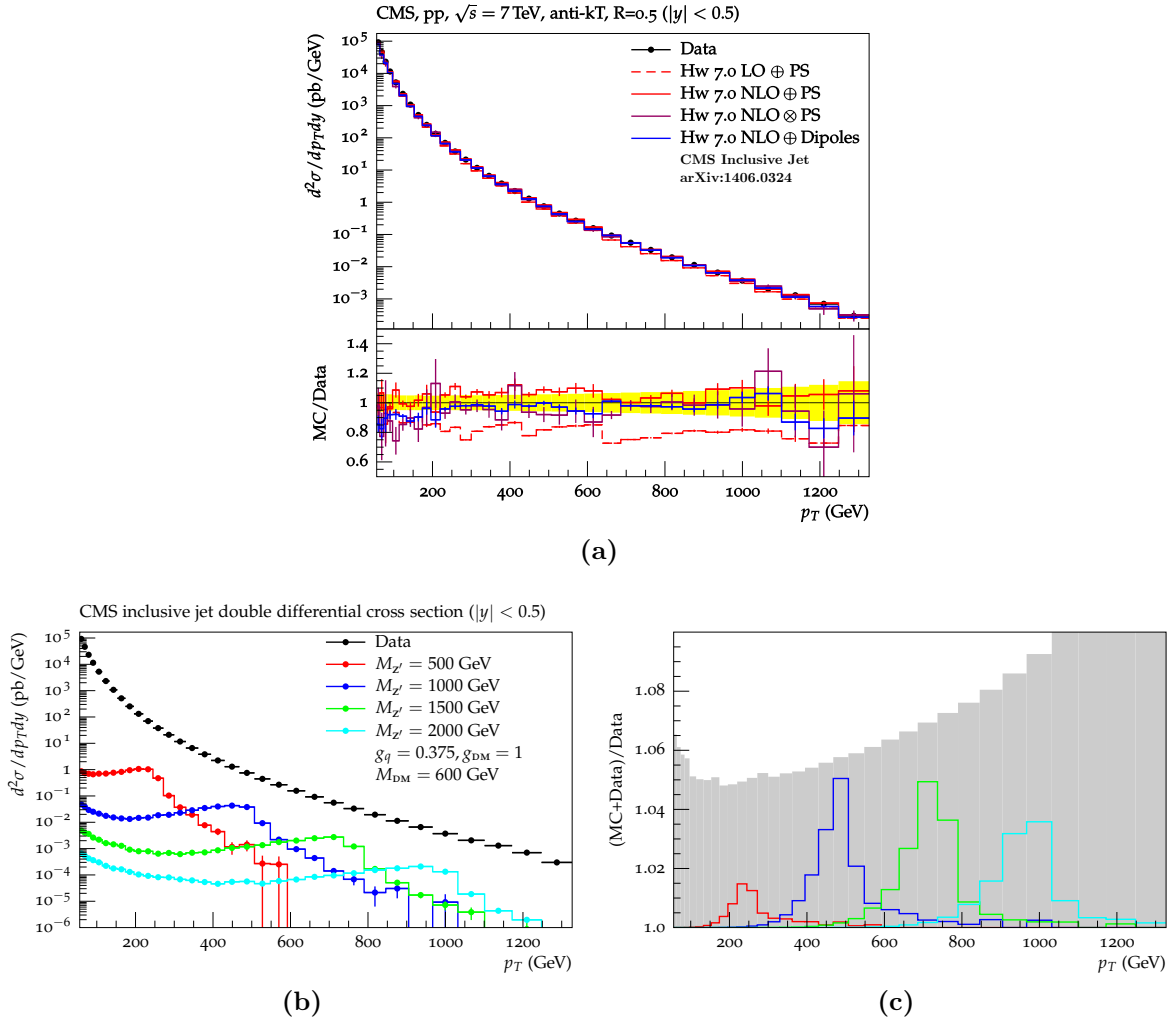

Figure 5.3.: A double differential cross-section measurement of the inclusive jet p_{T} spectrum in a central leading jet rapidity bin as measured by CMS at 7 TeV [140]. Figure 5.3a shows four algorithmic variations of the SM prediction for this spectrum made with the HERWIG 7 Matchbox. Figure 5.3b shows four different parameter points in a simplified dark matter model under the same particle level selection. Figure 5.3c shows the ratio of this BSM contribution to the observed data, where the uncertainty on the background model is represented by the shaded grey area.

through the same selection is shown in the corresponding Figure 5.3b, all 4 predictions shown are distinct parameter points in a simplified dark matter model. In both cases the observed data and its associated error is reproduced alongside the generator predictions for comparison. From these two figures one can take 3 vectors; one representing the signal model counts, $\vec{s}$, one for the background model chosen, $\vec{b}$, and one for the observed data, $\vec{n}$. Additionally there can be vectors representing uncertainties on each of these quantities. This is the representation of the data now used to make a statistical inference about this signal point.

5.2.3. Likelihood of parameter points

The information defined as a series of counts towards 5.2.1, is what will be taken as the input for statistical inference. The available information can be formally written down as:

- The signal model counts, $\vec{s} = s_i$, for a given choice of parameter space values $\{x_0 \dots x_n\}$. It is typical to introduce a modulating signal strength parameter, μ such that $\vec{s}$ is replaced by $\mu\vec{s}$. The null hypothesis is then given by $\mu = 0$ and the nominal full signal strength is given by $\mu = 1$. Note that when including multiple histograms this μ will be a common parameter across all considered channels.
- The background model counts, $\vec{b} = b_i$. This model will typically have a series of systematic uncertainties which have to be included as nuisance parameters, see Section 5.2.4.
- The observed data counts, $\vec{n} = n_i$. This will also typically have a series of systematic uncertainties derived from the experimental uncertainties on the observation.

Now the use of the word *compatibility* in the initial question posed at the start of Section 5.1 can be expanded. One would like to know the probability of making an observation, n, given a hypothesised μ. This is called the likelihood, L, of this hypothesis and can be written as,

$$L(\mu) = \mathrm{P}(n \mid \mu). \tag{5.3}$$

In a case with vanishing nuisance parameters the likelihood of the set of observations, $\vec{n}$ given the hypothesis, μ can be described by a Poisson distribution as follows,

$$L(\mu) = \prod_i \frac{(\mu s_i + b_i)^{n_i}}{n_i!} e^{-(\mu s_i + b_i)}. \tag{5.4}$$

This expression represents the likelihood of the observed data under an assumed μ. A frequentist test of a hypothesised μ then is then a statement about which set of data values the hypothesis is rejected. This set is named the critical region, ω, and the hypothesis would be said to be rejected if,

$$P(n \in \omega \mid \mu) \leq \alpha\,, \tag{5.5}$$

where α is known as the size of the test, the probability of finding $n \in \omega$. If the observed data are found in this critical region then the hypothesis is rejected. The problem is then to classify if an observation $\vec{n}$ is composed of only events of type $\vec{b}$ ($\mu = 0$) or instead the combination $\vec{b} + \vec{s}$ ($\mu = 1$). The choice of critical region is optimally set using the Neyman-Pearson lemma [101],

which uses the ratio of the likelihoods of the two hypotheses to define a test statistic, t_μ as,

$$t_\mu = -2\ln\lambda(\mu) = -2\ln\frac{L(\mu=1)}{L(\mu=0)}\,. \tag{5.6}$$

This statistic can then be used to quantify the compatibility in terms of a probability, referred to as the p-value,

$$p = \int_{t_{\mu,\text{obs}}}^{\infty} f(t_\mu \mid \mu)dt_\mu. \tag{5.7}$$

With $f(t_\mu \mid \mu)$ being the probability density function (pdf) of the test statistic under the hypothesised μ and $t_{\mu,\text{obs}}$ is the observed value of the test statistic in equation (5.6). If $p < \alpha$ is found, the data observed was in the critical region and thus the hypothesis is rejected. Alternatively to the form given in equation (5.6), the test statistic, now t'_μ, can be written,

$$t'_\mu = -2\ln\lambda(\mu) = -2\ln\frac{L(\mu)}{L(\hat{\mu})}\,, \tag{5.8}$$

where $\hat{\mu}$ represents the (unconditional) maximum likelihood (ML) estimator of μ, found as the value of μ for which $\frac{\partial L}{\partial \mu} = 0$. This is commonly used in HEP and is included in the profile construction [141], the full profile construction is useful for including nuisance parameters into a frequentist inference. This is given in more detail in Section 5.2.4. For now it is noted that as $\vec{b}$ approaches $\vec{n}$, the value of $\hat{\mu}$ tends to zero.

Now the issue reduces to finding the pdf of the test statistic, $f(t_\mu \mid \mu)$. Initially it would appear that some kind of Monte Carlo toy generation is required to generate the form of this pdf. However an important result [142] that builds on the earlier results of Wilks and Wald [143, 144], states that in the asymptotic (large sample) limit, the test statistic constructed from a likelihood ratio is well approximated by known distributions. Specifically it was shown that,

$$t'_\mu = \frac{(\mu-\hat{\mu})^2}{\sigma^2} + \mathcal{O}\left(\frac{1}{\sqrt{N}}\right), \tag{5.9}$$

where N now is the sample size in question, or effectively the values of $\vec{n}$, and σ is the variance of μ. This variance is then estimated from the Fischer information matrix. A useful observation for limit setting using unfolded measurements is that such observables have to be formed from sufficient events for a statistical unfolding procedure to be valid as described in Chapter 4. Thus in CONTUR the approximation that this term in equation (5.9) is small is guaranteed for all included sources. This means that the test statistic is always well approximated by a chi-square distribution. In the large sample limit the pdf of the test statistic will follow a

standard normal distribution. Note that this formulation is built off the test statistic from equation (5.8), but an equivalent relation holds for the test statistic in equation (5.6).

The original CONTUR paper [145] followed the construction of the test statistic as a 1D chi-square as in equation (5.9), with the variance of μ being derived from the inverse of the Fischer information matrix. For all tests constructed in the original paper the background model was taken to be exactly equal to the data, $\vec{b} = \vec{n}$, the impact and reasoning for this is covered in Section 5.3.3, noting now that this means $\hat{\mu} = 0$. This will be referred to as the trivial background model. It was subsequently noted that in this case an equivalent test statistic to equation (5.9) could be written,

$$\chi^2_\mu = \frac{((\mu s_i + b_i) - n_i)^2}{\sigma_i^2}, \tag{5.10}$$

where this test statistic is now clearly labelled as a chi-square, χ^2_μ. In this case the variance, σ_i is now the variance on the counts, propagated into one uncertainty (as the discussion of nuisance parameters is set aside for now this is simply the sum of statistical errors on b_i and s_i). Note that the variance in this case is of a dimensional quantity, $b_i + s_i$, whereas in the previous formulation given in equation (5.9) this was a variance of the dimensionless scaling μ. This accounts for the apparent discrepancy in dimensionality of the numerator between equations 5.9 and 5.10. In the $\hat{\mu} = 0$ and large N case, the three test statistics are equivalent. Since this is a chi-square in the large sample limit the relation for the pdf of χ^2_μ also follows a normal distribution as in, this result follows simply from the Central Limit Theorem [101].

The conversion of an observed value of a test statistic to a probability following equation (5.7) is then modified slightly so that instead a frequentist confidence interval is constructed. This amounts to a rephrasing of equation (5.7) to,

$$p = P(n_1 < n < n_2 \mid \mu) = \int_{n_1}^{n_2} f(n \mid \mu) dn \geq 1 - \alpha. \tag{5.11}$$

Previously this was phrased such that for regions of $p > \alpha$ the hypothesis μ is rejected. In this construction now the region where $p \geq 1 - \alpha$ is known as the confidence interval that includes the true value of the parameter μ with a probability larger than $1 - \alpha$. This would then lead to the statement that the confidence interval covers the true parameter value with a *confidence level* (CL) greater than $1 - \alpha$. This is more intuitively shown graphically in Figure 5.4, where a measurement, x, is made of a Gaussian distributed variable, μ, with variance σ. The 90% CL then corresponds to the intervals of the integral of the unit Gaussian which has an area of $1 - \alpha = 0.9$.

A feature of these CL calculations is that the choice of test statistic will influence the coverage probabilities of the true parameter. In particle physics the desire is to set a limit on the

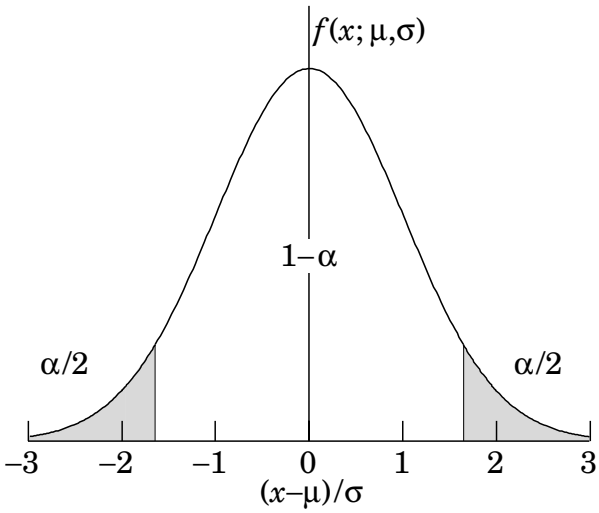

Figure 5.4.: The construction of a 90% for a measurement of a quantity following a Gaussian distribution, retrieved from the PDG Statistics review [23].

allowed values of these signal strengths, μ. Three test statistic constructions for the same case of a Gaussian distributed variable, are illustrated in Figure 5.5. The labelled "Classical" boundary is what one would obtain using a chi square as in equation (5.10) where an important feature is noted, namely that for sufficiently negative values of $\hat{\mu}$, the upper limit on the parameter set with the confidence band becomes negative too. This *flip flopping* of the limit is generally undesirable and unphysical and has been treated a few different ways in the HEP community. Two examples are shown in Figure 5.5, namely the Power Constrained Limits (PCL) [122] which is not widely used in the collider community, but represents a patching and cutoff at a positive value of μ everywhere. The more common construction, and indeed the accepted form for presenting LHC results is known as the $\mathrm{CL_s}$ formalism [146, 147]. This is defined as a ratio of two p-values as,

$$\mathrm{CL}_s = \frac{p_{s+b}}{1 - p_b}. \tag{5.12}$$

The numerator p-value, p_{s+b}, then is exactly what one would obtain for the $\mu = 1$ chi-square as written in equation (5.10), which as was just pointed out would give the upper limit corresponding the Classical case in Figure 5.5. The case of negative upper limits is then moderated by the p-value of the denominator, which is the same test statistic but with $\mu = 0$. This has the effect of reducing the power of statement made about models to which one has limited sensitivity, and patches the *flip flop* issue. This construction is harder to motivate from a formal statistical point of view, but has found wide acceptance in the LHC community. One reason as noted in Figure 5.5 is that for this Gaussian problem, the modified frequentist $\mathrm{CL_s}$ construction coincides exactly with the Bayesian credibility interval using a flat prior. This

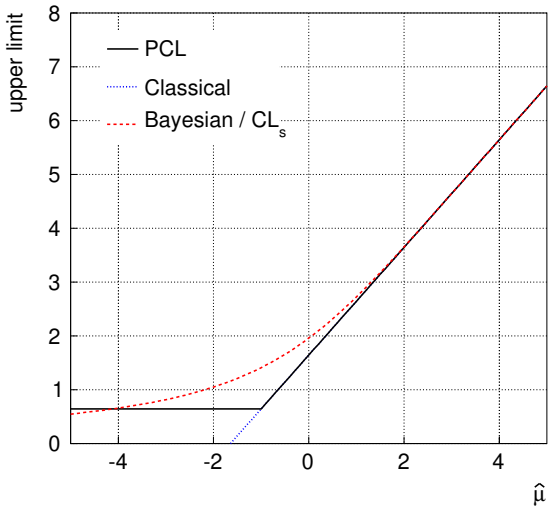

Figure 5.5.: The upper limit of the confidence belt according to three different test statistic constructions for a Gaussian distributed parameter μ as a function of the most likely function of this parameter given an observed value [122].

hints at least at some deeper connection to more rigorous Bayseian inferences. It is also noted again that the trivial background model was assumed which renders the CL_s construction trivial, the test statistic in equation (5.10) will always have p_b equal to a half.

More recent developments in CONTUR have started to include more non trivially constructed background models, breaking the $\vec{b} = \vec{n}$ degeneracy by using an event generator modelled background. This also allows statements to be made about points in parameter space where the most favoured point can be calculated, turning the pure exclusion case into one that could also enable claims of discovery significance. This transition necessitates modifications to the test statistics t_μ and t'_μ. Firstly both forms need to be extended in a similar manner to,

$$t_\mu = \begin{cases} -2\ln\lambda(\mu) & \hat{\mu} \leq \mu\,, \\ 0 & \hat{\mu} > \mu\,, \end{cases} \tag{5.13}$$

where the form of the log likelihood ratio $\lambda(\mu)$ is as given in equation (5.6) for t_μ and equation (5.8) for t'_μ. If the observed data gives $\hat{\mu} > \mu$ it would not be considered that this represents less compatibility with the tested μ than the observed data, so the test statistic is truncated at this point. This makes the test statistic one sided, so is only applicable in a limit setting context. The asymptotic form of the log likelihood ratio for t'_μ given in equation (5.9) clearly works for $\hat{\mu} \neq 0$, but the claim that both t_μ and t'_μ can be approximated by a simpler chi-square as given in equation (5.10) needs to be examined. Firstly it is noted that for the simpler hypothesis test of t_μ, this chi-square form still holds, the denominator of the likelihood

ratio is constant with respect to the parameter of interest μ so won't influence the limits behaviour. In order to make this valid for the asymptotic form of t'_μ when $\hat{\mu} \neq 0$ this needs to be modified as,

$$\Delta\chi'^2_\mu = \frac{((\mu s_i + b_i) - n_i)^2}{\sigma_i^2} - \frac{((\hat{\mu} s_i + b_i) - n_i)^2}{\sigma_i^2}\,, \tag{5.14}$$

where this has been more clearly marked as $\Delta\chi'^2_\mu$ to now differentiate it, this is sometimes phrased as $\Delta\chi^2$ in the literature. This construction renders the simpler chi-square form equivalent to the canonical asymptotic form given in equation (5.9) even when $\hat{\mu} \neq 0$. Now the role of $\mathrm{CL_s}$ becomes clearer too, previously it was a trivial dressing, but with $\hat{\mu} \neq 0$ the coverage can now be seen to follow as in Figure 5.5. More heuristically, this is phrased as covering up a claimed parameter exclusion in the case that the background fluctuation could have faked the signal, effectively the case when the background count is large and the test statistic distributions between t_μ and t_0 are very similar.

An alternative construction for a confidence interval on a parameter is instead to follow the procedure of Feldman and Cousins (FC) [148]. This resembles more closely a classical frequentist interval following the Neyman construction. The reason for following the profile construction, using either the test statistic in equation (5.14) or equation (5.9), appropriately treating the $\hat{\mu} > \mu$ case with equation (5.13) in both cases, corresponds to the FC construction. That is to say that a CL can be quoted using the pdf of these test statistics as in equation (5.11). Counter intuitively a construction like this, or similarly the test statistics defined in the asymptotic formula paper [142] already form a Feldman Cousins interval, but are often still presented in the $\mathrm{CL_s}$ formalism in the LHC community. Some advantages of following FC over $\mathrm{CL_s}$ are that one can instead form a two sided confidence belt allowing the $\mu = 0$ cases to be excluded as well. Additionally if the question as posed in Section 5.2.1 is to be extended to, *"Which parameter values in a proposed physics model fit best with the observed LHC data?"*, knowledge of the most likely value $\hat{\mu}$ given the observed data will be needed. As work to start finding the best fit points hasn't started in CONTUR this will be set aside but it is an alternative statistical test following similar constructions to those already outlined for the exclusion case. There are still some latent issues with this construction however, for example it has been noted that this can lead to cases where given no observation of a signal, experiments with higher expected backgrounds set a better limit than those with little or no background [149].

In summation then, the purpose of this subsection has been to outline what statistical tools will be needed to answer the question posed. What has been shown is that following the following procedure will produce the required modified frequentist confidence level ($\mathrm{CL_s}$) :

1. Take the simple absolute chi-square test statistic, χ^2_μ in equation (5.10).

2. Treat the test statistic at the boundary region where the test is defined, equation (5.13).
3. In the large sample limit the pdf of χ^2_μ follows a standard normal distribution.
4. Use the ratio of test statistics to construct an modified frequentist $\mathrm{CL_s}$ confidence interval, equation (5.12).

The assumptions of asymptotic nature of the test statistic are guaranteed by the nature of the data to be included, often due to the nature a simplified background model will be taken as $\vec{b} = \vec{n}$ which simplifies the case even futher. This simple hypothesis test requires then no numerical methods such as polynomial minimisation or matrix inversion which renders the calculation simple and fast to perform.

An alternative to be investigated, particularly for parameter fitting in future work, is to build a more formally frequentist confidence level (FC), by following:

1. Take the delta chi-square test statistic, $\Delta\chi'^2_\mu$ in equation (5.14).
2. Treat the test statistic at the boundary region where the test is defined, equation (5.13).
3. In the large sample limit the pdf of $\Delta\chi'^2_\mu$ follows a standard normal distribution.
4. Construct the frequentist FC confidence interval from the integral of this pdf.

The two constructions (FC and $\mathrm{CL_s}$) are similar in a lot of respects but FC requires a polynomial minimisation to find the best fit $\hat{\mu}$. There are a great deal more choices one could make here, but for now there are sufficient tools to start exploring parameter spaces.

5.2.4. Likelihoods in the presence of nuisance parameters

The discussion so far in Section 5.2.3 has centred on a likelihood containing no nuisance parameters as defined for a Poisson counting test in equation (5.4). Any realistic physical case will have a series of systematic uncertainties, typically on the background model used. These are often phrased as nuisance parameters in the context of statistical inference. The likelihood discussed thus far could be extended in the following way,

$$L(\mu, \vec{\nu}) = \prod_i \frac{(\mu s_i + b_i + \nu_i)^{n_i}}{n_i!} e^{-(\mu s_i + b_i + \nu_i)} \times \exp - \left(\frac{\nu_i^2}{2\sigma^2_{\nu,i}} \right), \tag{5.15}$$

$$= \prod_i \mathrm{Pois}(\mu s_i + b_i + \nu_i \mid n_i) \times \mathrm{Gauss}(\nu_i \mid 0, \sigma_{\nu,i}), \tag{5.16}$$

where a nuisance parameter, ν_i, has been added to the likelihood for each background model count, b_i. This parameter has been assumed to follow a Gaussian pdf with mean zero and

variance, $\sigma_{\nu,i}$, where the normalisation terms have been omitted as these won't influence the behavior of the likelihood ratio test statistic. Realistically the true pdf this nuisance follows won't typically be Gaussian but is is often the best pragmatic choice of pdf. Motivated in part again by the guarantee that all observables used will be in the large sample limit, and in part by practical concerns that typically all information published from the experiments pertaining to the form of this pdf are plus and minus uncertainty values. Retracing the steps through the test statistic constructions to now include the nuisance parameter information then, the full profile likelihood is rewritten as,

$$t'_\mu = -2\ln\lambda(\mu) = -2\ln\frac{L(\mu,\hat{\hat{\nu}}(\mu))}{L(\hat{\mu},\hat{\nu}(\hat{\mu}))}\,, \tag{5.17}$$

where $\hat{\hat{\nu}}(\mu)$ are the conditional ML estimators for the nuisances and $\hat{\nu}(\hat{\mu})$ are the unconditional ML estimators at the μ value that maximises the likelihood. As noted previously this was the construction followed for the original CONTUR paper. Nuisance parameters are incorporated by adding them into the evaluation of the Fischer information matrix. From this matrix one can extract the variance of μ, called simply σ previously in equation (5.9). For the simple hypothesis test based on the likelihood ratio given in equation (5.6) this can be incorporated as,

$$t_\mu = -2\ln\lambda(\mu) = -2\ln\frac{L(\mu,\hat{\hat{\nu}}(\mu))}{L(0,\hat{\nu}(0))}\,, \tag{5.18}$$

where now the unconditional ML estimators are evaluated in the trivial case of $\mu = 0$, so the nuisances will always stay at their means. The impact of these two constructions on the forms of the chi-square test statistics is then a case of working out the relevant maximum likelihood estimates to use in the evaluation of the chi square. Explicitly in the case of $\Delta\chi'^2_\mu$, this is,

$$\Delta\chi'^2_\mu = \frac{\left((\mu s_i + b_i + \hat{\hat{\nu}}_i) - n_i\right)^2}{\sigma_i^2} - \frac{\left((\hat{\mu} s_i + b_i + \hat{\nu}_i) - n_i\right)^2}{\sigma_i^2}\,, \tag{5.19}$$

where for χ^2_μ the first term on the right hand side of equation (5.19) is all that is needed. These estimators can be obtained from the Fischer information matrix as mentioned previously. Explicitly using the likelihood form in equation (5.15) the following expression can be written to obtain the maximum likelihood estimators,

$$\frac{\partial \ln L}{\partial \nu_i} = \frac{n_i}{\mu s_i + b_i + \nu_i} - 1 - \frac{\nu_i}{\sigma^2_{\nu,i}}\,. \tag{5.20}$$

The estimators are found for the desired μ value by finding the roots of this equation, these roots can be found analytically for this simple example. Implicit constraints in CONTUR give two further observations to this:

- The lack of availability of true nuisance pdfs means a Gaussian approximation is almost always invoked for their distribution. This means the likelihood has nuisance constraints that are always Gaussian constrained about the Poisson count mean. It is hard to go beyond the simple model for nuisances shown here without additional information from the experiments, even though this is in reality never the true distribution of the nuisance.
- In the trivial background model case, $\vec{b} = \vec{n}$, used in many of the studies, this minimization of the second term on the RHS of equation (5.19) is implicitly done already. The nuisances already sit at the means of their allowed distributions. It also leads to simplifications that can be put into the numerical routine to find the roots in equation (5.20).

The simple likelihood extension given in equation (5.15) needs one more practical extension. Namely that in practise the nuisance parameters between different Poisson counting tests will be correlated to some degree. The full CONTUR specific treatment of these correlations is given in Section 5.3.3, here it is noted that incorporating the correlation information between two parameters is captured in the chi-square cases by inclusion of off-diagonal elements in the covariance matrix (equivalently in the full profile construction off-diagonal elements in the Fischer matrix). To make an explicit example the likelihood from equation (5.15) can be written for a two bin counting test case, each bin count with a separate nuisance parameter, as,

$$\chi^2_\mu = \begin{pmatrix} \mu s_1 + b_1 + \hat{\hat{\nu}}_1 - n_1 \\ \mu s_2 + b_2 + \hat{\hat{\nu}}_2 - n_2 \end{pmatrix}^T \cdot \begin{pmatrix} c_{11} & c_{12} \\ c_{21} & c_{22} \end{pmatrix}^{-1} \cdot \begin{pmatrix} \mu s_1 + b_1 + \hat{\hat{\nu}}_1 - n_1 \\ \mu s_2 + b_2 + \hat{\hat{\nu}}_2 - n_2 \end{pmatrix}, \tag{5.21}$$

with c_{ij} being the covariances of the two observations. In this example, the two nuisances are uncorrelated as they were considered unique to each background, the covariance matrix then would be diagonal. If they were considered as the same uncertainty, and were fully correlated between the two counts then the off diagonal elements of the covariance matrix would be non zero to reflect this. It is fairly easy to extend this construction to have an arbitrary number of nuisances on each count and an arbitrary number of counting tests included. However if lots of correlated systematics are introduced for a large number of counts, the analogue of equation (5.20) requires numerical methods like gradient descent to find the roots which can get computationally intensive.

The correlated chi-square will form the building block then of the CONTUR limit setting function, but similar constructions are common to a variety of LHC limit setting codes. An example of a similar construction has been the introduction of *Simplified Likelihoods* [150], which is in effect an agreed form to publish directly the covariance matrix for a series of search signals. This has found use in some of the previously mentioned LHC limit setting frameworks at the start of this Chapter. As the fiducial unfolded measurements used do not publish this information this will have to be built on the fly for CONTUR, this is discussed in Section 5.3.3.

5.2.5. Building a likelihood of parameter space

The likelihood construction for a single point in parameter space was given in Section 5.2.3. A physics signal model was specified by a chosen set its free parameters, $\{x_0 \dots x_n\}$. A generator implementation and the conditions defining the observables gave a set of signal counts s_i, which was used as input to calculate a CL of these signal counts. In the likelihood function the signal model was the set of counts s_i which were parameterized with a common scaling μ, this is more than just a convenient choice for parameterizing the tested hypotheses. The Poisson likelihood given in equation (5.4) could be written,

$$L(\vec{x}) = \prod_i \frac{(s_i(x_0 \dots x_n) + b_i)^{n_i}}{n_i!} e^{-(s_i(x_0 \dots x_n)+b_i)} , \tag{5.22}$$

where the parameter of interest, μ, has been replaced by the full set of model parameters, $\{x_0 \dots x_n\}$. This is not a feasible likelihood to use as there is no clear way to define the pdf for $s_i(x_0 \dots x_n)$. In the examples given for a test statistic based on the profile likelihood, $\Delta\chi'_\mu$, the $\hat{\mu}$ value used as reference for the delta does not necessarily correspond to any physical signal model. For values of μ in the simple parameterized likelihood of equation (5.4) not equal to the tested value of $\mu = 1$, there is not necessarily a corresponding ensemble of $\{x_0 \dots x_n\}$ to produce the same signal model counts. The implication of this is that the signal model in the sense of the likelihood function is only specified at a single point in the physics model parameter space. The best thing one can do to understand the full parameter space is to interpolate the statistical metric calculated at each point with the parametrized likelihood. Provided the interpolation is performed on sampled parameters of the model, the interpolation is valid provided the granularity of the scan catches all the features in the parameter space. This is not guaranteed and must be considered as part of presenting the result of such a scan.

Understanding a parameter space is then a question of drawing a set of ensembles of the parameter values, calculating the CL_s (or equivalent metric) for each ensemble, and interpolating the result. An example of a simple way of doing this is shown for the model discussed in Section 6.3, is shown in Figure 5.6. This shows a two parameter plane of a model, with the remaining free parameters fully determined. Both parameters are uniformly sampled with set ranges, the sampled points are shown explicitly in the figure with black plus marks with the corresponding calculated CL_s printed next to them. The interpolated result of two fitted contours of constant confidence are shown in cyan, the 1σ or 68% CL (short dash) and 2σ or 95% CL (long dash). Some observations are noted,

- There are many points sampled that have $CL_s = 1$ or $CL_s = 0$. Prior to calculating the CL_s for the set of parameter points displayed in the figure this is not known, but any subsequent sampling of this space would not benefit from selecting points from these

regions. Moreover, if the goal is to accurately build the contour of 2σ CL for example, one would want to bias any subsequent sampling to select more parameter points around the current level obtained.

- In the two parameter case reasonable convergence on a shape is reached with a relatively small uniform amount of sample points over quite a large (logarithmic) range. Scaling this to higher dimensional scans is a difficult problem however.

It is this idea that closes the loop back to Section 5.2.1. If uniform sampling of granularity N for each parameter in a parameter space of dimension D is used, the number of points requiring simulation will be $\mathcal{O}\left(N^D\right)$. Typically if the dimensionality exceeds two or three parameters this will be too complicated to achieve a convergent fitted contour. The idea then is to drop the granularity and iteratively select a set of points in this parameter space of fixed total size (typically the size of this set will relate to the computational power available), then a layer to the procedure can be added that iteratively resamples the space based on some criteria until a convergent fitted contour is obtained. This criteria could for example be the uncertainty in $\mathrm{CL_s}$, or effectively the variance of μ. The sampling in each parameter can also be random rather than uniform, or follow some prior expectation if this is useful to the problem tackled.

Parameter sampling requires as complicated a tool kit as the dimensionality of the parameter space under study. The Contur parameter sampling, covered in Section 5.3.1 is rudimentary and essentially limited to a small number of parameters but sufficient for a lot of useful physics studies. It is sufficient to cover a lot of simplified models, which is the initial goal in the design of the toolkit. Examples of attempts to tackle higher dimensional scanning can be seen in studies from the Gambit working groups, which builds on the ScannerBit [151] module for parameter sampling. The ATLAS collaboration has also performed comprehensive scans of the 16 dimensional pMSSM [152], this is similar in spirit to sampling as performed in Contur, however $\mathcal{O}\left(10^6\right)$ model points were considered in this scan which required vast computational resources. The ATLAS scan also involved applications of additional constraints on the chosen model points, prior to event generation to speed up the process.

5.3. The anatomy of Contur

With the building blocks of an LHC reinterpretation tool defined in Section 5.2, the specific details of the implementation of the workflow in Contur can be given. This section is more focused on the technical aspects. The general design philosophy is to introduce as little new code as possible whilst requiring as few external dependencies as possible. Firstly some observations are made about the requirements to serve up observables outlined in Section 5.2.2:

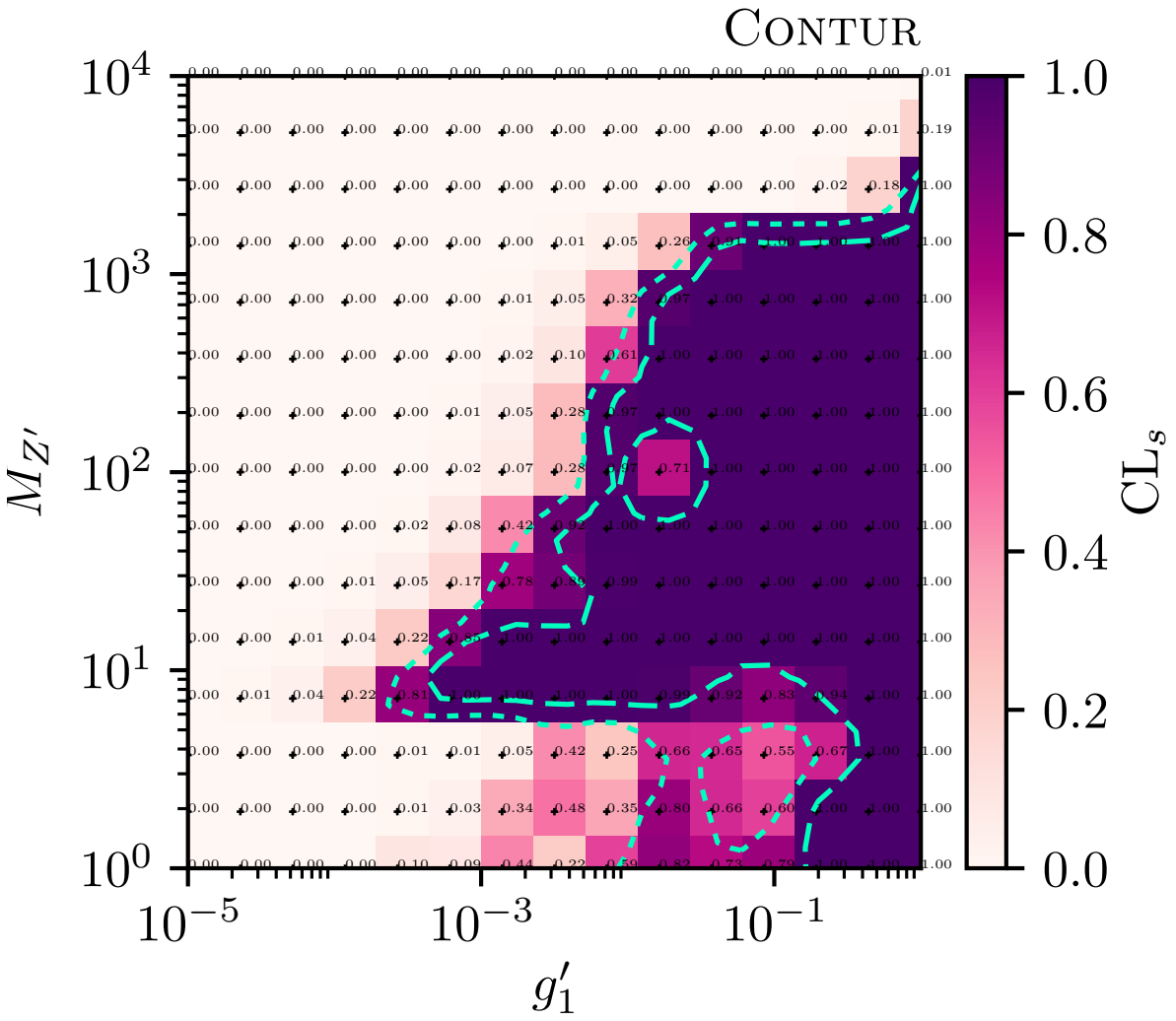

Figure 5.6.: A prototype CONTUR plot of a parameter space scan of the gauged B-L model discussed in Chapter 6. The black plus signs show the true sampled value of the parameters, with text indicating the CL_s at this point. The boxes surrounding are then coloured accordingly and the cyan dashed lines show the interpolated 68% (short dash) and 95% (long dash) confidence levels.

- At the start of the generator flow, most generators have a bespoke flat file reader to define the configuration. Python is a natural choice with simple text file manipulation and scripting capabilities.
- At the end of the flow, Rivet outputs a data format YODA with native C++ and Python API. Python is a natural choice again as a well defined API exists to the data storage format.

- The software dependencies between these two points are already vast, running into gigabytes of installed code. Python still remains sensible as it induces little additional size to this installed stack, and is natively available on most UNIX systems.

A purely pythonic implementation of the tool chain then fits naturally. Python is increasingly being used in the HEP community, and is the predominant language for modern data science techniques too (e.g. the python library Keras [153]). For HEP software projects going forwards Python is the best choice of implementation language where possible. The main big gap in the required workflow is how to efficiently calculate the likelihoods as outlined in Section 5.2.3. The first port of call for the types of construction outlined in HEP would be in the RooStats package [154]. This has a significant downside, that despite having a Python API, relies on the more substantial ROOT [155] backend to be installed[3]. As previously noted the budget of large external dependency codes is effectively maxed out by the generator toolchain making this unfavourable. ROOT is a package that is largely only used by the experimental HEP community, since Contur is intended to be used by HEP phenomenologists it is best to use tools common to the experimental and phenomenological communities. Thankfully as shown in Section 5.2.3 the forms of the test statistics simplify greatly, at least under the initial assumptions used to construct Contur. This means that the required statistics framework can be realised with a custom implementation using the standard Python libraries. All other parts of the procedure, namely interfacing and visualisation are well catered for in the standard libraries too. Hence, in summation, a purely pythonic package can be constructed minimally on top of the required generator tools.

The toolkit needed is necessarily as complex as the studies that require it. Contur has mostly been designed and used thus far to scope a limit number of parameters, usually in phenomenological models with a smaller subset of parameters. This *Simplified Models* paradigm and the wider context of extending the capabilities in Contur to higher dimensional spaces is discussed when the physics results are presented in Chapter 6. Where relevant in the following sections in this chapter, code (or pseudocode) snippets are given. The most up to date information on the project can be found on the project webpage at[4] and the code is publicly available and hosted on the project BitBucket repository[5]. Instructions to run, as well as pre compiled containers with all the required software are also available on the web documentation.

[3] It is noted that at the start of the work on this project there was no viable pure Python RooStats implementation, efforts to address this have started to appear.

[4] Available at contur.hepforge.org.

[5] Available at gitlab.com/hepcedar/contur.

5.3.1. Parameter sampling in Contur

Parameter sampling in CONTUR is steered with a custom template `.dat` file, an example of which is shown in Listing 5.1. This is based on the input/output structure defined by the Python configObj package [156]. This is chosen as it is a minimal pythonic solution that reads into, or writes files directly out from python dictionaries, and is more easily human understandable than some more complete template languages. Entries delineated by square braces define dictionaries named as the contained string. Double braces are a dictionary within the parent dictionary. The following options are defined in the CONTUR steering interface:

- `Run` dictionary, parameters pertaining to steering the event generation. Available options are,
  - `generator`, path to a shell script that configures the necessary variables to setup the event generator.
  - `contur`, path to a shell script that configures the necessary variables to load the contur module.
- `Parameter` dictionary, contains a dictionary for each free parameter the user wants to control in the model. The string used as the name of this dictionary is the name of the parameter as far as CONTUR is concerned. The key field present for each parameter is `mode`, this defines the behaviour of the parameter and then opens additional allowed fields for each parameter. The following lists the available modes, with the sub list detailing the unique additional parameters for each mode:
  - `CONST`, a constant parameter
    - `value` a float with the value to assume for this parameter
  - `LOG/LIN`, a uniform logarithmically or linearly spaced parameter.
    - `start/stop`, the floats of the boundaries of the target sampled space for this parameter (note: start must be a smaller number than stop).
    - `number`, an integer number of values to sample in the range.
  - `REL`, a relative parameter, defined with reference to one of more of the other parameters.
    - `form`, any mathematical expression that python can evaluate is a valid form for this parameter. Curly brace delineated strings are the names of the relative parameter values to insert, these have to match other parameter dictionary names in the `Parameter` block.

Listing 5.1: An example CONTUR configuration file for a model with 3 free parameters

```
#CONTUR parameter sampler steering file
#Built with configObj package

[Run]
generator = "/path/to/generatorSetup.sh"
contur = "/path/to/setupContur.sh"

[Parameters]
[[x0]]
mode = LOG
start = 1.0
stop = 10000.0
number = 15
[[x1]]
mode = CONST
value = 2.0
[[x2]]
mode = REL
form = {x0}/(2.0*{x1})
```

With these tools then however many parameters available in the model can be scoped into the CONTUR parameter sampler. The parameters whose `mode` is either `LOG` or `LIN` are the scanned parameters, and the number of such parameters is the dimensionality of the scan. `REL` or `CONST` parameters are then ways to correctly set the additional parameters of the model. Any dimension of scan is technically possible but due to the reasons mentioned in Section 5.2.5 practically only up to two or three dimensions are numerically feasible with this simple parameter scanner. One pending extension to improve this simple scanner is to allow the `start/stop` values for scanned parameters to be defined in the same way as the `form` of `REL` parameters.

5.3.2. Observable calculation in Contur

Following the description given in Section 5.2.2 on serving up observables, it was noted that for the unfolded measurements in question, Rivet is the unambiguous choice to provide both the selection criteria of the fiducial region and the unfolded data to compare to. As such this is a non-negotiable criteria in the construction of CONTUR, to use Rivet. It was noted that there are a multitude of choices one can make to produce the events to pass through Rivet, and indeed some recent work has removed specific generator dependence. The studies presented in

Listing 5.2: Snippet of a HERWIG input card for the same 3 free parameters as previously defined in Listing 5.1

```
#Snippet of a pseudo template Herwig input card to match the CONTUR template
read FRModel.model
set /Herwig/FRModel/Particles/X:NominalMass {x0}
set /Herwig/FRModel/FRModel:x1 {x1}
set /Herwig/FRModel/FRModel:x2 {x2}

insert HPConstructor:Incoming 0 /Herwig/Particles/u
insert HPConstructor:Incoming 0 /Herwig/Particles/ubar
insert HPConstructor:Outgoing 0 /Herwig/FRModel/Particles/X
set HPConstructor:Processes SingleParticleInclusive
```

Chapter 6 use HERWIG to power the event generation so the workflow here is described with this particular choice.

The physics results derived using CONTUR, detailed in Chapter 6, have mostly been from study of simplified models. The limited number of free parameters in such extensions to the SM mean they are well suited to study with the simple parameter sampler already described in CONTUR. Simplified models are also well suited to the automated approach to BSM event generation described in Section 5.2.2, which additionally means any model defined in a UFO python package [133] can be studied in a similar manner. This makes the HERWIG event generator chain flexible and well suited to study a large array of BSM extensions.

Simulation of BSM physics in HERWIG historically centred on complete SUSY models [157], consequently it was designed to generate inclusively all allowed particle $2 \to 2$ interactions from a specified model's particle content. To interact with the CONTUR parameter sampler, a template generator input has to be provided. The parameters are scoped in CONTUR as described in Section 5.3.1 are then substituted into a file that defines the generator run conditions. Following the example Listing 5.1 of a CONTUR parameter file, a snippet of the matching HERWIG input card is shown in Listing 5.2.

Much of the syntax is HERWIG specific so is left to the HERWIG documentation. Important features to notice are that the parameters are being defined in the HERWIG `FRModel` (short for FEYNRULES, the placeholder for a HERWIG parsed UFO model file). This functions in the same way as the `form` field described in the CONTUR parameter file, where the curly braces match the parameter dictionary names allowing numeric values for each to be substituted in, following the rules defined in the corresponding CONTUR card. As this is based off string parsing and substitution, any event generator configuration that can be steered in a similar way can be substituted in here. An example of the process definition is also included for this toy model. In this example the instruction given to the generator is to inclusively generate all $2 \to 2$ processes

with incoming u and $\overline{\text{u}}$ quarks, and an outgoing hypothesised X particle. According to the Feynman rules in the parsed `FRModel.model` file, all allowed diagrams will be generated. The mass of this particle has been scanned in with the Contur sampler by varying the defined parameter, `x0`.

The execution of this in Contur is then realised in two steps. Firstly a directory is made for each point in parameter space the sampler creates, then all associated generator files, including the input card with the substituted numerical values are copied to each directory and a shell script containing all the commands to execute the generator run from a fresh login are written. These files can then be automatically sent to a High Performance Computing (HPC) node to execute each point in parameter space. The commands needed to run relevant Rivet jobs on the output of the event stream are also included. This is a break point in the current design of Contur, to extend to higher dimension scans with adaptive sampling, the evaluation of the output histograms would have to be a continuously running job. Instead the creation of the map of the likelihoods of parameter space is run once all jobs have returned the necessary histograms. This is a current limitation, but does not inhibit useful parameter space exploration particularly for many interesting models to study.

Once the generator has reached the requested number of events, the observables are stored as filled histograms in the YODA histogram format. Each point in a scan will have a separate directory containing the YODA histograms and information about the point in parameter space that the sampler chose. Typically around 300 parameter points will be used to make a convergent scan in two dimensions.

5.3.3. Likelihoods in Contur

As Contur has been developed, one area that has seen a lot of revision is the construction of the likelihood. This is central to the whole process and is the basis of the results. In Chapter 6, Section 6.2 the results of the original Contur paper are presented [145]. The likelihood construction used for this result is given in detail here as it is the simplest case. More recent results using Contur shown in Chapter 6, Section 6.3 and Section 6.4 improve on the original setup described here. Where improvements have been made this will be highlighted in this text.

In Section 5.2.3 a series of test statistics and confidence interval constructions were given. The original Contur paper followed the full profile likelihood ratio test statistic construction, t'_μ, given in equation (5.17). Nuisance parameters were incorporated in this likelihood as given in equation (5.15). The resulting p-values were then treated with the CL_s prescription as given in equation (5.12). The available Rivet routines that were validated for use in Contur at the time the paper was composed are given in Table 5.1. A more up to date list of Rivet routines

validated for use in CONTUR at the time of composing this document is given in Appendix A, Table A.1. A series of observations are made about the initially available data set in Table 5.1:

- Almost all the results were taken from analyses performed with the 7 TeV dataset. Unfolded results are more complicated for the experiment to produce so tend to take longer to complete. This means there is often a gap between the exclusion limits from explicit search reinterpretations and the CONTUR method. This is looked at in more detail in Chapter 6

- The bulk of the results are from ATLAS measurements. This is mostly due to sociological differences between the ATLAS and CMS collaborations, although CMS are making increasing efforts to preserve more results in Rivet[6].

- The information on the uncertainties propagated from HEPData is not necessarily uniform, and was not automatically propagated to being available in Rivet. Often only a single plus and minus uncertainty is given on a data point, particularly for older measurements. The granularity of information is improving in Rivet but this is a noted limitation of some older measurements.

- Typically no information on the background, or SM expectation for these observables is provided. To this end, and as discussed at some length previously, a simple background model is taken by assuming the background model is exactly equal to the observed data, $\vec{b} = \vec{n}$. The experiments are increasingly making effort to provide a full background model in HEPData but again this is absent for most older measurements. CONTUR is also internally making increasing effort to study providing its own background model. The physical implications of these choices are covered further in Chapter 6

With the available dataset now defined, the task is now to maximise the information included into the likelihood. Given the information available from the Rivet routines listed, a simple likelihood model as a product of Poisson counts convoluted with a single nuisance parameter following a Gaussian distribution taken from the uncertainty on the observed data points is chosen. This is the likelihood as written out in equation (5.15). Maximising the information in this likelihood means including as many Poisson counting tests (bins) as possible into the product the likelihood is taken over. However the presence of nuisance parameters complicate this, if the nuisance from one counting test is highly correlated with that from another counting test, both tests should not be included in the likelihood unless the degree of correlation is known. As noted this information is not readily available for old measurements, so a lot of bins will have to be thrown away. In the initial results of CONTUR the degree of correlation was decided

[6] The ALICE and LHCb collaborations are also making increased use of Rivet, and where the routines are measurements of applicable processes they can be used in CONTUR as well.

CONTUR Category	Rivet/ Inspire ID	Rivet description
ATLAS 7 Jets	ATLAS_2014_I1325553 [158]	Measurement of the inclusive jet cross-section
	ATLAS_2014_I1268975 [159]	High-mass dijet cross-section
	ATLAS_2014_I1326641 [160]	3-jet cross-section
	ATLAS_2014_I1307243 [161]	Measurements of jet vetoes and azimuthal decorrelations in dijet events
CMS 7 Jets	CMS_2014_I1298810 [140]	Ratios of jet pT spectra, which relate to the ratios of inclusive, differential jet cross-sections
ATLAS 8 Jets	ATLAS_2015_I1394679 [162]	Multijets at 8 TeV
ATLAS 7 Z Jets	ATLAS_2013_I1230812 [163]	Z + jets
CMS 7 Z Jets	CMS_2015_I1310737 [164]	Jet multiplicity and differential cross-sections of Z+jets events
CMS 7 W Jets	CMS_2014_I1303894 [165]	Differential cross-section of W bosons + jets
ATLAS 7 W jets	ATLAS_2014_I1319490 [62]	W + jets
ATLAS 7 Photon Jet	ATLAS_2013_I1263495 [166]	Inclusive isolated prompt photon analysis with 2011 LHC data
	ATLAS_2012_I1093738 [167]	Isolated prompt photon + jet cross-section
CMS 7 Photon Jet	CMS_2014_I1266056 [168]	Photon + jets triple differential cross-section
ATLAS 7 Diphoton	ATLAS_2012_I1199269 [169]	Inclusive diphoton $+X$ events
ATLAS 7 ZZ	ATLAS_2012_I1203852 [170]	Measurement of the $ZZ(*)$ production cross-section
ATLAS W/Z gamma	ATLAS_2013_I1217863 [171]	W/Z gamma production

Table 5.1.: Table of all Rivet routines included in the limit-setting scan. With the one indicated exception, they are all based on 7 TeV data.

manually. By grouping the analyses into similar final state signatures, the overlap between analyses is minimised. Whilst there will still be correlated nuisance parameters between the groups, these effects are generally considered acceptable for preliminary studies. As will be discussed in Section 6.4.2, progress has been made on correlating named systematic breakdowns within an analysis. Perhaps more ambitiously in the future, if a common naming of nuisances between all analyses is decided on, a correlation matrix across all analyses to be included in a scan could be derived.

The algorithm to sort the total bins output from all the considered Rivet routines, to a list of bins that are sufficiently uncorrelated such that they can be included into the same likelihood is as follows:

- The Rivet routines are sorted in the table into CONTUR categories. These are said to represent non overlapping experimental final states. For example, an event selected in a purely hadronic final state analysis covered by the "ATLAS 7 Jets" category, will have a negligible probability of also being selected for an analysis in the "ATLAS 7 Z Jets" category. This effectively negates the effect of any statistical correlation between the Poisson counts included in the likelihood, which is not available information. Where multiple Rivet analyses are identified as being in the some CONTUR category, the most sensitive (giving the highest CL_s) measurement will be chosen to represent this category.

- Within each Rivet analyses, typically multiple histograms are produced. Usually these histograms will be statistically correlated, and also have largely correlated systematics. It is normally not safe to combine bins from different histograms, so the highest CL_s histogram will be chosen as representative of the Rivet analysis.

- Within each histogram there are typically multiple bins. Within a histogram the correlation of the nuisance parameters is almost always non-negligible so the safe route is to pick the binned counting test that gives the largest CL_s as representing the histogram.

The end result is a series of single bin counting tests being constructed for each CONTUR category, coming from the largest CL_s bin of all histograms in the pool. This is the maximal *safe* (i.e. not overstating the exclusion power of the observations) combination of information one can put into a single likelihood from the available data and granularity of information. Discarding all except the highest CL_s bin is an approximation that has a varying degree of impact on the derived limit depending on the model being studied. Where the model produces resonant structures (bumps in an otherwise smoothly falling spectrum) it is a close approximation. If the model produces more subtle effects then it can represent a limiting factor in the success of the CONTUR approach. CONTUR also has the ability to uncorrelate specific histograms in an analysis, that is to take multiple histograms within a Rivet analysis as being statistically

uncorrelated. This can be used to increase the information included from a given analysis if it is safe to do so.

More recent results, such as those shown in Chapter 6, Section 6.3 use a different test statistic construction. Due to it being a simpler construction the simple likelihood ratio giving the χ^2_μ statistic as in equation (5.10) is used. When treated with CL_s this produces required coverage of the confidence interval despite being an absolute chi-square. The results were cross checked with the full profile construction and found to be consistent. Recent work has also investigated relaxing the trivial background model; either by inclusion of experiment provided background model, or by direct study of state of the art theory predictions. In cases where a non trivial background model has a impact on the results, it will be highlighted. Even more recent results, such as those shown in Section 6.4, have also started incorporating correlation between the nuisance parameters, incorporated as mentioned into the chi-square as in equation (5.21). The covariance matrix is built on the fly using new functionality included in the Rivet 3.0.X series. This model assumes that each bin with the same named systematic in a full breakdown of the systematic sources is one hundred percent correlated, and builds the covariance from that model. The validity of this depends on the granularity of information in the uncertainty breakdown. This is an area of ongoing work and study.

Contur has implemented the construction of each test statistic and calculation of the confidence levels internally. Due to the noted simplifications throughout Section 5.2.3 this can be realised in Python by using the SciPy library [172] to implement the necessary standard statistical tools as building blocks.

5.3.4. Data model and visualisation in Contur

As outlined in Section 5.2.5, Contur currently makes no great distinction between running a single point in parameter space or running a large collection. The sampler can steer a multi-dimensional sampling of a parameter space, but the resultant statistical test isn't treated any differently than evaluating the likelihood of a single parameter space point. As the current model simply interpolates the calculated CL_s, the granularity of a scan is set by availability of CPU time to run the event generator at each model point. This hasn't generally been a limiting factor in most studies using Contur thus far. The limitations on number of dimensions one can scan in also hasn't proved that limiting for the projects undertaken so far. Often a combination of some simple two dimensional Contur scans can build an adequate picture of the type of models that Contur has been designed to currently tackle (predominantly simplified models). Usage of Contur to extract a detailed phenomenology of models is showcased throughout Chapter 6.

Without a sampler capable of efficiently scanning multiple dimensions, the CONTUR data structure and visualisation tools are mostly limited to representing two dimensional scans only. A panel showing four example scans made with CONTUR are shown in Figure 5.7. The filled contours represent the area where the observed data have a CL greater than 68% (green) and 95% (yellow) of excluding the hypothesised parameter values. The visualisation is all built using the Matplotlib library [173], and the interpolation of the levels is performed using this library as well[7]. Corresponding *heatmaps* are made alongside these filled contours, which represent the CL calculated at each sampled point. The top left panel in Figure 5.7 shows an additional capability, to draw filled contours from other sources overlaid on the CONTUR maps. These can either be calculated internally using the parameter points sampled by CONTUR or input from external data tables. This is currently the level of interoperability CONTUR has with other BSM limit setting tools, importing their resultant CL into CONTUR for visualisation. The ongoing hope is to provide ways to include this information directly into the CONTUR likelihood, allowing true combined limits rather than overlays. Another option to explore is to interface CONTUR as a backend likelihood calculator to more complete scanning tools such as Gambit.

[7] Matplotlib contour interpolation is based on a Marching Squares algorithm as implemented in MATLAB [174].

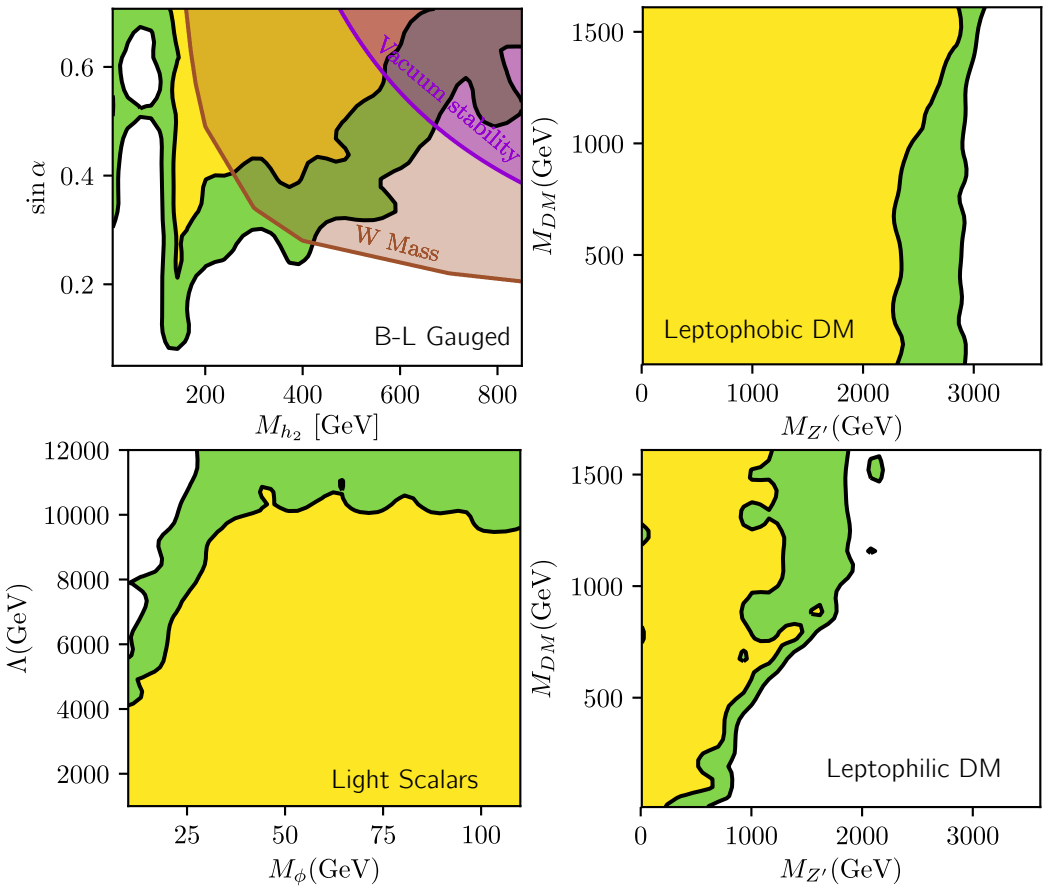

Figure 5.7.: An example of 2D scans made using CONTUR of four different models. In each case the model is named on the panel, and the filled contours represent the 68% (green) and 95% (yellow) CL interpolated contours [175].

Chapter 6.

Constraints on new theories using Rivet

The methodology behind CONTUR was presented in Chapter 5. CONTUR was introduced in the context of a LHC reinterpretation tool, where it differs from other LHC recasting tools primarily in the source of data that is considered. Rather than utilising the detector level searches for new physics to set limits on alternative physics models, CONTUR uses the unfolded particle level measurements. This approach should be roughly equivalent when the fiducial phase space measured mirrors the detector level search criteria, and potentially reveal areas the more exclusive selections typically employed in searches do not cover in a model's parameter space. The only way to really evaluate the performance is in practical application to some case studies of BSM models, making comparison where available to the detector level results already established.

In this chapter two studies using CONTUR are presented. Firstly to frame the discussions of the CONTUR results, a more thorough description of the simplified model paradigm is given in Section 6.1. In Section 6.2 a simplified model for dark matter production at the LHC is considered, the results presented are those that formed the original CONTUR paper [145]. In addition to studies presented in the original published work, some additional exploration of this model space is presented. In Section 6.3 a more recent application to a model for neutrino mass generation via a gauged $B - L$ symmetry is presented [176]. Lastly in Section 6.4 some developments in CONTUR such as applications of correlation information are presented. The work in Section 6.4 is ongoing and form preliminary contributions towards some planned future publications.

6.1. Simplified models and the model space spectrum

The simplified model paradigm was described in Chapter 2 as part of a bottom-up approach to BSM model building. This is in contrast to the 'classical' approach of constructing a full UV complete model valid to the Planck scale (often motivated by SUSY) and working top-down. Within the simplified model paradigm there is implicitly a promise that the introduced physics in the simplified model has some UV completion. This means some new dynamics are introduced to the simplified model at a scale beyond the scales that the LHC probes, which make the model valid into the UV regime. Enforcing such UV completion is often set aside when building simplified models. However, generally some basic criteria of a perturbative QFT, such as cancellation of anomalies and unitarity violating amplitudes [1] are imposed, at least to the scales experimentally accessible. Provided an introduced theory is free of such issues up to the LHC collision energies, it can be used as an effective description of potential interactions at the LHC. Simplified models are not, however, a justification to throw away all concepts of UV completion. If the UV completion of a model is provided by SUSY, it could well mean that the model embeds into a class of SUSY models already disfavoured by other observation, or that the parameter space being probed by the simplified models is already less well motivated from classic UV complete model building arguments such as naturalness [177]. There is a balance between the pragmatic bottom-up approach and more formal classical top-down ideas.

A simplified model generally attempts to explain a particular observable. A popular motivation for model building at the time of composing this thesis are the hints of lepton universality violation seen at the LHCb experiment [178]. Simplified models can be constructed that can explain these anomalies, e.g. by introducing a new massive U(1) vector Z' boson. Such a simplified model has only a small number of free parameters so can be rapidly checked for consistency against the other observed collider data [179], or any other source. In essence it is the flexibility and simplicity of the simplified models that are attractive. Without having to fold in many theoretical preconceptions on how to build the overarching UV complete theory, potential anomalies can be prototyped and explored.

In spirit the simplified model paradigm bares some similarity to SM effective field theory (SMEFT). In this framework all possible gauge and Lorentz invariant interactions of the SM particle fields are characterised by effective operators. An example subset of terms in this Lagrangian including a generalized fermion field F and the scalar Higgs field H, could be written,

$$\mathcal{L}_{\text{SMEFT}} \supset \Lambda_{\text{UV}}^2 H^\dagger H + y_{ij} H F_i \overline{F}_j + \frac{1}{\Lambda_{\text{UV}}^2} F_i \overline{F}_j F_k \overline{F}_l \,, \tag{6.1}$$

where y_{ij} are generalized Yukawa coupling parameters for the general fermion field, and Λ_{UV} represents the UV scale of new physics. Overall all terms have to have a mass dimension of four, such that the action is dimensionless. The first term can be recognised as the Higgs propagator, in the SM the coefficient of this term was formed of the dimensional parameters of the EW vacuum. It was noted the Higgs propagator received corrections proportional to the scale of new physics, hence in this form is written in terms of this scale. The second term is a generalized Yukawa term, the SM is formed from such gauge invariant operators with a mass dimension of four. Terms already included in the SM would not usually be considered as part of SMEFT, as they aren't effective operators, but are included here for illustrative purposes. The final term is a new operator not observed in the SM. This is a four fermion operator with mass dimension of six, so is suppressed by two inverse powers of the dimensional new physics scale. This is an alternative way to view the fine tuning and hierarchy problem. The new physics operator parametrized by SMEFT must be suppressed by large values of the scale, Λ_{UV}, to explain its lack of observation. However increasing this scale means the corrections to the Higgs mass get consequently larger so require increasing fine tuning. Popular mechanisms for neutrino mass generation involve SMEFT operators of dimension five, so would be suppressed by one power of the new physics scale. The smallness of observed neutrino masses is perfectly 'natural' in the SM and congruent with the lack of observation of operators of dimension six or greater, the problem is in fixing the Higgs mass to its EW scale value.

This is the most generic way to introduce physics BSM if the available degrees of freedom are equivalent to the SM, all possible operators are written down which should span all possible observable final states of SM fields. A simplified model could be thought of as taking a subset of these possible operators, and giving them additional propagating degrees of freedom. This is useful as the LHC could be operating at large enough scales that the effect of the mediators of these operators starts to be resolved. However, more degrees of freedom come at a cost of introducing more model dependence, and more parameters to discuss. Ideologically, simplified models lie somewhere between a full UV complete model like SUSY and the fully generic parametrization of SMEFT; they are useful pragmatic tools to explore LHC physics. SMEFT has thousands of free parameters, coefficients for the introduced operators, as computational techniques improve increasingly larger sets of these coefficients are being fitted to data [180,181]. The technology introduced in Contur can be used for these purposes too, this is another application that Contur is considering to study in the future.

6.2. Simplified models for LHC dark matter production

It was mentioned in Chapter 2 that one of the observations in the universe that the SM can't explain is the apparent abundance of gravitationally interacting non-baryonic matter. In the ΛCDM model of cosmology a universe composed of $\sim$69% dark energy, $\sim$26% dark matter and only $\sim$5% SM baryonic matter is proposed [182]. A component of the dark matter would be provided by the SM neutrinos as hot (relativistic) dark matter, but most of this observed dark matter cannot be explained with the SM particle content. A popular solution comes from introducing hypothesised weakly interacting massive particles (WIMPs) as a cold dark matter candidate. The standard model of cosmology favoured a WIMP with particle mass around the EW scale, primarily due to considerations of the thermal history of the universe and resultant structure formation after freeze out. This happened to be similar to predictions from the favoured (prior to the LHC data taking) SUSY extensions to the SM which predicted lightest stable supersymmetric particles (LSPs) with around the same mass. This coincidence of favoured models from either end of the distance scales in physics was called the WIMP miracle. Due to the increasing bounds on DM-SM interaction cross-section from direct DM detection experiments [183] combined with the increasing tension on LSP mass in some SUSY models observed at the collider experiments, this paradigm is becoming less favoured.

It should be emphasised that the stress on the WIMP miracle is mostly on the interpretation of how the signatures would manifest at the LHC. There are competing ideologies to explain the cosmological observations that motivate the construction of the ΛCDM model [184]. However issues such as explaining structure formation, which ΛCDM caters for excellently [185], means a particle explanation of DM is still favoured by many in the field. The nature of the particle interactions at high energy colliders is then what needs to be addressed, and this is where the introduction of simplified models for DM production come in [124,186,187]. These can be viewed as extensions of the types of effective operators direct detection experiments parameterize their results in terms of. These direct detection experiments look for nuclear recoil of dark matter candidates scattering off a nucleon, and are characterized by very low momentum exchange. As such an EFT for such an interaction will generally always be valid, any realistic particle mediator of such an interaction will be of a much higher scale than the experiment can probe. To extend this to the LHC energies requires a simplified model, as the LHC could well be probing the scale of the effective operator. Simplified dark matter models at the LHC characterize well motivated cosmological interactions, and enable complementarity of direct detection and collider production to be probed.

6.2.1. Defining the parameter space of LHC DM production

In the original published CONTUR study [145] a DM model that introduces a new U(1) gauge symmetry on top of the SM was probed. This gauge symmetry introduces a new vector spin one boson, Z'. A Majorana stable dark matter candidate fermion is introduced, ψ, which is charged under this new gauge symmetry but otherwise it is uncharged under the SM gauge groups. To couple this candidate DM to the SM such that potential signatures can be generated, the SM quarks are also charged under the new U(1) gauge group. This leads to an interaction Lagrangian for this theory being defined as,

$$\mathcal{L}_{\mathrm{DM}} \supset g_{\mathrm{DM}}\,\overline{\psi}\gamma_\mu\gamma_5\psi\,Z'^{\mu} + g_q\sum_q \bar{q}\gamma_\mu q\,Z'^{\mu}\,, \tag{6.2}$$

where the flavours of quark are summed over. In the initial studies this sum was restricted to just the first generation, $q \in \{u, d\}$, mainly for practical concerns as this was just considered a toy model. There is no reason this new gauge symmetry should be flavour universal but it is perhaps more natural. The mass generation mechanism for this Z' boson is not considered at this point, it could be incorporated via a Higgs mechanism but Abelian gauge theories can also acquire masses in a way that decouples from the rest of the theory [188].

The Lagrangian in equation (6.2) is a subset of the full space of possible spin one vector interactions of such a mediator. A more complete interaction Lagrangian of such a theory could be written,

$$\mathcal{L}_{\mathrm{DM}} = Z'^{\mu}\bar{\psi}[g^V_{\mathrm{DM}}\gamma_\mu + g^A_{\mathrm{DM}}\gamma_\mu\gamma_5]\psi + \sum_{f=q,l} Z'^{\mu}\bar{f}[g^V_f\gamma_\mu + g^A_f\gamma_\mu\gamma_5]f\,, \tag{6.3}$$

where now the possible couplings are labelled as V denoting a vector coupling, and A denoting an axial-vector coupling. The sum over SM fermion fields now includes leptons, such interactions are already strongly constrained by measurements at LEP so were not considered in the original CONTUR study. The reduced Lagrangian presented in equation (6.2) corresponds to setting $g^V_{\mathrm{DM}} = g^A_{\mathrm{f}} = 0$. The choice of chiral structure of the couplings is largely irrelevant for LHC physics as at LHC scales the mediator will largely be produced on shell. The main motivation for choosing a purely axial DM to purely vector SM coupling is that this is the choice that is least constrained by direct detection experiments [189]. This model has event generator implementations at NLO in QCD [135, 190], however for the purposes of the study presented a custom implementation of the reduced Lagrangian in equation (6.2) was used.

The Feynman diagrams that are relevant for LHC physics resulting from the Lagrangian in equation (6.2) are shown in Figure 6.1. The model parameter space is spanned by four parameters, $\{g_{\mathrm{DM}}, g_q, M_\psi \equiv M_{\mathrm{DM}}, M_{Z'}\}$, and the phase space the generated events occupy will

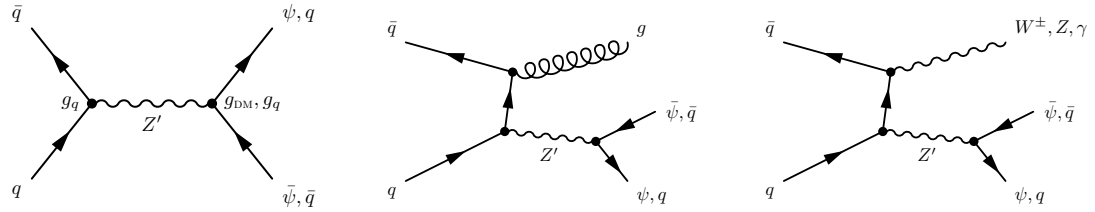

Figure 6.1.: Relevant Feynman diagrams introduced by the simplified model at leading order. Figure 6.1a shows s-channel mediator production followed by decay to quarks or to DM, Figure 6.1b shows mediator with associated jet production and Figure 6.1c with associated gauge boson production.

be a function of these parameters. Following convention, this is reduced to a 2D parameter space and the mass plane, $M_{\mathrm{DM}} - M_{Z'}$ is what is generally studied. For the LHC this choice is in part motivated by the fact that the Z' can be produced on shell at the LHC giving sensitivity not just to production of the DM candidate, but to production of the mediator directly. The Z' production rate at a fixed choice of g_q will be proportional to $1/M_{Z'}^2$. For fixed g_q and g_{DM}, the decay branching ratio of $Z' \to \psi\psi$ will kinematically suppressed when $2M_{\mathrm{DM}} > M_{Z'}$. In this half of the mass plane, the events will be purely $Z' \to q\bar{q}$, so the experimental signature will be resonant production of dijets for the most part. In the other half of the mass plane, there will still be some production of dijets depending on the ratio of g_q/g_{DM}, however most analyses targeting these areas of parameter space are searches for the $Z' \to \psi\psi$ process which at the LHC is seen as events with large $E_{\mathrm{T}}^{\mathrm{miss}}$. Such analyses exploit a feature seen in Figure 6.1b and Figure 6.1c, that there is a probability for the incoming quarks to radiate an initial state (ISR) SM particle at high energy. This gives a distinctive experimental signature of a single high energy particle back to back in the ϕ plane with a large inferred $E_{\mathrm{T}}^{\mathrm{miss}}$. These are typically called mono-X signatures, where mono-jet would be reasonably expected to drive the sensitivity due to the larger strong coupling [108]. Even if the mediator decays back to SM quarks in such a configuration, the ISR particle can still be exploited to get sensitivity to lower $M_{Z'}$ regions than typical dijet searches [191]. It was noted in Chapter 4 that there is limited coverage of particle level measurements with large $E_{\mathrm{T}}^{\mathrm{miss}}$, CONTUR will mostly pick up resonant dijet signatures based on the available analysis coverage.

The parameter spaces considered will be scans in M_{DM} and $M_{Z'}$ at four points for the coupling values, $(g_q, g_{\mathrm{DM}}) = (0.25, 1.0), (0.375, 1.0), (0.5, 1.0), (0.375, 0.25)$. The first three coupling points represent a very coarse scan in g_q corresponding to weak, medium and strong coupling of the mediator to the SM respectively, and the additional point with $g_{\mathrm{DM}} = 0.25$ corresponds to a suppressed DM production scenario. The weak scenario, $g_q = 0.25$, is motivated as one of the benchmark points the experimental collaborations use to present the detector level searches for this model.

6.2.2. Theoretical considerations for consistent DM models

With the parameter space of the model defined, it is essentially a free choice of how much information one wants to include to further constrain the considered parameter space at this stage. The motivation for simplified models was to move away from the complications of constructing a UV complete model that can explain multiple observations. For example in this example of a DM production model one could require that the co-annihilation rate of DM to SM one calculates from the Feynman diagrams of the processes in $\psi\psi \rightarrow$SM gives a predicted relic density consistent with the $\sim 26\%$ observed in the ΛCDM model. Whilst the points in parameter space that give this are interesting to highlight, it would fold in a degree of dependence both on the assumed thermal history of the universe, and that the simplified model parametrizes the entire possible dark sector [192]. As such the approach taken is to not try to include other observations to inform the parameter space at this point, but rather to just define a model that will be self consistent for LHC physics at least up to the energies probed at the collider.

Firstly the width of the mediator is considered in the target parameter space. There isn't a well defined hard boundary on sensible values for this quantity but at very large values the interpretation of the Z' as a particle would be strained. Hence it is required that over the space considered the ratio of width to mass of the mediator, $\Gamma_{Z'}/M_{Z'} < 0.5$. The maximum values of this ratio occurring over the parameter spaces considered are shown in Table 6.1, where the widths are calculated using the values from Herwig. All of the points considered are safe from this condition so no modification to the parameter space is needed.

g_q	g_{DM}	$M_{Z'}$ [GeV]	M_{DM} [GeV]	$\Gamma_{Z'}/M_{Z'}$
0.25	1	3000	100	0.0626
0.375	1	3000	100	0.0751
0.5	1	3000	100	0.0925
0.375	0.25	3000	100	0.0257

Table 6.1.: Table of maximal $\Gamma_{Z'}/M_{Z'}$ occurring over the mass ranges for the four heatmaps shown in Figure 6.3.

Considerations on the perturbative unitarity of the processes the model introduces are also applied. In the scattering amplitudes relevant to LHC searches, the mediator production via the vector coupling will not violate unitarity unless the couplings are large [193], $g_q \gtrsim \mathcal{O}(4\pi)$. For the parameter spaces considered $g_q \leq 1$ so all spaces respect this requirement. There are complications arising from the axial DM coupling vertex. In the UV limit a partial wave

analysis of the annihilation process $\overline{\psi}\psi \to Z'Z'$ gives a unitarity limit of [194],

$$M_f \lesssim \sqrt{\frac{\pi}{2}} \frac{M_{Z'}}{g_f^A}, \tag{6.4}$$

where f denotes the fermion with an axial coupling, ψ in our case. This effectively defines a region where the DM relic density is calculable in the model, this requirement will be shown on the parameter space scans, but the CONTUR sampler will run into this region. Complete studies of the impact of the choices of chiral structure in the couplings as the theoretical consistency is dependent on these choices are available [194]. Further complexity arises for the axial couplings, an additional Higgs mechanism is needed to generate the dark sector masses as well as introducing new physics to restore unitarity in $\overline{\psi}\psi \to Z'Z'$ process. There will then be some mixing between the SM and dark sector Higgs which will lead to constraints from SM Higgs and precision EW measurements. Such considerations are left out of this work, introducing such a mechanism starts to move away from the key attraction of the simplified model approach.

6.2.3. Contur scans of a DM model

The procedure used to assess this model space with CONTUR follows that outlined in Chapter 5, Section 5.3. The model is coded in FEYNRULES and passed to HERWIG in a UFO format [133]. The model is simulated at LO in QCD for simplicity and all diagrams corresponding to any $2 \to 2$ process with any outgoing[1] BSM particle are simulated. The full particle level events are simulated in HERWIG 7.0.1 and Rivet 2.4.1 is used to analyse the events and form the histograms. The included analyses in the scan were listed in Chapter 5, Table 5.1 and the limits derived from the histograms were computed using an early alpha version of CONTUR.

Three example Rivet histogram outputs are shown from four of the sampled points in the model space in Figure 6.2. The model points sampled form a 1D scan in $M_{Z'}$, with $M_{\mathrm{DM}} = 600$ GeV, $g_q = 0.375$ and $g_{\mathrm{DM}} = 1$. The most sensitive measurement across most of the range considered is the ATLAS 7 TeV dijet [161] measurement. The histogram in Figure 6.2a shows the differential cross-section in bins of m_{jj} of the two leading jets in the event. Figure 6.2b shows the same signal histograms but this time they have been stacked on top of the observed data and the ratio to the observed data taken. This gives a sense of the relative size of the signal contribution against the grey error bars in the data, and this is essentially the information that is encoded in the statistical test. The bin giving the largest $\mathrm{CL_s}$ for each signal point is also

[1] Outgoing particles can also be unstable heavy particles, where HERWIG can handle their subsequent decay after the diagrams are constructed.

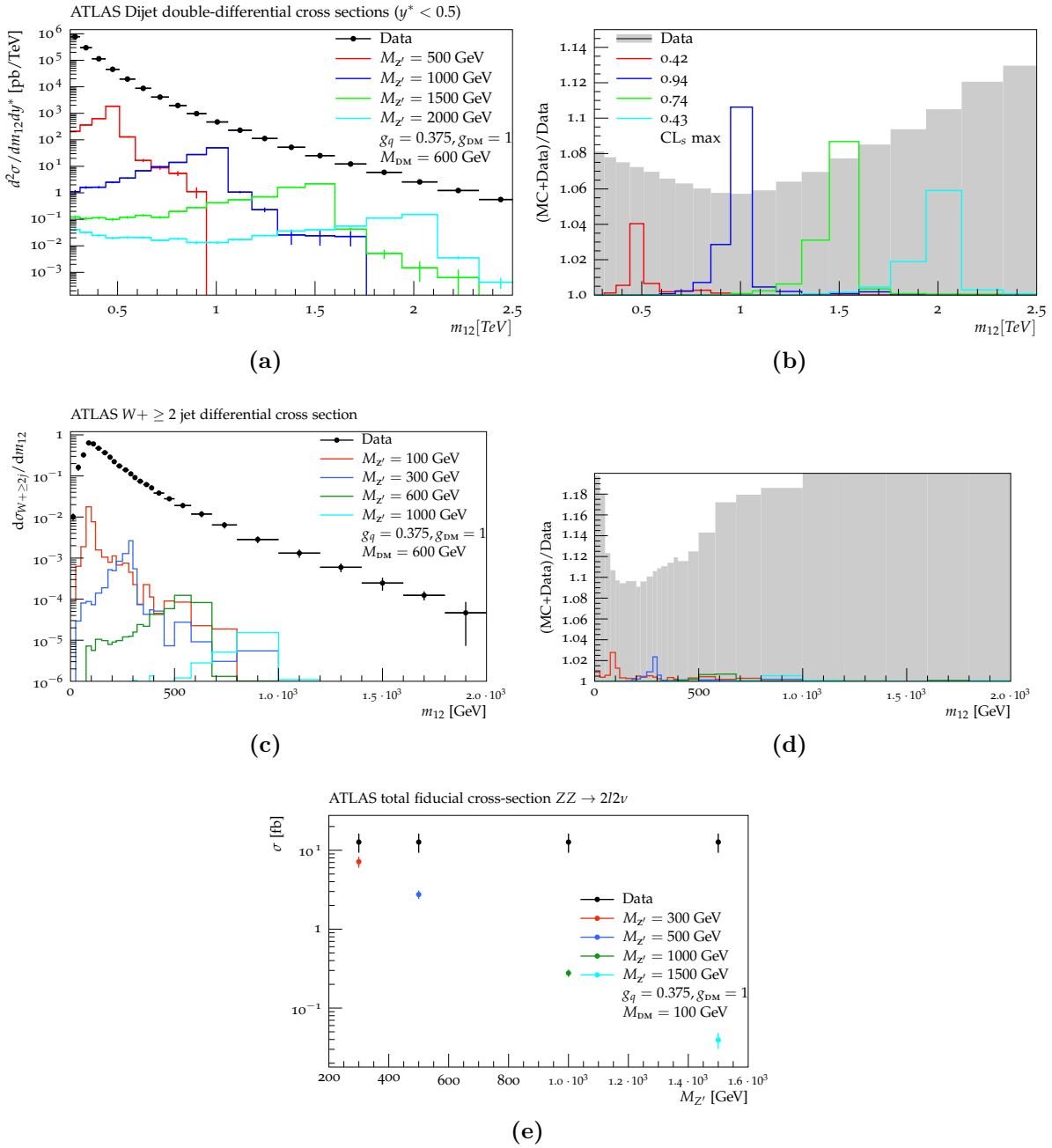

Figure 6.2.: Output from three example Rivet analysis routines included in the CONTUR process. Simulated signals of a simplified DM model are shown for four mediator mass working points. The signals form a 1D parameter space scan in mediator mass for fixed dark matter mass and mediator couplings; $M_{\mathrm{DM}} = 600$ GeV (100 GeV for the ZZ measurement), $g_q = 0.375$ and $g_{\mathrm{DM}} = 1$. All plots show a comparison of the observed cross-section to the model simulation, where the measurement is differential, the corresponding ratio of induced BSM perturbation to relative uncertainty in the measurement is shown. Figure 6.2a shows the ATLAS 7 TeV dijet [161] with the ratio shown in Figure 6.2b. Figure 6.2c shows the ATLAS 7 TeV W+jet [62] measurement with the corresponding ratio in Figure 6.2d. Figure 6.2e shows the ATLAS 7 TeV ZZ [170] measurement.

shown in the legend to the ratio, in this measurement resonant structures approximately equal to $M_{Z'}$ are being reconstructed which is why this measurement dominates the sensitivity.

A similar set of cross-section calculation and resultant ratio are shown in Figure 6.2c and Figure 6.2d respectively for an ATLAS 7 TeV W+jet [62] measurement. This is a measurement of a leptonically decaying W, so again the most sensitive histogram shown is when the W is produced in association with two jets, the differential cross-section in bins of m_{jj} is again the most sensitive. The cross-section for these processes is suppressed by the strength of the weak coupling compared to the strong coupling so these don't offer much sensitivity unless g_q is large. There is potential for coverage of a region of parameter space that the dijet measurements struggle with. Due to the lower trigger threshold for single leptons than all hadronic final states, the reach in mediator mass is potentially lower for these ISR type measurements.

In the 7 TeV analyses available and included in this scan there is only one fiducial measurement of $E_{\mathrm{T}}^{\mathrm{miss}}$ without a charged lepton in the final state. This is a single total cross-section measurement of the $ZZ \to 2l2\nu$ process. This is the only measurement that is sensitive to DM production in this dataset, so the same scan is shown with $M_{\mathrm{DM}} = 100$ GeV, so that DM production is no longer suppressed. The cross-section is shown for the four model points in Figure 6.2e. This is also effectively an ISR type measurement so the coverage of parameter space will be towards the lower $M_{Z'}$ range.

To form a parameter space scan then M_{DM} is sampled in steps of 100 GeV in the range $(100, 2000)$ and $M_{Z'}$ is sampled in steps of 100 GeV in the range $(100, 3000)$. The output set of Rivet histograms similar to those shown in Figure 6.2 are generated at each model point and the resulting $\mathrm{CL_s}$ is calculated following the methodology outlined in Chapter 5, Section 5.3. The resultant heatmap of the calculated $\mathrm{CL_s}$ at each sampled point in each of the four scenarios is shown in Figure 6.3. The sampled points are then interpolated to give a 95% confidence excluded contour in the parameter space plane. These are shown by the pink shaded areas in the contour plots for the four scenarios shown in Figure 6.4, where the bound on perturbative unitarity of the co-annihilation process is overlaid in blue.

In the weakly coupled mediator scenario shown in Figure 6.3a and Figure 6.4a, no exclusion at 95% confidence is observed across the entire space. However there is a visible right trapezoid shape of around 68% CL exclusion seen in the 1 TeV $< \mathrm{M_{Z'}} <$ 2 TeV range, this is primarily driven by the dijet measurement shown in Figure 6.2a and Figure 6.2b. As this measurement is from the 7 TeV dataset it is reasonable to expect that this analysis performed in the larger and higher energy 8 or 13 TeV datasets would indeed give an observed exclusion. Also there is no equivalent measurement of this same final state from the CMS collaboration available in Rivet, one of the potential nice features of Contur is that CMS and ATLAS data can be combined easily if available. It is expected this would also greatly increase the sensitivity across

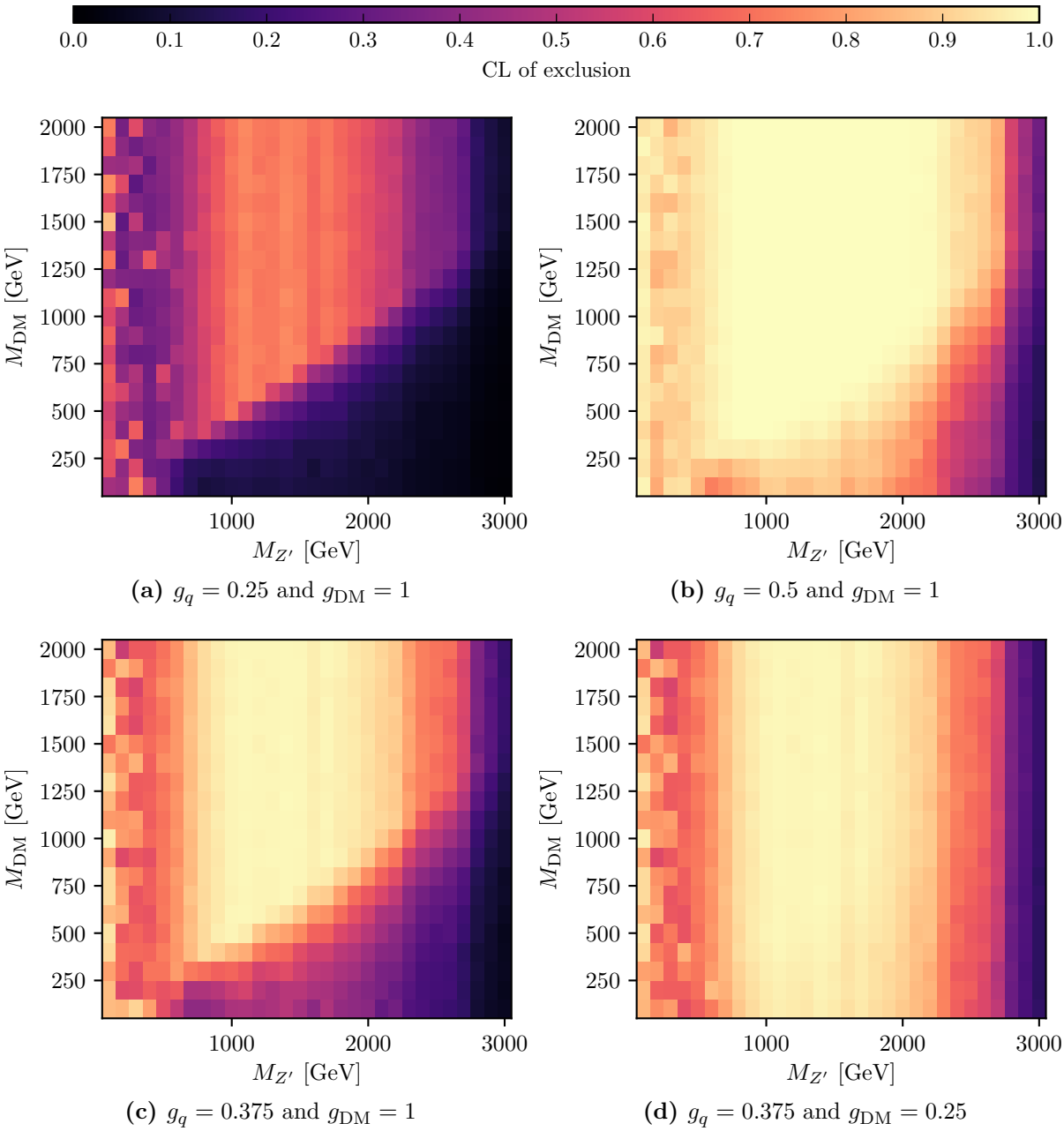

(a) $g_q = 0.25$ and $g_{\mathrm{DM}} = 1$

(b) $g_q = 0.5$ and $g_{\mathrm{DM}} = 1$

(c) $g_q = 0.375$ and $g_{\mathrm{DM}} = 1$

(d) $g_q = 0.375$ and $g_{\mathrm{DM}} = 0.25$

Figure 6.3.: Heatmaps displaying 2D parameter space scans in the planes of the mass parameters, $M_{Z'}$ and M_{DM}. The confidence level of exclusion represented corresponds to testing the full signal strength hypothesis against the background-only hypothesis. The combination of measurements entering into the confidence level presented here is the maximally sensitive allowed grouping.

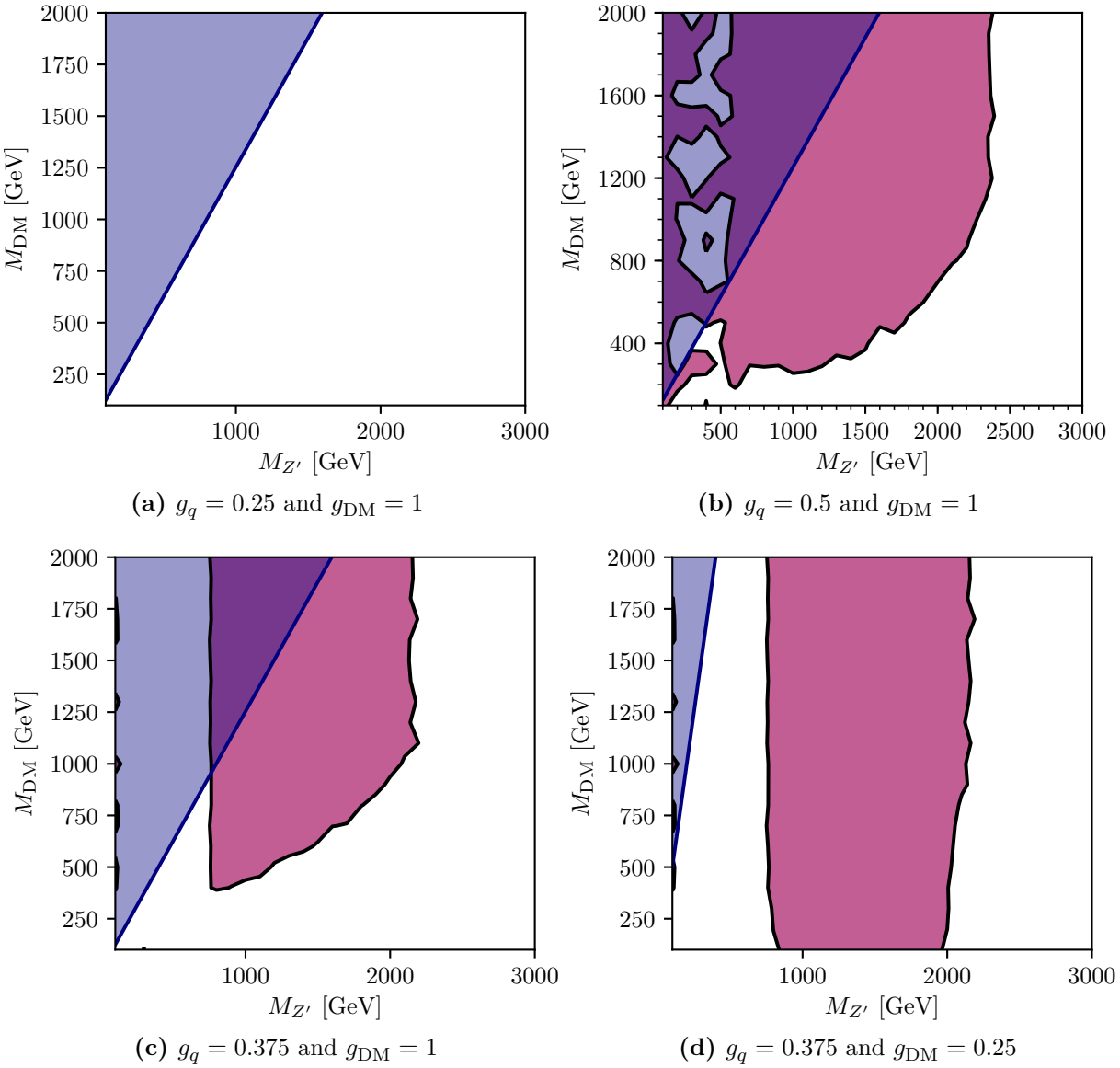

(a) $g_q = 0.25$ and $g_{\mathrm{DM}} = 1$

(b) $g_q = 0.5$ and $g_{\mathrm{DM}} = 1$

(c) $g_q = 0.375$ and $g_{\mathrm{DM}} = 1$

(d) $g_q = 0.375$ and $g_{\mathrm{DM}} = 0.25$

Figure 6.4.: Contours in the $M_{Z'}$ and M_{DM} plane for the considered values of g_{DM} and g_q, indicating the excluded region at 95% confidence level. The triangular shaded area is the region in which perturbative unitary is violated by the model.

the space. The diagonal boundary seen in the heatmap corresponds to the $2M_{\mathrm{DM}} = M_{Z'}$ limit, below this diagonal the DM production is no longer suppressed so is open as a decay channel for the mediator, as such the sensitivity drops off in this region due to lack of coverage for final states with large $E_{\mathrm{T}}^{\mathrm{miss}}$.

As the strength of the coupling is increased to the medium (in Figure 6.3c and Figure 6.4c) and strong (in Figure 6.3b and Figure 6.4b) mediator coupling scenarios, the same trends continue for both. The mediator production cross-section is increasing so the exclusion power grows correspondingly. The observed shape of 68% exclusion driven by the dijet mass measurement observed in the weakly coupled mediator case grows to represent a 95% CL excluded contour. Additional exclusion at low mediator masses starts to become more relevant, the ISR measurements shown in Figure 6.2e and Figure 6.2c for example start to contribute more. There are some statistical fluctuations seen in this region, in part due to MC statistics in signal generation and in part due to genuine statistical fluctuations in data, for the most part these are not important and not addressed in this study.

The final extra scenario considered is the suppressed DM production scenario, where g_{DM} is lowered below g_q. This is shown in Figure 6.3d and Figure 6.4d. The overall mediator production rate is the same as in the medium mediator couple scenario, $g_q = 0.375$, so much of the exclusion is the same and driven by similar contributions from the underlying histograms. However the reduced exclusion when the DM decay channel opens up noted when $2M_{\mathrm{DM}} < M_{Z'}$ no longer appears, even when the decay channel is open its coupling is smaller such that the rate of SM dijet production from mediator decays is not reduced much at all. This scenario demonstrates the ease with which one can explore the space with CONTUR which is a nice feature. This, combined with the fairly predictable behaviour seen by changing the g_q coupling strength, goes some way to motivate not attempting a more complicated 4D scan of this space. The couplings in general don't change the phenomenology a great deal and their impact could be roughly assessed just by scaling the cross-sections in the histogram calculations.

6.2.4. Comparison to existing phenomenology

The figures shown in Section 6.2.3 formed a proof of principle paper. To understand the merits of the approach, specifically in using unfolded data rather than detector level results, reinterpretations from the two different data sources have to be compared. One of the appeals of choosing this model as the original proof of principle is that the exact model that the experiment interprets its detector level searches in terms of can be recreated by setting the parameters appropriately. Firstly one of the key attractions of basing the method on Rivet is that this sits on an established pipeline of publishing results. With an updated version of Rivet typically comes a new set of plugins provided by the collaborations, continually improving the analysis

coverage of CONTUR with minimal effort internally required to implement these. As such the results are updated to a version of Rivet containing much more 8 TeV and 13 TeV data for the $g_q = 0.25$, $g_{\mathrm{DM}} = 1.0$ scenario [195]. A more up to date list of Rivet routines validated for use in CONTUR at the time of composing this document is given in Appendix A, Table A.1. These are shown for the original light quark flavour only model in Figure 6.5a for context, and for the universal all flavour coupling version of the model in Figure 6.5b. Updating the dataset has increased sensitivity markedly in Figure 6.5a with respect to Figure 6.4a, there is now 95% $\mathrm{CL_s}$ exclusion up to mediator masses of around 800 GeV, where previously there was none.

Figure 6.5b now represents exactly the same model that is used in ATLAS as a benchmark point, and for a dataset that is reflective of the analysis coverage available in Rivet at the time of composing this thesis. A summary of the status of the various direct searches for dark matter or dark sector mediator production from the ATLAS experiment is shown in Figure 6.6. In the CONTUR version of the figure, exclusion in mediator mass is noted for low DM masses up to around 2000 GeV, extending to around 2500 GeV for higher DM masses. In the ATLAS version exclusion in mediator mass for low DM masses is seen to around 2500 GeV, extending to 2900 GeV for higher DM masses. The results are competitive between the two benchmarks. The jump in upper reach in the mediator masses exclusion in CONTUR between Figure 6.5a and Figure 6.5b is primarily driven by the availability of particle level $t\bar{t}$ measurements from ATLAS and CMS at 8 TeV and 13 TeV available in Rivet [196, 197]. When all quark flavour couplings are allowed, and when $2M_t \geq M_{Z'}$, this decay mode becomes open and drives the CONTUR exclusion. There are no 13 TeV dijet particle level results included in these figures from either collaboration which accounts for some of the larger reach of the ATLAS detector level result, however such measurements have started to become available in Rivet. Additionally the ATLAS detector level results are generally still benefiting from the larger dataset available as these results are produced faster. The ATLAS dijet search that drives the upper limit on the mediator mass is made using the 13 TeV 37 fb^{-1} dataset, where detector corrected data is available at 13 TeV it is usually based on the smaller 3.2 fb^{-1} dataset. The searches still benefit from faster access to larger datasets. If the dijet search is removed from the ATLAS summary, the upper limit in mediator mass would then be driven by the $\bar{t}t$ search, and then the limits would be largely similar to the CONTUR result.

In summation, CONTUR can be used to produce competitive exclusions on benchmark models considered by ATLAS. The CONTUR reinterpretation is fast and can change the model configuration to any of the possible choices outlined in this section without any loss of information from the available datasets. There are still some gaps in experimental coverage between the measurement and search program but the resulting differences in exclusions are well understood and under control.

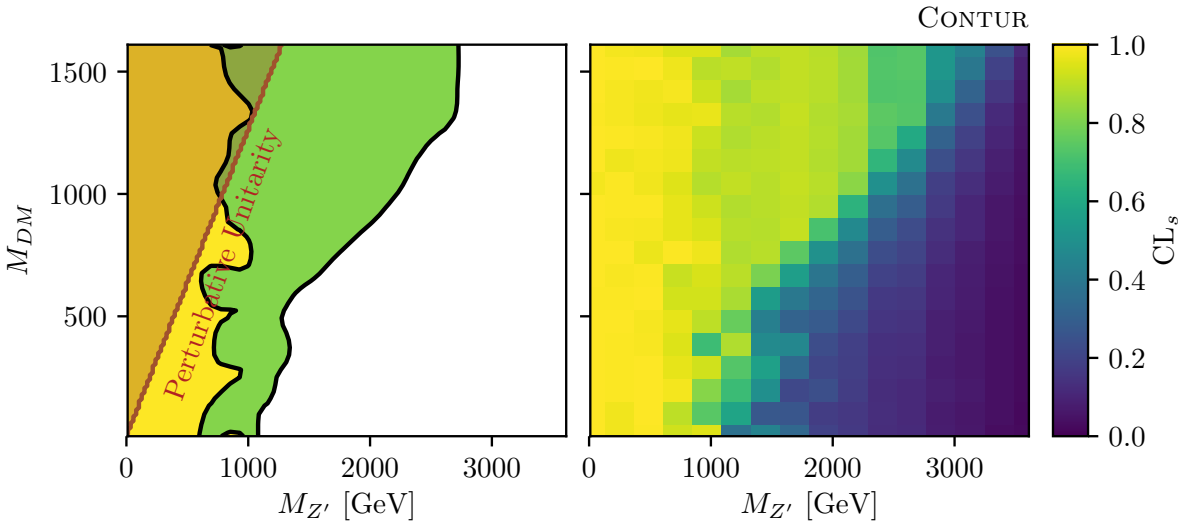

(a) Light quark flavours

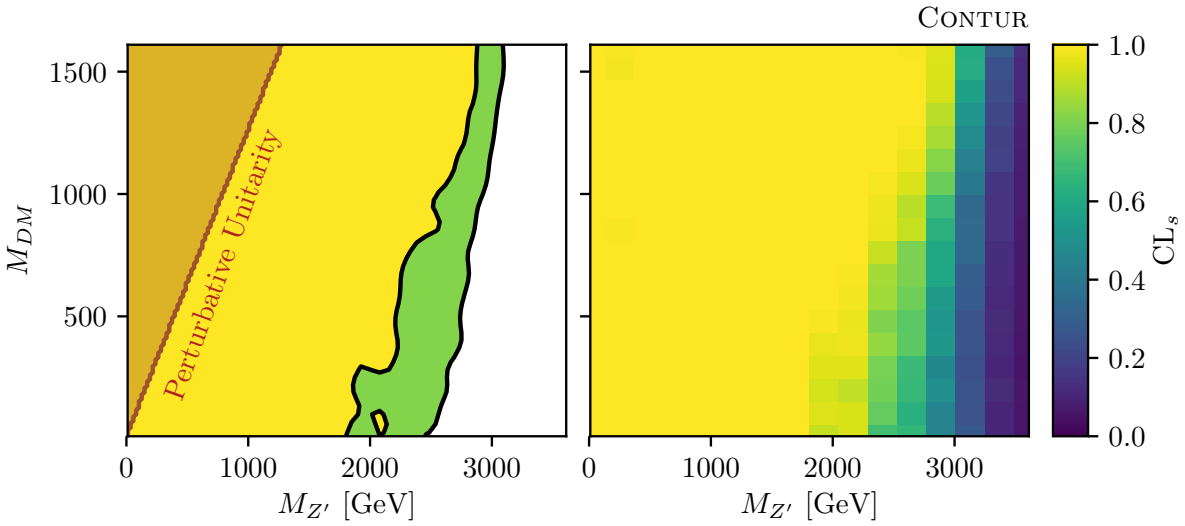

(b) Heavy quark flavours

Figure 6.5.: Updated contours in the $M_{Z'}$ and M_{DM} plane for $g_{\mathrm{DM}} = 1.0$ and $g_q = 0.25$. The left panel shows the 68% and 95% $\mathrm{CL_s}$ contours in green and yellow respectively. The triangular region where perturbative unitarity is violated is also indicated. The right panel shows a heatmap of the $\mathrm{CL_s}$ at the underlying sampled points. Figure 6.5a corresponds to the original light flavour only model and Figure 6.5b corresponds to a universal coupling to all quark flavours.

6.3. Gauged $B - L$ model and neutrino masses

A more recent study of CONTUR [176] is an application to a model that at its core has some similarities to the simplified DM model, but introduces a larger new BSM particle content and larger parameter space to survey. It was also a useful testing ground for developments made

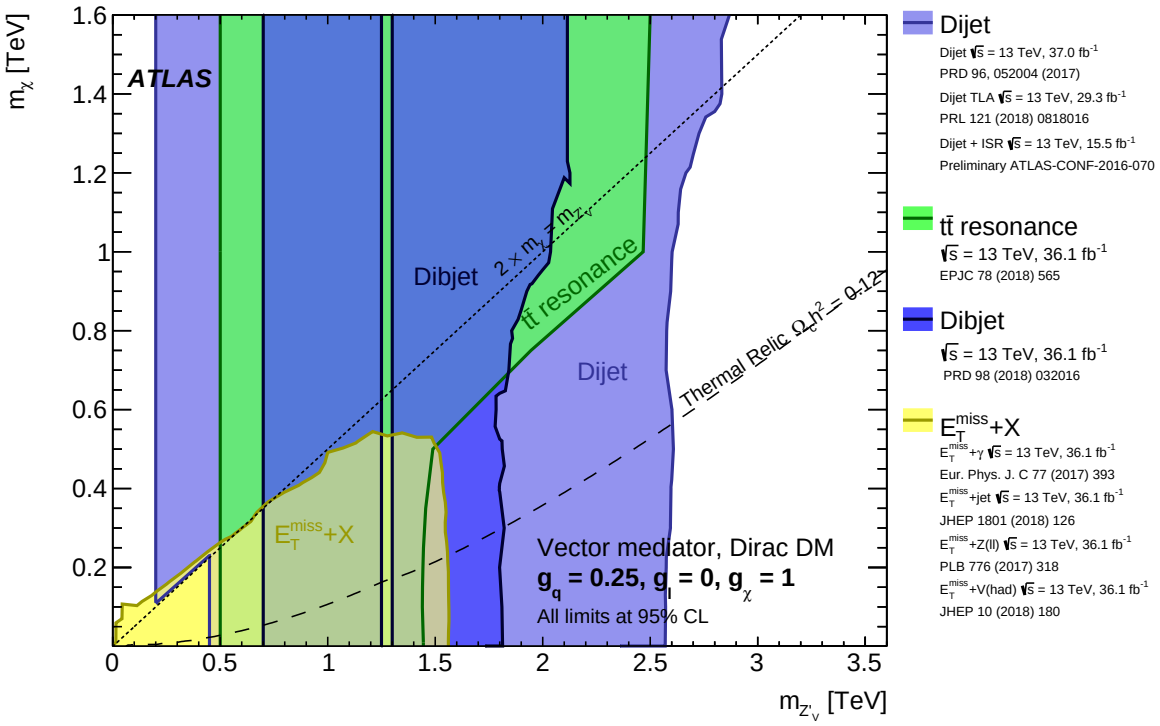

Figure 6.6.: Summary plot of ATLAS detector level searches interpreted in terms of a simplified dark matter model [198].

internally in CONTUR and represents the first study with a release candidate version of the package.

The SM exhibits a global $B - L$ (Baryon number minus Lepton number) symmetry. This symmetry is gauged via a $U(1)_{B-L}$ group, introducing an associated new gauge boson. At its core this would fall under a similar category to other U(1) symmetry group extensions as other Z' models, such as the DM model discussed in Section 6.2. In this version the $U(1)_{B-L}$ symmetry is spontaneously broken by an additional singlet Higgs. The model also introduces heavy neutrinos that are sterile (uncharged) under the SM to cancel anomalies which can in turn be implemented in a see-saw mechanism to generate the light SM neutrino masses. This variant of the model has been studied for its particular relevance as a potential source of long lived particle (LLP) type signatures [199]. Analyses looking for these signals are inherently detector level results as they look for events without a well defined fiducial particle level definition, as such these regions of the model highlighted as producing these types of final states will be avoided in this work. Classes of models involving gauging the $B - L$ symmetry are studied in lots of guises in the literature [200, 201] so there are well established LHC limits on variants of these models from detector level searches that the CONTUR particle level approach can be

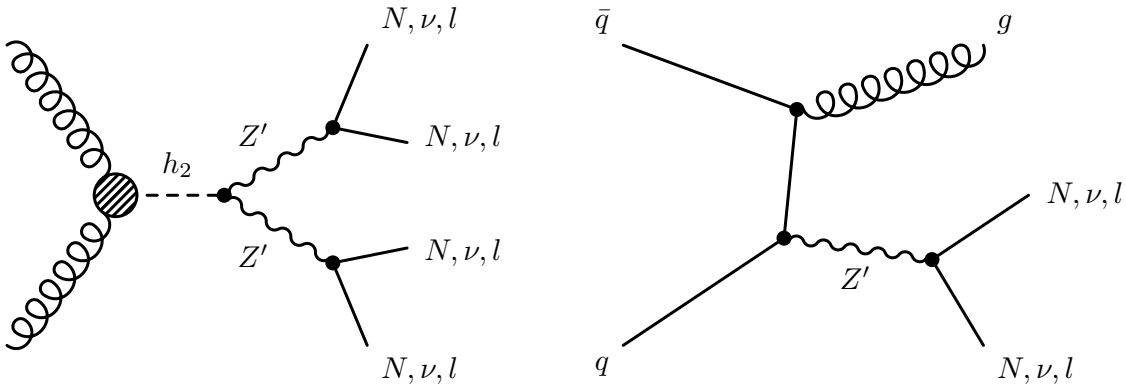

Figure 6.7.: Two example Feynman diagrams involving production of the heavy Z' mediator in the $B-L$ model. Stable final states can be composed entirely of SM particles or involve production of a heavy sterile neutrino, N.

compared to. Two example Feynman diagrams of signatures relevant for LHC phenomenology are shown in Figure 6.7.

6.3.1. Defining the LHC parameter space

The considered $B-L$ model introduces an Abelian gauge field B'_μ, a SM singlet scalar field χ, three right handed (RH) neutrinos N_i and an additional singlet χ which mixes with the SM Higgs doublet Φ. The scalar sector Lagrangian is extended from the SM case as,

$$\mathcal{L} \supset (D^\mu \Phi)^\dagger (D_\mu \Phi) + (D^\mu \chi)^\dagger D_\mu \chi - \mathcal{V}(\Phi, \chi)\,, \tag{6.5}$$

with the covariant derivative defined as in the SM but with an additional term, analogous to $U(1)_Y$, for fields charged under $B-L$ (Abelian mixing between $U(1)_Y$ and $U(1)_{B-L}$ is ignored in this analysis). The expanded scalar potential $\mathcal{V}(\Phi, \chi)$ takes the form,

$$\mathcal{V}(\Phi, \chi) = m^2 \Phi^\dagger \Phi + \mu^2 |\chi|^2 + \lambda_1 (\Phi^\dagger \Phi)^2 + \lambda_2 |\chi|^4 + \lambda_3 \Phi^\dagger \Phi |\chi|^2\,. \tag{6.6}$$

The Z' boson gauging $U(1)_{B-L}$ arises in a similar construction to in the SM, with an associated gauge coupling strength g'_1 and gains its mass $M_{Z'}$ in a way analogously to the EW Spontaneous Symmetry Breaking (SSB) as outlined in Chapter 2, Section 2.1.2. The SM fermionic fields for quarks and leptons have charges under the $U(1)_{B-L}$ of $Y_{B-L} = +1/3$ and -1 respectively, with all other SM fields uncharged. The new singlet scalar and the RH neutrinos have $Y_{B-L} = +2$

and -1 respectively. The RH neutrinos interact with the SM fields via Yukawa terms as,

$$\mathcal{L} \supset -y^{\nu}_{ij}\overline{L_i}\nu_{Rj}\tilde{\Phi} - y^{M}_{ij}\overline{\nu^{c}_{Ri}}\nu_{Rj}\chi + \text{h.c.}\,, \tag{6.7}$$

where y^{ν}_{ij} and y^{M}_{ij} are general Yukawa 3×3 matrices. Again analogously to the SM the RH neutrinos gain a mass by introducing a vev for the χ potential, x, giving RH neutrino masses of the form $M_R = \sqrt{2}y^{M}x$. Breaking the EW symmetry as before gives Dirac mass mixing terms between the light and RH neutrinos as $m_D = y^{\nu}v/\sqrt{2}$. This gives a mass matrix in the (ν_L, ν^{c}_{R}) basis of,

$$\mathcal{M} = \begin{pmatrix} 0 & m_D \\ m_D & M_R \end{pmatrix}, \tag{6.8}$$

which in the see-saw limit of $M_R \gg m_D$, gives light and heavy neutrino masses of $m_\nu \sim -m_D M_R^{-1} m_D^T$ and $M_N \sim M_R$ respectively. The rotation from flavour to mass eigenstates is then,

$$\begin{pmatrix} \nu_L \\ \nu_R \end{pmatrix} = \begin{pmatrix} V_{LL} & V_{LR} \\ V_{RL} & V_{RR} \end{pmatrix} \begin{pmatrix} \nu \\ N \end{pmatrix}, \tag{6.9}$$

where the elements of this are also 3×3 matrices, with V_{LL} being the SM PMNS matrix. For simplicity, the mixing between flavours is neglected in this study so the generations decouple. This corresponds to a diagonal Yukawa coupling matrix $y^{\nu}_{ii} = \sqrt{2}M_{N_i}V_{iN}/v$ with $i = e, \mu, \tau$ and using the neutrino see-saw relation. Where V_{iN} is the active-sterile neutrino mixing, for the purposes of this analysis this will be set to be small.

Expansion of the scalar potential Lagrangian from equation (6.5) will also give a Higgs mass matrix, which can be diagonalised to give two Higgs mass states, (h_1, h_2). Convention is to take the lightest mass eigenstate as h_1 and identify this as having the observed properties of the SM Higgs. These mass eigenstates relative to the gauge states (Φ, χ) via an additional mixing,

$$\begin{pmatrix} h_1 \\ h_2 \end{pmatrix} = \begin{pmatrix} \cos\alpha & -\sin\alpha \\ \sin\alpha & \cos\alpha \end{pmatrix} \begin{pmatrix} \Phi \\ \chi \end{pmatrix}. \tag{6.10}$$

This angle of mixing in the scalar sector, α, can be written in terms of the values of the potential and symmetry breaking scales as,

$$\tan(2\alpha) = \frac{\lambda_3 v x}{\lambda_2 x^2 - \lambda_1 v^2}. \tag{6.11}$$

This model then has three main components; a vector boson sector (governed by $M_{Z'}$ and g'_1), a scalar sector (governed by M_{h_2} and $\sin\alpha$) and a sterile neutrino sector (governed by M_{Ni}

and V_{iN}). There is additional scope to expand this model by considering the $Z - Z'$ mixing and flavour mixing in the neutrino sector. By taking appropriate limits one or two of these sectors can be decoupled leaving a simpler model that has well established phenomenology. For example by turning off the Higgs and sterile-active neutrino mixing one is left with a simplified Z' model, similar to the DM case in Section 6.2. The appeal of taking this model for study in CONTUR is that by keeping two or even all three of the sectors relevant for the phenomenology, a *next to simplified* model that often has less well clearly established phenomenology is considered.

Five scenarios are considered as a part of this study. In all five cases the sterile neutrino sector is set consistently. The active-sterile mixing is motivated by the Type-I see-saw outlined so is set as $V_{iN} = \sqrt{\frac{m_\nu}{M_{Ni}}}$ where $m_\nu = 0.1$ eV is the mass scale of light neutrinos. Consequently $M_{Ni} = M_{Z'}/5$ is chosen for the RH neutrino masses, across the considered parameter space this gives mixing consistent with observed upper bounds [202]. Scenarios A, B and C target the vector boson sector so are formed as scans of the $M_{Z'} - g_1'$ plane. Scenario A turns off the effects of Higgs mixing by setting $\sin\alpha = 0$, the heavy Higgs mass is set consistently to $M_{h_2} = M_{Z'}/(2g_1')$. Scenario B sets the heavy Higgs mass the same as A, but now admits a Higgs mixing of $\sin\alpha = 0.2$. Finally scenario C studies the effect of both mixing by keeping the mixing as in B, and setting the heavy Higgs mass constant across the plane $M_{h_2} = 200$ GeV. Scenario D and E target the scalar sector so are formed as scans of the $\sin\alpha - M_{h_2}$ plane. The choices of the vector parameters are fixed somewhat by requiring that the $B - L$ breaking scale is sufficiently large, $x \equiv M_{Z'}/(2g_1') \geq 3.45$ TeV. Scenario D takes a stronger coupling $g_1' = 0.2$ and a heavy Z', $M_{Z'} = 7$ TeV. Scenario E takes a light Z', $M_{Z'} = 35$ GeV, and a small coupling $g_1' = 10^{-3}$. The choices of all parameter spaces are summarized in Table 6.2

Scenario	$M_{Z'}$ [GeV]	g_1'	M_{h_2} [GeV]	$\sin\alpha$	M_{N_i} [GeV]
A	$[1, 10^4]$	$[3\times10^{-5}, 0.6]$	$M_{Z'}/(2g_1')$	0	$M_{Z'}/5$
B	$[1, 10^4]$	$[3\times10^{-5}, 0.6]$	$M_{Z'}/(2g_1')$	0.2	$M_{Z'}/5$
C	$[1, 10^4]$	$[3\times10^{-5}, 0.6]$	200 GeV	0.2	$M_{Z'}/5$
D	7000	0.2	[0, 800] GeV	[0, 0.7]	$M_{Z'}/5$
E	35	10^{-3}	[0, 800] GeV	[0, 0.7]	$M_{Z'}/5$

Table 6.2.: Benchmark scenarios used in this analysis. In addition, the active-sterile neutrino mixing is fixed as $V_{iN} = \sqrt{0.1 \text{ eV}/M_{Ni}}$, independent of the generation of the heavy neutrino.

6.3.2. Theoretical considerations for an LHC gauged $B-L$ model

Following similar ideas to the DM simplified model requirements of theoretical consistency, at least to a scale larger than that probed by the LHC, are considered. Firstly it is required that the vacuum is stable, this puts bounds on the parameters in the scalar potential given in equation (6.5) [203],

$$4\lambda_1\lambda_2 - {\lambda_3}^2 > 0, \quad \lambda_1 > 0, \quad \lambda_2 > 0\,. \tag{6.12}$$

Additionally perturbativity requires the couplings in the model to be small enough such that loop corrections remain bounded. So upper limits on these parameters are chosen conservatively to be $\left|\lambda_{1,2,3}\right| < 1$. Similarly the gauge and fermion Yukawa couplings are also kept pertubative by requiring $g_1' < 1$, $M_{Ni}/x < 1$. By taking all the points considered in Table 6.2 at the EW scale and evolving them to some higher scale, Q_{Max}, using the RGE equations for the model, one can assess the scale to which perturbative unitarity holds in the model. If it is assumed that this gauged $B-L$ extension is the only new physics above the SM, then one would require the model to remain perturbative up to the Planck scale. This would represent a strong theory bias, so for the purposes of this study the region where the model is perturbative up to a scale of 10 TeV is indicated for the results shown in Section 6.3.3. This is deemed as highlighting the area in parameter space that is safe for LHC probed scattering amplitudes. The RGEs for the $\mathrm{SU}(3)_C \times \mathrm{SU}(2)_L \times \mathrm{U}(1)_Y \times U(1)_{B-L}$ are used [203] to determine the highest allowed Q_{Max}, this is shown for the planes considered in scenario B and D in Figure 6.8

Mixing in the scalar potential also opens up the possibility that precision EW observables are modified by the model. The most stringent constraint will come from precise measurement of the W boson mass. The corrections to this arise from Higgs loops in the W propagator and can be derived as a function of the scalar sector parameters $\sin\alpha$ and M_{h_2} [204]. Where relevant this will also be shown as a constraint overlaid in parameter space by requiring that the corrections leave the calculated m_W within 2σ of its experimental value [205]. This constraint is also additionally overlaid for the two scenarios in Figure 6.8.

There is some concern that production of the heavy RH neutrinos will give misleading signatures when simulated at particle level. Depending on their lifetime they will range from decaying fast enough to appear as a prompt decay in the detector to being stable enough to escape the detector and being seen as $E_{\text{T}}^{\text{miss}}$ in an LHC analysis. A particularly tricky point is when the RH neutrino lifetime is in some intermediate value, so decays at some point in the detector. Dedicated searches of such LLP signatures have been performed for this model [199]. By tracking both the lifetime, $c\tau$, of the RH neutrino and the total inclusive cross-section for its

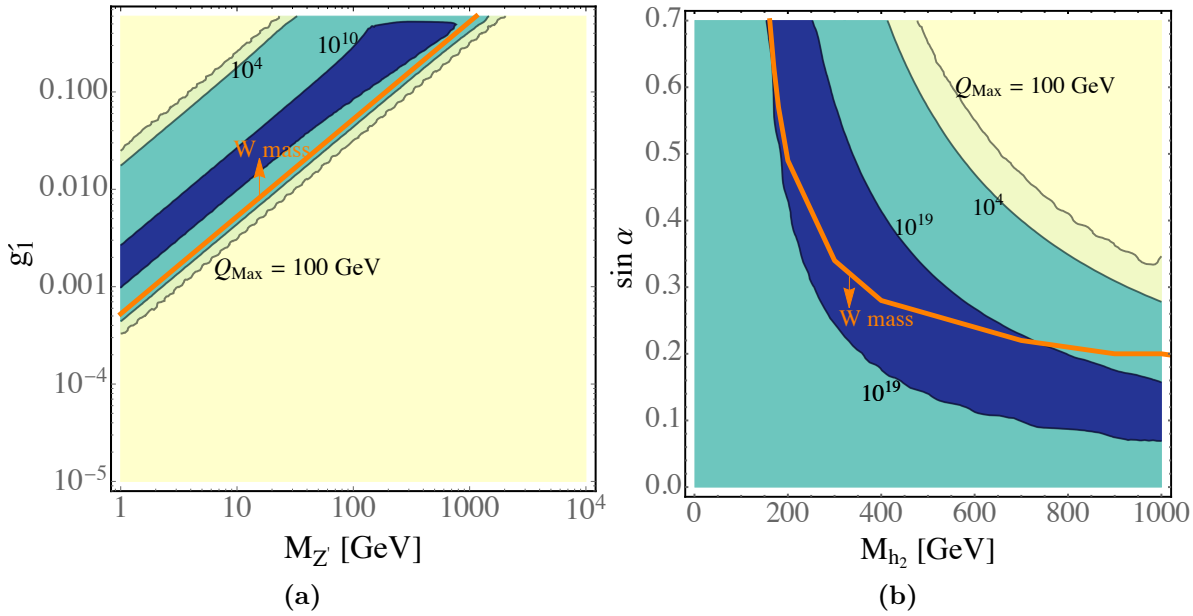

Figure 6.8.: Maximal perturbative scale Q_{Max} in GeV and constraint from electroweak W mass corrections as a function of (a) g_1' and $M_{Z'}$ with $M_{h_2} = M_{Z'}/(2g_1')$ and $\sin\alpha = 0.2$ (Scenario B) and (b) M_{h_2} and $\sin\alpha$ with $M_{Z'} = 7$ TeV and $g_1' = 0.2$ (Scenario D). The W mass constraint is satisfied above (below) the depicted contour in panel a (b), as indicated by the arrows.

production across the parameter space in scenario B, shown in Figure 6.9, it can be motivated that the analysis here will be safe from these concerns. The cross-section is either small enough that an appreciable amount of RH neutrinos are not produced, or are either in the range of being a prompt decay or stable. Where the cross-section is large and the RH neutrinos are LLPs, all of the other cross-sections are also large, and no signatures from these particles drive any exclusion calculated in Contur. As such the RH neutrinos are set to be artificially stable in this analysis.

6.3.3. Contur scans of the gauged $B - L$ model

The scan of the five scenarios using Contur is performed in a similar manner to the DM model. The χ^2_μ statistic defined in Chapter 5 is used and a CL on μ is presented using CL_s. In general the simplifying $\vec{n} = \vec{b}$ model is used[2], with an uncorrelated set of counting tests being included into the likelihood calculation as described previously. The model was encoded as a UFO library, which was uploaded to the FeynRules model database as a result of this work.

[2] This analysis included data from a fiducial ratio measurement [107], which provided the necessary background model for this measurement.

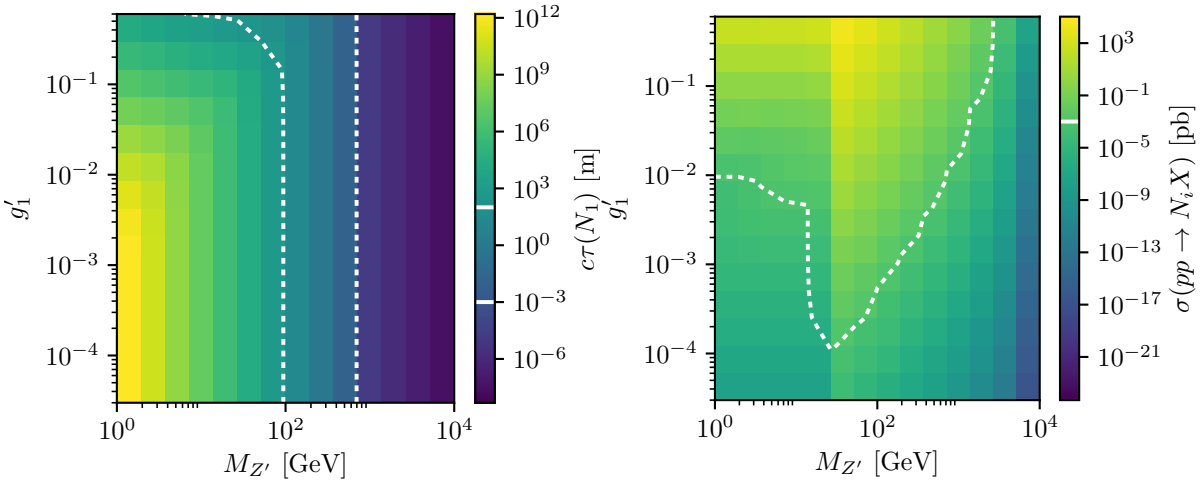

Figure 6.9.: (a) The proper decay length of the heavy RH neutrino for Case B. The dashed lines indicate the boundaries of region between 100 m $> c\tau >$ 1 mm within which the neutrino would manifest a "long-lived particle" signal. (b) the total production cross-section for the RH neutrino in Case B, for 8 TeV pp collisions. The dashed line indicates the 1 fb contour, corresponding to roughly 30 events before any cuts, for the maximum luminosity considered here.

The processes were generated in a release candidate version of Herwig 7.1.5 and analysed using the available Rivet routines in Rivet 2.6.1 that were validated for use in Contur. This includes many more 8 and 13 TeV analyses than original available for the study shown in Section 6.2. In Appendix A, Table A.1, the full available set of Rivet analyses for inclusion in Contur included is listed. The theoretical constraints described in Section 6.3.2 are overlaid in all scenarios.

The scans for scenarios A, B and C are shown in Figure 6.10. In all three of these scenarios an additional experimental constraint arising from electron-neutrino scattering will be relevant so is derived and overlaid on these parameter scans [206]. This constraint arises since electron-SM neutrino scattering can proceed via a Z' mediator in the model, so is essentially constant in the $M_{Z'} - g'_1$ plane and largely independent of the other parameters of the model. Scenario A, Figure 6.10a, represents a simple case where the Higgs mixing is turned off and the heavy Higgs state is kinematically unavailable. As such this scenario A resembles closely cases discussed in the literature [201, 207]. Additional experimental constraints arising from LHCb dark photon searches [208] are included using the Darkcast program [201], as well as constraints from the ATLAS search using lepton pairs [209]. This ATLAS search displays the complementary between detector level search and particle level measurement, but is performed with a 13 TeV dataset whereas the measurement result in this region is driven by an 8 TeV result. The majority of the Contur exclusion is driven by various analyses sensitive to the leptonic decays of Z'. The

ATLAS 7 and 8 TeV Drell-Yan measurements [210–212] have a big impact for 12 GeV $< M_{Z'} <$ 1500 GeV, with the WWW cross-section [213] also having an impact at the highest $M_{Z'}$. For the most part the excluded region is covered by existing experimental constraints, however there is a window around $70 < M_{Z'} < 150$ GeV where the CONTUR exclusion is unique. This demonstrates some of the power of using the precision measurements, searches optimized with cuts may be cutting out regions of phase space that are important to exclude certain models.

Scenario B, shown in Figure 6.10b is similar to scenario A but now has a non zero Higgs mixing. This can modify the production and decay of the Z', so without specific reinterpretation the limits previously overlaid sensitive to the Z' cannot be trivially overlaid. The electron-neutrino scattering constraint still applies as this isn't sensitive to the Z' dynamics. The theoretical constraints now start to play a larger role too, and between the combined theory constrains and the electron-neutrino scattering only a small sliver of parameter space is uncovered. However this band is excluded with 95% confidence by the LHC measurements in CONTUR.

Scenario C, shown in Figure 6.10c is similar to B but now fixes the heavy Higgs mass to $M_{h_2} = 200$ GeV. This opens up direct production of the heavy Higgs via gluon fusion which is now constant across the plane. The heatmap now shows a residual $\sim$60% confidence exclusion across the previously totally unconstrained region. This is a result of the h_2 production followed by the dominant $h_2 \to WW$ decay, which contributes in the phase space of the ATLAS $l\nu$-jet-jet measurement [213]. Otherwise the CONTUR excluded region is similar to scenario B, and whilst the electron-neutrino experimental constraint remains the same, the theoretically excluded region has decreased appreciably with respect to scenario B. This leaves a much larger region that is constrained by CONTUR, but otherwise unconstrained. The composition of the excluded CONTUR in scenario C is broken down into its contributing component CONTUR analysis pools in Figure 6.11. The particle level final state each pool is sensitive to is noted in the bottom right of each figure. Each figure represents a component included in the product of counting tests in the likelihood, and the total observed contour in Figure 6.10c is retried by taking this product. This illustrates the increasing depth of analysis coverage, the full exclusion contour is built from a patchwork of different final states and analyses across a parameter space.

This decomposition of the likelihood can be further illustrated by looking at the underlying histograms which the likelihood is built from. Figure 6.11e is the contour built from ATLAS 8 TeV $pp \to l^+l^-(j)$ measurements. Two histograms contributing to this contour are shown in Figure 6.12a, a dimuon mass measurement [211] and Figure 6.12c showing a dijet mass measurement in leptonically decaying Z events [119]. Four parameter space points are chosen and shown in comparison to the observed data, with the choice of $M_{Z'}$ and g'_1 for each point written in the legend. The same four points are also shown against an ATLAS 7 TeV $pp \to llll$ measurement [170] in Figure 6.12b, which contribute to building the contour shown

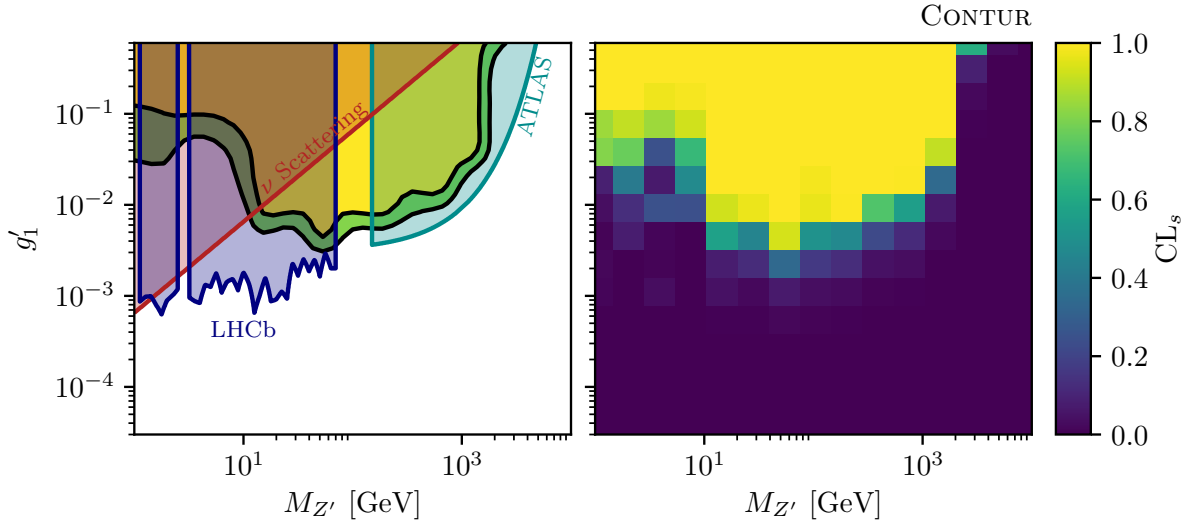
CONTUR
g'_1
10^{-1}
10^{-2}
10^{-3}
10^{-4}
ν Scattering
ATLAS
LHCb
10^1
10^3
$M_{Z'}$ [GeV]
$M_{Z'}$ [GeV]
1.0
0.8
0.6
0.4
0.2
0.0
CL_s

(a)

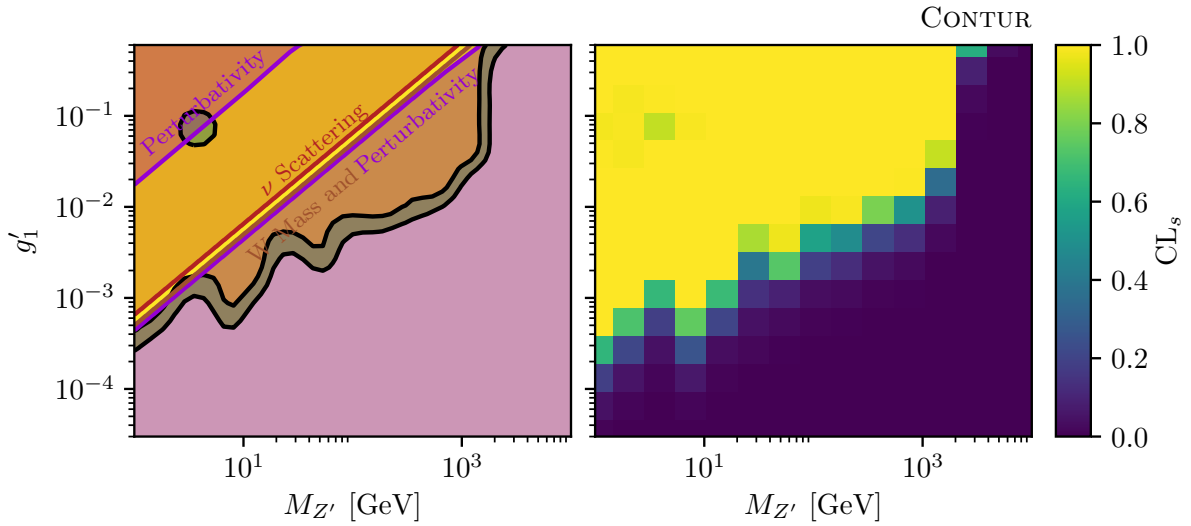
CONTUR
g'_1
10^{-1}
10^{-2}
10^{-3}
10^{-4}
Perturbativity
ν Scattering
m_H mass and Perturbativity
10^1
10^3
$M_{Z'}$ [GeV]
$M_{Z'}$ [GeV]
1.0
0.8
0.6
0.4
0.2
0.0
CL_s

(b)

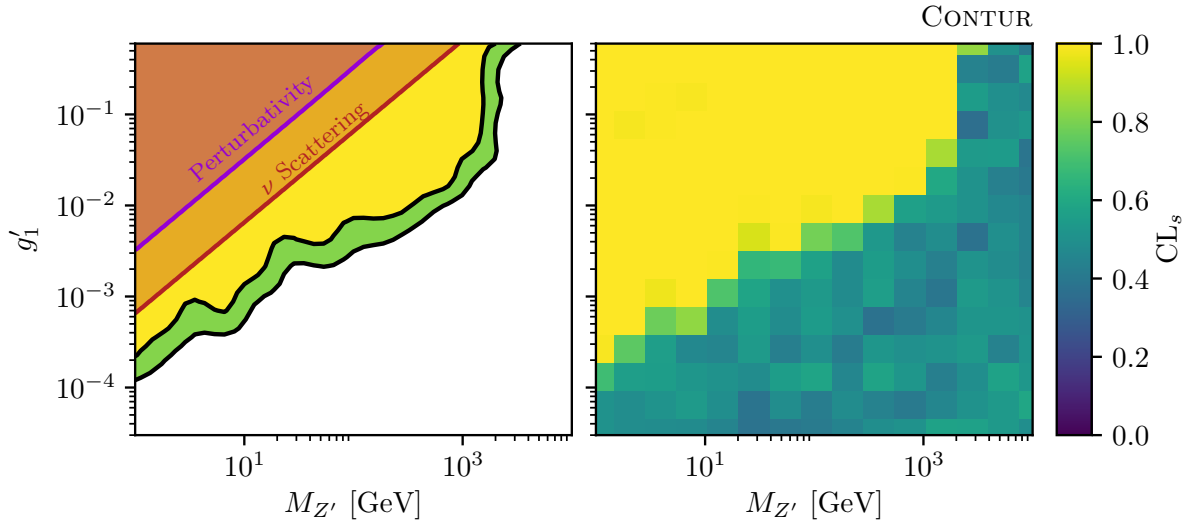

(c)

Figure 6.10.: Sensitivity of LHC measurements to the BSM contribution from a gauged B-L model in the $M_{Z'}$ vs g_1' plane. Figure 6.10a shows scenario A, $\sin\alpha = 0$, $M_{h_2} = \frac{M_{Z'}}{2g_1'}$; Left, 95% (yellow) and 68% (green) excluded contours. Right, underlying heatmap of exclusion at each scanned parameter space point. The 95% CL limits from the ATLAS search using lepton pairs [209], from electron-neutrino scattering, from the Darkcast reinterpretation [201] of the LHCb dark photon search [208] and the vacuum stability and perturbativity constraints up to a scale of at least 10 TeV are also indicated. Figure 6.10b shows scenario B, $\sin\alpha = 0.2, M_{h_2} = \frac{M_{Z'}}{2g_1'}$; as in Figure 6.10a but for scenario B, with additional theory bounds and constraints from M_W and electron-neutrino scattering shown. Figure 6.10c shows scenario C, $\sin\alpha = 0.2, M_{h_2} = 200$ GeV; as in Figure 6.10b but for scenario C.

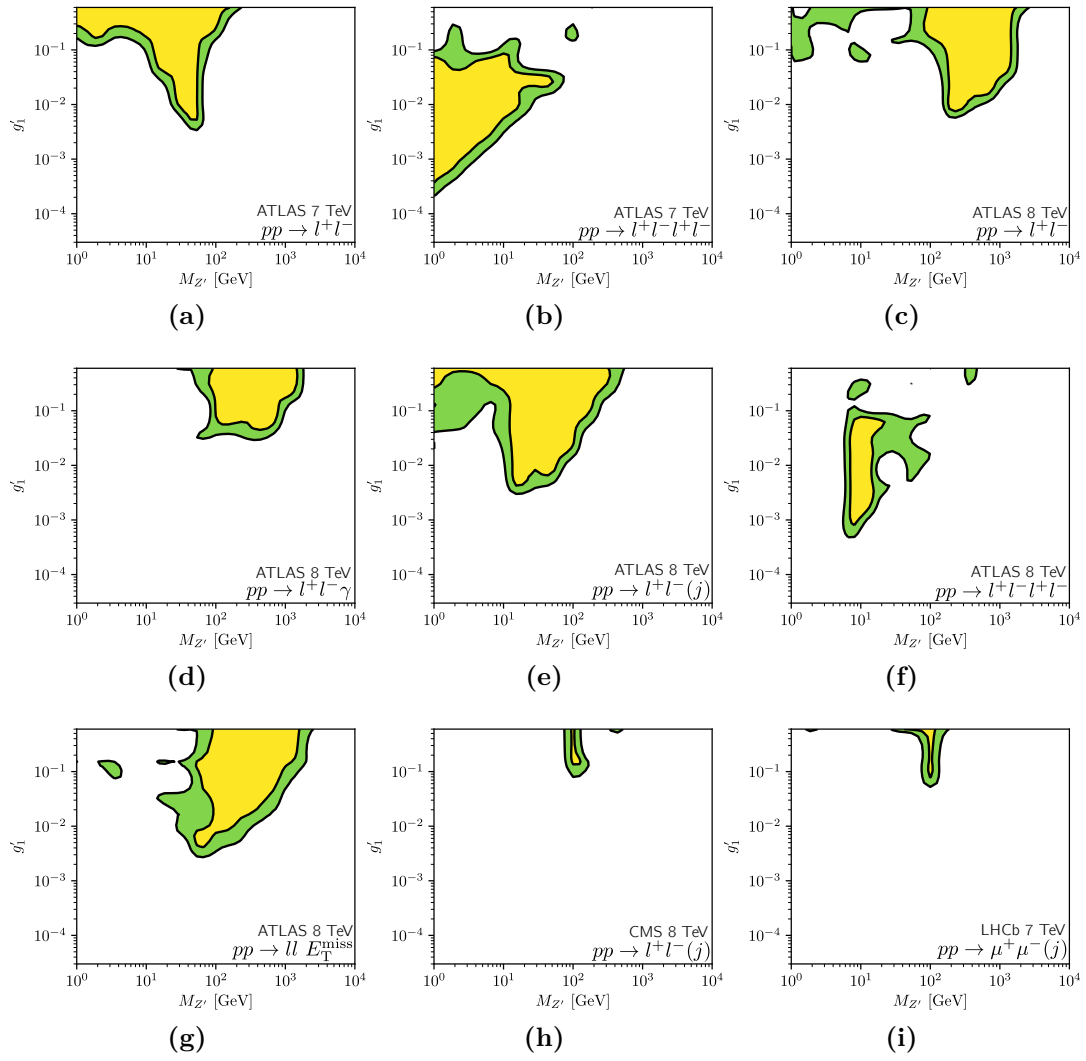

Figure 6.11.: Disfavoured regions for different, independent measurement classes for scenario C. Figure 6.11a ATLAS 7 TeV Low mass Drell-Yan measurement [210], Figure 6.11b ATLAS 7 TeV Four-lepton measurements [170], Figure 6.11c ATLAS 8 TeV High mass Drell-Yan measurement [212], Figure 6.11d ATLAS 8 TeV dilepton plus photon measurements [214], Figure 6.11e ATLAS 8 TeV Dilepton plus jet measurements [119, 211, 215], Figure 6.11f ATLAS 8 TeV Four-lepton measurements [216, 217], Figure 6.11g ATLAS 8 TeV Dilepton plus missing transverse energy measurements [213, 218], Figure 6.11h CMS 8 TeV dilepton plus jet measurements [219], Figure 6.11i LHCb 7 TeV dimuon plus jet measurement [220].

in Figure 6.11b. The four parameter points shown are also complemented by the information shown in Table 6.3. This table shows the key process production cross-section and decay branching ratios as calculated by HERWIG for each of the four points. Points in parameter space create events that contribute to signals seen in multiple analyses and multiple orthogonal analysis pools. CONTUR can capture a variety of physics with its ever increasing array of experimental analyses, this is increasingly important for such next to simplified models which can have very varied signatures across their parameter space.

$M_{Z'}$ (GeV)	g'_1	Production Process	Cross Section (σ, pb)	Decay	Branching Fraction
1	0.0005	$gg \to Z'Z'$	0.6	$Z' \to l^+l^-$	0.36
		$gg \to gh_2$	0.078	$h_2 \to Z'Z'$	0.58
14	0.009	$u\bar{u} \to gZ'$	40.6	$Z' \to l^+l^-$	0.27
100	0.07	$u\bar{u} \to Z' \to l^+l^-$	31	$Z' \to l^+l^-$	0.27
370	0.6	$u\bar{u} \to Z' \to l^+l^-$	30	$Z' \to l^+l^-$	0.27

Table 6.3.: Cross sections (in 8 TeV pp collisions) and branching fractions for the main processes contributing to Figure 6.12.

Scenarios D and E were motivated to study the scalar sector, are shown in Figure 6.13a and Figure 6.13b respectively. Some of the same theory constraints apply to these scenarios, mainly considerations of perturbativity and the W mass. There could potentially be upper limits on the allowed M_{h_2}, however these are generally less constraining than the W mass so are omitted [221]. There are also indirect constraints valid for all $M_{h_2} > M_{h_1}$, from considerations of perturbations induced to the SM Higgs decay measurements [200, 222]. These constrain the Higgs mixing angle to $\sin^2\alpha \lesssim 0.31$, but aren't shown in this study. Most of the range will avoid these constraints, but inclusion of SM Higgs constraints directly into CONTUR via the simplified template cross-section measurements [223] is an area of interest. The heatmaps for both of these scenarios end up excluding a similar region using CONTUR. This is primarily driven by h_2 production and decay into either heavy vector bosons or top pairs. The main difference between D and E is that in scenario E, the Z' is sufficiently light that Z' Z' is an allowed decay channel of h_2. The W mass theoretical constraint covers a lot of the considered region in both scenarios, but there is a region around $M_{h_2} = 200$ GeV in both scenarios where CONTUR excludes a previously allowed region. An interesting feature of the CONTUR analysis of these regions is that there is a large band of 68% CL exclusion around the 95% CL excluded region. This indicates there is good potential for larger dataset and higher $\sqrt{s}$ analyses to exclude these regions.

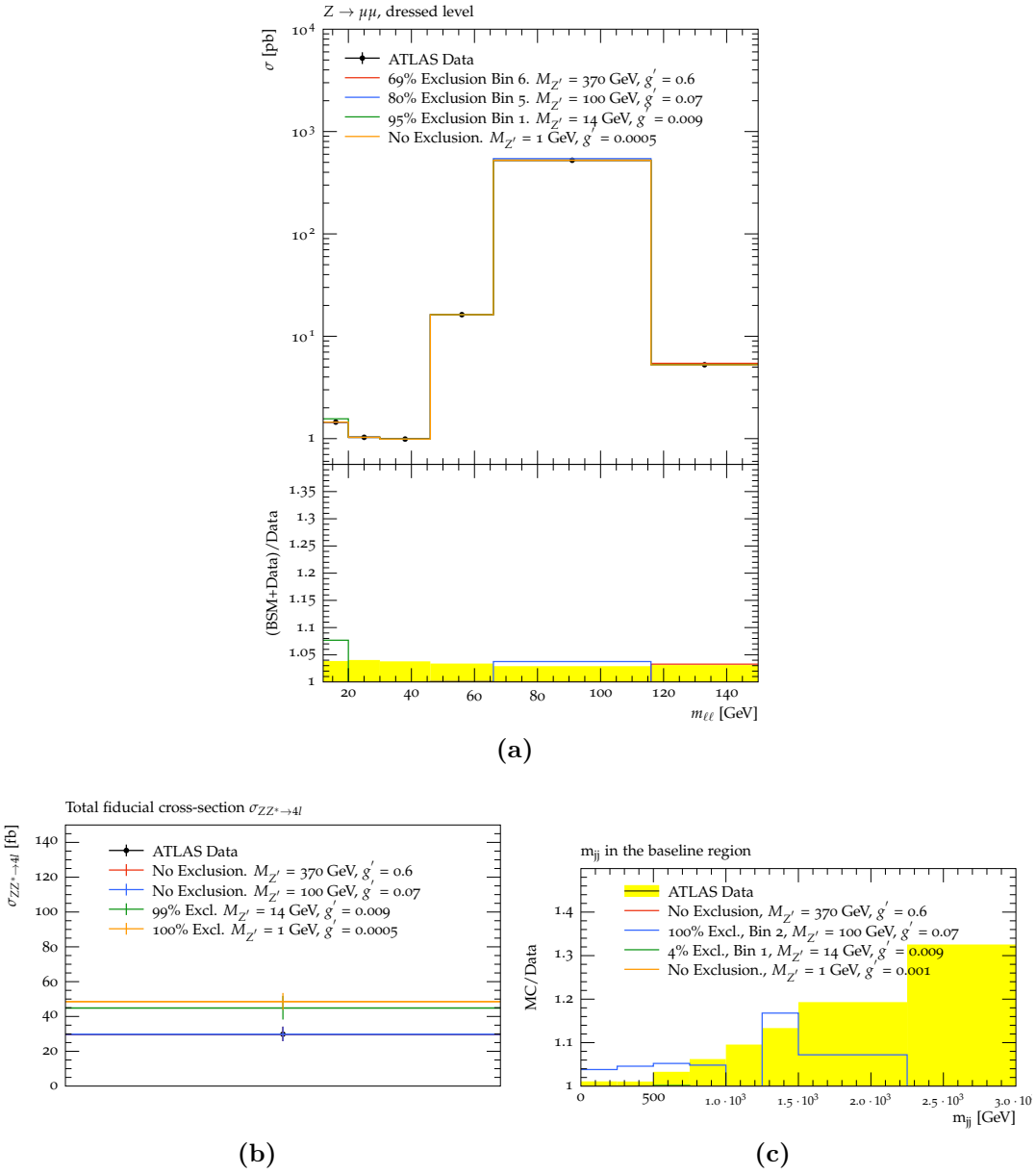

Figure 6.12.: Examples of the histograms from four points in the parameter space moving along the below the region of scenario C excluded by neutrino scattering, Figure 6.10c. Figure 6.12a The dimuon mass measurement [211], Figure 6.12b The ZZ^* (four lepton) measurement [170], Figure 6.12c The dijet mass in Z events [119]. The legend indicates the parameter point in $M_{Z'}$ and g_1' space and the bin of the plot which gives the sensitivity. The exclusion values, "Excl.", quoted are CL_s values quoted as percentages.

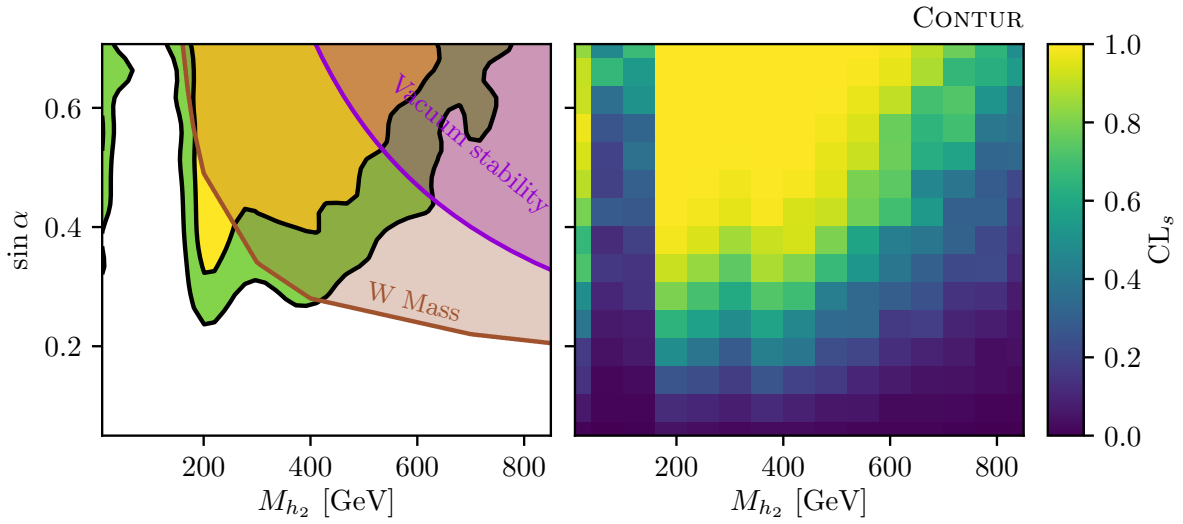

(a)

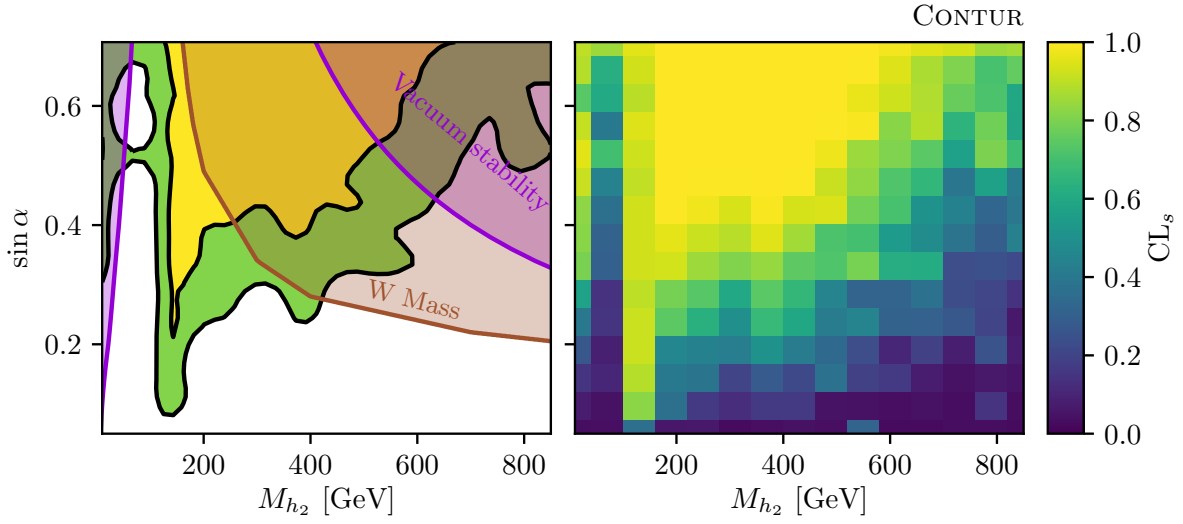

(b)

Figure 6.13.: Sensitivity of LHC measurements to the BSM contribution from a gauged B-L model in the M_{h_2} vs $\sin\alpha$ plane, Figure 6.13a scenario D, $g_1' = 0.2$, $M_{Z'} = 7$ TeV. Left, 95% (yellow) and 68% (green) excluded contours. Right, underlying heatmap of exclusion at each scanned parameter space point. The theory constraints from perturbativity and vacuum stability, requiring the model to be well behaved up to at least 10 TeV, as well as the constraint from M_W are also shown. Figure 6.13b scenario E, $g_1' = 0.001$, $M_{Z'} = 35$ GeV. Figures as in Figure 6.13a but for scenario E.

The decomposition to two example underlying histograms is shown for scenario D in Figure 6.14. Similar to the examples shown for scenario C, four model parameter space points are shown corresponding to four M_{h_2} values for fixed $\sin\alpha = 0.42$ are shown. Figure 6.14a shows an ATLAS cross-section measurement for a fiducial dilepton plus dijet selection at 8 TeV [213]. Figure 6.14b shows a differential cross-section of a candidate reconstructed Z in a fiducial four lepton ATLAS measurement at 8 TeV [224]. The corresponding table of leading processes cross-sections and the branching ratios of leading decays as calculated by HERWIG are shown in Table 6.4. This further highlights the array of analyses, and the power of combining the various channels available in CONTUR.

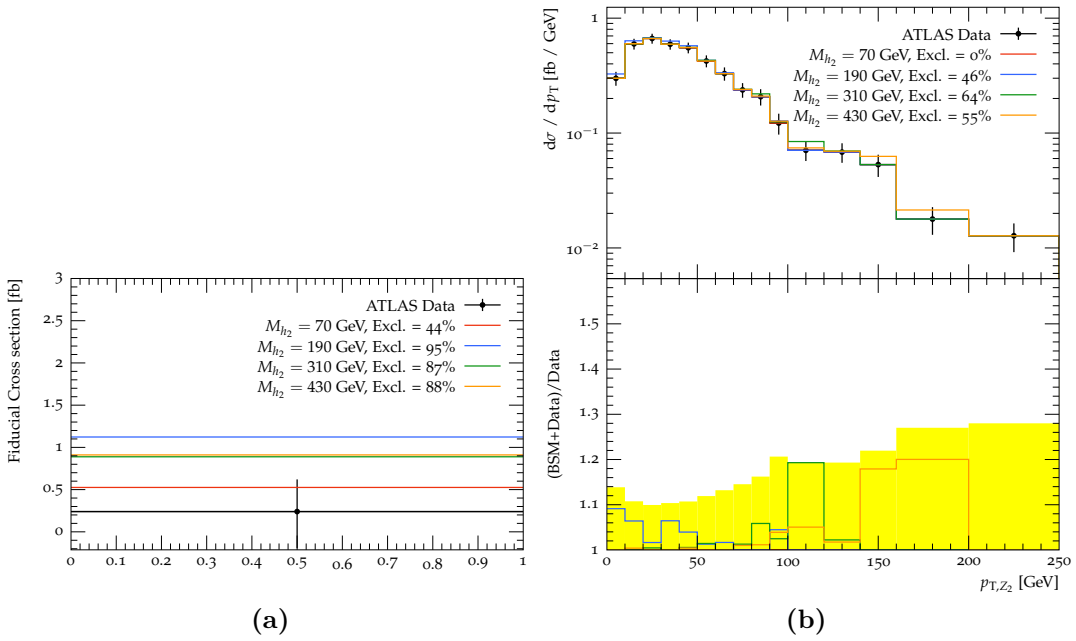

(a) **(b)**

Figure 6.14.: Examples of the histograms from four points in the parameter space moving along the lower edge of the theoretically allowed region of Figure 6.13a. Figure 6.14a the dilepton plus dijet measurement [213], Figure 6.14b the ZZ^* (four lepton) measurement [224], The legend indicates the parameter point in M_{h_2}, with the other free parameters set as; $M_{Z'} = 7$ TeV, $g'_1 = 0.2$ and $\sin\alpha = 0.42$. The exclusion values, "Excl.", quoted are CL_s values quoted as percentages.

6.4. Future improvements to Contur

The results presented in Section 6.2 and Section 6.3 used different versions of the CONTUR package and largely rewritten internal structure. Functionally however the construction of the

M_{h_2} (GeV)	Production Process	Cross Section (σ, pb)	Decay	Branching Fraction
70	$u\bar{u} \to Zh_2$	0.13	$h_2 \to b\bar{b}$	0.88
190	$gg \to gh_2$	0.37	$h_2 \to WW$	0.78
			$h_2 \to ZZ$	0.21
310	$gg \to gh_2$	0.20	$h_2 \to WW$	0.51
			$h_2 \to ZZ$	0.27
			$h_2 \to hh$	0.22
430	$gg \to gh_2$	0.14	$h_2 \to WW$	0.46
			$h_2 \to ZZ$	0.22
			$h_2 \to hh$	0.21
			$h_2 \to t\bar{t}$	0.11

Table 6.4.: Cross sections (in 8 TeV pp collisions) and branching fractions for the main processes contributing to Figure 6.14.

likelihood was the same in two key respects; a trivial background model $\vec{b} = \vec{n}$ was assumed in the likelihood, and the correlation between bins in a histograms was not considered. This meant a single bin was taken from each histogram. These two assumptions rendered the likelihood simple to calculate but effective for many studies. Breaking these two assumptions is part of an ongoing effort to use Contur for more ambitious fits.

6.4.1. Altering the background model

The trivial background model is more than just a convenient choice, although it was initially motivated by the lack of availability of ready made state of the art particle level calculations for many observables. The question posed using such a background model is *"Assuming the data observed in a fiducial region is arises purely from the SM, to what degree does this preclude the hypothesised new physics"*. In some ways this assumption is already implicitly a part of the results of the colliders. Tuning generators and PDF fitting for example, go some way towards including the exact data probed by Contur into the calculated background models already. Experimental techniques such as data driven backgrounds estimated from control regions also inherently assume the observed data in a control fiducial region represents an all orders calculation of the SM. Even the fact that it is known that the experiments operate in regions of phase space that become increasingly hard to model with event generators, mean that by including an event generator modelled background one can unwittingly be asking how well the event generator implementation of the SM fits the data, more than how much do we exclude this new physics.

Where possible including a calculated background model is being explored to understand the impact this has on a particle level exclusion. This can come from the values provided by the experiment, which are becoming increasingly complicated to replicate without the vast computational resources available to the collaborations. It was mentioned in Chapter 4 that one of the key uses of Rivet is in validation of new phenomenological techniques, which means in turn that older analyses may have been used to develop more advanced background calculations than were available at the time of the analysis. As an example, one of the ATLAS 7 TeV dataset measurements of diphoton production [169] has a calculation for differential diphoton production with QCD corrections up to NNLO available [225]. To demonstrate the usage of this in Contur, a model that predicts some deviation to this spectrum is useful. Axion-like-particle (ALP) models [226] are a good candidate, and have been studied in Contur already [227]. ALP models can be used to introduce effective operators for diphoton production in proton collisions. A contribution from a simulation of an example effective coupling parameter strength for an ALP of $M_{\mathrm{ALP}} = 50$ GeV to the measured diphoton mass spectrum is shown in Figure 6.15. Figure 6.15a shows the effect of using the background model as provided from the NNLO QCD prediction, and gives a calculated $\mathrm{CL_s}$ of exclusion of 0.62, arising from a bin in the tail of the distribution. Figure 6.15b shows the trivial background model using the observed data, the $\mathrm{CL_s}$ calculated increases to >0.99, arising from a bin around the ALP mass. At some level the jump in sensitivity represents the fact that this is an observable that is very hard to model theoretically, even with this NNLO calculation the background model around the ALP mass is already outside of the error bands on the observed data. Continued studies of such effects, where the backgrounds are poorly modelled is needed, and ongoing in Contur.

Being able to update the background model as more advanced theoretical calculations become available is one key advantage of setting limits with detector corrected data. It is an interesting area to see at what difference between emulating a data driven correction in the $\vec{b} = \vec{n}$ background model and a more pure theoretical comparison for data has on the resultant limits.

6.4.2. Including correlated observables

The likelihood construction given in Chapter 5, Section 5.2.4 was essentially a recipe for combining uncorrelated counting tests, although it was noted that it would be possible to extend this to include the effects of correlations between these counting tests. The likelihood given in equation (5.15) introduced a single uncorrelated nuisance parameter for each background count. This can be extended by first writing a similar counting test likelihood for a single

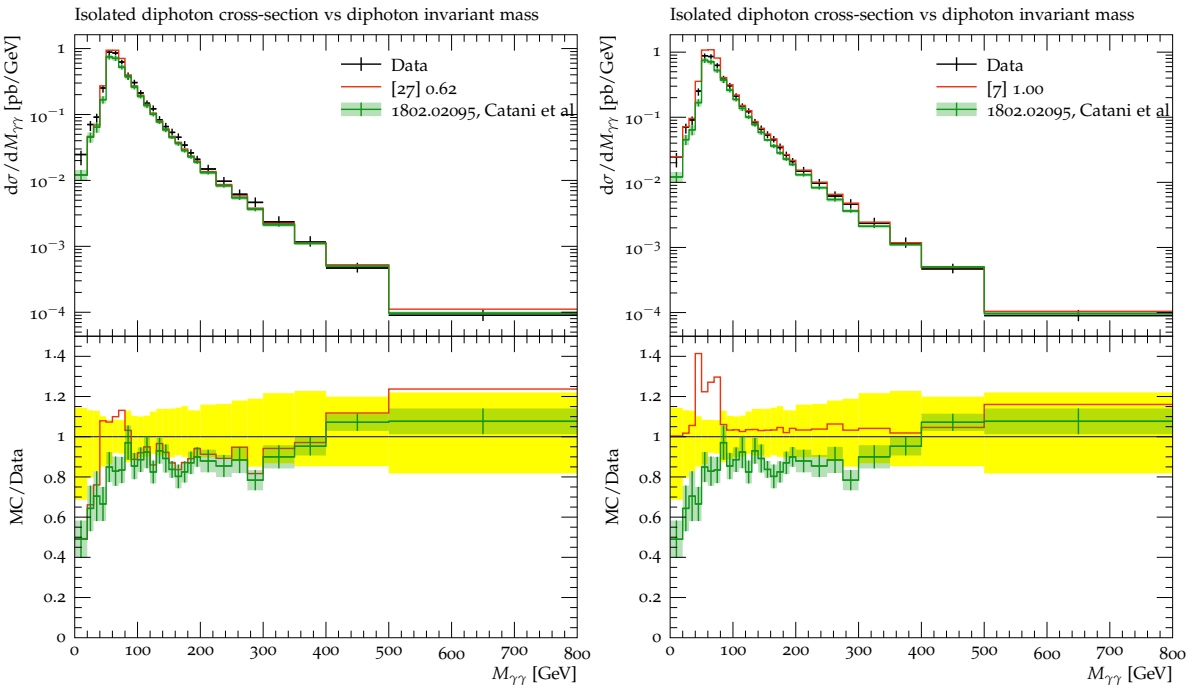

(a) **(b)**

Figure 6.15.: BSM simulation of an ALP model with $M_{\text{ALP}} = 50$ GeV in red, with an NNLO QCD diphoton background prediction in green [225], compared to ATLAS 7 TeV diphoton mass, $M_{\gamma\gamma}$, measurement in black [169]. The CL_s calculated with CONTUR and the bin index with the maximum CL_s is shown in the legend. Figure 6.15a shows the effect of using the theoretically calculated background prediction, with Figure 6.15b showing the trivial background model.

histogram with i bins, now with j nuisances introduced,

$$L(\mu, \vec{\nu}) = \prod_i \frac{(\mu s_i + b_i + \sum_j \nu_j)^{n_i}}{n_i!} e^{-(\mu s_i + b_i + \sum_j \nu_j)} \prod_j \exp(\vec{\nu}^\top \Sigma^{-1} \vec{\nu}) \,, \tag{6.13}$$

$$= \prod_i \text{Pois}(\mu s_i + b_i + \sum_j \nu_j \mid n_i) \prod_j \text{Gauss}_{iD}(\vec{\nu} \mid 0, \Sigma) \,, \tag{6.14}$$

with Σ being the covariance matrix for the nuisance parameters as defined in the simple one nuisance per bin case given in equation (5.21). In this case there are now multiple nuisances common to each counting test, or bin in the histogram. In this example there would be j different sources of nuisance, so there are j constraints. The constraints are now i dimensional Gaussians to take into account the potential covariance of each nuisance between bins. Each individual nuisance can be profiled by maximising the log likelihood for the hypothesised μ. The practical implementation of this has relied on the inclusion of the uncertainty breakdown into the YODA reference data files included with Rivet. Assuming each named uncertainty is 100% correlated then the correlation matrix for each uncertainty can be built, which gives the information needed of Σ to maximise the likelihood. Minimising this series of equations gives the requisite conditional maximum likelihood estimators needed for each nuisance, $\hat{\hat{\nu}}_i$. The sum of the correlation matrices built from each named uncertainty then gives the full correlation matrix between the bins which can be used to calculate the likelihood combing all bins in a histogram. Currently there isn't the drive to correlate named systematics between histograms, allowing combination of all bins in an entire analysis for example, for most purposes correlating a given histogram gives the information needed. Combining different histograms is then taking a product of the likelihood in equation (6.13), where the histograms chosen to combine correspond to a similar sorting algorithm already described in CONTUR.

Utilising this correlation information is a recent development and is part of a body of work, alongside the inclusion of theoretically calculated background models, expected to appear in the proceedings of the Les Houches 2019 new physics workshop series. A prototype of the correlation model implemented in a physics study is shown in Figure 6.16. This shows a parameter scan for two parameters in a two Higgs doublet model plus pseudoscalar mediator (2HDM+a) [228]. As this is work in progress the details of the model are omitted here, however it is noted that the parameter plane surveyed and the setting of the other parameters in the model correspond to the benchmark Figure 19b in the ATLAS dark sector mediator review paper [198]. The data included in this scan just arises from the collection of 13 TeV analyses available in Rivet 2.6.2, and the exclusion in this plane is driven by a CMS $t\bar{t}$ measurement [229]. A jump in reach in $\tan\beta$ of the exclusion contour is observed between Figure 6.16a where the correlations between bins are built automatically as described, and Figure 6.16b where no correlations are built and only a single bin from each histogram can be included into the likelihood. This jump in exclusion reach is likely to be overambitious in this case however, the

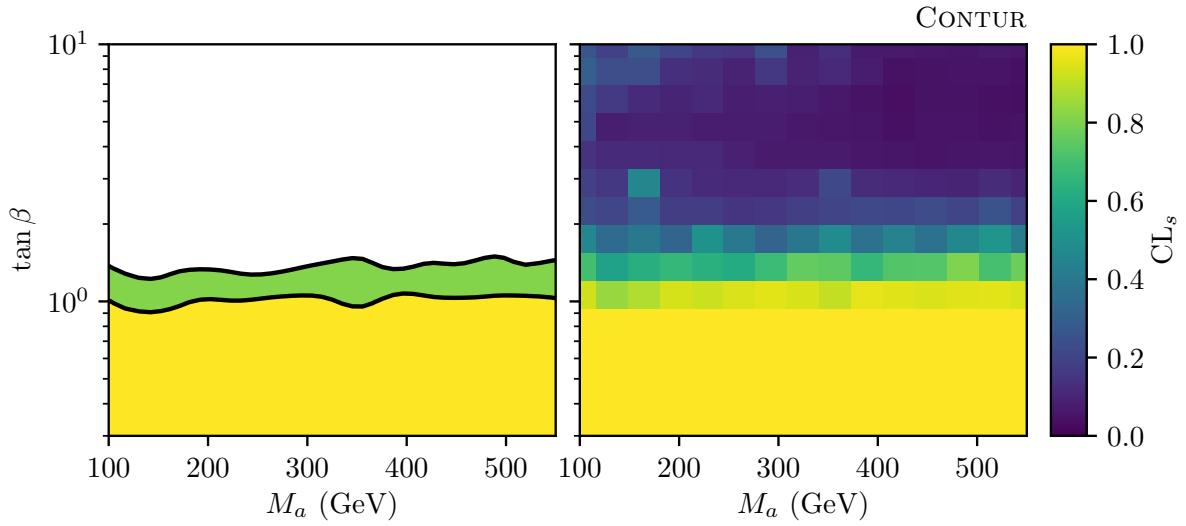

(a)

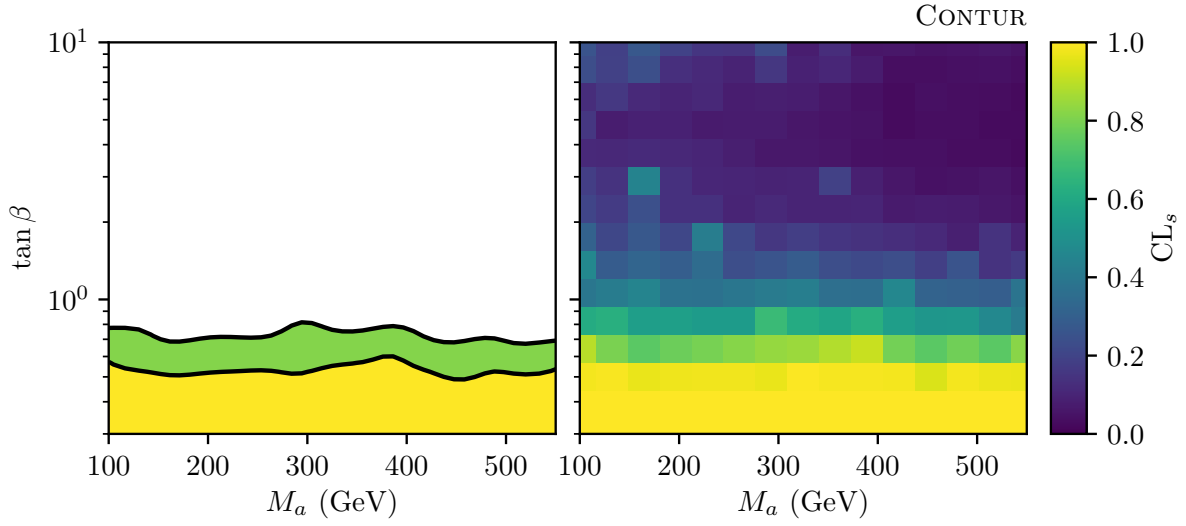

(b)

Figure 6.16.: Parameter scan of the 2HDM+a model [228] with parameters chosen as in the ATLAS dark sector mediators review [198]. Figure 6.16a shows the CONTUR exclusion calculated with automatically constructed correlations between individual histogram bins, Figure 6.16b shows the default case where only a single bin from each histogram is used.

information included in the error breakdown on HEPData for the differential distributions in the driving measurement only include an error breakdown composed of statistical plus systematic error. The correlation matrix built then will assume all systematic effects are 100% correlated which will not be the case. Such cases need to be studied in more detail, however it is noted that this measurement and many others increasingly directly include correlation matrices for the differential distributions. Rather than building the correlation on the fly Contur can be extended to make use of the provided correlations as well.

Including both theoretically calculated background models and profiled correlated nuisance parameters is still work in progress but it is expected to open up some new and interesting physics studies with Contur in the future.

Chapter 7.

Conclusion

The program of making precision measurements of particle collision properties at the LHC covers many final states and targets measurements of many processes predicted by the SM. The data taken thus far show good agreement with predictions from the SM. This program of precision measurement is complemented by the search program at the LHC which looks for hints of hypothesised BSM physics. These two approaches use the same recorded data but are often quite different in philosophy.

With no more jumps in centre of mass collision energy at the LHC, which historically have stoked excitement with the promise of increased BSM cross-sections with respect to the SM, the mindset of the collaborations is undergoing a shift. The potential for discovery of new physics now only grows as a reduction of the statistical uncertainty, which requires long runs of the LHC to acquire. The HL-LHC project will deliver this dataset over the course of the coming decades, but the mindset of the approach to analyse this data is changing. If new physics does exist at the TeV scale that the LHC probes, it seems most likely to be a more marginal effect, rather than a resonance in an otherwise smoothly falling spectrum. This prompts increased ingenuity in the search program, making use of data below the online trigger thresholds or looking for signatures of meta-stable particles outside of the usual SM reconstruction algorithms, to name two examples.

The measurement program will continue to operate in much the same way, making increasingly fine grained (as far as statistics allow) measurements of particle collisions. These measurements will form the main legacy of the collider. The precision measurements made at the Tevatron, of the W mass for example, continue to be important constraints informing the BSM search program to this day. In contrast the searches for new physics at the Tevatron are largely superseded by LHC limits. It is part of the natural life cycle of an energy frontier collider, when the collision energy jumps into previously unseen territories the excitement

centres on searching for new phenomena. If no such phenomena are found the focus naturally turns to precise measurement of what was observed.

As long as the searches at the LHC continue to find no significant deviation from the SM, and the measurements continue to demonstrate that the predictions of the SM agree with the data, an overarching question that links the two programs becomes apparent. *"To what degree does the observed agreement with the SM preclude a hypothesised BSM scenario?"* The body of work presented in this thesis attempted to approach this question from two angles. Firstly by production of a measurement with the ATLAS detector that was inherently designed to be useful for reinterpretation to BSM final states, this bridges the gap between the measurement and search programs by measuring (and unfolding) a signature that would typically be the domain of exotic new physics searches. Secondly a program to use the unfolded particle level measurements from all of the LHC collaborations was developed, this bridges the gap between search and measurement by applying the measurements as constraints to the hypothesised BSM model parameter space. With such a framework defined, new measurements can be made, added and recast onto any model that can be simulated at particle level at the LHC.

The last main aspect of this work is in the application of the tools developed. By performing a practical demonstration of the power of such an approach it is hoped that new and interesting statements about the phenomenology of BSM physics can be made. In the case study of DM production models it was shown that competitive limits can be derived, excluding mediator based interactions up to a mass of 2 TeV. In the case study of a gauged $B - L$ theory, again competitive limits with existing searches were derived, and the flexibility of the technique allowed surveys of previously unconsidered scenarios to be performed. The toolkit developed also serves the purpose of demonstrating the utility of the measurement program to the collaborations themselves, beyond what was perhaps initially intended. It is an important exercise in 'closing the loop', by understanding what one can make of the information published by the experimental collaborations, one can more clearly understand how to improve this picture. It is hoped that the techniques demonstrated here will be continually developed, beyond what was shown in this thesis. There are phenomenological possibilities for more ambitious surveys of BSM physics and many practical opportunities in maximising the information that can be extracted from the experimental results.

Appendix A.

Data included in scans with Contur

In Section 5.3.3, Table 5.1, a list of the analysis data used in the limit setting routine for the original CONTUR paper [145] was shown. In Table A.1, a list of all of the analysis data validated for use in CONTUR at the time of composing this document (06/03/2020) is shown. The analyses are grouped based on the *pool* within CONTUR they are included in.

Contur pool	Pool final state description	Rivet/Inspire ID	Rivet analysis description	Reference
ATLAS_13_3L	Trileptons	ATLAS_2016_I1469071	Measurement of the WZ production cross section at 13 TeV	[230]
ATLAS_13_4L	Four leptons	ATLAS_2019_I1720442	Inclusive 4-lepton lineshape at 13 TeV	[231]
		ATLAS_2017_I1625109	Measurement of $ZZ \to 4\ell$ production at 13 TeV	[224]
ATLAS_13_EEJET	e+e- at the Z pole, plus optional jets	ATLAS_2017_I1514251	Z plus jets at 13 TeV	[232]
		ATLAS_2019_I1718132	Control region measurements for leptoquark search at 13 TeV	[233]
ATLAS_13_GAMMA	Inclusive (multi)photons	ATLAS_2017_I1645627	Isolated photon + jets at 13 TeV	[234]
ATLAS_13_HMDY	Dileptons above the Z pole	ATLAS_2019_I1725190	Dilepton mass spectrum in 13 TeV pp collisions with 139 fb^{-1} Run 2 dataset	[235]
ATLAS_13_JETS	Inclusive hadronic final states	ATLAS_2018_I1634970	ATLAS Inclusive jet and dijet cross section measurement at $\sqrt{s} = 13$ TeV	[236]
		ATLAS_2019_I1724098	Jet substructure at 13 TeV	[237]
ATLAS_13_LMETJET	Lepton, missing transverse momentum, plus optional jets (typically W, semi-leptonic ttbar analyses)	ATLAS_2018_I1656578	Differential $t\bar{t}$ l+jets cross-sections at 13 TeV	[238]
		ATLAS_2017_I1614149	Resolved and boosted ttbar l+jets cross sections at 13 TeV	[239]
		ATLAS_2018_I1705857	ttbb at 13 TeV	[240]
ATLAS_13_METJET	missing transverse momentum plus jets	ATLAS_2017_I1609448	p_T^{miss}+jets cross-section ratios at 13 TeV	[107]
		ATLAS_2016_I1458270	0-lepton SUSY search with 3.2 fb^{-1} of 13 TeV pp data	[241]
ATLAS_13_MMJET	$\mu + \mu-$ at the Z pole, plus optional jets	ATLAS_2017_I1514251	Z plus jets at 13 TeV	[232]
		ATLAS_2019_I1718132	Control region measurements for leptoquark search at 13 TeV	[233]
ATLAS_13_TTHAD	Fully hadronic top events	ATLAS_2018_I1646686	All-hadronic boosted ttbar at 13 TeV	[242]
ATLAS_13_WW	WW analyses in dilepton plus missing transverse momentum channel	ATLAS_2019_I1718132	Control region measurements for leptoquark search at 13 TeV	[233]
ATLAS_7_4L	Four leptons	ATLAS_2012_I1203852	Measurement of the $ZZ(*)$ production cross-section in pp collisions at 7 TeV with ATLAS	[170]
ATLAS_7_EEJET	e+e- at the Z pole, plus optional jets	ATLAS_2016_I1502620	W and Z inclusive cross sections at 7 TeV	[243]
		ATLAS_2013_I1230812	Z + jets in pp at 7 TeV	[62]
		ATLAS_2014_I1306294	Measurement of Z boson in association with b-jets at 7 TeV in ATLAS (electron channel)	[244]
ATLAS_7_EE_GAMMA	e+e- plus photon(s)	ATLAS_2013_I1217863	W/Z + gamma production at 7 TeV	[171]
ATLAS_7_EMETJET	Electron, missing transverse momentum, plus optional jets (typically W, semi-leptonic ttbar analyses)	ATLAS_2013_I1219109	W + b production at 7 TeV	[245]
		ATLAS_2014_I1319490	W + jets	[163]

		ATLAS_2016_I1502620	W and Z inclusive cross sections at 7 TeV	[243]
ATLAS_7_EMET_GAMMA	Electron, missing transverse momentum, plus photon	ATLAS_2013_I1217863	W/Z + gamma production at 7 TeV	[171]
ATLAS_7_GAMMA	Inclusive (multi)photons	ATLAS_2013_I1244522	Photon + jets	[246]
		ATLAS_2012_I1093738	Isolated prompt photon + jet cross-section	[247]
		ATLAS_2012_I1199269	Inclusive diphoton $+X$ events at $\sqrt{s} = 7$ TeV	[169]
		ATLAS_2013_I1263495	Inclusive isolated prompt photon analysis with 2011 LHC data	[166]
ATLAS_7_HMDY	Dileptons above the Z pole	ATLAS_2013_I1234228	High-mass Drell-Yan at 7 TeV	[248]
ATLAS_7_JETS	Inclusive hadronic final states	ATLAS_2014_I1307243	Measurements of jet vetoes and azimuthal decorrelations in dijet events produced in pp collisions at $\sqrt{s} = 7$ TeV using the ATLAS detector	[161]
		ATLAS_2014_I1326641	3-jet cross section with 7 TeV data	[160]
		ATLAS_2014_I1325553	Measurement of the inclusive jet cross-section at 7 TeV	[158]
		ATLAS_2014_I1268975	High-mass dijet cross section	[159]
ATLAS_7_LMDY	Dileptons below the Z pole	ATLAS_2014_I1288706	Measurement of the low-mass Drell-Yan differential cross section at 7 TeV	[210]
ATLAS_7_LMETJET	Lepton, missing transverse momentum, plus optional jets (typically W, semi-leptonic ttbar analyses)	ATLAS_2014_I1282447	W + charm production at 7 TeV	[249]
		ATLAS_2015_I1345452	Pseudo-top-antitop cross sections	[250]
ATLAS_7_MMETJET	Muon, missing transverse momentum, plus optional jets (typically W, semi-leptonic ttbar analyses)	ATLAS_2013_I1219109	W + b production at 7 TeV	[245]
		ATLAS_2014_I1319490	W + jets	[163]
		ATLAS_2016_I1502620	W and Z inclusive cross sections at 7 TeV	[243]
ATLAS_7_MMET_GAMMA	Muon, missing transverse momentum, plus photon	ATLAS_2013_I1217863	W/Z + gamma production at 7 TeV	[171]
ATLAS_7_MMJET	$\mu + \mu-$ at the Z pole, plus optional jets	ATLAS_2014_I1306294	Measurement of Z boson in association with b-jets at 7 TeV in ATLAS (electron channel)	[244]
		ATLAS_2016_I1502620	W and Z inclusive cross sections at 7 TeV	[243]
		ATLAS_2013_I1230812	Z + jets in pp at 7 TeV	[62]
ATLAS_7_MM_GAMMA	$\mu + \mu-$ plus photon(s)	ATLAS_2013_I1217863	W/Z + gamma production at 7 TeV	[171]
ATLAS_7_WW	WW analyses in dilepton plus missing transverse momentum channel	ATLAS_2013_I1190187	Measurement of the W^+W^- production cross-section at 7 TeV	[251]
ATLAS_8_3L	Trileptons	ATLAS_2016_I1492320	WWW production at 8 TeV	[213]
ATLAS_8_4L	Four leptons	ATLAS_2015_I1394865	Inclusive 4-lepton lineshape	[216]
		ATLAS_2014_I1310835	$H(125) \to 4l$ at 8 TeV	[217]
ATLAS_8_EEJET	e+e- at the Z pole, plus optional jets	ATLAS_2017_I1589844	k_T splittings in Z events at 8 TeV	[215]
		ATLAS_2015_I1408516	Z p_T and Z ϕ^*	[211]

ATLAS_8_EMETJET	Electron, missing transverse momentum, plus optional jets (typically W, semi-leptonic ttbar analyses)	ATLAS_2017_I1517194	Electroweak Wjj production at 8 TeV	[252]
ATLAS_8_GAMMA	Inclusive (multi)photons	ATLAS_2017_I1591327	Inclusive diphoton cross-sections at 8 TeV	[253]
		ATLAS_2017_I1632756	Photon + heavy flavour at 8 TeV	[254]
		ATLAS_2014_I1306615	Higgs diphoton events at 8 TeV in ATLAS	[255]
		ATLAS_2016_I1457605	Inclusive prompt photons at 8 TeV	[113]
		ATLAS_2017_I1644367	Isolated triphotons at 8 TeV	[256]
ATLAS_8_GAMMA_MET	Photon plus missing transverse momentum	ATLAS_2016_I1448301	$Z\gamma(\gamma)$ cross sections at 8 TeV	[214]
ATLAS_8_HMDY_EL	Dileptons above the Z pole	ATLAS_2016_I1467454	High-mass Drell-Yan at 8 TeV	[212]
ATLAS_8_HMDY_MU	Dileptons above the Z pole	ATLAS_2016_I1467454	High-mass Drell-Yan at 8 TeV	[212]
ATLAS_8_JETS	Inclusive hadronic final states	ATLAS_2015_I1394679	Multijets at 8 TeV	[162]
		ATLAS_2017_I1604271	ATLAS Inclusive jet cross section measurement at sqrt(s)=8TeV	[257]
		ATLAS_2017_I1598613	BB to Jpsi plus mu at 8 TeV	[258]
ATLAS_8_LLJET	Dileptons at the Z pole, plus optional jets	ATLAS_2014_I1279489	Measurements of electroweak production of dijets + Z boson, and distributions sensitive to vector boson fusion	[119]
ATLAS_8_LMETJET	Lepton, missing transverse momentum, plus optional jets (typically W, semi-leptonic ttbar analyses)	ATLAS_2015_I1404878	ttbar (to l+jets) differential cross sections at 8 TeV	[259]
		ATLAS_2015_I1397637	Boosted ttbar differential cross-section	[260]
ATLAS_8_MMETJET	Muon, missing transverse momentum, plus optional jets (typically W, semi-leptonic ttbar analyses)	ATLAS_2017_I1517194	Electroweak Wjj production at 8 TeV	[252]
ATLAS_8_MMJET	$\mu+\mu-$ at the Z pole, plus optional jets	ATLAS_2017_I1589844	k_T splittings in Z events at 8 TeV	[215]
		ATLAS_2015_I1408516	Z p_T and Z ϕ^*	[211]
ATLAS_8_MM_GAMMA	$\mu+\mu-$ plus photon(s)	ATLAS_2016_I1448301	$Z\gamma(\gamma)$ cross sections at 8 TeV	[214]
ATLAS_8_WW	WW analyses in dilepton plus missing transverse momentum channel	ATLAS_2016_I1444991	Higgs-to-WW differential cross sections at 8 TeV	[261]
		ATLAS_2016_I1426515	WW production at 8 TeV	[218]
		ATLAS_2016_I1492320	WWW production at 8 TeV	[213]
CMS_13_HMDY	Dileptons above the Z pole	CMS_2018_I1711625	Measurement of the differential Drell-Yan cross section in proton-proton collisions at $\sqrt{s} = 13\,TeV$	[262]
CMS_13_JETS	Inclusive hadronic final states	CMS_2018_I1682495	Jet mass in dijet events in pp collisions at 13 TeV	[263]
		CMS_2016_I1459051	Measurement of the inclusive jet cross-section in pp collisions at $\sqrt{s}$ = 13 TeV	[264]

CMS_13_LMETJET	Lepton, missing transverse momentum, plus optional jets (typically W, semi-leptonic ttbar analyses)	CMS_2018_I1663958	Differential cross sections for top quark pair production using the lepton+jets final state in proton proton collisions at 13 TeV	[229]
		CMS_2016_I1491950	Differential cross sections for top quark pair production using the lepton+jets final state in proton proton collisions at 13 TeV	[265]
		CMS_2018_I1662081	Measurement of the differential cross sections of top quark pair production as a function of kinematic event variables in pp collisions at sqrt(s) = 13 TeV	[266]
CMS_13_MMETJET	Muon, missing transverse momentum, plus optional jets (typically W, semi-leptonic ttbar analyses)	CMS_2017_I1610623	Measurements of differential cross sections for the associated production of a W boson and jets in proton-proton collisions at sqrt(s) = 13 TeV	[267]
CMS_7_EEJET	e+e- at the Z pole, plus optional jets	CMS_2013_I1224539_ZJET	CMS jet mass measurement in Z + jet events	[268]
CMS_7_EMETJET	electron, missing transverse momentum, plus optional jets (typically W, semi-leptonic ttbar analyses)	CMS_2013_I1224539_WJET	CMS jet mass measurement in W + jet events	[268]
CMS_7_GAMMA	Inclusive (multi)photons	CMS_2014_I1266056	Photon + jets triple differential cross-section	[168]
CMS_7_JETS	Inclusive hadronic final states	CMS_2014_I1298810	Ratios of jet pT spectra, which relate to the ratios of inclusive, differential jet cross sections	[140]
		CMS_2013_I1273574	Studies of 4-jet production in proton-proton collisions at $\sqrt{s} = 7$ TeV	[269]
		CMS_2013_I1208923	Jet-pT and dijet mass at sqrt(s) = 7 TeV	[270]
CMS_7_LLJET	dileptons at the Z pole, plus optional jets	CMS_2013_I1256943	Cross-section and angular correlations in Z boson with b-hadrons events at $\sqrt{s} = 7$ TeV	[271]
		CMS_2015_I1310737	Jet multiplicity and differential cross-sections of Z+jets events in pp at $\sqrt{s} = 7$ TeV	[164]
CMS_7_MMETJET	Muon, missing transverse momentum, plus optional jets (typically W, semi-leptonic ttbar analyses)	CMS_2014_I1303894	Differential cross-section of W bosons + jets in pp collisions at $\sqrt{s} = 7$ TeV	[165]
CMS_8_3L	Trileptons	CMS_2016_I1487288	WZ production cross-section in pp collisions at 8 TeV	[272]
CMS_8_JETS	Inclusive hadronic final states	CMS_2017_I1598460	Triple-differential dijet pT cross section and PDF constraints at 8 TeV	[273]
		CMS_2016_I1487277	Measurement and QCD analysis of double-differential inclusive jet cross sections in pp collisions at $\sqrt{s}$ = 8 TeV and cross section ratios to 2.76 and 7 TeV	[274]

CMS_8_LLJET	Dileptons at the Z pole, plus optional jets	CMS_2017_I1499471	Measurements of the associated production of a Z boson and b jets in pp collisions at $\sqrt{s} = 8$ TeV	[219]
CMS_8_LMETJET	Lepton, missing transverse momentum, plus optional jets (typically W, semi-leptonic ttbar analyses)	CMS_2016_I1454211	Boosted $t\bar{t}$ in pp collisions at $\sqrt{s} = 8$ TeV	[196]
		CMS_2017_I1518399	Differential $t\bar{t}$ production cross-section as a function of the leading jet mass for boosted top quarks at 8 TeV	[275]
CMS_8_MMETJET	Muon, missing transverse momentum, plus optional jets (typically W, semi-leptonic ttbar analyses)	CMS_2016_I1491953	Differential cross sections for associated production of a W boson and jets at 8 TeV	[276]
CMS_8_WW	WW analyses in dilepton plus missing transverse momentum channel	CMS_2017_I1467451	Measurement of the transverse momentum spectrum of the Higgs boson produced in ppcollisions at $\sqrt{s} = 8$ TeV using H to WW decays	[277]
LHCB_7_EEJET	e+e- at the Z pole, plus optional jets	LHCB_2012_I1208102	Differential cross-sections of $Z/\gamma^* \to e^+e^-$ vs rapidity and ϕ^*	[278]
LHCB_7_MMJET	$\mu + \mu-$ at the Z pole, plus optional jets	LHCB_2014_I1262703	Study of forward Z + jet production in pp collisions at $\sqrt{s} = 7$ TeV in the LHCb fiducial phase-space	[220]

Table A.1.: List of all the analyses validated for inclusion in a Contur limit as of Contur release 1.0.0 (06/03/20).

Bibliography

[1] M. Schwartz, *Quantum Field Theory and the Standard Model*. Cambridge University Press, 2014.

[2] Peskin and Schroeder, *An Introduction to Quantum Field Theory*. Addison-Wesley, 1995.

[3] D0 collaboration, S. Abachi et al., *Observation of the top quark*, *Phys. Rev. Lett.* **74** (1995) 2632–2637, [hep-ex/9503003].

[4] CDF collaboration, F. Abe et al., *Observation of top quark production in $\bar{p}p$ collisions*, *Phys. Rev. Lett.* **74** (1995) 2626–2631, [hep-ex/9503002].

[5] DONUT collaboration, K. Kodama et al., *Observation of tau neutrino interactions*, *Phys. Lett.* **B504** (2001) 218–224, [hep-ex/0012035].

[6] ATLAS Collaboration collaboration, G. Aad et al., *Observation of a new particle in the search for the Standard Model Higgs boson with the ATLAS detector at the LHC*, *Phys.Lett.* **B716** (2012) 1–29, [1207.7214].

[7] CMS collaboration, S. Chatrchyan et al., *Observation of a New Boson at a Mass of 125 GeV with the CMS Experiment at the LHC*, *Phys. Lett.* **B716** (2012) 30–61, [1207.7235].

[8] D. Galbraith and C. Burgard, "Standard model tikz diagram." http://davidgalbraith.org/portfolio/ux-standard-model-of-the-standard-model, Ret. 2019.

[9] S. Weinberg, *A model of leptons*, *Phys. Rev. Lett.* **19** (Nov, 1967) 1264–1266.

[10] S. L. Glashow, *The renormalizability of vector meson interactions*, *Nuclear Physics* **10** (Feb., 1959) 107–117.

[11] A. Salam and J. C. Ward, *Weak and electromagnetic interactions*, *Il Nuovo Cimento (1955-1965)* **11** (Feb, 1959) 568–577.

[12] Super-Kamiokande Collaboration collaboration, Y. Fukuda, T. Hayakawa, E. Ichihara, K. Inoue, K. Ishihara, H. Ishino et al., *Evidence for oscillation of atmospheric neutrinos*, *Phys. Rev. Lett.* **81** (Aug, 1998) 1562–1567.

[13] SNO Collaboration collaboration, Q. R. Ahmad, R. C. Allen, T. C. Andersen, J. D.Anglin, J. C. Barton, E. W. Beier et al., *Direct evidence for neutrino flavor transformation from neutral-current interactions in the sudbury neutrino observatory*, *Phys. Rev. Lett.* **89** (Jun, 2002) 011301.

[14] F. Englert and R. Brout, *Broken symmetry and the mass of gauge vector mesons*, *Phys. Rev. Lett.* **13** (Aug, 1964) 321–323.

[15] P. W. Higgs, *Broken symmetries and the masses of gauge bosons*, *Phys. Rev. Lett.* **13** (Oct, 1964) 508–509.

[16] N. Cabibbo, *Unitary symmetry and leptonic decays*, *Phys. Rev. Lett.* **10** (Jun, 1963) 531–533.

[17] M. Kobayashi and T. Maskawa, *CP Violation in the Renormalizable Theory of Weak Interaction*, *Prog. Theor. Phys.* **49** (1973) 652–657.

[18] Z. Maki, M. Nakagawa and S. Sakata, *Remarks on the unified model of elementary particles*, *Prog. Theor. Phys.* **28** (1962) 870–880.

[19] B. Pontecorvo, *Inverse beta processes and nonconservation of lepton charge*, *Sov. Phys. JETP* **7** (1958) 172–173.

[20] H. D. Politzer, *Reliable perturbative results for strong interactions?*, *Phys. Rev. Lett.* **30** (Jun, 1973) 1346–1349.

[21] D. J. Gross and F. Wilczek, *Ultraviolet behavior of non-abelian gauge theories*, *Phys. Rev. Lett.* **30** (Jun, 1973) 1343–1346.

[22] G. 't Hooft and M. J. G. Veltman, *Regularization and Renormalization of Gauge Fields*, *Nucl. Phys.* **B44** (1972) 189–213.

[23] Particle Data Group collaboration, M. Tanabashi, K. Hagiwara, K. Hikasa, K. Nakamura, Y. Sumino, F. Takahashi et al., *Review of particle physics*, *Phys. Rev. D* **98** (Aug, 2018) 030001.

[24] K. G. Wilson, *Confinement of quarks*, *Phys. Rev. D* **10** (Oct, 1974) 2445–2459.

[25] G. Dissertori, I. Knowles and M. Schmelling, *Quantum Chromodynamics: High Energy Experiments and Theory*. Oxford University Press, 2009.

[26] K. Ellis, J. Stirling and B. Webber, *QCD and Collider Physics*. Cambridge University Press, 2003.

[27] C. G. Papadopoulos, *PHEGAS: A Phase space generator for automatic cross-section*

computation, *Comput. Phys. Commun.* **137** (2001) 247–254, [hep-ph/0007335].

[28] J. Ellis, *The Discovery of the Gluon*, *Int. J. Mod. Phys.* **A29** (2014) 1430072, [1409.4232].

[29] G. Altarelli and G. Parisi, *Asymptotic freedom in parton language*, *Nuclear Physics B* **126** (Aug., 1977) 298–318.

[30] J. M. Campbell, R. K. Ellis and C. Williams, *Vector boson pair production at the LHC*, *JHEP* **07** (2011) 018, [1105.0020].

[31] A. Banfi, H. McAslan, P. F. Monni and G. Zanderighi, *A general method for the resummation of event-shape distributions in e^+e^- annihilation*, *JHEP* **05** (2015) 102, [1412.2126].

[32] M. Dasgupta, F. A. Dreyer, K. Hamilton, P. F. Monni and G. P. Salam, *Logarithmic accuracy of parton showers: a fixed-order study*, *JHEP* **09** (2018) 033, [1805.09327].

[33] T. Sjöstrand, S. Ask, J. R. Christiansen, R. Corke, N. Desai, P. Ilten et al., *An Introduction to PYTHIA 8.2*, *Comput. Phys. Commun.* **191** (2015) 159–177, [1410.3012].

[34] M. Bahr et al., *Herwig++ Physics and Manual*, *Eur. Phys. J.* **C58** (2008) 639–707, [0803.0883].

[35] S. Gieseke, F. Loshaj and P. Kirchgaeßer, *Soft and diffractive scattering with the cluster model in Herwig*, *Eur. Phys. J.* **C77** (2017) 156, [1612.04701].

[36] S. Catani, Y. L. Dokshitzer, M. H. Seymour and B. R. Webber, *Longitudinally invariant k(t) clustering algorithms for hadron hadron collisions*, *Nucl. Phys.* **B406** (1993) 187–224.

[37] M. Cacciari, G. P. Salam and G. Soyez, *The anti-k_t jet clustering algorithm*, *JHEP* **04** (2008) 063, [0802.1189].

[38] M. Cacciari, G. P. Salam and G. Soyez, *FastJet User Manual*, *Eur.Phys.J.* **C72** (2012) 1896, [1111.6097].

[39] A. Buckley et al., *General-purpose event generators for LHC physics*, *Phys. Rept.* **504** (2011) 145–233, [1101.2599].

[40] T. Gleisberg, S. Hoeche, F. Krauss, M. Schonherr, S. Schumann, F. Siegert et al., *Event generation with SHERPA 1.1*, *JHEP* **02** (2009) 007, [0811.4622].

[41] L. A. Harland-Lang, A. D. Martin, P. Motylinski and R. S. Thorne, *Parton distributions*

in the LHC era: MMHT 2014 PDFs, *Eur. Phys. J.* **C75** (2015) 204, [1412.3989].

[42] A. Buckley, J. Ferrando, S. Lloyd, K. Nordström, B. Page, M. Rüfenacht et al., *LHAPDF6: parton density access in the LHC precision era*, *Eur. Phys. J.* **C75** (2015) 132, [1412.7420].

[43] J. R. Andersen et al., *Les Houches 2013: Physics at TeV Colliders: Standard Model Working Group Report*, 1405.1067.

[44] J. Alwall, M. Herquet, F. Maltoni, O. Mattelaer and T. Stelzer, *MadGraph 5 : Going Beyond*, *JHEP* **06** (2011) 128, [1106.0522].

[45] F. Buccioni, S. Pozzorini and M. Zoller, *On-the-fly reduction of open loops*, *Eur. Phys. J.* **C78** (2018) 70, [1710.11452].

[46] S. Catani and M. H. Seymour, *A General algorithm for calculating jet cross-sections in NLO QCD*, *Nucl. Phys.* **B485** (1997) 291–419, [hep-ph/9605323].

[47] S. Alioli, P. Nason, C. Oleari and E. Re, *A general framework for implementing NLO calculations in shower Monte Carlo programs: the POWHEG BOX*, *JHEP* **06** (2010) 043, [1002.2581].

[48] S. Hoeche, F. Krauss, M. Schonherr and F. Siegert, *A critical appraisal of NLO+PS matching methods*, *JHEP* **09** (2012) 049, [1111.1220].

[49] P. Nason, *A New method for combining NLO QCD with shower Monte Carlo algorithms*, *JHEP* **11** (2004) 040, [hep-ph/0409146].

[50] S. Frixione and B. R. Webber, *Matching NLO QCD computations and parton shower simulations*, *JHEP* **06** (2002) 029, [hep-ph/0204244].

[51] P. Nason and B. Webber, *Next-to-Leading-Order Event Generators*, *Ann. Rev. Nucl. Part. Sci.* **62** (2012) 187–213, [1202.1251].

[52] K. Hamilton, P. Nason, E. Re and G. Zanderighi, *NNLOPS simulation of Higgs boson production*, *JHEP* **10** (2013) 222, [1309.0017].

[53] S. Catani, F. Krauss, R. Kuhn and B. R. Webber, *QCD matrix elements + parton showers*, *JHEP* **11** (2001) 063, [hep-ph/0109231].

[54] S. Plätzer, *Controlling inclusive cross sections in parton shower + matrix element merging*, *JHEP* **08** (2013) 114, [1211.5467].

[55] S. Hoeche, F. Krauss, M. Schonherr and F. Siegert, *QCD matrix elements + parton showers: The NLO case*, *JHEP* **04** (2013) 027, [1207.5030].

[56] R. Frederix and S. Frixione, *Merging meets matching in MC@NLO*, *JHEP* **12** (2012) 061, [1209.6215].

[57] L. Lönnblad and S. Prestel, *Merging Multi-leg NLO Matrix Elements with Parton Showers*, *JHEP* **03** (2013) 166, [1211.7278].

[58] K. Hamilton, P. Nason and G. Zanderighi, *MINLO: Multi-Scale Improved NLO*, *JHEP* **10** (2012) 155, [1206.3572].

[59] J. Bellm, G. Nail, S. Plätzer, P. Schichtel and A. Siódmok, *Parton Shower Uncertainties with Herwig 7: Benchmarks at Leading Order*, 1605.01338.

[60] J. Bellm, S. Gieseke and S. Plätzer, *Merging NLO Multi-jet Calculations with Improved Unitarization*, *Eur. Phys. J.* **C78** (2018) 244, [1705.06700].

[61] J. Bellm et al., *Herwig 7.0/Herwig++ 3.0 release note*, *Eur. Phys. J.* **C76** (2016) 196, [1512.01178].

[62] ATLAS collaboration, G. Aad et al., *Measurement of the production cross section of jets in association with a Z boson in pp collisions at $\sqrt{s}$ = 7 TeV with the ATLAS detector*, *JHEP* **07** (2013) 032, [1304.7098].

[63] ATLAS collaboration, G. Aad et al., *Measurement of the Z/γ^* boson transverse momentum distribution in pp collisions at $\sqrt{s}$ = 7 TeV with the ATLAS detector*, *JHEP* **09** (2014) 145, [1406.3660].

[64] C. S. Frenk and S. D. M. White, *Dark matter and cosmic structure*, *Annalen Phys.* **524** (2012) 507–534, [1210.0544].

[65] G. F. Giudice, *Naturally Speaking: The Naturalness Criterion and Physics at the LHC*, 0801.2562.

[66] S. P. Martin, *A Supersymmetry primer*, hep-ph/9709356.

[67] N. Arkani-Hamed, S. Dimopoulos and G. R. Dvali, *The Hierarchy problem and new dimensions at a millimeter*, *Phys. Lett.* **B429** (1998) 263–272, [hep-ph/9803315].

[68] L. Evans and P. Bryant, *LHC machine*, *Journal of Instrumentation* **3** (aug, 2008) S08001–S08001.

[69] ATLAS collaboration, G. Aad et al., *The ATLAS Experiment at the CERN Large Hadron Collider*, *JINST* **3** (2008) S08003.

[70] CMS collaboration, S. Chatrchyan et al., *The CMS Experiment at the CERN LHC*, *JINST* **3** (2008) S08004.

[71] ALICE collaboration, K. Aamodt et al., *The ALICE experiment at the CERN LHC*, *JINST* **3** (2008) S08002.

[72] LHCb collaboration, A. A. Alves, Jr. et al., *The LHCb Detector at the LHC*, *JINST* **3** (2008) S08005.

[73] N. Konstantinidis et al., *The Atlantis event visualisation program for the ATLAS experiment*, in *Computing in high energy physics and nuclear physics. Proceedings, Conference, CHEP'04, Interlaken, Switzerland, September 27-October 1, 2004*, pp. 361–364, 2005.

[74] *LEP Design Report: Vol.2. The LEP Main Ring*, *CERN-LEP-84-01* (1984) .

[75] E. Mobs, *The CERN accelerator complex - August 2018. Complexe des accélérateurs du CERN - Août 2018*, *OPEN-PHO-ACCEL-2018-005* (Aug, 2018) .

[76] G. Apollinari, I. Béjar Alonso, O. Brüning, P. Fessia, M. Lamont, L. Rossi et al., *High-Luminosity Large Hadron Collider (HL-LHC)*, *CERN Yellow Rep. Monogr.* **4** (2017) 1–516.

[77] J. Pequenao, "Computer generated image of the whole ATLAS detector." Mar, 2008.

[78] ATLAS collaboration, M. Aaboud et al., *Performance of the ATLAS Trigger System in 2015*, *Eur. Phys. J.* **C77** (2017) 317, [1611.09661].

[79] M. Shochet, L. Tompkins, V. Cavaliere, P. Giannetti, A. Annovi and G. Volpi, *Fast TracKer (FTK) Technical Design Report*, Tech. Rep. CERN-LHCC-2013-007. ATLAS-TDR-021, Jun, 2013.

[80] ATLAS collaboration, M. Aaboud et al., *Luminosity determination in pp collisions at $\sqrt{s}$ = 8 TeV using the ATLAS detector at the LHC*, *Eur. Phys. J.* **C76** (2016) 653, [1608.03953].

[81] ATLAS collaboration, M. Aaboud et al., "Luminosity public results." https://twiki.cern.ch/twiki/bin/view/AtlasPublic/LuminosityPublicResultsRun2, Ret. 2019.

[82] ATLAS collaboration, M. Aaboud et al., *Performance of the ATLAS Track Reconstruction Algorithms in Dense Environments in LHC Run 2*, *Eur. Phys. J.* **C77** (2017) 673, [1704.07983].

[83] ATLAS collaboration, G. Aad et al., *Topological cell clustering in the ATLAS calorimeters and its performance in LHC Run 1*, *Eur. Phys. J.* **C77** (2017) 490, [1603.02934].

[84] ATLAS collaboration, M. Aaboud et al., *Electron reconstruction and identification in the ATLAS experiment using the 2015 and 2016 LHC proton-proton collision data at* $\sqrt{s}$ *= 13 TeV*, *Eur. Phys. J.* **C79** (2019) 639, [1902.04655].

[85] *Proposal for truth particle observable definitions in physics measurements*, Tech. Rep. ATL-PHYS-PUB-2015-013, CERN, Geneva, Jun, 2015.

[86] ATLAS collaboration, M. Aaboud et al., *Jet reconstruction and performance using particle flow with the ATLAS Detector*, *Eur. Phys. J.* **C77** (2017) 466, [1703.10485].

[87] ATLAS collaboration, M. Aaboud et al., *Jet energy scale measurements and their systematic uncertainties in proton-proton collisions at* $\sqrt{s} = 13$ *TeV with the ATLAS detector*, *Phys. Rev.* **D96** (2017) 072002, [1703.09665].

[88] ATLAS collaboration, G. Aad et al., *Jet energy resolution in proton-proton collisions at* $\sqrt{s} = 7$ *TeV recorded in 2010 with the ATLAS detector*, *Eur. Phys. J.* **C73** (2013) 2306, [1210.6210].

[89] *Expected performance of the ATLAS b-tagging algorithms in Run-2*, Tech. Rep. ATL-PHYS-PUB-2015-022, CERN, Geneva, Jul, 2015.

[90] *Expected performance of missing transverse momentum reconstruction for the ATLAS detector at* $\sqrt{s} = 13$ *TeV*, Tech. Rep. ATL-PHYS-PUB-2015-023, CERN, Geneva, Jul, 2015.

[91] T. Kittelmann, V. Tsulaia, J. Boudreau and E. Moyse, *The virtual point 1 event display for the ATLAS experiment*, *Journal of Physics: Conference Series* **219** (apr, 2010) 032012.

[92] P. van Gemmeren and D. Malon, *The event data store and i/o framework for the atlas experiment at the large hadron collider*, in *2009 IEEE International Conference on Cluster Computing and Workshops*, pp. 1–8, Aug, 2009. DOI.

[93] Quantizer collaboration, "Quantizer - sonification of high energy physics events." http://quantizer.media.mit.edu/, Retrieved July 2019.

[94] A. Buckley, T. Eifert, M. Elsing, D. Gillberg, K. Koeneke, A. Krasznahorkay et al., *Implementation of the ATLAS run 2 event data model*, *Journal of Physics: Conference Series* **664** (dec, 2015) 072045.

[95] J. M. Butterworth, A. R. Davison, M. Rubin and G. P. Salam, *Jet substructure as a new Higgs search channel at the LHC*, *Phys. Rev. Lett.* **100** (2008) 242001, [0802.2470].

[96] ATLAS collaboration, "First beam splashes of 2017 data taking at ATLAS."

https://atlas.cern/updates/atlas-news/beams-return-atlas-experiment, Retrieved July 2019.

[97] ATLAS collaboration, M. Aaboud et al., "Standard Model cross section measurement summary plot." https://atlas.web.cern.ch/Atlas/GROUPS/PHYSICS/CombinedSummaryPlots/SM/, Retrieved Aug 2019.

[98] A. Buckley, H. Hoeth, H. Lacker, H. Schulz and J. E. von Seggern, *Systematic event generator tuning for the LHC*, *Eur. Phys. J.* **C65** (2010) 331–357, [0907.2973].

[99] ATLAS collaboration, G. Aad et al., *The ATLAS Simulation Infrastructure*, *Eur. Phys. J.* **C70** (2010) 823–874, [1005.4568].

[100] GEANT4 collaboration, S. Agostinelli et al., *GEANT4: A Simulation toolkit*, *Nucl. Instrum. Meth.* **A506** (2003) 250–303.

[101] G. Cowan, *Statistical data analysis*. Oxford University Press, USA, 1998.

[102] G. D'Agostini, *A Multidimensional unfolding method based on Bayes' theorem*, *Nucl. Instrum. Meth.* **A362** (1995) 487–498.

[103] ATLAS collaboration, G. Choudalakis, *Unfolding in ATLAS*, in *Proceedings, PHYSTAT 2011 Workshop on Statistical Issues Related to Discovery Claims in Search Experiments and Unfolding, CERN,Geneva, Switzerland 17-20 January 2011*, (Geneva), pp. 297–308, CERN, CERN, 2011. 1104.2962. DOI.

[104] E. Maguire, L. Heinrich and G. Watt, *HEPData: a repository for high energy physics data*, *J. Phys. Conf. Ser.* **898** (2017) 102006, [1704.05473].

[105] M. Dobbs and J. B. Hansen, *The HepMC C++ Monte Carlo event record for High Energy Physics*, *Comput. Phys. Commun.* **134** (2001) 41–46.

[106] A. Buckley, J. Butterworth, L. Lonnblad, D. Grellscheid, H. Hoeth et al., *Rivet user manual*, *Comput.Phys.Commun.* **184** (2013) 2803–2819, [1003.0694].

[107] ATLAS collaboration, M. Aaboud et al., *Measurement of detector-corrected observables sensitive to the anomalous production of events with jets and large missing transverse momentum in pp collisions at* $\sqrt{\mathbf{s}} = \mathbf{13}$ *TeV using the ATLAS detector*, *Eur. Phys. J.* **C77** (2017) 765, [1707.03263].

[108] ATLAS collaboration, M. Aaboud et al., *Search for dark matter and other new phenomena in events with an energetic jet and large missing transverse momentum using the ATLAS detector*, *JHEP* **01** (2018) 126, [1711.03301].

[109] M. Rauch, *Vector-Boson Fusion and Vector-Boson Scattering*, 1610.08420.

[110] O. J. P. Eboli and D. Zeppenfeld, *Observing an invisible Higgs boson*, *Phys. Lett.* **B495** (2000) 147–154, [hep-ph/0009158].

[111] J. R. Andersen and J. M. Smillie, *QCD and electroweak interference in Higgs production by gauge boson fusion*, *Phys. Rev.* **D75** (2007) 037301, [hep-ph/0611281].

[112] ATLAS collaboration, G. Aad et al., *Search for invisible decays of a Higgs boson using vector-boson fusion in pp collisions at $\sqrt{s} = 8$ TeV with the ATLAS detector*, *JHEP* **01** (2016) 172, [1508.07869].

[113] ATLAS collaboration, G. Aad et al., *Measurement of the inclusive isolated prompt photon cross section in pp collisions at $\sqrt{s} = 8$ TeV with the ATLAS detector*, *JHEP* **08** (2016) 005, [1605.03495].

[114] S. Frixione, *Isolated photons in perturbative QCD*, *Phys. Lett.* **B429** (1998) 369–374, [hep-ph/9801442].

[115] J. Baglio et al., *Release Note - VBFNLO 2.7.0*, 1404.3940.

[116] Z. Bern, G. Diana, L. J. Dixon, F. Febres Cordero, S. Hoche, H. Ita et al., *Driving Missing Data at Next-to-Leading Order*, *Phys. Rev.* **D84** (2011) 114002, [1106.1423].

[117] J. M. Lindert et al., *Precise predictions for V+ jets dark matter backgrounds*, *Eur. Phys. J.* **C77** (2017) 829, [1705.04664].

[118] L. A. Harland-Lang, A. D. Martin, R. Nathvani and R. S. Thorne, *Ad Lucem: QED Parton Distribution Functions in the MMHT Framework*, 1907.02750.

[119] ATLAS collaboration, G. Aad et al., *Measurement of the electroweak production of dijets in association with a Z-boson and distributions sensitive to vector boson fusion in proton-proton collisions at $\sqrt{s} = 8$ TeV using the ATLAS detector*, *JHEP* **04** (2014) 031, [1401.7610].

[120] U. Haisch and G. Polesello, *Searching for dark matter in final states with two jets and missing transverse energy*, *JHEP* **02** (2019) 128, [1812.08129].

[121] R. D. Cousins, J. T. Linnemann and J. Tucker, *Evaluation of three methods for calculating statistical significance when incorporating a systematic uncertainty into a test of the background-only hypothesis for a poisson process*, *Nuclear Instruments and Methods in Physics Research Section A: Accelerators, Spectrometers, Detectors and Associated Equipment* **595** (2008) 480 – 501.

[122] G. Cowan, K. Cranmer, E. Gross and O. Vitells, *Power-Constrained Limits*, 1105.3166.

[123] ATLAS collaboration, M. Aaboud et al., *Combination of searches for invisible Higgs boson decays with the ATLAS experiment*, *Phys. Rev. Lett.* **122** (2019) 231801, [1904.05105].

[124] G. Busoni et al., *Recommendations on presenting LHC searches for missing transverse energy signals using simplified s-channel models of dark matter*, 1603.04156.

[125] ATLAS collaboration, M. Aaboud et al., *Measurement of the W-boson mass in pp collisions at $\sqrt{s} = 7$ TeV with the ATLAS detector*, *Eur. Phys. J.* **C78** (2018) 110, [1701.07240].

[126] D. Dercks, N. Desai, J. S. Kim, K. Rolbiecki, J. Tattersall and T. Weber, *CheckMATE 2: From the model to the limit*, *Comput. Phys. Commun.* **221** (2017) 383–418, [1611.09856].

[127] E. Conte, B. Dumont, B. Fuks and C. Wymant, *Designing and recasting LHC analyses with MadAnalysis 5*, *Eur. Phys. J.* **C74** (2014) 3103, [1405.3982].

[128] F. Ambrogi et al., *SModelS v1.2: long-lived particles, combination of signal regions, and other novelties*, 1811.10624.

[129] GAMBIT collaboration, P. Athron et al., *GAMBIT: The Global and Modular Beyond-the-Standard-Model Inference Tool*, *Eur. Phys. J.* **C77** (2017) 784, [1705.07908].

[130] GAMBIT collaboration, P. Athron et al., *Combined collider constraints on neutralinos and charginos*, *Eur. Phys. J.* **C79** (2019) 395, [1809.02097].

[131] K. Cranmer and I. Yavin, *RECAST: Extending the Impact of Existing Analyses*, *JHEP* **04** (2011) 038, [1010.2506].

[132] A. Alloul, N. D. Christensen, C. Degrande, C. Duhr and B. Fuks, *FeynRules 2.0 - A complete toolbox for tree-level phenomenology*, *Comput. Phys. Commun.* **185** (2014) 2250–2300, [1310.1921].

[133] C. Degrande, C. Duhr, B. Fuks, D. Grellscheid, O. Mattelaer and T. Reiter, *UFO - The Universal FeynRules Output*, *Comput. Phys. Commun.* **183** (2012) 1201–1214, [1108.2040].

[134] J. Alwall et al., *A Standard format for Les Houches event files*, *Comput. Phys. Commun.* **176** (2007) 300–304, [hep-ph/0609017].

[135] U. Haisch, F. Kahlhoefer and E. Re, *QCD effects in mono-jet searches for dark matter*, *JHEP* **12** (2013) 007, [1310.4491].

[136] ATLAS collaboration, G. Aad et al., *Search for a heavy charged boson in events with a*

charged lepton and missing transverse momentum from pp collisions at $\sqrt{s} = 13$ *TeV with the ATLAS detector*, 1906.05609.

[137] DELPHES 3 collaboration, J. de Favereau, C. Delaere, P. Demin, A. Giammanco, V. Lemaître, A. Mertens et al., *DELPHES 3, A modular framework for fast simulation of a generic collider experiment*, *JHEP* **02** (2014) 057, [1307.6346].

[138] L. Darmé and B. Fuks, *MadAnalysis5 implementation of the four-top analysis of CMS with 35.9 fb-1 of data (CMS-TOP-17-009)*, .

[139] G. Facini, K. Merkotan, M. Schott and A. Sydorenko, *On the Model Dependence of Fiducial Cross Section Measurements in View of Reinterpretations*, 1906.01278.

[140] CMS collaboration, S. Chatrchyan et al., *Measurement of the ratio of inclusive jet cross sections using the anti-*k_T *algorithm with radius parameters R=0.5 and 0.7 in pp collisions at* $\sqrt{s} = 7$ *TeV*, *Phys. Rev.* **D90** (2014) 072006, [1406.0324].

[141] L. Demortier, *P values and nuisance parameters*, in *Statistical issues for LHC physics. Proceedings, Workshop, PHYSTAT-LHC, Geneva, Switzerland, June 27-29, 2007*, pp. 23–33, 2007.

[142] G. Cowan, K. Cranmer, E. Gross and O. Vitells, *Asymptotic formulae for likelihood-based tests of new physics*, *Eur. Phys. J.* **C71** (2011) 1554, [1007.1727].

[143] S. S. Wilks, *The Large-Sample Distribution of the Likelihood Ratio for Testing Composite Hypotheses*, *Annals Math. Statist.* **9** (1938) 60–62.

[144] A. Wald, *An extension of Wilks' method for setting tolerance limits*, *Annals Math. Statist.* **14** (Mar., 1943) 45–55.

[145] J. M. Butterworth, D. Grellscheid, M. Krämer, B. Sarrazin and D. Yallup, *Constraining new physics with collider measurements of Standard Model signatures*, *JHEP* **03** (2017) 078, [1606.05296].

[146] T. Junk, *Confidence level computation for combining searches with small statistics*, *Nucl. Instrum. Meth.* **A434** (1999) 435–443, [hep-ex/9902006].

[147] A. L. Read, *Presentation of search results: The CL(s) technique*, *J. Phys.* **G28** (2002) 2693–2704.

[148] G. J. Feldman and R. D. Cousins, *A Unified approach to the classical statistical analysis of small signals*, *Phys. Rev.* **D57** (1998) 3873–3889, [physics/9711021].

[149] E. Gross, *LHC Statistics for Pedestrians*, *10.5170/CERN-2008-001.205* (2008) .

[150] A. Buckley, M. Citron, S. Fichet, S. Kraml, W. Waltenberger and N. Wardle, *The Simplified Likelihood Framework*, *JHEP* **04** (2019) 064, [1809.05548].

[151] GAMBIT collaboration, G. D. Martinez, J. McKay, B. Farmer, P. Scott, E. Roebber, A. Putze et al., *Comparison of statistical sampling methods with ScannerBit, the GAMBIT scanning module*, *Eur. Phys. J.* **C77** (2017) 761, [1705.07959].

[152] ATLAS collaboration, G. Aad et al., *Summary of the ATLAS experiment's sensitivity to supersymmetry after LHC Run 1 — interpreted in the phenomenological MSSM*, *JHEP* **10** (2015) 134, [1508.06608].

[153] F. Chollet et al., "Keras." https://keras.io, 2014.

[154] L. Moneta, K. Belasco, K. Cranmer, A. Lazzaro, D. Piparo, G. Schott et al., *The RooStats Project*, *PoS* **ACAT2010** (Sep, 2010) 057.

[155] R. Brun and F. Rademakers, *ROOT: An object oriented data analysis framework*, *Nucl. Instrum. Meth.* **A389** (1997) 81–86.

[156] M. Foord, N. Larosa, R. Dennis and E. Courtwright, "Configobj - pythonic config files." https://github.com/DiffSK/configobj, 2015.

[157] M. Gigg and P. Richardson, *Simulation of beyond standard model physics in Herwig++*, *Eur. Phys. J.* **C51** (2007) 989–1008, [hep-ph/0703199].

[158] ATLAS collaboration, G. Aad et al., *Measurement of the inclusive jet cross-section in proton-proton collisions at $\sqrt{s} = 7$ TeV using 4.5 fb^{-1} of data with the ATLAS detector*, *JHEP* **02** (2015) 153, [1410.8857].

[159] ATLAS collaboration, G. Aad et al., *Measurement of dijet cross sections in pp collisions at 7 TeV centre-of-mass energy using the ATLAS detector*, *JHEP* **05** (2014) 059, [1312.3524].

[160] ATLAS collaboration, G. Aad et al., *Measurement of three-jet production cross-sections in pp collisions at 7 TeV centre-of-mass energy using the ATLAS detector*, *Eur. Phys. J.* **C75** (2015) 228, [1411.1855].

[161] ATLAS collaboration, G. Aad et al., *Measurements of jet vetoes and azimuthal decorrelations in dijet events produced in pp collisions at $\sqrt{s} = 7$ TeV using the ATLAS detector*, *Eur. Phys. J.* **C74** (2014) 3117, [1407.5756].

[162] ATLAS collaboration, G. Aad et al., *Measurement of four-jet differential cross sections in $\sqrt{s} = 8$ TeV proton-proton collisions using the ATLAS detector*, *JHEP* **12** (2015) 105, [1509.07335].

[163] ATLAS collaboration, G. Aad et al., *Measurements of the W production cross sections in association with jets with the ATLAS detector*, *Eur. Phys. J.* **C75** (2015) 82, [1409.8639].

[164] CMS collaboration, V. Khachatryan et al., *Measurements of jet multiplicity and differential production cross sections of Z+ jets events in proton-proton collisions at* $\sqrt{s} = 7$ *TeV*, *Phys. Rev.* **D91** (2015) 052008, [1408.3104].

[165] CMS collaboration, V. Khachatryan et al., *Differential cross section measurements for the production of a W boson in association with jets in proton–proton collisions at* $\sqrt{s} = 7$ *TeV*, *Phys. Lett.* **B741** (2015) 12–37, [1406.7533].

[166] ATLAS collaboration, G. Aad et al., *Measurement of the inclusive isolated prompt photons cross section in pp collisions at* $\sqrt{s} = 7$ *TeV with the ATLAS detector using 4.6* fb^{-1}, *Phys. Rev.* **D89** (2014) 052004, [1311.1440].

[167] ATLAS collaboration, G. Aad et al., *Measurement of the production cross section of an isolated photon associated with jets in proton-proton collisions at* $\sqrt{s} = 7$ *TeV with the ATLAS detector*, *Phys. Rev.* **D85** (2012) 092014, [1203.3161].

[168] CMS collaboration, S. Chatrchyan et al., *Measurement of the triple-differential cross section for photon+jets production in proton-proton collisions at* $\sqrt{s}$*=7 TeV*, *JHEP* **06** (2014) 009, [1311.6141].

[169] ATLAS collaboration, G. Aad et al., *Measurement of isolated-photon pair production in pp collisions at* $\sqrt{s} = 7$ *TeV with the ATLAS detector*, *JHEP* **01** (2013) 086, [1211.1913].

[170] ATLAS collaboration, G. Aad et al., *Measurement of ZZ production in pp collisions at* $\sqrt{s} = 7$ *TeV and limits on anomalous ZZZ and ZZ*γ *couplings with the ATLAS detector*, *JHEP* **03** (2013) 128, [1211.6096].

[171] ATLAS collaboration, G. Aad et al., *Measurements of* $W\gamma$ *and* $Z\gamma$ *production in pp collisions at* $\sqrt{s}$*=7 TeV with the ATLAS detector at the LHC*, *Phys. Rev.* **D87** (2013) 112003, [1302.1283].

[172] T. E. Oliphant, *Python for scientific computing*, *Computing in Science & Engineering* **9** (2007) 10–20.

[173] J. D. Hunter, *Matplotlib: A 2d graphics environment*, *Computing in Science & Engineering* **9** (2007) 90–95.

[174] The Mathworks, Inc., Natick, Massachusetts, *MATLAB version 9.3.0.713579 (R2017b)*, 2017.

[175] D. Yallup, "BSM Constraints from Standard Model measurements with Contur." To appear in Rencontres de Moriond Electroweak proceedings, 2019.

[176] S. Amrith, J. M. Butterworth, F. F. Deppisch, W. Liu, A. Varma and D. Yallup, *LHC Constraints on a $B-L$ Gauge Model using Contur*, 1811.11452.

[177] M. van Beekveld, S. Caron and R. Ruiz de Austri, *The current status of fine-tuning in supersymmetry*, 1906.10706.

[178] LHCb collaboration, R. Aaij et al., *Search for lepton-universality violation in $B^+ \to K^+ \ell^+ \ell^-$ decays*, *Phys. Rev. Lett.* **122** (2019) 191801, [1903.09252].

[179] B. C. Allanach, J. M. Butterworth and T. Corbett, *Collider Constraints on Z' Models for Neutral Current $B-$Anomalies*, *JHEP* **08** (2019) 106, [1904.10954].

[180] J. Ellis, C. W. Murphy, V. Sanz and T. You, *Updated Global SMEFT Fit to Higgs, Diboson and Electroweak Data*, *JHEP* **06** (2018) 146, [1803.03252].

[181] A. Buckley, C. Englert, J. Ferrando, D. J. Miller, L. Moore, M. Russell et al., *Global fit of top quark effective theory to data*, *Phys. Rev.* **D92** (2015) 091501, [1506.08845].

[182] Planck collaboration, P. A. R. Ade et al., *Planck 2015 results. XIII. Cosmological parameters*, *Astron. Astrophys.* **594** (2016) A13, [1502.01589].

[183] LUX collaboration, D. S. Akerib et al., *Results from a search for dark matter in the complete LUX exposure*, *Phys. Rev. Lett.* **118** (2017) 021303, [1608.07648].

[184] M. Milgrom, *A Modification of the Newtonian dynamics as a possible alternative to the hidden mass hypothesis*, *Astrophys. J.* **270** (1983) 365–370.

[185] V. Springel et al., *Simulating the joint evolution of quasars, galaxies and their large-scale distribution*, *Nature* **435** (2005) 629–636, [astro-ph/0504097].

[186] D. Abercrombie et al., *Dark Matter Benchmark Models for Early LHC Run-2 Searches: Report of the ATLAS/CMS Dark Matter Forum*, tech. rep., 2015.

[187] A. Albert et al., *Recommendations of the LHC Dark Matter Working Group: Comparing LHC searches for heavy mediators of dark matter production in visible and invisible decay channels*, 1703.05703.

[188] H. Ruegg and M. Ruiz-Altaba, *The Stueckelberg field*, *Int. J. Mod. Phys.* **A19** (2004) 3265–3348, [hep-th/0304245].

[189] T. Jacques, A. Katz, E. Morgante, D. Racco, M. Rameez and A. Riotto, *Complementarity of DM Searches in a Consistent Simplified Model: the Case of Z'*,

1605.06513.

[190] M. Backović, M. Krämer, F. Maltoni, A. Martini, K. Mawatari and M. Pellen, *Higher-order QCD predictions for dark matter production at the LHC in simplified models with s-channel mediators*, *Eur. Phys. J.* **C75** (2015) 482, [1508.05327].

[191] ATLAS collaboration, M. Aaboud et al., *Search for low-mass resonances decaying into two jets and produced in association with a photon using pp collisions at $\sqrt{s} = 13$ TeV with the ATLAS detector*, *Phys. Lett.* **B795** (2019) 56–75, [1901.10917].

[192] G. Busoni, A. De Simone, T. Jacques, E. Morgante and A. Riotto, *Making the Most of the Relic Density for Dark Matter Searches at the LHC 14 TeV Run*, *JCAP* **1503** (2015) 022, [1410.7409].

[193] C. Englert, M. McCullough and M. Spannowsky, *S-Channel Dark Matter Simplified Models and Unitarity*, 1604.07975.

[194] F. Kahlhoefer, K. Schmidt-Hoberg, T. Schwetz and S. Vogl, *Implications of unitarity and gauge invariance for simplified dark matter models*, *JHEP* **02** (2016) 016, [1510.02110].

[195] J. Butterworth, *BSM constraints from model-independent measurements: A Contur Update*, *J. Phys. Conf. Ser.* **1271** (2019) 012013, [1902.03067].

[196] CMS collaboration, V. Khachatryan et al., *Measurement of the integrated and differential $t\bar{t}$ production cross sections for high-p_t top quarks in pp collisions at $\sqrt{s} = 8$ TeV*, *Phys. Rev.* **D94** (2016) 072002, [1605.00116].

[197] ATLAS collaboration, M. Aaboud et al., *Measurement of jet activity produced in top-quark events with an electron, a muon and two b-tagged jets in the final state in pp collisions at $\sqrt{s} = 13$ TeV with the ATLAS detector*, *Eur. Phys. J.* **C77** (2017) 220, [1610.09978].

[198] ATLAS collaboration, M. Aaboud et al., *Constraints on mediator-based dark matter and scalar dark energy models using $\sqrt{s} = 13$ TeV pp collision data collected by the ATLAS detector*, *JHEP* **05** (2019) 142, [1903.01400].

[199] F. F. Deppisch, W. Liu and M. Mitra, *Long-lived Heavy Neutrinos from Higgs Decays*, *JHEP* **08** (2018) 181, [1804.04075].

[200] S. Banerjee, M. Mitra and M. Spannowsky, *Searching for a Heavy Higgs boson in a Higgs-portal B-L Model*, *Phys. Rev.* **D92** (2015) 055013, [1506.06415].

[201] P. Ilten, Y. Soreq, M. Williams and W. Xue, *Serendipity in dark photon searches*, *JHEP* **06** (2018) 004, [1801.04847].

[202] CMS collaboration, V. Khachatryan et al., *Search for heavy Majorana neutrinos in $\mu^{\pm}\mu^{\pm}$ + jets events in proton-proton collisions at $\sqrt{s} = 8$ TeV*, *Phys. Lett.* **B748** (2015) 144–166, [1501.05566].

[203] J. Chakrabortty, P. Konar and T. Mondal, *Constraining a class of B-L extended models from vacuum stability and perturbativity*, *Phys. Rev.* **D89** (2014) 056014, [1308.1291].

[204] D. López-Val and T. Robens, *Δr and the W-boson mass in the singlet extension of the standard model*, *Phys. Rev.* **D90** (2014) 114018, [1406.1043].

[205] T. Robens and T. Stefaniak, *Status of the Higgs Singlet Extension of the Standard Model after LHC Run 1*, *Eur. Phys. J.* **C75** (2015) 104, [1501.02234].

[206] M. Lindner, F. S. Queiroz, W. Rodejohann and X.-J. Xu, *Neutrino-electron scattering: general constraints on $Z^{'}$ and dark photon models*, *JHEP* **05** (2018) 098, [1803.00060].

[207] B. Batell, M. Pospelov and B. Shuve, *Shedding Light on Neutrino Masses with Dark Forces*, *JHEP* **08** (2016) 052, [1604.06099].

[208] LHCb collaboration, R. Aaij et al., *Search for Dark Photons Produced in 13 TeV pp Collisions*, *Phys. Rev. Lett.* **120** (2018) 061801, [1710.02867].

[209] ATLAS collaboration, M. Aaboud et al., *Search for new high-mass phenomena in the dilepton final state using 36 fb^{-1} of proton-proton collision data at $\sqrt{s} = 13$ TeV with the ATLAS detector*, *JHEP* **10** (2017) 182, [1707.02424].

[210] ATLAS collaboration, G. Aad et al., *Measurement of the low-mass Drell-Yan differential cross section at $\sqrt{s} = 7$ TeV using the ATLAS detector*, *JHEP* **06** (2014) 112, [1404.1212].

[211] ATLAS collaboration, G. Aad et al., *Measurement of the transverse momentum and ϕ^*_η distributions of Drell–Yan lepton pairs in proton–proton collisions at $\sqrt{s} = 8$ TeV with the ATLAS detector*, *Eur. Phys. J.* **C76** (2016) 291, [1512.02192].

[212] ATLAS collaboration, G. Aad et al., *Measurement of the double-differential high-mass Drell-Yan cross section in pp collisions at $\sqrt{s} = 8$ TeV with the ATLAS detector*, *JHEP* **08** (2016) 009, [1606.01736].

[213] ATLAS collaboration, M. Aaboud et al., *Search for triboson $W^{\pm}W^{\pm}W^{\mp}$ production in pp collisions at $\sqrt{s} = 8$ TeV with the ATLAS detector*, *Eur. Phys. J.* **C77** (2017) 141, [1610.05088].

[214] ATLAS collaboration, G. Aad et al., *Measurements of $Z\gamma$ and $Z\gamma\gamma$ production in pp collisions at $\sqrt{s} = 8$ TeV with the ATLAS detector*, *Phys. Rev.* **D93** (2016) 112002,

[1604.05232].

[215] ATLAS collaboration, M. Aaboud et al., *Measurement of the k_t splitting scales in $Z \to \ell\ell$ events in pp collisions at $\sqrt{s} = 8$ TeV with the ATLAS detector*, *JHEP* **08** (2017) 026, [1704.01530].

[216] ATLAS collaboration, G. Aad et al., *Measurements of four-lepton production in pp collisions at $\sqrt{s} = 8$ TeV with the ATLAS detector*, *Phys. Lett.* **B753** (2016) 552–572, [1509.07844].

[217] ATLAS collaboration, G. Aad et al., *Fiducial and differential cross sections of Higgs boson production measured in the four-lepton decay channel in pp collisions at $\sqrt{s}$=8 TeV with the ATLAS detector*, *Phys. Lett.* **B738** (2014) 234–253, [1408.3226].

[218] ATLAS collaboration, G. Aad et al., *Measurement of total and differential W^+W^- production cross sections in proton-proton collisions at $\sqrt{s} = 8$ TeV with the ATLAS detector and limits on anomalous triple-gauge-boson couplings*, *JHEP* **09** (2016) 029, [1603.01702].

[219] CMS collaboration, V. Khachatryan et al., *Measurements of the associated production of a Z boson and b jets in pp collisions at $\sqrt{s} = 8$ TeV*, *Eur. Phys. J.* **C77** (2017) 751, [1611.06507].

[220] LHCb collaboration, R. Aaij et al., *Study of forward Z + jet production in pp collisions at $\sqrt{s} = 7$ TeV*, *JHEP* **01** (2014) 033, [1310.8197].

[221] G. M. Pruna, *Phenomenology of the minimal $B - L$ Model: the Higgs sector at the Large Hadron Collider and future Linear Colliders*. PhD thesis, Southampton U., 2011. 1106.4691.

[222] CMS collaboration, V. Khachatryan et al., *Precise determination of the mass of the Higgs boson and tests of compatibility of its couplings with the standard model predictions using proton collisions at 7 and 8 TeV*, *Eur. Phys. J.* **C75** (2015) 212, [1412.8662].

[223] N. Berger et al., *Simplified Template Cross Sections - Stage 1.1*, 1906.02754.

[224] ATLAS collaboration, M. Aaboud et al., *$ZZ \to \ell^+\ell^-\ell'^+\ell'^-$ cross-section measurements and search for anomalous triple gauge couplings in 13 TeV pp collisions with the ATLAS detector*, *Phys. Rev.* **D97** (2018) 032005, [1709.07703].

[225] S. Catani, L. Cieri, D. de Florian, G. Ferrera and M. Grazzini, *Diphoton production at the LHC: a QCD study up to NNLO*, *JHEP* **04** (2018) 142, [1802.02095].

[226] M. Bauer, M. Neubert and A. Thamm, *Collider Probes of Axion-Like Particles*, *JHEP*

12 (2017) 044, [1708.00443].

[227] G. Brooijmans et al., *Les Houches 2017: Physics at TeV Colliders New Physics Working Group Report*, in *Les Houches 2017: Physics at TeV Colliders New Physics Working Group Report*, 2018. 1803.10379.

[228] M. Bauer, U. Haisch and F. Kahlhoefer, *Simplified dark matter models with two Higgs doublets: I. Pseudoscalar mediators*, *JHEP* **05** (2017) 138, [1701.07427].

[229] CMS collaboration, A. M. Sirunyan et al., *Measurement of differential cross sections for the production of top quark pairs and of additional jets in lepton+jets events from pp collisions at* $\sqrt{s} = 13$ *TeV*, *Phys. Rev.* **D97** (2018) 112003, [1803.08856].

[230] ATLAS collaboration, M. Aaboud et al., *Measurement of the* $W^{\pm}Z$ *boson pair-production cross section in pp collisions at* $\sqrt{s} = 13$ *TeV with the ATLAS Detector*, *Phys. Lett.* **B762** (2016) 1–22, [1606.04017].

[231] ATLAS collaboration, M. Aaboud et al., *Measurement of the four-lepton invariant mass spectrum in 13 TeV proton-proton collisions with the ATLAS detector*, tech. rep., CERN, 2019.

[232] ATLAS collaboration, M. Aaboud et al., *Measurements of the production cross section of a Z boson in association with jets in pp collisions at* $\sqrt{s} = 13$ *TeV with the ATLAS detector*, *Eur. Phys. J.* **C77** (2017) 361, [1702.05725].

[233] ATLAS collaboration, M. Aaboud et al., *Searches for scalar leptoquarks and differential cross-section measurements in dilepton-dijet events in proton-proton collisions at a centre-of-mass energy of* $\sqrt{s} = 13$ *TeV with the ATLAS experiment*, *Eur. Phys. J.* **C79** (2019) 733, [1902.00377].

[234] ATLAS collaboration, M. Aaboud et al., *Measurement of the cross section for isolated-photon plus jet production in pp collisions at* $\sqrt{s} = 13$ *TeV using the ATLAS detector*, *Phys. Lett.* **B780** (2018) 578–602, [1801.00112].

[235] ATLAS collaboration, G. Aad et al., *Search for high-mass dilepton resonances using 139* fb^{-1} *of pp collision data collected at* $\sqrt{s} = 13$ *TeV with the ATLAS detector*, *Phys. Lett.* **B796** (2019) 68–87, [1903.06248].

[236] ATLAS collaboration, M. Aaboud et al., *Measurement of inclusive jet and dijet cross-sections in proton-proton collisions at* $\sqrt{s} = 13$ *TeV with the ATLAS detector*, *JHEP* **05** (2018) 195, [1711.02692].

[237] ATLAS collaboration, M. Aaboud et al., *Measurement of jet-substructure observables in top quark, W boson and light jet production in proton-proton collisions at* $\sqrt{s} = 13$ *TeV*

with the ATLAS detector, *JHEP* **08** (2019) 033, [1903.02942].

[238] ATLAS collaboration, M. Aaboud et al., *Measurements of differential cross sections of top quark pair production in association with jets in pp collisions at* $\sqrt{s} = 13$ *TeV using the ATLAS detector*, *JHEP* **10** (2018) 159, [1802.06572].

[239] ATLAS collaboration, M. Aaboud et al., *Measurements of top-quark pair differential cross-sections in the lepton+jets channel in pp collisions at* $\sqrt{s} = 13$ *TeV using the ATLAS detector*, *JHEP* **11** (2017) 191, [1708.00727].

[240] ATLAS collaboration, M. Aaboud et al., *Measurements of inclusive and differential fiducial cross-sections of* $t\bar{t}$ *production with additional heavy-flavour jets in proton-proton collisions at* $\sqrt{s} = 13$ *TeV with the ATLAS detector*, *JHEP* **04** (2019) 046, [1811.12113].

[241] ATLAS collaboration, M. Aaboud et al., *Search for squarks and gluinos in final states with jets and missing transverse momentum at* $\sqrt{s} = 13$ *TeV with the ATLAS detector*, *Eur. Phys. J.* **C76** (2016) 392, [1605.03814].

[242] ATLAS collaboration, M. Aaboud et al., *Measurements of* $t\bar{t}$ *differential cross-sections of highly boosted top quarks decaying to all-hadronic final states in pp collisions at* $\sqrt{s} = 13$ *TeV using the ATLAS detector*, *Phys. Rev.* **D98** (2018) 012003, [1801.02052].

[243] ATLAS collaboration, M. Aaboud et al., *Precision measurement and interpretation of inclusive* W^+ *,* W^- *and* Z/γ^* *production cross sections with the ATLAS detector*, *Eur. Phys. J.* **C77** (2017) 367, [1612.03016].

[244] ATLAS collaboration, G. Aad et al., *Measurement of differential production cross-sections for a* Z *boson in association with b-jets in 7 TeV proton-proton collisions with the ATLAS detector*, *JHEP* **10** (2014) 141, [1407.3643].

[245] ATLAS collaboration, G. Aad et al., *Measurement of the cross-section for* W *boson production in association with b-jets in pp collisions at* $\sqrt{s} = 7$ *TeV with the ATLAS detector*, *JHEP* **06** (2013) 084, [1302.2929].

[246] ATLAS collaboration, G. Aad et al., *Dynamics of isolated-photon plus jet production in pp collisions at* $\sqrt{(s)} = 7$ *TeV with the ATLAS detector*, *Nucl. Phys.* **B875** (2013) 483–535, [1307.6795].

[247] ATLAS collaboration, G. Aad et al., *Measurement of the production cross section of an isolated photon associated with jets in proton-proton collisions at* $\sqrt{s} = 7$ *TeV with the ATLAS detector*, *Phys. Rev.* **D85** (2012) 092014, [1203.3161].

[248] ATLAS collaboration, G. Aad et al., *Measurement of the high-mass Drell–Yan differential cross-section in pp collisions at sqrt(s)=7 TeV with the ATLAS detector*,

Phys. Lett. **B725** (2013) 223–242, [1305.4192].

[249] ATLAS collaboration, G. Aad et al., *Measurement of the production of a W boson in association with a charm quark in pp collisions at $\sqrt{s} = 7$ TeV with the ATLAS detector*, *JHEP* **05** (2014) 068, [1402.6263].

[250] ATLAS collaboration, G. Aad et al., *Differential top-antitop cross-section measurements as a function of observables constructed from final-state particles using pp collisions at $\sqrt{s} = 7$ TeV in the ATLAS detector*, *JHEP* **06** (2015) 100, [1502.05923].

[251] ATLAS collaboration, G. Aad et al., *Measurement of W^+W^- production in pp collisions at $\sqrt{s}$=7 TeV with the ATLAS detector and limits on anomalous WWZ and $WW\gamma$ couplings*, *Phys. Rev.* **D87** (2013) 112001, [1210.2979].

[252] ATLAS collaboration, M. Aaboud et al., *Measurements of electroweak Wjj production and constraints on anomalous gauge couplings with the ATLAS detector*, *Eur. Phys. J.* **C77** (2017) 474, [1703.04362].

[253] ATLAS collaboration, M. Aaboud et al., *Measurements of integrated and differential cross sections for isolated photon pair production in pp collisions at $\sqrt{s} = 8$ TeV with the ATLAS detector*, *Phys. Rev.* **D95** (2017) 112005, [1704.03839].

[254] ATLAS collaboration, M. Aaboud et al., *Measurement of differential cross sections of isolated-photon plus heavy-flavour jet production in pp collisions at $\sqrt{s} = 8$ TeV using the ATLAS detector*, *Phys. Lett.* **B776** (2018) 295–317, [1710.09560].

[255] ATLAS collaboration, G. Aad et al., *Measurements of fiducial and differential cross sections for Higgs boson production in the diphoton decay channel at $\sqrt{s} = 8$ TeV with ATLAS*, *JHEP* **09** (2014) 112, [1407.4222].

[256] ATLAS collaboration, M. Aaboud et al., *Measurement of the production cross section of three isolated photons in pp collisions at $\sqrt{s} = 8$ TeV using the ATLAS detector*, *Phys. Lett.* **B781** (2018) 55–76, [1712.07291].

[257] ATLAS collaboration, M. Aaboud et al., *Measurement of the inclusive jet cross-sections in proton-proton collisions at $\sqrt{s} = 8$ TeV with the ATLAS detector*, *JHEP* **09** (2017) 020, [1706.03192].

[258] ATLAS collaboration, M. Aaboud et al., *Measurement of b-hadron pair production with the ATLAS detector in proton-proton collisions at $\sqrt{s} = 8$ TeV*, *JHEP* **11** (2017) 062, [1705.03374].

[259] ATLAS collaboration, G. Aad et al., *Measurements of top-quark pair differential cross-sections in the lepton+jets channel in pp collisions at $\sqrt{s} = 8$ TeV using the*

ATLAS detector, *Eur. Phys. J.* **C76** (2016) 538, [1511.04716].

[260] ATLAS collaboration, G. Aad et al., *Measurement of the differential cross-section of highly boosted top quarks as a function of their transverse momentum in* $\sqrt{s} = 8$ *TeV proton-proton collisions using the ATLAS detector*, *Phys. Rev.* **D93** (2016) 032009, [1510.03818].

[261] ATLAS collaboration, G. Aad et al., *Measurement of fiducial differential cross sections of gluon-fusion production of Higgs bosons decaying to* $WW^* \to e\nu\mu\mu$ *with the ATLAS detector at* $\sqrt{s} = 8$ *TeV*, *JHEP* **08** (2016) 104, [1604.02997].

[262] CMS collaboration, A. M. Sirunyan et al., *Measurement of the differential Drell-Yan cross section in proton-proton collisions at* $\sqrt{s} = 13$ *TeV*, *JHEP* **12** (2019) 059, [1812.10529].

[263] CMS collaboration, A. M. Sirunyan et al., *Measurements of the differential jet cross section as a function of the jet mass in dijet events from proton-proton collisions at* $\sqrt{s} = 13$ *TeV*, *JHEP* **11** (2018) 113, [1807.05974].

[264] CMS collaboration, V. Khachatryan et al., *Measurement of the double-differential inclusive jet cross section in proton-proton collisions at sqrt(s) = 13 TeV*, 1605.04436.

[265] CMS collaboration, V. Khachatryan et al., *Measurement of differential cross sections for top quark pair production using the lepton+jets final state in proton-proton collisions at 13 TeV*, *Phys. Rev.* **D95** (2017) 092001, [1610.04191].

[266] CMS collaboration, A. M. Sirunyan et al., *Measurements of differential cross sections of top quark pair production as a function of kinematic event variables in proton-proton collisions at* $\sqrt{s} = 13$ *TeV*, *JHEP* **06** (2018) 002, [1803.03991].

[267] CMS collaboration, A. M. Sirunyan et al., *Measurement of the differential cross sections for the associated production of a* W *boson and jets in proton-proton collisions at* $\sqrt{s} = 13$ *TeV*, *Phys. Rev.* **D96** (2017) 072005, [1707.05979].

[268] CMS collaboration, S. Chatrchyan et al., *Studies of jet mass in dijet and W/Z + jet events*, *JHEP* **05** (2013) 090, [1303.4811].

[269] CMS collaboration, S. Chatrchyan et al., *Measurement of Four-Jet Production in Proton-Proton Collisions at* $\sqrt{s} = 7$ *TeV*, *Phys. Rev.* **D89** (2014) 092010, [1312.6440].

[270] CMS Collaboration collaboration, S. Chatrchyan et al., *Measurements of differential jet cross sections in proton-proton collisions at* $\sqrt{s} = 7$ *TeV with the CMS detector*, *Phys.Rev.* **D87** (2013) 112002, [1212.6660].

[271] CMS Collaboration collaboration, S. Chatrchyan et al., *Measurement of the cross section and angular correlations for associated production of a Z boson with b-hadrons in pp collisions at $\sqrt{s} = 7$ TeV*, *JHEP* **1312** (2013) 039, [1310.1349].

[272] CMS collaboration, V. Khachatryan et al., *Measurement of the WZ production cross section in pp collisions at $\sqrt{s} = 7$ and 8 TeV and search for anomalous triple gauge couplings at $\sqrt{s} = 8$ TeV*, *Eur. Phys. J.* **C77** (2017) 236, [1609.05721].

[273] CMS collaboration, A. M. Sirunyan et al., *Measurement of the triple-differential dijet cross section in proton-proton collisions at $\sqrt{s} = 8$ TeV and constraints on parton distribution functions*, *Eur. Phys. J.* **C77** (2017) 746, [1705.02628].

[274] CMS collaboration, V. Khachatryan et al., *Measurement and QCD analysis of double-differential inclusive jet cross sections in pp collisions at $\sqrt{s} = 8$ TeV and cross section ratios to 2.76 and 7 TeV*, *JHEP* **03** (2017) 156, [1609.05331].

[275] CMS collaboration, A. M. Sirunyan et al., *Measurement of the jet mass in highly boosted $\mathrm{t\bar{t}}$ events from pp collisions at $\sqrt{s} = 8$ TeV*, *Eur. Phys. J.* **C77** (2017) 467, [1703.06330].

[276] CMS collaboration, V. Khachatryan et al., *Measurements of differential cross sections for associated production of a W boson and jets in proton-proton collisions at $\sqrt{s} = 8$ TeV*, *Phys. Rev.* **D95** (2017) 052002, [1610.04222].

[277] CMS collaboration, V. Khachatryan et al., *Measurement of the transverse momentum spectrum of the Higgs boson produced in pp collisions at $\sqrt{s} = 8$ TeV using $H \to WW$ decays*, *JHEP* **03** (2017) 032, [1606.01522].

[278] LHCb collaboration, R. Aaij et al., *Measurement of the cross-section for $Z \to e^+e^-$ production in pp collisions at $\sqrt{s} = 7$ TeV*, *JHEP* **02** (2013) 106, [1212.4620].

List of figures

List of tables